Eruption Dynamics of Vulcanian and Sub-Plinian Volcanoes:

From the Generation of Pulses to the Formation of Clouds

Zur Erlangung des Doktorgrades der Naturwissenschaften im Department Geowissenschaften der Universität Hamburg

vorgelegt von

Lea Scharff

aus

Uelzen

Hamburg

2012

Als Dissertation angenommen vom Fachbereich Geowissenschaften
der Universität Hamburg

Auf Grund der Gutachten von Prof. Dr. Matthias Hort
und PD Dr. Armin Freundt

Hamburg, den 11. Juli 2012

Prof. Dr. Jürgen Oßenbrügge
Leiter des Fachbereichs Geowissenschaften

Zusammenfassung

Das Verständnis der Eruptionsdynamik ist ein Schlüsselfaktor in der Vorhersage des Ascheeintrags und atmosphärischen Aschetransports. Für diese Voraussage sind präzise Messungen des Masseflusses am Schlotausgang und in den ersten hundert Metern der Eruptionswolkenbildung notwendig. Mit der Dopplerradar-Technik werden die Partikelgeschwindigkeiten und ein Schätzwert für den Massefluss gemessen. Sie wird hier in zwei Experimenten an den Vulkanen Santiaguito in Guatemala und Colima in Mexiko verwendet, um die Dynamik in der Nähe des Schlotausgangs zu bestimmen.

Mit Hilfe des Dopplerradars kann ich zeigen, dass die Eruptionen am Vulkan Santiaguito aus mehreren, aufeinander folgenden, explosiven Entgasungen mit einer Frequenz von 0,2 bis 0,3 Hz bestehen. In vier Tagen und Nächten wurden insgesamt 157 Ereignisse beobachtet. Die Dopplerradar-Daten zeigen eine vertikale Hebung der Domoberfläche unmittelbar vor der ersten explosiven Entgasung, welche Partikelgeschwindigkeiten im Bereich von 10 bis 15 m/s (parallel zum Radarstrahl) aufweist. In 80% der beobachteten Eruptionen tritt ein zweiter Entgasungspuls mit deutlich höheren Partikelgeschwindigkeiten (20–25 m/s auch parallel zum Radarstrahl) und erhöhter Echoleistung auf. Letztere deutet auf einen größeren Massefluss hin. Mit Hilfe eines numerischen Modells für ballistischen Transport von Partikeln und der Berechnung der entsprechenden synthetischen Radarsignale kann ich zeigen, dass die Beobachtungen einer gepulsten Freisetzung von Material entsprechen.

Um die mögliche Ursache gepulster Events zu erklären, habe ich zwei einfache mechanische Modelle entwickelt: (A) eine vertikal oszillierende kompressible Magmasäule und (B) eine feste Gesteinskappe, die die Domoberfläche darstellt und auf einer an Gasblasen reichen Magmaschicht ruht, die mittels einer Schicht heißen vulkanischen Gases angenähert wird. Diese Modelle sind durch das Wissen inspiriert, dass das hochviskose Magma beim Aufstieg durch den Schlot an den Schlotwänden hohen Scherspannungen ausgesetzt ist und dadurch fragmentiert: Eine kontinuierliche Versorgung mit Magma aus der Tiefe erhöht die Schubspannungen in der darüber liegenden Magmasäule bis die Festigkeit an den Schlotwänden überschritten und die gesamte Magmasäule mechanisch von dem umgebenden Gestein entkoppelt wird. Dabei wird die Magmasäule ein kleines Stück nach oben geschoben. In Modell (A) wird, vorausgesetzt das Magma ist kompressibel, diese plötzliche Verschiebung der Magmasäule longitudinale Schwingungen der Säule selbst auslösen. Schwingungsamplitude und Frequenz hängen in diesem Fall vom Kompressionsmodul des Magmas (10^7–10^9 Pa), bzw. der Länge der schwingenden Magmasäule ab (hier 50 bis 400 m). In Modell (B) kompri-

miert die plötzliche Aufwärtsbewegung der Magmasäule die darüberliegende Schicht aus hypothetischem, blasenreichen Magma, das zwischen der Magmasäule und der darüberliegenden Gesteinskappe liegt. Druckaufbau im Inneren dieser Schicht bewirkt eine Anhebung der Gesteinskappe mit gleichzeitigem Ausströmen von Gas. Die Kappe sinkt aufgrund ihres Gewichts aber wieder zurück. Diese wiederholte Bewegung kann als eine Oszillation der Domoberfläche beobachtet werden. Eine Gasschicht von 0,5 m Dicke in 80 m Tiefe führt zu einer Schwingung — mit gleichzeitiger gepulster Entgasung — von etwa der Frequenz, wie sie mit dem Dopplerradar gemessen wurde.

Für die Messung der dynamischen Prozesse in der frühen Phase der Eruptionswolkenbildung, habe ich eine Dopplerradar-Messstation am Volcán de Colima in Mexiko installiert. Während des sechsmonatigen Experiments wurden insgesamt 91 Eruptionen mit einer Dauer von 20 bis 200 Sekunden detektiert. Die Events können anhand ihrer Geschwindigkeiten in ballistische (Santiaguito-ähnliche) und nicht-ballistische Ereignisse klassifiziert werden. Die ballistischen Ereignisse sind durch (a) intensives Gasjetting von kurzer Dauer (1–5 s) mit Geschwindigkeiten von bis zu 55 m/s entlang des Radarstrahls ($\sim$150 m über dem Schlot gemessen) und (b) hohen Fallgeschwindigkeiten charakterisiert und treten häufig als Serie von Pulsen auf. Die Fallgeschwindigkeit schränkt die maximale Partikelgröße, die in einem Ausbruch vorkommt, ein. Partikel mit Radien >1 cm entkoppeln bevorzugt aus dem Gasstrom und fallen mit ihrer terminalen Sinkgeschwindigkeit aus der aufsteigenden Wolke, während die Partikel <1 mm dazu neigen, sich mit dem Gas zu bewegen und konvektiven Flugbahnen zu folgen.

Mit (1) dem „active tracer high-resolution atmospheric model“ (ATHAM) und (2) einem Multiphasen-fluiddynamischen Modell für die Dispersion von Vulkanasche (PDAC) modelliere ich die ersten 400 m der Eruptionswolkenbildung und kann dabei zeigen, dass die nicht-ballistischen Ereignisse den konvektiv, auftriebsbedingt aufsteigenden Wolken zugeschrieben werden können. Für einen Vergleich mit den gemessenen Dopplerradar-Daten habe ich synthetische Daten aus den numerischen Modellergebnissen durch Umwandlung der Partikeleigenschaften (Größe, Geschwindigkeit und Rückstreueigenschaften) in synthetische Dopplerradar-Geschwindigkeitsspektren berechnet. Darüber hinaus zeigen die zweidimensionalen achsensymmetrischen Simulationen, dass (a) Pulse ein lokales Phänomen darstellen und nur im Gasjet zu beobachten sind und (b) eine gepulste Freisetzung von Gas und Asche bedeutenden Einfluss auf die Steighöhe der Wolke und damit auch auf die Injektionshöhe von feiner Asche in die Atmosphäre hat.

Beide Dopplerradar Datensätze zeigen, dass sowohl Santiaguito als auch Colima einen gepulsten, bzw. unsteten, Massefluss haben. Pulse wurden mittels Dopplerradar auch schon an anderen Vulkanen (z.B. Stromboli und Ätna in Italien, Arenal in Costa Rica und Yasur in Vanuatu) beobachtet und könnten daher weiter verbreitet sein als bisher gedacht. Mit dem Colima Datensatz konnte ich zeigen, dass Masseflussfluktuationen unter bestimmten Bedingungen auch dann beobachtet werden können, wenn eine Messung direkt am Schlotausgang unmöglich ist.

Abstract

Understanding the dynamics of ongoing volcanic eruptions is a key factor in predicting the input and transport of volcanic ash in the atmosphere. For this prediction precise measurements of the mass flux at the volcanic vent and in the first few hundred meters of eruption cloud formation are necessary. The Doppler radar technique provides particle velocities and a proxy of the mass flux, and is used here in two field experiments at Santiaguito volcano (Guatemala) and Volcán de Colima (Mexico) to constrain the near-vent dynamics of volcanic events.

Using the Doppler radar technology I am able to show that eruptions at Santiaguito volcano are comprised of multiple explosive degassing pulses occurring at a frequency of 0.2 to 0.3 Hz. During four days of continuous measurement a total of 157 eruptive events were recorded. The Doppler radar data reveals a vertical uplift of the dome surface immediately prior to a first degassing pulse and particle velocities range from 10–15 m/s (velocity component parallel to the radar beam). In 80% of the observed eruptions a second degassing pulse emanates from the dome with significantly higher particle velocities (20–25 m/s again along-beam) and increased echo power, which translates to an increase in massflux. Using a numerical model for ballistic particle transport and calculating corresponding synthetic radar signals I show that the observations are consistent with a pulsed release of material from the dome of Santiaguito volcano.

To explain the possible origin of the pulsed events, I developed two simple mechanical models: (A) a vertically oscillating compressible magma column and (B) a rigid cap-rock representing the dome resting on a gas-bubble rich magma layer, here approximated by a layer of hot volcanic gas. These models have been inspired by the knowledge that a highly viscous magma rising through a conduit is often subject to shear fragmentation near the conduit walls: A continuous magma supply from depth increases shear stresses on the overlying magma column until the yield strength is exceeded and the entire magma column shifts upward. In model (A) this sudden displacement of the magma column is assumed to lead to longitudinal oscillations of the column itself, provided that the magma is compressible. Here the oscillation amplitude and frequency are controlled by the bulk modulus of the magma (10^7–10^9 Pa) and the length of the displaced magma column (here 50–400 m), resp. In model (B) the sudden upward motion of the magma column compresses an overlying hypothetical layer of bubble rich magma sandwiched between magma column and overlying cap-rock. Pressure buildup inside this layer causes the cap-rock to uplift and release gas, but it sinks

back because of its weight. This repeated movement is observed as an oscillation of the dome surface. Assuming a gas layer of 0.5 m at 80 m depth leads to oscillations and concurrent exhalations of about the same frequency as observed with the Doppler radar measurement.

For the measurement of the evolution of dynamic processes during the few hundred meters of eruption cloud formation, I installed a standalone Doppler radar monitoring station at Volcán de Colima, Mexico. A total of 91 events with durations of 20 to 200 seconds have been recorded during six months. The velocity measurements can be classified into ballistic, i.e. Santiaguito-like, and non-ballistic events. The ballistic events are characterized by (a) intense jetting of short duration (1–5 s) with velocities of up to 55 m/s along the radar beam (measured $\sim$150 m above the vent) and (b) high settling velocities, often occurring as series of pulses. The settling velocity constrains the maximum particle size involved in an eruption. Particles with radii >1 cm preferentially decouple from the gas flow and fall out of the rising cloud with their terminal settling velocity, whereas particles <1 mm tend to move with the gas and eventually follow convective trajectories.

Using (1) the "active tracer high-resolution atmospheric model" (ATHAM) and (2) a multi-phase fluid dynamics model for dispersion of volcanic ash (PDAC), I model the first 400 m of eruption cloud formation and find that non-ballistic events can be attributed to buoyantly rising clouds. For a comparison with the measured Doppler radar data, synthetic data are calculated from the numerical model results by converting particle properties (size, velocity, and backscatter-efficiency) into synthetic Doppler radar velocity spectra. In addition, the two-dimensional axis-symmetric simulations show that (a) pulses are local phenomena and can only be observed in the jet region of the cloud and (b) a pulsed release of gas and ash significantly affects the total rise height of the cloud and hence the injection height of fine ash into the atmosphere.

The two Doppler radar datasets show that pulsed, or non-continuous, mass flux occurs at both volcanoes Santiaguito and Colima. Pulses have also been observed at other volcanoes (e.g. Stromboli and Etna, Italy, Arenal volcano, Costa Rica, and Yasur, Vanuatu) using Doppler radar and may be a more common feature than previously assumed. The Colima dataset shows that under certain circumstances a fluctuating mass flux can even be observed few hundred meters above the dome if a direct measurement of the dynamics at the vent is not possible.

Contents

Chapter 1

Introduction

1.1 Motivation

“Volcanoes and their hazards are one of the main threats to our modern society.”
A sentence like this or similar is used as opener in many publications related to volcano research, which does not prove but underlines the importance of this research field in geoscience. The physical processes that lead to volcanic eruptions (melt migration, associated decompression and eventually degassing) have already been identified and the immediate threat to civilization from lava flows, ash clouds, and collapsing eruption columns (so-called pyroclastic flows, PF, or pyroclastic density currents, PDC) are continuously monitored at the most densely populated volcanic areas (e.g. Vesuvius and the bay of Naples, Italy).

The recent shutdown of air traffic over northern and central Europe due to the volcanic ash cloud expelled by Eyjafjallajökull (Iceland) highlighted the enormous impact that even volcanoes located in remote areas can have on modern civilization. Thorough monitoring of all active volcanoes worldwide would be desirable, but currently less than 25% of them are monitored (*Ewert and Miller*, 1995). So-called ‘dormant’ volcanoes, which are most probably not monitored, or volcanoes that are not known to be active can become active in very short times (e.g. the recent reawakening of Eyjafjallajökull in Iceland or Chaiten in Chile), which prohibits the installation of a monitoring system in sufficient time to issue warnings about the activity status. Monitoring at volcanoes is mostly done using seismometers measuring the ground movement. However, it has been shown that the seismicity is not always representative for the surface activity (*Vöge and Hort*, 2008b; *Valade et al.*, 2012) but rather for the overall state of unrest (or activity status) of a volcano. Volcanoes may also be monitored using remote sensing techniques (on satellites or weather radars) that capture the surface activity and possibly ash distribution, but satellite measurements are very scarce due to the infrequent passages and neither satellites nor weather radars can resolve the eruption cloud dynamics (in time and space).

After several incidents with air crafts flying through ash clouds of the eruptions of e.g. Mount St. Helens (USA, 1980), Galunggung volcano (Indonesia, 1982), and Redoubt volcano

(Alaska, 1989–90, see Table 17.8 in *Sparks et al.*, 1997; *Miller and Casadevall*, 2000), nine Volcanic Ash Advisory Centers (VAACs) were established during the 1990s all over the world, to issue ash cloud warnings for aviation safety (*Mastin et al.*, 2009). Those warnings are based on volcanic ash dispersal and transportation models (VATDs). In these numerical models fine ash is injected into the atmosphere at prescribed heights above the volcano and transported under realistic meteorological conditions. The model predictions depend critically on so-called "eruption source parameters", which are plume height, mass eruption rate, duration and mass fraction of fine ash particles. Of these parameters, only plume height and duration may be estimated from radar, satellite or seismic data, if available in real-time at all. In a recent effort to assign default values to all active volcanoes worldwide, *Mastin et al.* (2009) validated the empirical formula that relates the mass flux at vent to the height of the eruption cloud by *Sparks et al.* (1997). However, atmospheric wind is neglected in this formula. A recent attempt to compare the mass flux of Eyjafjallajökull derived from cloud height and from the infrasonic record (Maurizio Ripepe, pers. comm.) highlighted the effect of side wind on the plume height. In numerical studies, side wind has been shown to significantly reduce the cloud height (*Graf et al.*, 1999). Whether this formula is also valid for non-steady eruptions that produce finite clouds rather than steady columns has not been investigated before due to the lack of in-situ observations of the dynamics at or near the vent.

An implicit assumption of all eruption cloud models is that a steady mass flux at the vent is feeding the plume. However, *Barsotti and Neri* (2008) compared two model runs with (a) a cloud height based estimate and (b) a deposit based estimate for steady mass flux at the vent. From the differences in the modeled cloud they conclude that both estimates represent end-member values of the true mass flux and especially the deposit based estimate is highly influenced by local wind-fields and topography.

The dynamics inside the conduit (magma transport, degassing, bubble dynamics) and outside the conduit (ash transport, cloud development) that produce those hazardous eruptions have been widely studied. Owing to the complexity of the processes involved, studies had to focus on single processes or, more recently, the combination of a few effects. Nonetheless, the conduit and cloud studies have been mostly viewed separated and the few studies (e.g. *Neri et al.*, 1998; *Todesco et al.*, 2006) that combined models for conduit and cloud did explicitly exclude the highly dynamic region at the vent.

In this work I study the formation of eruption clouds originating at the vent and ascending to greater heights. To do so I compare Doppler radar measurements of cloud dynamics at different heights and numerically simulate eruption clouds. The Doppler radar measurement is a proxy for the amount of material moving inside the radar beam and the velocity of the scatterers (see Section 1.3.1 for more details). A Doppler radar measurement requires a clear line of sight and a non-perpendicular view onto the cloud. Directly above the vent or below the cloud would give the most accurate velocity measurements but this is impossible to achieve in most cases. Because the measurement of near-vent dynamics is only possible from above the vent whereas cloud dynamics (in the first 100–300 m of their rise) can only be measured from below, I use two different datasets from volcanoes with comparable activity to overcome this issue. At Santiaguito volcano (2550 m asl., Guatemala) the parent volcano Santa Maria (3772 m asl.) enables a unique view onto the vent-near dynamics from above. Colima volcano (3822 m asl., Mexico) is high enough that the Doppler radar can be installed above the vegetation line (∼2500 m asl.) but still being at a safe distance to the crater. Here the development of eruption clouds in their first few hundreds of meters of rise can be observed from below.

In the following sections I will give a short introduction to conduit processes and the origin of volcanic clouds. Afterwards I will describe the Doppler radar measurement technique, which is necessary to fully understand the radar data and its interpretation. I wrote two publications (one in press and one ready to be submitted) on the Doppler radar measurements at Santiaguito volcano, which are included in this thesis as separate chapters (chapters 2 and 3, resp.). A basic introduction into the Doppler radar measurement technique and a description of the Santiaguito experiment is therefore part of both chapters.

In chapter 2 the eruption dynamics of Santiaguito volcano are investigated. In order to interpret the complex Doppler radar data a numerical model is introduced, in which ash particles of different sizes are transported on ballistic trajectories in a parameterized atmosphere and corresponding synthetic Doppler radar spectra are calculated. By forward modeling of different vent and atmospheric conditions I find that the eruptions at Santiaguito volcano consist of individual pulses and hence are sequences of explosions. The Doppler radar data further supports the finding by *Johnson et al.* (2008) that the dome surface lifts up to 0.5 m immediately prior to the first explosion.

These pulsed eruptions are further investigated in chapter 3. A 2D cross-correlation of the Doppler radar data shows that the inter-eruptive pulses (explosions that produce a single eruption cloud) occur at an almost regular interval of about 3 s. To explain this regularity I develop a conduit model for shallow dome processes. Based on the previous finding (*Johnson et al.*, 2008) that the dome surface lifts up, I propose that the upper part of the dome sits on either a compressible gas cushion or a magma column. These two end-member cases have in common that after some excitation the entire dome-magma column system acts like a spring-mass-oscillator. Every time the dome is uplifted pathways for degassing open and regular explosions occur at the surface, ejecting volatiles and ash into the atmosphere.

In contrast to the temporary installation at Santiaguito volcano, the Colima experiment is part of the permanent installation of a Doppler radar monitoring station at Volcán de Colima. A description of the monitoring station and the first datasets of developing eruption clouds is given in chapter 4. It appears that the dynamics of the developing clouds are very similar to the at-vent dynamics at Santiaguito volcano and show pulsed rather than steady mass flux through the radar's field of view.

Chapter 5 is dedicated to the application of two numerical eruption cloud models and the coupling of those models to the synthetic Doppler radar model (introduced in chapter 2). In this chapter the key questions (i) do pulsed eruptions produce steady clouds and (ii) to which heights do these clouds rise, are investigated. In addition, the modeled dynamics of eruption clouds at different heights above the vent are compared to the Doppler radar data measured at Colima volcano, and I will show that a pulsed mass flux can only be observed near the vent but not necessarily at greater cloud height.

Finally, a conclusion and outlook of both experimental studies at Santiaguito and Colima volcano and the numerical modeling of the eruptive events is given in chapter 6.

1.2 Eruption Clouds and Their Origin

The term volcanic cloud covers a wide range of clouds produced by different styles of volcanic activity. A dilute, ash-free vapor cloud is covered by this term as well as a heavily ash-loaded steady Plinian eruption column as long as they all have a volcanic origin. The main factor that drives volcanic activity is gas (mainly H_2O, CO_2 and SO_2). Volatiles are soluble at high pressures, i.e. they are solved in source rocks and magmatic melt. As melt rises buoyantly through the earth's crust it starts to crystallize due to cooling and depressurization. Because the crystals cannot incorporate the volatile components into their crystal grid structures, volatiles become enriched in the residual silicate melt, which is driven out of equilibrium, and the gas exsolves, i.e. bubbles nucleate.

The key property that controls the flow of magma (and gases) is the viscosity, which relates the applied stress to the resulting strain rate. The viscosity hence describes the internal resistance to flow of the fluid (e.g. water has a low viscosity compared to honey). The magma viscosity depends on several parameters such as temperature and chemical composition (mainly SiO_2 content), and dissolved volatile content. Secondary effects due to the presence of crystals and gas bubbles can significantly alter the local bulk viscosity. As a consequence the viscosity of magma changes several orders of magnitude during its ascent towards the surface, mainly due to exsolution of volatiles and crystallization.

In addition, the increasing bubble content changes the bulk flow behavior. Depending on the viscosity gas bubbles may freely rise to the surface through the magma (e.g. basaltic magma, $\sim$50 wt.% SiO_2, low viscosity of 10^2–10^3 Pas, typically Strombolian activity) or become trapped in the magma and rise slowly (andesitic, dacitic, and rhyolitic magma, 55–77 wt.% SiO_2, high viscosity of 10^6–10^{12} Pas, e.g. at dome building volcanoes). Strombolian activity is therefore characterized by the bursting of single or consecutive gas bubbles at the magma-air interface inside a conduit. As this kind of activity is not the focus of this work, the reader is e.g. referred to *Gerst et al.* (2012) and references therein.

In this study I focus on two volcanoes of dacitic (Santiaguito, Guatemala) and andesitic (Colima, Mexico) composition. As the magma-gas-bubbles mixture rises in the conduit of such systems, bubbles become larger due to the decreasing lithostatic pressure, which drives (a) further gas exsolution and (b) gas expansion (the latter being dominant in shallow depths). Due to the high magma viscosity, however, the bubbles can not expand fast enough and an overpressure develops within them. At some depth in the conduit, the gas bubble volume

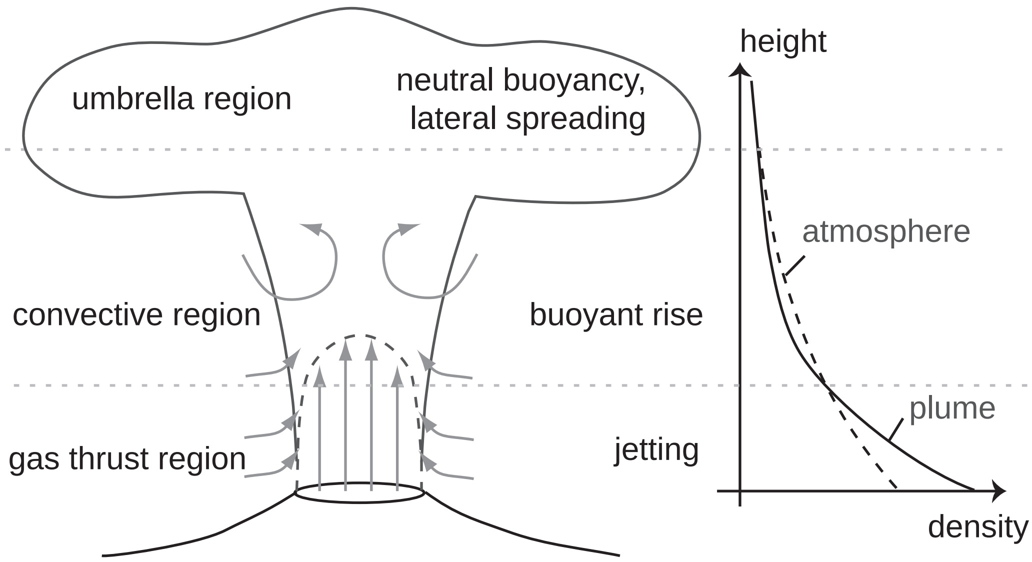

Figure 1.1: Schematic drawing of the development of an eruption cloud. The graph on the right shows the evolution of bulk and atmospheric density with height.

exceeds the magma volume, but the magma is still the continuous phase (magma foam). At the fragmentation level, the bubbles-in-magma flow changes to a magma fragments-in-gas flow due to the disruption of the foam. The high overpressure in the gas phase results in a rapid expansion and flow through the conduit and out of the vent. Therefore a gas-particle mixture is ejected as a turbulent flow through the vent into the atmosphere at high velocities and magmatic temperatures. This so-called jet has a bulk density that (depending on the mass loading) can be significantly higher than the atmospheric density (see Fig. 1.1). Due to the turbulent mixing of ambient air (entrainment) and its concurrent heating, the bulk density of the jet decreases, eventually reaching a value lower than local atmospheric density. If this happens buoyant forces will dominate the motion and the plume rises up to a height of neutral buoyancy where the bulk density equals the surrounding atmospheric density. Otherwise the plume collapses and the erupted mixture spreads as pyroclastic flows along the flanks of the volcano. A general and very detailed introduction to the physics of volcanic plumes is given in the books “Volcanic Plumes” by *Sparks et al.* (1997) and “Fundamentals of Physical Volcanology” by *Parfitt and Wilson* (2008).

In this work I focus on weak volcanic clouds, which are characterized by:

- rise heights of up to 1–4 km above vent;
- a limited life-time of 10s of minutes;
- a highly varying ash content that in most cases promotes buoyant rise;
- a short duration of a few seconds of vent forcing (or jetting);
- bent-over plumes (depending on wind conditions), which indicates low initial momentum.

Weak volcanian clouds are commonly associated with dome building volcanoes. Their magma is of intermediate composition (andesitic or dacitic) with a magma viscosity of 10^6–10^{10} Pas, which is on one hand high enough that the gas bubbles are significantly slowed down and on the other hand low enough that they do not become trapped. The major difference between the sustained Plinian eruption columns described above and the transient eruption clouds described here lies in the rise speed of the magma. When the magma rise is slow, only a certain mass of gas is trapped at a certain pressure and depth and hence every eruption is fed by a finite amount of energy. In addition, the top of the magma column has enough time to cool between those explosions to build a plug. When this plug is extruded by the slowly rising magma, a dome builds. The transition of effusive (dome building and associated transient explosions) to explosive (a sustained Plinian column) happens either when magma flow becomes faster or when a collapse of the dome suddenly depressurizes the magma column and an induced fragmentation wave ruptures the magma. A dome collapse caused for example the July 2003 eruption of Soufrière Hills volcano, Montserrat (*Edmonds and Herd*, 2007). This process can be compared to the opening of a pressurized (previously shaken) soda bottle or the explosive uncorking of a champagne bottle.

1.3 Short Introduction to the Principles of Doppler Radar Used in Volcanology

The radar technique (radio detection and ranging) has been used in science since its development in the mid 20th century, at first by meteorologists, who made use of the reflection properties of water. Its use in volcanology began with observations of ash clouds with weather radars. A pioneering study monitored the dispersal of ash of the 1976 Augustine eruption (*Kienle and Shaw*, 1979) and compared other observational data to the radar data. The introduction of a Doppler radar in volcanology was by *Hort and Seyfried* (1998), who successfully used a Doppler radar — originally designed to measured rain fall — at Stromboli volcano. In 1999, a second Doppler radar (VOLDORAD) was introduced to the community by *Dubosclard et al.* (1999). A comparison from a technical point of view of both mobile Doppler radars is given in *Vöge et al.* (2005). A nearly complete overview (up to 2010) on the volcanology-related use of the radar technique (pulsed, continuous wave, with and without Doppler capabilities) is given in *Gerst* (2010). More recently, a first study of volcanic ash clouds at Arenal volcano (Costa Rica, *Donnadieu et al.*, 2011) showed the possibility to derive the direction of a wind drifted ash plume from Doppler radar data.

1.3.1 How Does the Measurement Work?

In principle, two Doppler radar techniques exist, the pulsed and the frequency modulated continuous wave (FMCW) radar. In very simplified words, a pulsed radar measures the amplitude and time difference between sent and incoming signal, the latter corresponding to the distance of the scattering object(s). A pulsed radar with Doppler capabilities additionally measures the frequency shift δf of the incoming signal, which is direct proportional to the velocity v of the scatterer (Doppler effect):

$$\delta f = f_t - f_r = -f_t \left(\frac{v/c}{1 - v/c} \right)$$

with f being the frequency of the electro-magnetic wave and c being the speed of light. The subscript r denotes received and t transmitted properties. The amplitude can be expressed in terms of the object's scattering properties (σ), internal radar properties and the distance R (following *Currie*, 1989):

$$P_r = \underbrace{\left(\frac{P_t G_t}{4\pi R^2} \right)}_{\text{transmitting}} \underbrace{\left(\frac{\sigma}{4\pi R^2} \right)}_{\text{scattering}} \underbrace{\left(\frac{G_r \lambda^2}{4\pi} \right)}_{\text{receiving}} \tag{1.1}$$

where G is the antenna gain and P is the power of the signal. In a mono-static radar, as is used in this study, the same antenna is used for transmitting and receiving, hence $G_t = G_r$ and equation (1.1) simplifies to the conventionally called *radar range equation* or *radar equation*

$$P_r = \underbrace{\frac{P_t G^2 \lambda^2}{(4\pi)^3}}_{\text{radar constant}} \frac{\sigma}{R^4} \quad , \tag{1.2}$$

that relates the back-scatter cross-section σ or radar cross-section to the received power.

The FMCW-radar makes use of a trick to extract the same information (signal travel time, frequency shift and amplitude) from a continuous measurement. Instead of pulsed, the transmitted signal is frequency modulated (e.g. using a saw-tooth-like function). One cycle of modulation — a so-called sweep — corresponds to a pulse. Like in a pulsed radar, a measurement is started every time a sweep (or pulse) begins. Contrary to the pulsed system, the frequency measured by a FMCW-radar contains information on distance as well as velocity of the scatterer. However, a moving object changes its distance slightly at every single consecutive measurement. Therefore the frequency shift of consecutive measurements can be used to obtain both, the large scale distance (in so-called range intervals or range gates) and the small scale distance variation (i.e. the velocity). The extraction of both values is done using a 2D FFT. A detailed mathematical description of the range and velocity retrieval is given in *Barrick* (1973), *Scharff* (2006), *Vöge* (2007), and *Ziemen* (2008).

The characteristic values of pulsed (PU) and FMCW Doppler radars correspond in the following manner:

- The range gate length (or distance resolution) is defined by the pulse duration (PU) or the inverse of the sweep bandwidth (FMCW).
- The velocity resolution depends on (a) the pulse repetition frequency (PU) or sweep

duration (FMCW) and (b) the wavelength used by the instrument (PU and FMCW)).

- The signal-to-noise ratio depends on the squared pulse duration (PU) or the linear inverse of the bandwidth (FMCW). Therefore, when measuring comparable ranges, the transmitting power has to be much higher for the pulsed radar to obtain the same signal quality.

1.3.2 Scattering of Electro-magnetic Waves at Volcanic Ash

The theoretical description of scattering of electro-magnetic waves at spherical particles of various sizes has been derived from Maxwell's equations by *Mie* (1908). The so-called Mie-theory and its applications to scattering in the atmosphere can be found in literature (e.g. *Dave*, 1969; *Ackerman and Toon*, 1981; *Toon and Ackerman*, 1981). Here I will shortly summarize the most important aspects for the Doppler radar measurement.

As shown in Equation (1.2) the received power depends on the radar constant and the back-scatter cross-section of the scattering object. The back-scatter (or radar) cross-section is normally given in units of m^2 and is the radar analog to the optical cross-section in the frequency range of visible light. Hence it is the area of the object that the radar 'sees'. Scattering is the consequence of the interaction between the external and an induced internal electro-magnetic field of an object. In the end-member case where the scattering object is very large compared to the wavelength, the internal field will adjust to the external field and a small amount is reflected due to the impedance contrast at the object's surface. Hence the optical and radar cross-section are equal, when the scattering object is very large compared to the wavelength ($P_r \sim r^2$). In the second end-member case where the wavelength is large compared to the object, the internal electromagnetic field can be assumed to be homogeneous, which means that the object scatters isotropically in all directions. In this case, the so-called Rayleigh-scattering regime, the radar cross-section varies with r^6 (and hence $P_r \sim r^6$).

The gap between geometrical optics and Rayleigh-scattering is filled by the Mie-theory. When the object's size and the wavelength are of the same order of magnitude, the induced internal field interferes constructively or destructively with the external field. Hence the back-scattered energy strongly depends on the relative size and scattering occurs in preferred directions. In this study a Doppler radar with a wavelength of 1.25 cm (24 GHz) is used. Therefore the vast bulk of ash particles can be assumed to lie within the Mie-region, which roughly extends from 0.2 mm to ~10 cm.

The most prominent effect of the wavelength-dependency of scattering is the blue sky at daytime. The sun emits the whole spectrum of visible light (400–700 nm), but the blue part of the light (smallest wavelength) is scattered at the air molecules in the earth's atmosphere, while the longer wavelengths of green, yellow and red light penetrate the atmosphere almost undisturbed. The intense scattering of the blue light component makes the sky appear blue. However, when moisture or small aerosol particles are present, the sky turns into whiter color because then the longer wavelengths are also scattered.

Chapter 2

A Detailed View Into the Eruption Clouds of Santiaguito Volcano, Guatemala, Using Doppler Radar[1]

2.1 Introduction

Dome growth and explosive degassing are fundamental processes in continental arc volcanism. Both processes occur at various magnitudes from slow magma plug extrusion to hazardous dome collapse events that release gas and ash several km high into the atmosphere, produce block and ash flows, or pyroclastic flows. The activity at dome growing volcanoes can be characterized as vulcanian, sub-plinian, or plinian. Their explosive degassing events are highly complex but the infrequency of events, compared to for example strombolian (e.g. *Harris and Ripepe*, 2007) or hawaiian (*Heliker and Mattox*, 2003) eruptions, still hinders detailed in situ studies of their eruption dynamics. The fundamental processes of dome growth as a consequence of magma degassing and crystallization, thereby increasing its viscosity, have been modeled in various studies (e.g. *Voight and Elsworth*, 2000; *Hale and Wadge*, 2003; *Barmin et al.*, 2002; *Melnik and Sparks*, 2005; *de Michieli Vitturi et al.*, 2008; *Taisne and Jaupart*, 2008; *Massol and Jaupart*, 2009) as well as the buoyant ascent of (sub-)plinian eruption columns (e.g. *Wilson et al.*, 1978; *Sparks et al.*, 1997; *Oberhuber et al.*, 1998; *Esposti Ongaro et al.*, 2007). The dynamics of volatiles and ash particles directly at the vent during vulcanian-type explosive degassing events, however, is subject to ongoing research — mainly because a quantitative observation of these processes is rather difficult.

Unfortunately most dome building volcanoes (e.g. Merapi, Colima) are not as accessible as volcanoes exhibiting strombolian activity in terms of installing multi-parameter networks and

[1]An edited version of this chapter was published by AGU. Copyright (2012) American Geophysical Union. Lea Scharff, Florian Ziemen, Matthias Hort, Alexander Gerst, and Jeffrey B. Johnson (2012), A Detailed View Into the Eruption Clouds of Santiaguito Volcano, Guatemala, Using Doppler Radar, Journal of Geophysical Research - Solid Earth, Volume 117, doi: 10.1029/2011JB008542
To view the published open abstract, go to `http://dx.doi.org` and enter the DOI.

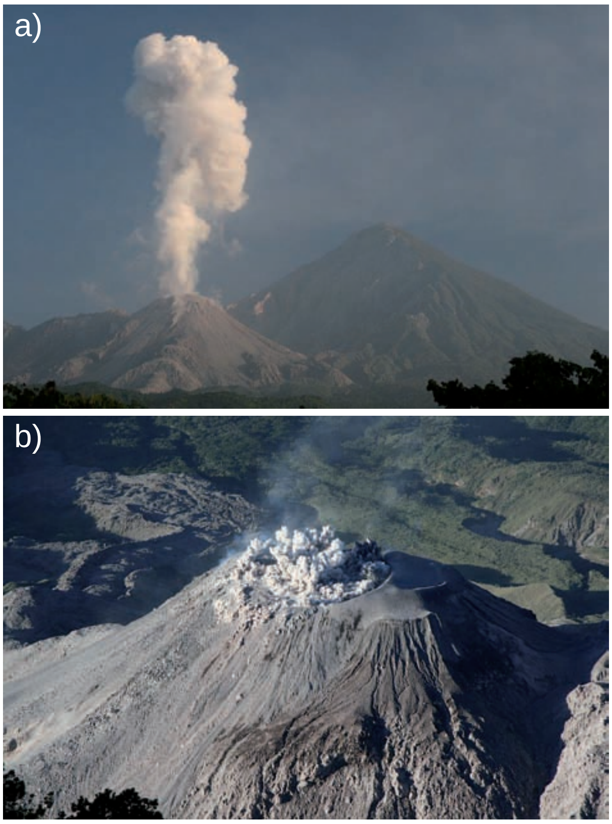

Figure 2.1: a) View from south towards Santiaguito volcano, which is located inside the collapse structure of the south-western wall of Santa Maria volcano. b) Onset of an eruption at Santiaguito volcano as viewed from the top of Santa Maria volcano (view towards south-west), where the Doppler radar was set up.

actually visually observing dome activity. In this regard the Santa Maria volcano complex, Guatemala, and its since 1922 growing child volcano Santiaguito are a "unique observation site" (*Bluth and Rose*, 2004) to study vulcanian eruption processes directly at the vent. Standing on top of Santa Maria volcano (3772 m asl) allows to directly view down the 100 year old horseshoe shaped scar onto Santiaguito volcano (∼2550 m asl) and its currently active dome named Caliente (see Fig. 2.1).

Surface degassing at Santiaguito has been subject of several studies based on infrasonic and thermal data (e.g. *Johnson et al.*, 2004; *Sahetapy-Engel et al.*, 2004; *Patrick et al.*, 2007; *Sahetapy-Engel and Harris*, 2009b; *Marchetti et al.*, 2009) as well as using a SO_2 camera (*Holland et al.*, 2011). Like plinian eruptions, vulcanian degassing events comprise a jet transporting a mixture of ash and gas. Once ejected, the hot particle-gas mixture entrains ambient air, eventually becomes buoyant and — following the terminology of *Patrick* (2007a) — *thermals* or *rooted thermals* develop. In contrast to plinian eruptions, vulcanian explosions are orders of magnitude smaller. If there is a gas jet at all at Santiaguito volcano, the transition from jet to buoyant regime occurs about 50 m above the vent (*Sahetapy-Engel and Harris*, 2009b). *Sahetapy-Engel and Harris* (2009b) further find that the plume height does not depend on exit velocity, but instead on buoyant ascent velocities, lateral spreading rates and feeder plume radii. Determining the exit velocity using the plume front velocity near the vent during the first second of an eruption, *Sahetapy-Engel and Harris* (2009b) find that the higher the total heat budget of the ascending plume, the higher is its buoyant ascent velocity.

Thermal imaging via camera or other sensors allows to estimate the velocity of the hot plume front by tracking isotherms. However, this is biased by rapid cooling of the plume front (due to e.g. entrainment of ambient air, adiabatic expansion, and condensation of juvenile and ambient moisture). In addition the plume front velocity does neither represent the gas' nor the particles' velocity. The dynamics at the source feeding the plume may be observed by tracking individual particles. Here one has to discriminate between large particles (>1 m) that can be detected from a safe distance with a regular camera and small particles (<10 cm) that are undetectable with this technique. Unfortunately, larger particles, which are inertially driven, often move decoupled from the plume on ballistic trajectories so that information on the small (mm-sized) particles is required to study the plume dynamics. In addition, the internal dynamics of a plume cannot be observed by a camera as they are obscured by the outer part of the plume, and the relationship between velocities in the inner core and the outer edge of the plume is unknown (*Patrick*, 2007a).

The Doppler radar provides highly accurate velocities of small-to-large particles and an estimate of the evolution of the mass flux, which allows us to reconstruct in detail the dynamics at the onset and during an explosive degassing event. We first summarize the multidisciplinary experiment and describe the data collected during the experiment. This is followed by a modeling section to calculate ballistic particle trajectories and corresponding synthetic Doppler radar spectra. Afterwards we compare synthetic and measured data to draw conclusions on the eruption dynamics at Santiaguito volcano and discuss our results.

2.2 Multidisciplinary Experiment at Santiaguito Volcano

In order to investigate the links between magmatic degassing and the dynamics of volcanic eruptions we participated in a multidisciplinary experiment at Santiaguito volcano, Guatemala that took place between January 3rd and 14th, 2007. During this experiment several different instruments (seismometers, University of North Carolina; infrasound sensors and a high-resolution video camera, Univ. of New Hampshire; Doppler radar, Hamburg University; infrared camera, Universidad de Colima) were deployed. The seismic and infrasound loggers were provided by PASSCAL (Program for Array Studies of the Continental Lithosphere, New Mexico Tech). More information on the setup, location and recording dates are given in *Johnson et al.* (2008). The Doppler radar was positioned near the top of Santa Maria volcano at 3600 m asl pointing downwards at the active dome Caliente of Santiaguito volcano (2550 m asl, inclination 27°, see Fig. 2.2). Also installed on top of Santa Maria were an acoustic sensor as well as a thermal and a high-resolution video camera. The Doppler radar operated from Jan. 9, 17:30 UTC to Jan. 13, 17:30 UTC and recorded 157 eruptive/explosive events. More details on the general aspects of the experiment can be found in *Johnson et al.* (2008). Here we focus on the interpretation of the Doppler radar data.

Figure 2.2: a) Setup geometry of the Doppler radar instrument near the summit of Santa Maria (view from south-east). The tick marks on the radar beam show the range resolution of the chosen radar setup, here 1000 m.
b) The relationship between measured (filled arrows) and true velocities (open arrows). The blue arrows (filled) indicate a positive radial velocity whereas red arrows (filled) represent negative radial velocities. Note that particles with different velocities may have the same radial velocity. Especially negative velocities may resemble falling as well as rising particles, but due to the geometry of this measurement and the mainly vertically ejected particles, we can assign negative velocities to falling particles. The black line marks the center of the radar beam (maximum intensity) and the gray lines show the beam opening (not to scale).

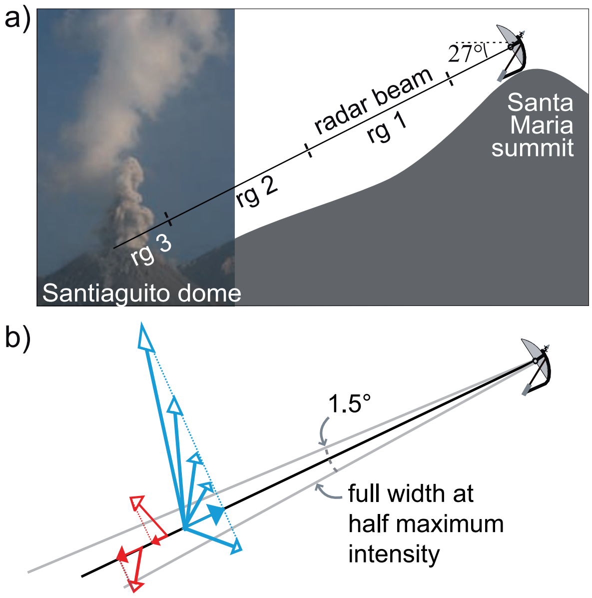

2.2.1 Activity of Santiaguito Volcano

Santiaguito's activity is mainly characterized by extrusive activity of silicate-rich lava flows and vulcanian explosions. In January 2007 vulcanian explosions occurred about every 90 minutes and emanated from a ring-shaped distribution of fractures on the dome center and circumference (Fig. 2.1b), which has been suggested to be related to the geometry of the conduit (e.g. *Bluth and Rose*, 2004). *Gonnermann and Manga* (2003) argue that the highest shear stresses in a non-Newtonian channel flow are located at the conduit walls. These high shear stresses may cause magma fragmentation and thereby lead to a ring-shaped arrangement of vents. This interpretation would imply a nearly cylindrical conduit that is blocked by a lava plug. However, *Johnson et al.* (2008) believe that these fractures are simply failure joints in the brittle lava flow carapace rather than persistent features. Explosions produced white and gray plumes that sometimes rose up to 4000 m above sea level.

2.2.2 The Doppler Radar

Doppler radar instruments transmit electromagnetic waves (wavelength between 3 m and 3 mm) that are reflected back to the instrument by a stationary or moving object (here volcanic ash). The reflected signal differs in frequency from the transmitted signal by a frequency shift (Doppler effect) that is proportional to the radial velocity of the particle (radial meaning the velocity component parallel to the radar beam, i.e. toward or away from the instrument). Two main Doppler radar designs have been established: pulsed and continuous wave (CW) systems. Our instrument is a frequency modulated continuous wave (FM-CW) radar, which can be deployed almost everywhere in the field due to its low weight

(50kg) and low power consumption (40W, both values include the data logger). It operates at a frequency of 24 GHz (wavelength of λ=1.25 cm) and transmits a power of 50 mW. The radar beam has a total aperture of 1.5° and the intensity of the transmitted energy inside the beam largely follows a Gaussian distribution (e.g. Fig. 5 in *Hort et al.*, 2003). In addition to the velocity measurement, the frequency modulation of our instrument allows us to determine the approximate distance of the moving object by subdividing the distance along the beam into so called range gates (*Barrick*, 1973).

Each particle inside the radar beam reflects a distinct amount of energy that depends on the particle's size, shape, and composition (*Adams et al.*, 1996). Particles with sizes on the order of the wavelength (here λ=1.25 cm) have a very complex reflection pattern, which can be calculated using Mie theory (*Mie*, 1908). Very small particles ($r \leq \lambda/10$) and larger particles ($r > 10\lambda$) are within the range of Rayleigh scattering and geometrical optics, respectively. As a zero-order approximation we can assume that bigger particles reflect more of the electromagnetic wave than smaller particles. Our small wavelength allows us to detect particles of e.g. 1 mm radius at a distance of 2.6 km when a minimum concentration of 2.66g/m^3 is exceeded (distributed homogeneously in probed volume). During a given time interval the Doppler radar records the reflected energy at discrete frequency shifts, i.e. discrete velocities (so-called bins). This means that the observed reflected energy for a certain velocity range is the sum of the reflected energy of all particles moving at different velocities within this range. The resulting output is a velocity spectrum, showing for each range gate, how much reflected energy is attributed to each velocity.

During the Santiaguito experiment the temporal resolution of our instrument was near 20 Hz, the velocity resolution was 0.39 m/s. Particles moving towards the radar show by definition positive velocities, whereas particles that move away from the radar have negative velocities. The maximum unambiguous radial velocity was ±49.92 m/s, which was never exceeded during our measurements. The large distance of 2.7 km led to a range gate length of 1000 m to record the signal in the third range gate (2500–3500 m along beam). At the target distance, the field of view (FOV) has an approximate diameter of 70 m (cross-beam, full width at half maximum of Gaussian intensity distribution). The illuminated area on the dome surface is an ellipse of 8500 m^2. For more technical aspects on our Doppler radar the reader is referred to *Vöge and Hort* (2009). For the use of pulsed Doppler radar systems in volcanology see *Dubosclard et al.* (1999) or *Gouhier and Donnadieu* (2008).

2.2.3 Data Processing and Presentation

Evaluating eruption characteristics requires the definition of some scalar values that can be used to characterize each spectrum. Each radar spectrum consists of discrete values: Each velocity v_i is associated with a certain amount of reflected energy P_i, where $i = 1, ..., n$ and n being the number of discrete velocity bins. From each spectrum we determine the maximum positive ($V^+_{\max}$) and negative ($V^-_{\max}$) radial velocity and sum the reflected energy of the positive and negative velocity range (*Hort et al.*, 2003):

$$
\begin{aligned}
P^{+} &= \sum_{i=1}^{i_{V^{+}_{max}}} P_i \quad , \\
P^{-} &= \sum_{i=-1}^{i_{V^{-}_{max}}} P_i \quad .
\end{aligned} \tag{2.1}
$$

The resulting values P^{+} and P^{-} are referred to as echo power and will be used as a proxy for the mass moving inside the considered range gate. Those definitions are similar to the ones used by *Dubosclard et al.* (2004). With the measurement setup at Santiaguito volcano, where the radar is tilted 27° downwards and the assumption that the particles' initial velocities are mainly directed in the vertical direction, positive radial velocities can be attributed to rising particles (see Fig. 2.2b). The same argument leads to the assignment of negative radial velocities to falling or settling particles. In the following we refer to radial velocities as velocities otherwise we will explicitly give the direction (e.g. vertical velocity).

In addition to the values of maximum velocities and echo power, we plot the complete Doppler radar information in a so-called velocigram (see also *Gerst*, 2010). An example of a velocigram is shown in Fig. 2.5 below, where the data is introduced. In a velocigram, each point holds the information on echo power (color) corresponding to a certain velocity (y-value) at a particular time (x-value). The colors represent the ratio of reflected energy to background noise in dB (dark blue is background noise).

$$
P_i^{dB} = 10 \log_{10} \frac{P_i}{P_{\text{noise}}} \tag{2.2}
$$

The value for background noise P_{noise} is a constant that is arbitrarily chosen for each experiment. The conversion of reflected energy to echo power in dB is done to eliminate the calibration constant, which contains antenna gain and internal system properties. Note that the echo power can not be converted to the usually given radar reflectivity Z, which is only applicable when the particle diameter is small compared to the wavelength.

2.2.4 A Simple Example and the Impact of the Measurement Geometry

As explained above, the radar only measures the radial velocity component of objects along the radar beam (see Fig. 2.2b), hence we measure a 1D velocity profile through the 3D processes occurring during an eruption. To enhance the readers' understanding of the recorded radar data we briefly discuss a simple eruption geometry and how it is seen by the radar using a synthetic model.

The simplest scenario in terms of an explosive event at a volcano is the ballistic transport of various particles ejected from a vent that represents a point source. In Fig. 2.3 we plot the trajectories and corresponding pseudo velocigrams for three particles moving through

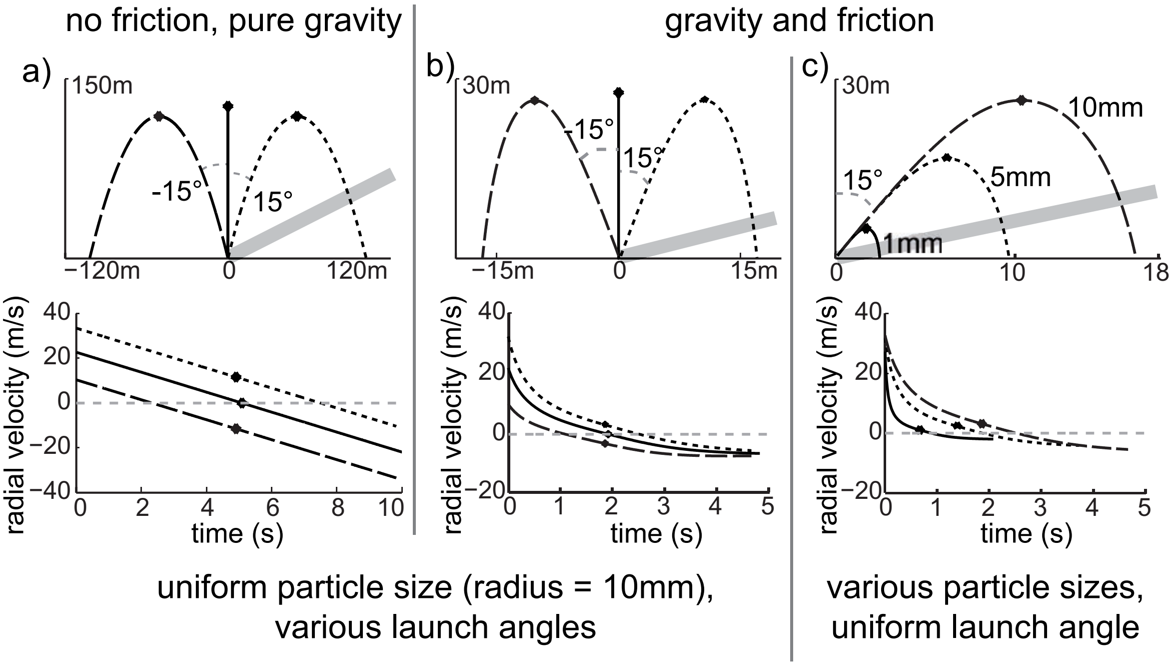

Figure 2.3: Simple examples of ballistic particle transport in non-moving air and their time lines of radial velocity (pseudo velocigram) as it would be measured with the Doppler radar. The top diagrams show the particle trajectories. In these examples particle transport is confined to the image plane. All particles are initialized with an absolute velocity of 50 m/s. The gray bar represents the radar beam direction. The lower diagrams show the pseudo velocigram, i.e. the particles radial velocity as a function of time. Note that in a pseudo velocigram the echo power of all particles is assumed constant and equal to unity. The horizontal gray dotted line marks the zero velocity. A particle's trajectory and the corresponding pseudo velocigram are coded using the same line style. The apex of the particles trajectories is marked with a black dot in space (upper diagrams) and time (lower diagrams). Examples a) and b) show the effect of the launch angle on the radial velocities. All particles have a radius of 1 cm. In example a) friction with air is neglected and only gravity acts on the particles, hence particle motion is independent of their size and acceleration is constant. Friction leads to a size-dependent terminal fall velocity as can be seen in b) and c). Example c) shows the effect of particle size on velocity. Here all particles have the same launch angle (15° towards the radar). Their radii are 1 mm, 5 mm, and 1 cm. For more explanation see text.

still air with a) neglecting friction and b) applying friction with air as described in appendix A.1. Pseudo velocigram means in this case that the velocity component parallel to the radar beam (beam inclination is 27° to the horizontal) is plotted as a function of time, but the value of reflected energy is constant and equal for all particles at all times. This is equivalent to the assumption that the illumination of the particles is always the same. All particles have the same radius (1 cm) and an initial velocity of 50 m/s. The only difference is the launch angle. One particle is launched vertically and the others are launched at an angle of ±15° to the vertical. All three trajectories lie in a plane that is defined by the radar beam, i.e. those examples are calculated in 2D. Consider a particle that is ejected vertically. Neglecting friction with air (Fig. 2.3a), this particle is only subject to gravity, which leads to a constant acceleration towards the ground. Ejecting particles on inclined trajectories shifts the recorded velocity towards positive or negative velocities by a constant that solely depends on the x-component of the initial velocity.

Introducing friction with air (see Appendix A.1 for a full description of friction and trajectory calculation) the trajectories of the three particles change (Fig. 2.3b). The vertically ejected particle's radial velocity representation in the velocigram is a curved line that bends towards a maximum falling velocity. The friction force acts in the direction opposite to velocity, gravity only influences the vertical velocity component. Hence the velocigrams of the sub-vertically ejected particles also follow curved lines and, because the horizontal velocity component decreases, the difference in radial velocity between the three particles decreases and those curved lines converge to the same settling velocity. This velocity is the terminal fall velocity.

The dependency of terminal fall velocity on particle size can clearly be seen in Fig. 2.3c). To illustrate the effect of different particle sizes on the velocity evolution, we show trajectories and pseudo velocigrams for three particles with 1 mm, 5 mm, and 1 cm radius. All particles are launched with 50 m/s at an angle of 15° to the vertical, towards the radar. Apparently, small particles (<5 mm) are more affected by friction. The larger a particle, the less curved is its velocigram representation and the higher is its terminal fall velocity.

The geometry of the instrument setup, i.e. non-vertical incident angle of the radar beam, has a major effect on the measured velocities. Using a vertical incidence Doppler radar, the assignment of positive radial velocities to rising particles (and negative to falling, respectively) is obvious because the horizontal velocity component is perpendicular to the radar beam and therefore not detected. This is also the main reason why a radar looking vertically upward is a very precise rain rate measurement (*Löffler-Mang et al.*, 1999). In the above examples, however, we used a radar beam inclination of 27° to the horizontal, which is similar to the measurement setup at Santiaguito volcano. Therefore the horizontal velocity component greatly influences the measured velocity and the above assignment of positive and negative velocities is only a first-order approximation. In Fig. 2.3 the transition from rising to falling (i.e. the apex of the trajectory) is marked in all diagrams. Particles on inclined trajectories obviously deviate from the assignment near their apex due to their significant horizontal velocity component. For bigger particles, which are less influenced by friction, the erroneously assigned positive velocity while already falling significantly differs from the true velocity. Particles that are departing from the radar might be even measured with a negative velocity during their entire rise time, given that their launch angle is larger than 27° to the vertical and away from the radar.

In the above examples, however, we only show pseudo velocigrams and neglect that the reflected energy depends on the number of particles, their position inside the radar beam and, in addition, on the particle radii. Particles might leave the field of view near their apex and hence their "false" radial velocity is not seen by the radar. The measured radial velocity also depends on the particles position inside the beam, because only the component in direction of the radar is measured. I.e. the angular distance of a particle at the beam edge (i.e. where the intensity decreased to 50%) and the radar beam direction is 0.75°. Due to our relatively narrow beam opening angle, those varying directions ($27° \pm 0.75°$) can be neglected.

In the simple examples particles are erupted into a non-moving atmosphere, i.e. there is no wind. At a volcano however, the air certainly moves and influences particle movement. Air motion is due to various contributors: e.g. background wind, volatile expansion and jetting, turbulent entrainment of ambient air, and hence buoyant updraft. Every single component leaves a trace in the velocigram, which is more or less characteristic. A wind that is parallel to the radar beam for example adds a constant velocity to the particle velocity (neglecting particle inertia) and hence shifts the whole measured velocity to higher or lower velocities, depending on the overall direction of the wind (positive for wind towards the radar, negative otherwise). A wind perpendicular to the beam blows particles out of, or into the field of view. Furthermore, gas expansion and jetting are very complex processes. Their main effect is the transport of small particles to greater heights, which means that those particles need longer to fall down. Buoyant updraft acts in the vertical direction and hinders particles from falling. In fact, it further expands the coda as particles might be even floating in the upwind. For a more detailed analysis of the influence of those environmental parameters on ballistic transport and resulting Doppler radar data, the reader is referred to Appendix A.2 and the auxiliary material[2].

2.3 Characteristics of Eruptions

For identifying events in our data set we use an automatic event detection algorithm, where the echo power P^+ (see Eq. (2.1)) is used as an indicator for volcanic activity. This basic event detection has been successfully applied to data from Stromboli (*Scharff et al.*, 2007) and Merapi (*Vöge and Hort*, 2008a,b). A total of 157 events has been detected, 120 of which show a good signal-to-noise ratio and were selected for analysis. In January 2007, events at Santiaguito volcano were randomly distributed over time and show no characteristic event duration: Events last from 10 s (weak single pulse) to 120 s (see Fig. 2.6C below) and on average the event duration was about 30 s.

At line-of-sight distance of 2.7 km the field of view (FOV) of the Doppler radar, projected on the dome surface, is an ellipse with a diameter of about 144 m (along beam, long axis) and 70 m (across, short axis). The radar beam intensity decreases to 50% at 40 m height above the target location (beam center hitting surface). Because the dome is ∼200 m wide, we changed the target location of the radar beam during the experiment (see Fig. 2.4) in order to observe different parts of the dome. Of the 120 eruptions evaluated, 34 were observed at

[2]The auxiliary material consists of three animations and two additional graphics. For the graphics see Appendix A.3. The animations can be found in the online version of the published paper. The animations show particle motions and particle properties, calculated by the three-dimensional ballistic model for particle motion under simple atmospheric conditions, which is described in Appendix A.1. The graphics are explanatory graphics that demonstrate (a) the effect of the particle size distribution (PSD) on the measured echo power and how we chose the PSD that was used in the main article and (b) the theoretical imprint of an entrainment vortex in a velocigram.

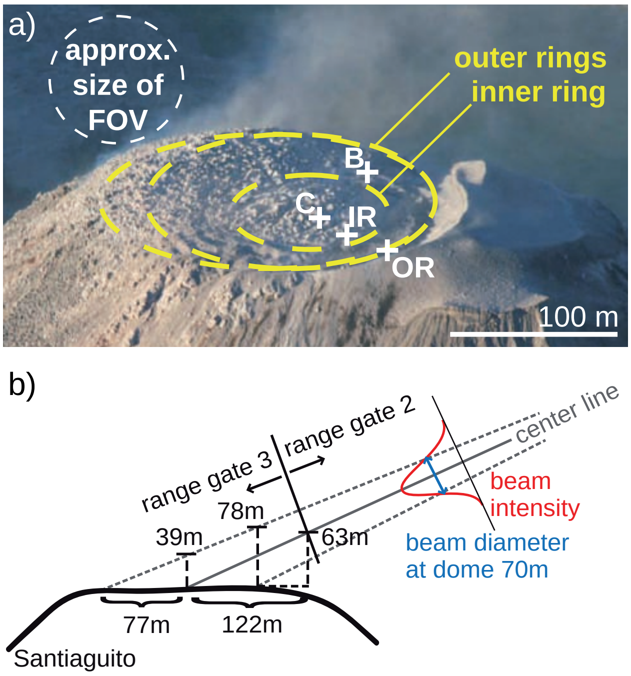

Figure 2.4: a) Beam target locations (white crosses) and approximate size of field of view (FOV) as seen from the radar location. Every cross marks the respective center of the FOV, whose footprint on the dome surface is also circular from this perspective. Yellow lines show the approximate location of inner and outer rings, the source of the explosive activity, in Jan. 2007. Note that at beam target location OR a significant amount of the FOV is filled by the supposedly non-moving flank, whereas at B a portion of the beam passes above the dome surface. b) Schematic drawing of the measurement geometry viewed perpendicular to the beam (from left in a). On the dome surface, the FOV footprint is elliptical and has a radius of 77 m (long axis) and 35 m (short axis). The radar beam edges (equal to the half maximum beam intensity) are indicated by gray dotted lines and their heights above the dome surface are given. In this study we focus on the processes directly at the vent and hence limit the data interpretation to range gate 3 (2500–3500 m slant distance). The beam crosses the dome surface at about 2640 m slant distance from the radar.

beam target location C (center of incandescence), 5 at IR (inner ring), 73 at OR (outer ring), and 8 at B (back side). All data shown here was recorded in range gate 3 (see Fig. 2.4b), i.e. show the lowermost 80 m of the eruption.

In Fig. 2.5 and Fig. 2.6 we show the data of 5 example eruptive events recorded at 4 different beam target locations (see Fig. 2.4). Each diagram shows a velocigram and the amount of reflected energy (calculated using Eq. (2.1)) as a function of time. For one of the events we show high-resolution video still images at 4 selected points in time. Directly at the onset of this event (white arrow in Fig. 2.6B) there is no visible degassing carrying ash. In the second image, a first ash cloud can be spotted near the dome center, after which the activity shifts to the outer ring at the circumference of the dome (see Fig. 2.6e). Interestingly, in some parts of the dome surface no fractures develop and the surface stays intact. After another 5 s into the eruption several ash-loaded plumes — preferentially at the outer rings — obscure the view onto the less ashy dynamics inside the eruption cloud(s) and the processes

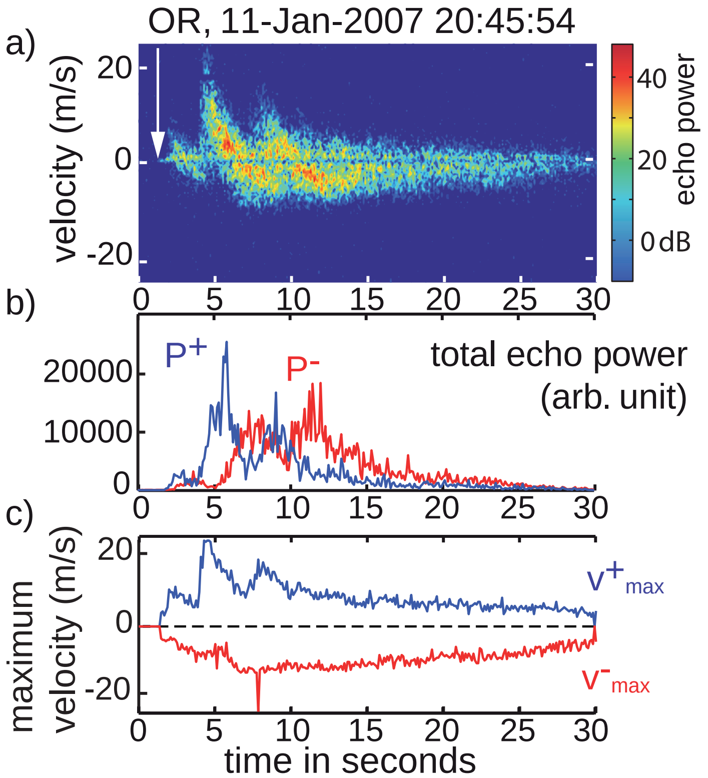

Figure 2.5: Dataset of one eruptive event recorded in range gate 3 (2500–3500 m slant distance) at beam target location OR (see Fig. 2.4a). We show the velocigram (panel a), the total reflected energy for positive and negative velocities (panel b), and the time lines of maximum velocities (positive and negative). a) Velocigram showing the echo power (color coded) as a function of velocity (y-axis) and time (x-axis). Note that the colors represent the ratio of echo power and background noise in dB, meaning dark blue (=0 dB) is background noise. This representation of the Doppler radar data gives an overview on an entire eruptive event and clearly shows periods of high and low activity. Note that the apparent gap at 18 m/s results from the removal of an interfering signal, which does not affect the quality of the data. The white arrow marks the onset of the eruptive event as detected by the radar. b) The amount of reflected energy as a function of time, calculated from Eq. (2.1). The blue line refers to the total energy reflected by particles having a positive velocity, the red one to negative velocities, respectively. c) The maximum radial velocity as a function of time. The blue line refers to the positive maximum radial velocity, the red one to the negative maximum radial velocity, respectively. Note that the lines of maximum velocity are essentially the envelope of the signal shown in the velocigram (transition from dark to light blue).

on the dome surface. *Patrick* (2007b) states that the gas mass fraction at Santiaguito is very high (>0.3), in which case we can assume that the radar beam penetrates the whole plume hence providing an integrated overview over particle velocities.

The Doppler radar data have two important features, which we interpret. Most of the eruptive events show a strong echo power at the lowest resolvable velocity (+0.39 m/s radial, see white arrows in Fig. 2.5 and Fig. 2.6A,B) that occurs 1–2 s before particles with higher velocities are detected. This strong signal at P_1 (echo power corresponding to $v_1 = 0.39$ m/s) lasts 0.5 to 1 s and there is no significant amount of reflected energy at any higher velocity during this time. Interestingly, the intensity and appearance of this feature depends on the beam target location (see Fig. 2.4a): It is clearly visible in 82% of the C ($P_1 \approx$16–19 dB) and IR ($P_1 \approx$16–17 dB) targeting events, whereas we found this signal in only 64% of the events recorded at OR ($P_1 \approx 15$ dB). In half of the B targeting events we do not observe this signal at all and in the other events, it is only very weak ($P_1 \approx 12$ dB). Note that P_1 values lie between 5 and 10 during the eruption, independent of the beam target location.

The second feature is a fluctuating eruption intensity throughout an eruption (Fig. 2.5 and Fig. 2.6), which can be seen in all 5 velocigrams (top of each panel). These fluctuations have a dominant period of 3–5 s and last for 3–12 s. They start with an increased echo power at high positive velocities, i.e. a sudden increase in maximum velocity, which is followed by a decrease in velocity. The maximum echo power eventually passes the zero velocity axis and the negative maximum velocity increases. During an eruption the echo power of rising (P^+) and settling (P^-) particles shows some local maxima, herein also termed pulse (for a precise definition of pulse see section 2.4.2). However, identifying individual pulses is more conspicuous using additional information from the temporal evolution of the velocities, which is summarized in the velocigram. Independent of the beam target location, 83% of all events show two or more pulses.

In addition to these two main features, (i) strong signal at the lowest resolvable positive velocity and (ii) pulses, 40% of the pulsed events show additional characteristics: (iii) an increasing intensity in echo power from 1st to 2nd pulse and (iv) a higher maximum velocity for the 2nd pulse (Fig. 2.5 and Fig. 2.6A,B,D). In contrast, Fig. 2.6C shows a long lasting stable sequence of very weak pulses. Almost all of the multiple pulsed events show an increasing intensity (in terms of maximum velocity as well as in terms of echo power) from the first to the second pulse. While this increase is small or non-existant for pulses observed at location B and C, we find a significant increase in both maximum velocity and echo power for the first two pulses at the rings (locations OR, 30% of events, and IR, all events, see Fig. 2.4). At OR and IR, velocities increase from 10–15 m/s to 15–25 m/s and total echo power from below 10^3 to 10^4 and more. At the same time the duration of single pulses increases from $\sim$3 s to more than 5 s.

Sequences of very weak pulses (Fig. 2.6C) are only visible at the OR-location (see Fig. 2.4) and account for 12% of OR targeting events. These 1-2 minutes long series of pulses with echo power around 10 dB are always followed by a few stronger pulses (higher velocities and

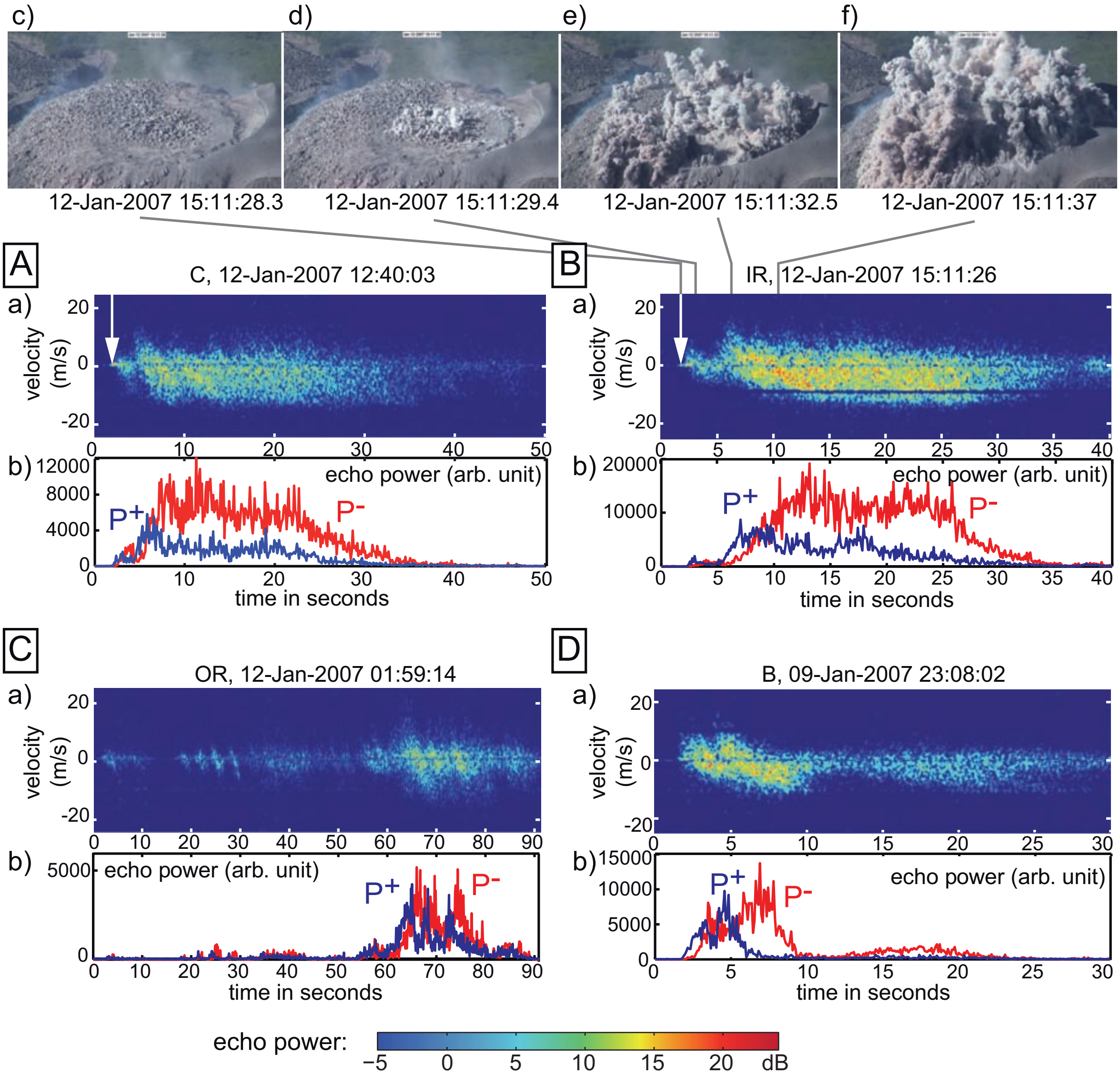

Figure 2.6: Datasets of four eruptive events recorded at different beam target locations (see Fig. 2.4a) and (c–f) video still images of eruptive event B. For each of the four events we show the velocigram (a) and the total reflected energy for positive and negative velocities (b). See Fig. 2.5 for an explanation of the radar data. High-resolution images show the dome surface directly before dome uplift (c), the first pulse in the center (d), the second pulse at the outer ring (e), and chaotic plumes afterwards (f). The respective point in time in the velocigram of event B is marked by the gray lines. The apparent gap in event B at -8 m/s results from the removal of an interfering signal which does not affect the quality of the data.

more echo power). The weak pulses occur nearly every 3 s (or multiples of 3 s) and last about 2 s. The reflected energy for rising and settling particles is of the same order, and maximum positive and maximum negative radial velocities are equal.

2.4 Data Interpretation

2.4.1 Low-Velocity Peak at Eruption Onset

In section 2.3 we mentioned a strong signal at the lowest resolvable velocity (+0.39 m/s, radial towards the radar), which appears up to a second before the onset of the explosive event. Interestingly, this low-velocity peak is almost not visible at location B on the far side of the dome (see Fig. 2.6D), where we recorded a total of 8 events. Except for observations targeted at B, 81% of all other events show this signal (see white arrows in Fig. 2.5 and Fig. 2.6A,B).

To be able to interpret this signal we have to take a more in depth look into the processing of the signal in the radar. Consider a particle that is moving at a velocity $v_p = v_i + \alpha\, dv$, between two velocity samples (v_i and $v_i + dv$, $0 < \alpha < 1$). The echo power of that particle is only distributed to those two velocity samples with respect to α. There is no contribution to any higher or lower velocity sample. The echo power of a very slow moving particle ($v_p < +0.39$ m/s) will hence be distributed between 0 m/s and the smallest velocity sample located at $v_1 = +0.39$ m/s. However, for data processing reasons the echo power at 0 m/s is being filtered out by a comb notch filter and cannot be used to deduce the particle's true velocity by comparing neighboring velocity samples. Because the signal appears at $v_1 = +0.39$ m/s but not at $v_2 = +0.78$ m/s we can assume that the true velocity measured here is less or equal +0.39 m/s (along beam).

The echo power value P_1 at $v_1 = +0.39$ m/s can be interpreted as the weighted integral over all reflecting surfaces that are moving with velocities between 0 and +0.39 m/s in the FOV towards the radar. The weighting factors depend on the lateral distance of the reflector from the radar beam center and the size and true velocity of the reflector. A strong signal at $v_1 = +0.39$ m/s without any signal at negative velocities before or afterwards could therefore be caused by (1) a volume with a high concentration of particles near the radar beam center that suddenly moves at less than +0.39 m/s and disappearing after 0.5 s or (2) the dome surface accelerating to a velocity of less than +0.39 m/s and stopping again after 0.5 s. We favor the latter explanation because:

1. no ash could be observed on the high-resolution videos at corresponding times (see online supplemental in *Johnson et al.*, 2008),

2. velocities are too slow to transport enough ash particles into the radar beam to explain the strong signal,

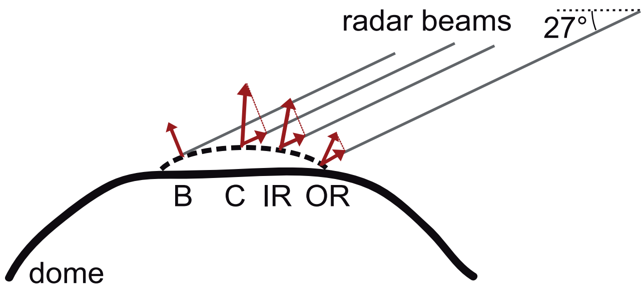

Figure 2.7: Schematic drawing of the uplift of the dome (view from south-east, same as in Fig. 2.2). Four beam target locations are marked and their corresponding radar beams are shown in gray. The uplift velocity and the corresponding radial velocity are given with red arrows for each beam target location. Because the distance of radar and beam target location is much bigger than the distance between the beam target locations, the radar beam angle can be considered as constant.

3. no negative velocities could be observed, hence no particles fall down directly before or after the strong signal,

4. the signal is almost similar for beam target locations C, IR, and OR, thus independent of the location of possible vent centers,

5. wind cannot explain the regular appearance 1.5 s before the explosion, and finally

6. the radial velocity component of a bulging dome surface would appear similar at beam target locations C, IR, and OR, but should be less detectable at location B (see Fig. 2.7). This is consistent with our data: 81% of the events at C, IR, and OR show this distinct signal but no event recorded at B shows this precursor.

We assume the observed low-velocity peak is caused by a non-uniform uplift of the dome surface (see Fig. 2.7). The illuminated dome surface is largest at target location C and IR. At B and OR a large fraction of the radar beam passes the dome surface or illuminates the flank, which leads to smaller echo power values at P_1 at those locations. At OR, however, the non-uniform uplift causes an almost 'along beam'-motion of the surface, which increases the echo power value of P_1 compared to B, where motion is almost perpendicular to the radar beam (i.e. zero radial velocity, see Fig. 2.7). The FOV at beam target location B also comprises a part of the FOV when targeting C, but due to the Gaussian intensity distribution of the radar beam, those contributions to the echo power are small.

Using particle image velocimetry (PIV) *Johnson et al.* (2008) found that large sections of the dome's surface are lifted 20–50 cm at eruption onset. Our data supports this finding. In addition, since the signals duration is ~0.5 s we calculate a radial uplift of 20 cm (44 cm vertical) which is in a very good agreement with *Johnson et al.* (2008), who obtained up to 0.5 m of vertical uplift.

2.4.2 Fluctuating Echo Power

As explained above, the echo power is related to the size of the reflecting surface. During the eruption, when ash is ejected with gas, this surface is the cumulative backscatter cross-section of all ash particles inside the probed volume. The backscatter cross-section (or radar cross-section, RCS) of a particle is related to its optical cross-section, the relation being highly complex and non-linear. As a first order approximation, however, we can assume that the bigger a particle, the more it reflects (see also below section 2.5.4).

The absolute amount of material moving through the beam cannot be calculated from the reflected energy, because the particle size distribution of the erupted material is unknown. However, the relative change in echo power does reflect changes in mass flux assuming the particle size distribution does not change dramatically from one eruption to another (for details on this see *Hort et al.*, 2006).

Every pulse in echo power starts with the sudden increase in echo power at high positive velocities, hence a sudden increase in maximum velocity. The maximum positive velocity decreases directly after reaching its maximum value at the beginning of a pulse. The total echo power P^+ increases in conjunction with the sudden velocity jump, but is less steep, which leads to the assumption that the particles are ejected over a longer time span during one pulse. After reaching its maximum, P^+ decreases again with almost the same rate as it increased before. At the same time P^- increases. This means that the particles of different size reach their individual apexes one after another (see also discussion of Fig. 2.3).

Interestingly, the maximum in P^+ always coincides with a minimum in P^- and vice versa. The sum of total echo power in the range gate $(P^+ + P^-)$ is almost constant after the second pulse, i.e. the volume of moving particles does not change dramatically. The maxima in P^+ (and also P^-) occur with a period of 3–5 s, which is similar to the time span a particle travels on its ballistic trajectory (see Fig. 2.3). The staggering of P^+ and P^- peaks can be explained for example by a wind (i.e. some turbulent gas motion) that forces a fixed volume of particles to move alternately up and down. The draw back of this explanation is the acceleration phase, when the wind direction shifts from down to up. We do not observe a slow increase in positive maximum velocity as would be required here. Another explanation is that the pulses are independent of each other and the volume flux into the FOV is constant and balances the volume flux out of the FOV (e.g. due to ash sedimentation).

The geometry of the measurement is such that we observe particles that exit the vent. Hence a sudden jump in maximum velocity and direct decrease afterwards means that particles enter the FOV with their highest velocity, i.e. they are accelerated to their respective maximum velocity either below the dome surface or somewhere else outside the FOV and behave like ballistic objects once they entered the FOV (compare to Fig. 2.3). Therefore every pulse (characterized by a sudden jump in maximum velocity in conjunction with an increase in total echo power P^+) is independent of the other pulses in an eruption. The term pulse therefore refers to the sudden release of (maybe overpressurized) gas that percolated through

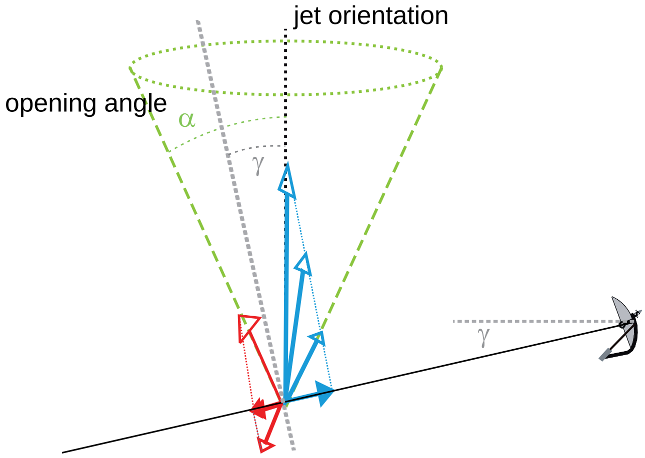

Figure 2.8: Geometry of initial velocities, opening angle (α) and radar beam inclination ($\gamma = 27°$). Arrows indicate velocity vectors of particles, vector length mirrors particle speed. Filled arrows show the radial velocity component as measured by the radar. Blue vectors show examples with a positive radial velocity, red vectors show negative velocity examples. Due to the 1D measurement we cannot distinguish between rising and falling particles that have the same velocity component into the direction of the radar beam. However, the velocity evolution over time can be used to separate the contribution of rising and falling particles to the echo power. The absence of negative radial velocities at the beginning of the eruption underlines that $\alpha < \gamma$ at Santiaguito volcano.

cracks in the conduit fill thereby accidentally entraining ash particles and accelerating them by air drag to their size dependent terminal settling velocity (relative to the gas jet velocity). The velocity observed by the radar is the radial component of the particles true velocity. This means that depending on the angle between radar beam and particle trajectory the measured radial velocity is always less than the particles true velocity (or equal at zero angle). Hence the maximum radial velocity is the minimum approximation for the velocity of the fastest particle and hence for the gas velocity, which we assume to be moving vertically. Therefore we use the maximum radial velocity converted to a vertical velocity to approximate the gas velocity of 20–35 m/s for the first pulse and 35–60 m/s for the second and later pulses.

Given that at the beginning of a pulse (at least for the first and second) no particles with negative velocities are observed, we can constrain the geometry of the pulse (see Fig. 2.8). High-resolution videos (see online supplemental in *Johnson et al.*, 2008), recorded from the location of the radar, indicate that at the onset of an eruption particle trajectories are not perfectly vertical but show a certain opening angle. For certain events the opening angle is observed to be bigger for the first pulse emanating from the center of the dome (±20–30°) than for the second pulse at the outer ring (±10–20°). This is in agreement with the radar data from which we can deduce that the opening angle of all eruptions must be smaller than 27°: Assuming that no particles fall down at the onset of a pulse, a negative radial velocity would correspond to particles that move at an inclination larger than 27° with respect to the vertical (red vectors in Fig. 2.8), which we do not observe.

Within the first pulse the echo power of rising particles is almost equal to that of settling particles, whereas during the second pulse the energy reflected by the settling particles is often up to two times larger, which can be explained by a) radar beam attenuation, b) the measurement setup and c) wind. The attenuation of the radar beam depends on the concentration of scatterers due to shadowing effects and multiple scattering. This means that the same particle volume returns less echo power when it is concentrated near the beam axis than evenly distributed in the probed volume. In an eruption, the bulk density of the erupting gas-particle mixture is presumable highest at the pulse onset and decreases as the particles decouple from the gas and spread out. Second, the probed volume atop the dome surface can be completely filled by falling particles, independent of the beam target location. Rising particles, however, are constrained to the volume of a top-down cone directly above the vent with an opening angle of less than the beam inclination (see Fig. 2.8). Due to the distribution of vents, the FOV only covers a few of them and hence only a small fraction of the rising particles is observed. The falling particles may be blown into the FOV from vents outside the FOV. A third explanation is based on a background wind that blows away from the radar, so that the measured radial velocities are all shifted towards negative velocities (for more details on this see Appendix A.2 and Fig. A.2). The difference between first ($P^- \approx P^+$) and secondary pulses ($P^- \approx 2P^+$) can not be explained solely by wind. It is rather an indication of the number and position of active vents: Equal echo power in positive and negative velocities means that everything that passed the FOV on its way up falls down through the FOV again. This is true for example, when assuming a single active vent somewhere inside the FOV and a narrow opening angle. When more falling as rising particles are observed, additional vents outside the FOV are active. This leads to the assumption that the first pulse preferentially emanates from a vent near the dome center and secondary pulses occur at vents at the outer rings. This finding is supported by the high-resolution videos (see online supplemental in *Johnson et al.*, 2008), where first activity can be spotted near the center before it spreads out to the dome circumference.

2.5 Simulating Doppler Radar Data

The radar was aiming at different target locations on the dome (see Fig. 2.4), which allows us to explore temporal as well as spatial characteristics of the ring eruptions. Because only one radar was deployed, we observed one eruption at one location at a time and therefore cannot interpret all details in a quasi 3D analysis. However, we were able to identify major characteristics for each beam target location (see section 2.4.2 above) and constrained parameters describing the 'standard eruption' at Santiaguito. In this section we use our numerical model to further strengthen the hypothesis that events at Santiaguito volcano are composed of a series of single explosive pulses of varying intensity and location, and to explore the influence of the beam target location on the measured data.

Before turning to the model results we note that unlike other studies (*Marzano et al.*, 2006; *Gouhier and Donnadieu*, 2008) we do not attempt to match the actual amount of echo power by adjusting the particle size distribution (PSD). As has been shown by *Ziemen* (2008) it is impossible to extract the particle size distribution as well as the total mass of particles from a single radar measurement without further assumptions. Any attempt to determine the actual mass of particles being erupted requires prescribing a distinct PSD. Hence the masses calculated in the following cannot be viewed as the true total mass but instead is a relative mass that depends exclusively on the assumed PSD.

2.5.1 The Numerical Model

The results shown here are produced using a numerical model to calculate ballistic particle transport and corresponding synthetic radar spectra. A complete description including all equations is given in Appendix A.1). For the dynamic part we use a Lagrangian formulation of ballistic particle transport in air. Following *Herzog et al.* (1998) atmospheric friction (atmospheric drag) is calculated for both Newtonian and Stokian friction for each particle and the higher of both values is applied to the particle. That means fast particles are subject to Newtonian friction whereas slow particles undergo Stokian friction. The gas thrust phase (jet) is parametrized through an upward wind, whose velocity depends on the radial distance to the center of the eruption column. This implementation of the atmosphere is similar to the model developed by *Dubosclard et al.* (2004) and *Gouhier and Donnadieu* (2008).

Crater and vent geometry as well as initial conditions like particle size distribution (PSD), gas velocity, and opening angle are free parameters of the model. It has been shown in previous studies that the PSD is well described by a Weibull distribution (*Weibull*, 1951; *Marzano et al.*, 2006, see also Fig. 2.9). Vent conditions may change with time during an eruptive event. Therefore the PSD and maximum launch velocity of particles are allowed to vary with time. Following *Chouet et al.* (1974) we assume the particle launch velocity $|v_{p0}|$ to depend on the particle radius r

$$|v_{p0}(r,t)| = w_{g0}(t) - \sqrt{\frac{8g\rho_s}{3c_w\rho_g}r} \quad , \tag{2.3}$$

where $c_W = 1$ is the empirically determined drag coefficient for ash (*Pfeiffer et al.*, 2005). ρ_g and ρ_s are the density of gas and solids and g is gravity. $w_{g0}(t)$ is equal to the gas jet velocity and varies with time according to a prescribed function (constant, increasing or decreasing). Gas jet velocity and particle size distribution can be configured for arbitrary time periods. Hence, we can build complex scenarios of vent near conditions for which we calculate synthetic radar spectra.

Once particle size, location, and velocity of the particles are determined from the ballistic part of the model described above, we calculate the amount of energy reflected by each particle as a function of time. We include geometric spreading but neglect atmospheric absorption, multiple scattering, and interference. The synthetic radar beam has an opening angle of 1.5° with the intensity inside the beam following a Gaussian distribution.

Scattering of electromagnetic waves at ash particles is calculated using Mie theory (*Mie*, 1908). In brief, Mie describes the interplay of a particle's internal and external electromagnetic fields. In the Mie region, the external field wavelength and the particle size are of the same order of magnitude (see Fig. 2.9a). Here a so-called creeping wave (*Currie*, 1989) travels around the particle interfering constructively or destructively, hence the amount of back-scattered energy strongly depends on the ratio of particle size and wavelength. In one end member case, when the wavelength of the external field is small compared to the particle size, the internal field will almost match the external field and the particle's back-scattering cross section is almost equal to its geometric (or optical) cross section. In the Rayleigh region (the other end member), when the particle is very small compared to the wavelength, the energy is scattered almost isotropically in all directions, hence only a very small fraction is scattered back towards the radar. Because we assume that size and dielectric properties do not change significantly over time, the back-scatter cross sections need to be calculated only once for each particle size. This is done by an external program in advance.

2.5.2 Initial Conditions

Here we try to fit the 'shape' and 'trends' of the event shown in Fig. 2.5 as it comprises three clearly visible pulses. The vent positions are fixed and not changed to reach a 'best fit'. The vent releasing the first pulse is located near the dome center at position C (see Fig. 2.4), while the second and third pulse are set to several vents that are positioned on a circle of diameter 200 m around the dome center (representing the outer ring). Fig. 2.10 shows the vent positions and measurement setup as well as the initial conditions derived from observations discussed above.

Particle directions are randomly distributed inside the opening angle (±25° here) around a directivity axis, which for simplicity is assumed to be vertical for all pulses. A more precisely constrained opening angle would require a 3D measurement using three radar systems, as has been successfully demonstrated by *Vöge et al.* (2005) and *Gerst et al.* (2008).

In summary, the modeled eruption consists of three pulses: a first pulse with a gas velocity of 35 m/s at a vent near the dome center, followed by two pulses from the vents located at the ring. The second and third pulse have a higher gas velocity (60 m/s). We observe an almost linear decay in maximum velocity. According to Fig. 2.3 particles with radii >5 mm are mainly affected by gravity and their velocity also decays almost linearly, where smaller particles (<1 mm) move with the gas. The big particles however are ejected with slower velocities due to their size and hence cannot be responsible for the almost linear decay in maximum velocity. We therefore assume that the gas jet velocity decays linearly.

The geometry of the example eruption was chosen to be similar to the setup of our instrument at Santiaguito, i.e. the distance to the vent is 2.6 km and the inclination of the radar beam is 27° (see Fig. 2.4b). The PSD is assumed to be the same for all pulses (see black lines in Fig. 2.9b–d), but the volume flux for the first pulse is half of the volume flux of later

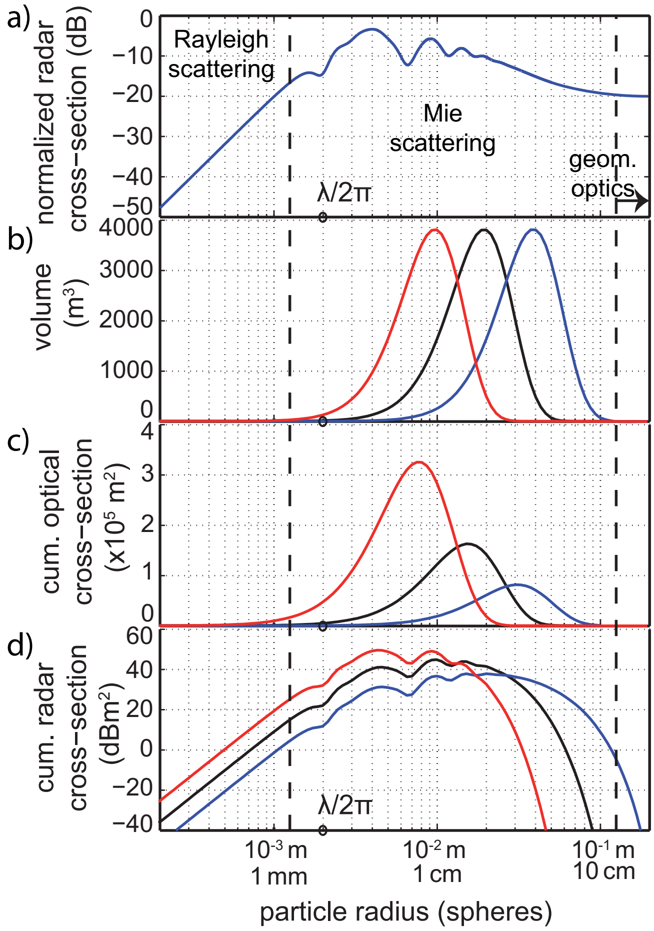

Figure 2.9: Radar cross-section (RCS) and particle size distributions (PSD) used in the model calculations presented here. a) Normalized radar cross-section (or back-scatter cross-section, dB) of a single particle normalized to its optical cross-section. RCS is calculated for a wavelength of $\lambda = 1.25$ cm and using the complex refractive index of ash at high frequency $\epsilon = 2.458{+}0.02197i$ (*Adams et al.*, 1996). RCS is a function of particle radius and wavelength. When $r < 0.1\lambda$ the normalized RCS increases proportional to r^4 (Rayleigh scattering). In the other direction, when $r > 10\lambda$ the normalized RCS increases proportional to the optical cross-section. In the region where $0.1\lambda < r < 10\lambda$, a so-called creeping wave travels around the conducting sphere interfering constructively or destructively (Mie scattering). I.e. using our 24 GHz-Doppler radar (wavelength $\lambda = 1.25$ cm) a 4 mm-sized particle reflects five times more energy per unit area than a 6 mm-sized particle. b) The PSDs follow a Weibull distribution and differ only in the mean particle radius, 5 mm (red lines), 10 mm (black lines), and 20 mm (blue lines). Minimum radius (0.6 mm), maximum radius (40 mm) and shape parameter of the Weibull distribution (1.5) are held constant. Note that using a shape parameter of 1.5, the radius corresponding to the maximum in volume is twice, whereas the radius corresponding to the maximum number of particles (mode of the PSD) is approximately half of the mean radius of the distribution. c) Cumulative optical cross-section of all particles in the PSD. This view represents the area that is covered when all particles are spread out. Because the total volume is constant, the cumulative optical cross-section is smaller for PSDs with higher mean particles sizes. d) The cumulative radar cross-section (dBm^2) is the summed RCS of all evenly sized particles in the PSD. Note that we use the black PSD (10 mm mean radius) in all model calculations unless stated otherwise.

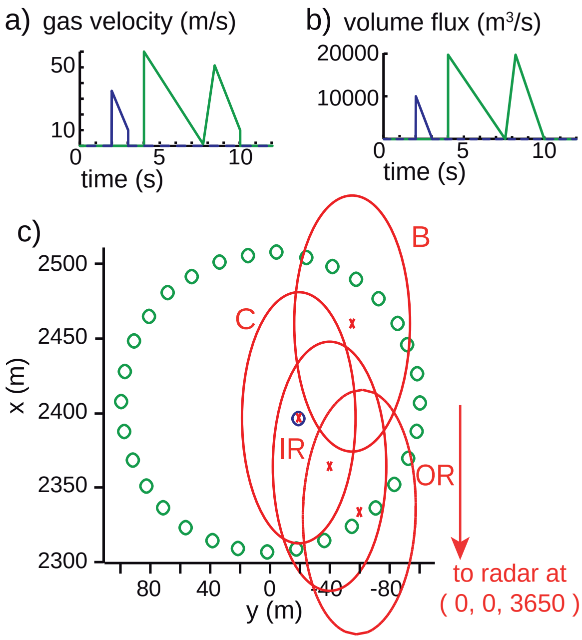

Figure 2.10: Initial conditions for the model calculations of the temporal evolution of the eruption. a) Evolution of maximum launch velocity over time. The launch velocity can be interpreted as initial gas velocity and is related to the particles launch velocity via the particles terminal fall velocity (see equation 2.3). The colors relate the velocity to the respective active vent. b) Assumed volume flux for the modeled eruption. The colors represent the vent(s) to which the volume flux is evenly distributed. c) Top view of the simulated dome surface (at z=2550 m) with its vent distribution. The first active vent is located near the center (blue circle). The very special ring-type eruptions of Santiaguito are modeled using a ring of radius 100 m consisting of 32 evenly spaced vents (green circles). We assume a constant vent diameter of 10 m. Red ellipses show the four different FOVs (from top to bottom: B, C, IR, and OR). The radar position is at coordinates (x=0 m, y=0 m, z=3650 m) and indicated with the red arrow. The PSD used in our model calculations is given in Fig. 2.9, input parameters for atmosphere and radar configuration are: $\rho_g = 0.897\,\mathrm{kg/m^3}$ at $T = 300\,\mathrm{K}$, $R_{air} = 287\,\mathrm{J/kg/K}$, $\mu = 1.82 \times 10^{-5}\,\mathrm{Pa\,s}$, $c_W = 1.0$, $z_{\mathrm{ref}} = 50\,m$ (gas jet reference height), range gate length=1000 m, $v_{Ny} = 49.92\,\mathrm{m/s}$ (maximum unambiguous velocity), $dv = 0.39\,\mathrm{m/s}$ and output is calculated for range gate 3 (2500–3500 m).

pulses where the volume is spread over the distributed vents (see Fig. 2.10b). We assume a linear decay in volume flux to account for the possible explosive nature of ash release. To show how the same event is seen by the radar from different beam target locations, we calculate the synthetic data for all 4 beam target locations.

Although the atmosphere is rarely at rest at a volcano, we neglect any background wind in our calculations to keep the model simple. We also do not account for entrainment of ambient air and buoyant updraft of the developing ash cloud as the radar is aiming at the source region of an eruption, which is dominated by the gas thrust so that buoyant rise and entrainment have little effect on the dynamics. The transition of an inertia driven gas jet to buoyantly driven plume rise is at Santiaguito slightly below 50 m height above the dome surface (*Sahetapy-Engel and Harris*, 2009b). Because the probed volume extends to ~40 m height above the beam center and the beam intensity is maximum near the dome surface (i.e. the vents), we neglect buoyant updraft in our model calculations. The effect of buoyancy on particle motion is shown in Appendix A.2. Main effects are a) an overall shift of echo power towards positive velocities since particles terminal velocities are relative to the surrounding gas velocity and b) a long coda of slowly falling and floating particles.

Patrick (2007a) observed at ash-rich Strombolian eruptions (Type 2a) that a vigorous entrainment vortex at the plume front could only develop after reaching fully buoyant behavior (i.e. above our FOV). The entrainment needed to reach the buoyant phase is due to small scale turbulent shearing along the edges of the jet (*Suzuki et al.*, 2005; *Patrick*, 2007a). Although the main mechanism that produces the gas jet differs (bubble bursting in the conduit at Stromboli versus gas flow through an interconnected network of fractures in dome surface at Santiaguito), the ash gets entrained incidentally by the gas flowing through a layer of ash (backfilling material at Stromboli or covering the dome surface at Santiaguito, see *Patrick*, 2007a,b). Once the gas-ash-mixture left the vent, the processes in the plume, which are investigated here, are independent of the conduit processes. How a vortex ring displays in a pseudo velocigram is given in the auxiliary material. Note that small scale turbulence is also neglected. Turbulence is often simulated as adding a small random velocity vector to the particle's velocity in every time step. The overall motion (diagonal bended streak due to gravity and air friction, see Fig. 2.3) will be superposed by random velocity deviations, but still dominate the velocigram. This means that sharp lines in a velocigram will become smeared across neighboring velocities in real data where turbulence is important.

2.5.3 Model Results

In Fig. 2.11 the real data and synthetic velocigrams are shown for the different radar beam target locations C, IR, OR, and B calculated from the ballistic model. The detailed motion of the particles is shown in three animations which are part of the auxiliary material. In each animation the particles are colored, highlighting a different variable (particle radius, beam intensity for beam target location OR and echo power for beam target position OR). Within their first 10–15 m of rise particles bigger than 1 mm (radius) decouple from the gas jet and eventually fall back to the ground (negative velocities, see Animation 1). The mm-sized particles rise with the gas and start settling when the gas jet faded. Hence small particles accumulate during the course of an eruption.

The overall shape (maximum velocities) and trends in P^+ and P^- for the real data (Fig. 2.11a) do fit those of the modeled eruption presented in Fig. 2.11e). As explained above, we did not try to fit the absolute values for echo power (arbitrary units). Importantly, the maximum velocities observed at the different locations on the dome are nearly the same, in agreement with the radar data, but the reflected energy of these signals varies significantly. For example, if we take the initial pulse (see first second in temporal evolution) that originates at the center of the plume, the amplitude of the reflected signal is highest at the location C, which is directly targeting this location. This pulse is hardly visible when the beam is aiming

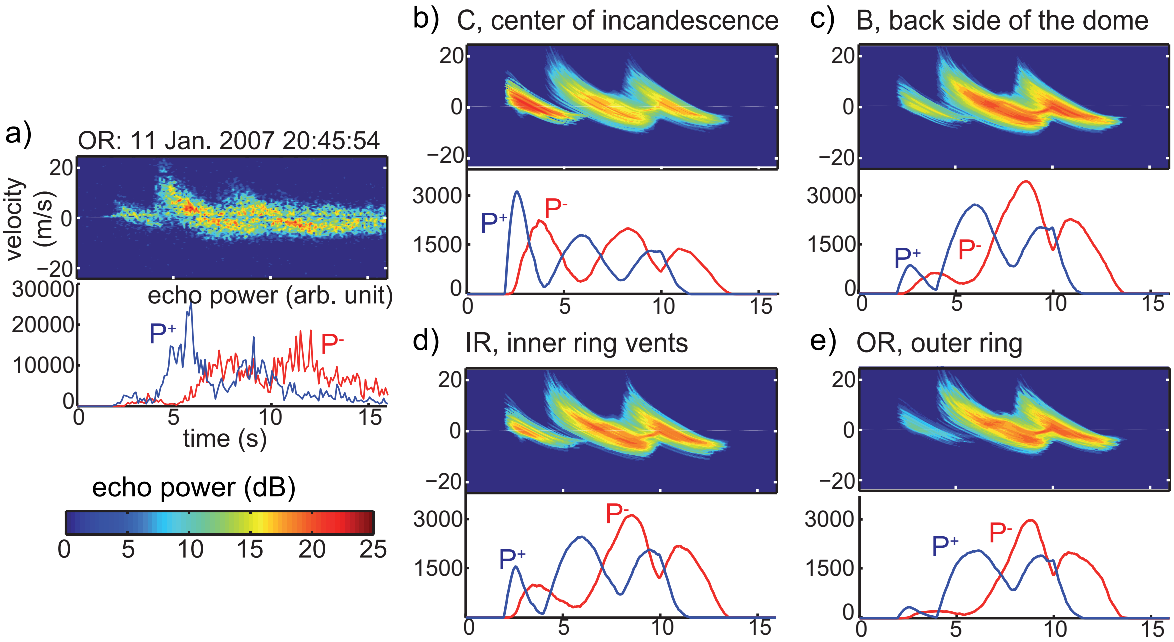

Figure 2.11: a) Real data and b)–e) synthetic datasets of one eruptive event, observed for different beam target locations. For a short description of displayed values see Fig. 2.5. The first pulse is most obvious in C and IR, whereas the echo power of outer ring pulses is higher in OR and B (see also Fig. 2.10). The model parameters (vent conditions, PSD and eruption geometry were chosen to result in a best fit. The best fit criterion is the similarity of velocigrams a) and e) in maximum velocity and total echo power trend. For further discussion see text.

at location OR, where only a small fraction of the transmitted energy is reflected by erupted material (see Animations 2 and 3). This is because the radar beam has an opening angle of 1.5° and the intensity inside the beam follows a Gaussian distribution (see Fig. 2.10).

All velocigrams have alternating peaks in P^+ and P^-. They show a slow increase in P^+ (compared to the jump in maximum velocity). After reaching its maximum P^+ decreases at almost the same rate as it increased before and P^- increases. Hence assuming a pulsed volume flux seems to fit our data. Nevertheless contrary to the real data, the summed echo power ($P^+ + P^-$) increases slightly in the synthetic data sets (after the second pulse). Hence the true volume flux seems to decrease with eruption duration as more and more particles accumulate in the FOV.

The maximum velocity at pulse onset in the synthetic velocigrams equals those in the real data set (Fig. 2.11a), which justifies our simple assumption to use the maximum radial velocity converted to a vertical velocity as gas jet velocity. However, the decay in the synthetic data differs from the almost linear decay in Fig. 2.11a, which indicates that during the pulse the maximum radial velocity underestimates the true gas jet velocity.

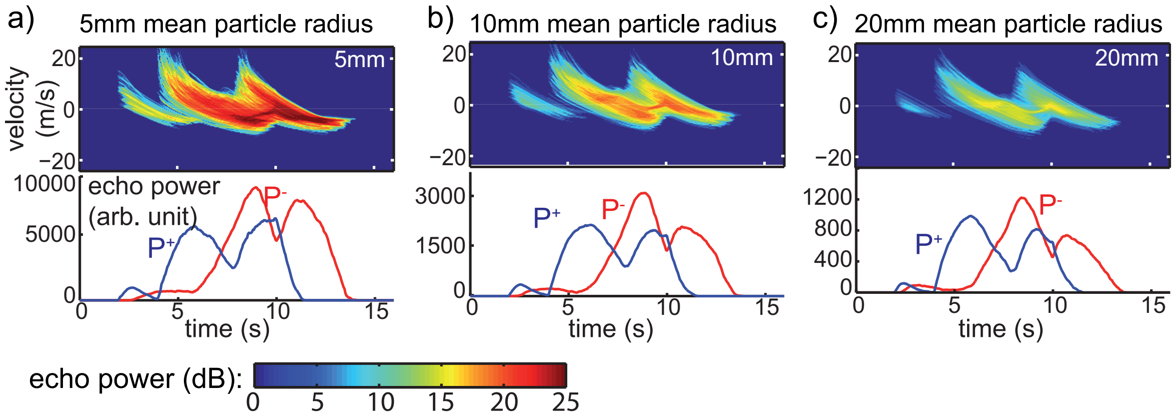

Figure 2.12: The same eruptive event (see Fig. 2.11) observed at OR using different particle size distributions (PSD). The range of particles and the total volume is constant, but the mean particle radius is varied from 5 mm (a), 10 mm (b) to 20 mm (c). Note that b) is the same velocigram as shown in Fig. 2.11e). The PSDs are given in Fig. 2.9. The synthetic velocigrams for the other beam target locations are given in the auxiliary material.

2.5.4 The Particle Size Distribution

The particle size distribution (PSD) is a badly constrained parameter since no published PSD exists for Santiaguito. We have tested different PSD (different mean grain sizes) and find a good agreement with the radar data using the PSD shown in Fig. 2.9b–d (black line, 10 mm). Grain sizes at Santiaguito are smaller than at for example Stromboli (see *Marchetti et al.*, 2009) due to the different fragmentation mechanism. We assume that the PSD does not change significantly from one event to the other and especially not during one event.

While exploring the effect of single parameters, we found that the main parameter controlling total echo power is the total erupted volume. The more particles move inside the radar beam, the higher the echo power. A smaller effect can be achieved by changing the range of particle sizes to smaller or bigger at constant eruptive volume, but this effect is not linear (see below and Fig. 2.9). In our model the PSD controls the echo power of particles and their initial velocities. When we increase the gas velocity, for example, we also have to increase the minimum particle size to give the same maximum initial velocity. To get the same echo power values as with the slower gas velocity, we also have to increase the total volume of the PSD (to keep the cumulative radar cross-section constant). Therefore we can reproduce a single velocity spectrum with a large number of different PSDs. Initial velocity and size of a particle, however, affect its ballistic motion due to the size-dependent drag force. Hence using consecutive spectra constrain the PSD. We can therefore deduce from the evolution of maximum velocity and total echo power if our assumed PSD is correct within an order of magnitude.

The range of particles sizes used here is kept constant and is chosen due to the following reasons: the minimum particle size that can be calculated by our model (numerically stable using a time step of 0.01 s) is 0.6 mm, which is already in the Rayleigh scattering region (see

Fig. 2.9a). Hence the radar cross-section of even smaller particles diminishes with the sixth power of their radius and can be neglected. Second, the maximum particle size is constrained by the gas jet velocity. We use equation 2.3 to assign an initial velocity to the particle. Hence, only particles whose radius satisfies $r > 1/2(w_{g0}/k)^2$ exit the vent and therefore particles $r > 4 - 5\,\mathrm{cm}$ can be neglected here.

In Fig. 2.12 we show the same model calculation as in Fig. 2.11e with a smaller (a) and a larger (c) mean particle size. The corresponding PSDs are given in Fig. 2.9b–d. The most prominent effect of changing the mean grain size at constant total volume is that the cumulative optical cross-section for increasing mean particle radius decreases. Hence also the echo power is less for a larger mean grain size. In addition, the normalized radar cross-section of mm-sized particles is bigger than that of the cm-sized (see Fig. 2.9a), which means they reflect more energy per unit area than the big particles.

2.6 Discussion and Conclusive Remarks

In this paper we have demonstrated how Doppler radar observations can be used to shed new light on the dynamics of Santiaguito volcano, Guatemala. Our observations reveal that the eruptions at Santiaguito volcano are composed of several single pulses about once every 3-5 seconds during an event.

Most of the 157 events recorded during the experiment with the Doppler radar were pulsed eruptions with several single explosions during one eruptive event (85% for locations C and IR and 49% for location B and OR). Video footage shows that the eruptions often begin at the center of the dome and then move to the outer rings. Using a single radar we were not able to resolve this change in eruption location during a single event. Instead we targeted different locations of the dome and see clear evidence that the center as well as the outer rings are involved. The first pulse is different from the following ones: it has a slower maximum velocity and less echo power. In addition, $v^+_{\mathrm{max}} \approx |v^-_{\mathrm{max}}|$ indicates that the first pulse is almost not influenced by any wind and comprises mainly ballistically flying particles that are subvertically ejected. The total echo power depends on the beam target location, which indicates that every FOV illuminates the active vent(s) of the first pulse, but with different intensity. On the contrary, the echo power of secondary pulses is almost the same at every beam target location. Hence every FOV comprises several active vents, but maybe different ones. There is almost no difference between the second and following pulses, which in turn suggests that those later pulses originate also at the outer rings, which cannot be seen in the videos.

The short wavelength of our instrument (1.25 cm) enables us to simultaneously detect small buoyantly rising as well as larger particles that move ballistically. Hence we collected 1D measurements through processes that are inherently 3D, which complicates data evaluation. Therefore we make use of numerical modeling of particle transport during explosive degassing at multiple locations and calculate the corresponding radar spectra.

Synthetic velocigrams (see Fig. 2.11) and real data sets (see Fig. 2.6) both show similar features. Repeated sudden increase in positive maximum velocity, followed by a slow increase in negative maximum velocity and alternating peaks in echo power of rising and settling particles can for example be explained by repeated degassing pulses.

The retrieval of synthetic spectra is based on a simple ballistic model, where the particle's initial velocity is related to its size. Using Eq. (2.3) we assume that all particles have been accelerated in a conduit by the ejecting gas and that all particles have reached their terminal fall velocity relative to the gas (*Steinberg and Babenko*, 1978). In other words, the particle velocity is equal to the gas velocity minus terminal settling velocity. In nature particles will reach their terminal velocity only at open conduit systems with conduits wide and long enough and without internal obstructions, and assuming that the particle concentration inside the conduit does not influence the two-phase flow itself. At Santiaguito, however, gas erupts through small cracks and fractures of the dome surface, hence the above conditions are not exactly satisfied.

Our approximation of the gas exit velocity using the maximum radial velocity converted to a vertical velocity tends to overestimate the true gas velocity. The maximum radial velocity most probably belongs to a particle that is not moving vertical (*Gouhier and Donnadieu*, 2011). Assuming all particles have the same absolute velocity the maximum radial velocity belongs to the most inclined particle and the gas velocity is overestimated by a factor of 1.7, which is the ratio of particle velocities on a vertical and the most inclined trajectory (27° towards the radar) that result in the same radial velocity. Nevertheless, this definition of the initial particle velocity provides a simple scaling between each particle's size and velocity that has the advantage of being intuitive but tends to overestimate the true exit velocity as it marks the upper limit for the gas and particle velocities. Furthermore we only interpret the temporal evolution of maximum velocities (rising and falling), for which we could also use random exit velocities in a defined range for every individual particle.

We observe an almost constant total echo power ($P^+ + P^-$) during secondary pulses. Both our interpretations that the volume fluxes into and out of the FOV balance until the last pulse ends, and that the net volume flux is hence zero, are not reproduced by the model. Big particles move on ballistic trajectories, but small particles move with the gas and hence are blown upwards. Therefore they still move in the FOV, when the next pulse ejects gas and new particles. Small particles accumulate in the FOV and the total echo power increases with time. Nevertheless, the attenuation of the radar beam depends on the concentration of particles, which means that at high concentration the beam does not penetrate the whole volume. This attenuation is neglected in our model. In reality, a constant total echo power can represent either a constant or an increasing volume, when the particle concentration is high enough.

The main difference between synthetic and real datasets is that the most energetic events (in terms of echo power) show very high negative velocities that cannot be explained by simple ballistic motion. In principle, we were able to reproduce these velocities with several models of higher complexity. Adding turbulence to the ballistic model, for instance, broadens the region of high echo power around zero. A deviation of the directivity axis away from the radar shifts the whole velocigram towards negative velocities without changing any other pattern. A wind component away from the Doppler radar (e.g. down-slope wind) also shifts the whole velocigram towards negative velocities (see Appendix A.2 and Fig. A.2). A high total echo power might also represent a high concentration, which in turn indicates that attenuation of the radar beam in the ash cloud is not negligible. Hence, we would only see the front of the cloud. In that case, the velocigram of an entrainment vortex ring will give only falling particles, because ash is dragged up in the column center (invisible to the radar) and falls down at the cloud edges (see auxiliary material for more explanation). Coupling the synthetic radar model to more accurate 3D eruption column models like ATHAM (*Oberhuber et al.*, 1998) or PDAC (*Esposti Ongaro et al.*, 2007) will enhance our understanding in future investigations. Nevertheless, the first pulse is always the same, independent of the echo power of the following pulses, whereas the second and following pulses always have a total echo power of the same order of magnitude.

Although we measured comparable or even lower exit gas velocities than at Stromboli, eruption clouds at Santiaguito volcano reach heights of up to 1000–4000 m above the vent, which is one order of magnitude higher than at Stromboli. This seems indicating that buoyancy and hence the thermal potential of the erupting mixture controls the plume height rather than the gas exit velocity. However, analysis and modeling of the Doppler radar velocigrams recorded at Arenal volcano (Costa Rica) using a different Doppler radar and setting (different range gate dimensions compared to the plume, different viewing geometry) show that ballistic and ash plume dynamics can effectively be discriminated by Doppler radar and therefore be quantified separately (*Valade and Donnadieu*, 2011).

In conclusion a typical eruptive event at Santiaguito seems to start with an uplift of the dome center that takes 0.5 to 1 s. No ash is visible during that time. First ash particles at higher velocities (10–15 m/s along beam) appear 1.5–2 s after the onset of uplift (i.e. $\sim$1 s after the uplift signal vanishes). Another 2–3 s later, a faster (20–25 m/s along beam) and more intense pulse (up to 20 dB increase) can be observed at the outer ring. This second pulse is in 83% of the observed events followed by pulses of same or less strength in terms of echo power and maximum velocity. The recurrence period of these subsequent pulses is 2–5 s with an average of 3 s.

According to *Johnson et al.* (2008), the dome uplift starts in the center and migrates outwards with 30–50 m/s. Considering that the distance between the dome center and the outer ring is $\sim$100 m the time between center uplift and beginning of outer ring deformation is 2–3 s, which is almost identical to the time span between the first pulse (at dome center) and the second pulse (at the ring). It seems that uplift is the trigger for the eruption and initiated by a process that also mobilizes volatiles. But the volatiles need to percolate through a system of fractures in the dome before they reach the surface, which explains the time span between the onset of uplift and the first degassing ($\sim$1.5 s).

Comparing the velocigrams of the example calculations (see Fig. 2.11) and the real data, it stands to reason that the multiple streaks observed during the eruptions are actually a sequence of single pulses. In fact such pulses have also been observed during thermal observations at Santiaguito volcano (*Sahetapy-Engel and Harris*, 2009b) but their data do not reveal details on the near-vent eruption velocities. The pulsed nature of events has also been observed at other volcanoes, e.g. using infrasound at Karymsky volcano, Russia (*Lees and Bolton*, 1998; *Johnson and Lees*, 2000), photoballistics or Doppler radar at Stromboli, Italy (*Chouet et al.*, 1974; *Ripepe et al.*, 1993; *Scharff et al.*, 2008), and seismics or Doppler radar at Arenal volcano, Costa Rica (*Lesage et al.*, 2006; *Donnadieu et al.*, 2008). At Stromboli pulses can be explained by a chain of successive bursting gas bubbles. At Karymsky, a model analogue to a pressure cooker has been proposed to explain those pulses (*Lees and Bolton*, 1998). A somewhat similar model has been proposed by *Lesage et al.* (2006) for Arenal volcano. In their model cracks open and close rhythmically under the influence of pressure oscillations in a bubble-filled closed conduit.

A possible mechanism that explains both the initial dome uplift and the occurrence of repetitive pulses during an eruptive event at Santiaguito has been proposed by *Scharff et al.* (2009) and is the focus of ongoing research. *Bluth and Rose* (2004) proposed that the magma column undergoes stick-slip motion, i.e. step-wise emergent upward displacement of the magma. Based on the model by *Johnson et al.* (2008), we assume that below the marginal permeable dome surface uprising magma degasses increasing its gas mass fraction with height in the conduit. This magma/gas mixture becomes highly compressible due to the large amount of gas bubbles. The sudden upward motion of the magma column compresses the magma foam and triggers uplift and consecutive oscillations of the dome surface, at which in turn opening fractures give way for explosive degassing. Future work will combine our findings from the analysis of Doppler radar data with the other data sets of this multidisciplinary experiment such as infrasonic and seismic data.

Acknowledgments

Success of the field portion of this experiment was made possible with support from many people who we want to acknowledge: Raul Salguero, Rudiger Wolf, Oto Matias, Eddy Sanchez, Bill Elderbaum, Bill Rose, Richard Sanderson, Omar Marcillo, the tourist police from Panajachel, the staff at the Santiaguito Observatory, IRIS PASSCAL (providing expertise and geophysical equipment loan), and Nick Varley. Furthermore, we thank Stefan Kinne for providing insight and support for the software to calculate reflectivity coefficients. Discussions with Jörg Hasenclever and Kristina Meier regarding data interpretation were also highly appreciated. Funding for the field work of this project was provided in part by NSF EAR Grant #0440225. LS was supported by a stipend of University of Hamburg and through DFG Grant Ho1411 20-1. We thank M. Todesco, F. Donnadieu and an anonymous reviewer for their thoughtful reviews, which tremendously helped to improve the manuscript. We also thank the editor A. Revil for handling the manuscript.

Chapter 3

Dome Dynamics at Santiaguito Volcano, Guatemala[1]

3.1 Introduction

Dome growth and collapse are one source of major volcanic eruptions. The high viscosity of the magma hinders the segregation of volatiles and hence gas becomes trapped below the surface and is released in transient explosions during dome growth (slow extrusion of degassed magma). Dome collapse (gravitational or caused by internal pressure) leads to a sudden depressurization of the magma column, which triggers fragmentation in the conduit and a subsequent ejection of gas and ash into the atmosphere.

Many studies have so far focused on the process of repeated explosive magma extrusion at Santiaguito volcano using visual (*Bluth and Rose*, 2004; *Johnson et al.*, 2008) and thermal observation (*Sahetapy-Engel et al.*, 2008; *Yamamoto et al.*, 2008; *Sahetapy-Engel and Harris*, 2009a), as well as seismic (*Sanderson et al.*, 2010), infrasound (*Johnson and Lees*, 2010; *Jones and Johnson*, 2011), and SO_2 measurements (*Holland et al.*, 2011). The stick-slip behavior of Santiaguito's currently active Caliente dome has also been explored numerically (*Barmin et al.*, 2002; *Melnik and Sparks*, 2005; *Massol and Jaupart*, 2009), however, the dome processes during Vulcanian type explosive degassing events are subject to ongoing research mainly because a quantitative observation of processes inside or beneath the eruption cloud is rather difficult.

Observations by *Bluth and Rose* (2004) led to a first model for the eruptive mechanism at Santiaguito volcano: During shear-induced fragmentation pathways preferentially develop at conduit margins as suggested by *Gonnermann and Manga* (2003), relating the observed ring-shaped vent distribution on the dome to the conduit walls. *Bluth and Rose* (2004) also report that the diameter of the ring increased almost constantly during three years of observation from 70 m in 2002 to 120 m in 2004.

[1]To be submitted to Journal of Geophysical Research
Co-authors are Matthias Hort, and Jeffrey B. Johnson

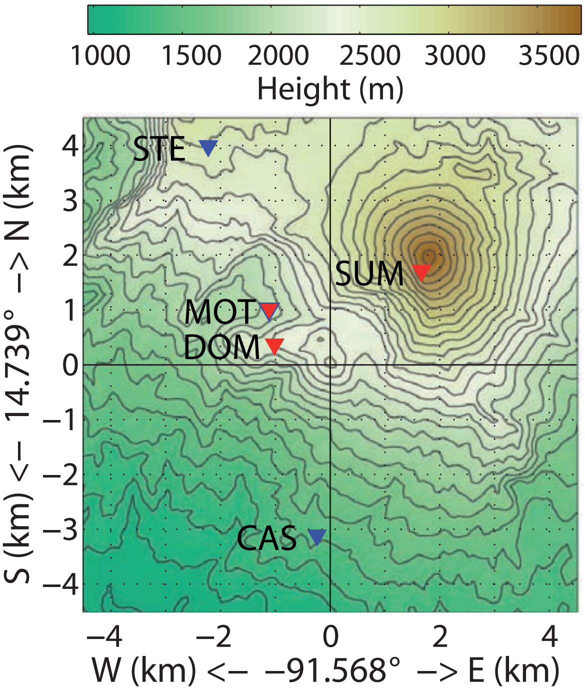

Figure 3.1: Topographic map of the Santa Maria-Santiaguito volcanic dome complex (centered on the Santiaguito dome) including the locations of infrasound (red) and seismic sensors (blue triangles). Doppler radar and cameras where set up at station SUM (NE of the dome) close to the summit of Santa Maria volcano (DEM data from *USGS*, 2004b; *Farr et al.*, 2007).

Combined thermal and infrasonic observations by *Sahetapy-Engel et al.* (2008) support the model of shear-induced fragmentation by *Gonnermann and Manga* (2003). The travel time delay of their thermal and infrasonic data suggest a highly variable fragmentation source depth of 100 to 620 m, which they conclude disqualifies other possible source mechanisms such as phreato-magmatic activity (proposed by *Sanchez Bennett et al.*, 1992) or pressure build-up beneath an obstruction in the conduit. A detailed study of infrared images taken of the dome surface in Jan. 2005 (*Sahetapy-Engel and Harris*, 2009a) revealed ring-shaped structures of an outer hot annulus (diameter ∼150 m), a relatively cold inner annulus (width ∼40 m), and a hot center (diameter ∼36 m). *Sahetapy-Engel and Harris* (2009a) interpreted these structures as a rigid center plug of degassed fresh lava that broke an overlying sheet of old, cold lava. Some gas escapes through small radial cracks in the cold annulus but most volatiles escape through the outer annulus along the walls of the extruding plug. Their data set was the first that revealed inner and outer ring structures.

Johnson et al. (2008) proposed a slightly different model for the processes during an eruption. Inferred from seismic data, they explain episodic dome inflations by building up pressure that eventually overcomes the lithospheric load of the overlying impermeable carapace (200 m in diameter, 20–80 m thick). Particle image velocimetry of these episodic dome inflations reveals an uplift of the carapace (0.2–0.5 m vertical displacement) at the same time and position where degassing starts. Uplift is initiated at the dome center and propagates at 30–50 m/s radially outwards until the whole carapace ‘floats’ on a hypothesized gas-pocket. This non-uniform uplift should cause high local strain rates that induce brittle failure facilitating explosive surface degassing. The gas is preferentially released at the circumference of the uplifted dome surface. This is further supported by the observation that over the course of hours to days the cracks on the dome surface substantially change their location, meaning degassing emanates from wherever the dome happens to be 'broken' and does not directly reflect the underlying conduit geometry. More recently *Johnson and Lees* (2010) showed that non-uniform dome uplift also produces a measurable N-shaped pulse in the infrasonic signal.

Dome uplift and concurrent explosive degassing was also observed using Doppler radar. *Scharff et al.* (2012) found that 83% of the eruptive events comprise more than one explosive pulse. They also found that eruptive events start with a dome uplift ∼1.5 s before the first explosion (maximum radial velocity <12 m/s, small echo power) near the center of the dome and commence ∼2–3 s later with an explosion of high echo power and maximum radial velocities up to 25 m/s at the outer rim of the dome. This second explosion is then followed by repeated explosions of similar or smaller strength occuring every 2–3 s.

In a more recent deployment of seismic and infrasonic sensors as well as high resolution cameras in January 2009, *Sanderson et al.* (2010) used pseudo-tilt measurements calculated from ultra long period waveforms (>30 s) to locate a Mogi source 200 m west of and 250 m below the center of the dome. Interestingly, the timing of volume loss and (explosive) surface degassing matches. However, due to the ultra long period, they are not able to resolve single degassing pulses within one deflation event.

A localization of the complex eruptive activity during one event has been done by *Johnson et al.* (2011) who used network infrasound semblance. They found that sub-events occur all over the dome and that the infrasonic signal is either produced by the uplifting dome surface or explosive degassing that is strong enough to produce coherent infrasound.

In this study we combine the observations of *Johnson et al.* (2008); *Johnson and Lees* (2010); *Sanderson et al.* (2010); *Jones and Johnson* (2011) and *Scharff et al.* (2012) into a single model for conduit dynamics during a typical eruption of Santiaguito volcano. In the following two sections we will first summarize the multidisciplinary experiment and describe those data that are relevant to our model. In section 3.4 we will introduce a mechanical model that incorporates a magma column of variable compressibility to explain the repeated release of gas during a single degassing event. The mechanical model is afterwards compared to various models for plug flow proposed in the literature. All those models are then compared to the data. Finally, we propose a sequence of physical processes that occur during a typical Vulcanian event at Santiaguito volcano and lead to its famous ring shaped eruptions.

3.2 Multidisciplinary Experiment at Santiaguito Volcano

Santiaguito volcano, Guatemala, hosted a multidisciplinary experiment between January 3rd and 14th, 2007. Different types of sensors were deployed around the volcano to study the links between magmatic degassing and the dynamics of volcanic eruptions. The experiment comprised the measurement of atmospheric pressure disturbances (infrasound sensors, Univ. of New Hampshire), ground movement using seismometers (Univ. of North Carolina), particle image velocimetry (PIV, high-resolution video camera, Univ. of New Hampshire), and mass flux and velocity of ash particles (Doppler radar, Univ. Hamburg).

The seismometers and further infrasonic microphones were distributed around the active dome (see Fig. 3.1). The frequency modulated continuous wave (FM-CW) Doppler radar was setup at station "SUM" near the top of Santa Maria volcano at about 3600 m asl (see Fig. 3.1) pointing down (inclination 27°) towards the active dome Caliente of Santiaguito volcano (2550 m asl). Station SUM also included an acoustic sensor, as well as the high-resolution video camera. For the purpose of a detailed study, Santiaguito volcano is the best choice, because the parent volcano Santa Maria provides an observation site, 1500 m above the dome, where cameras and Doppler radar have a unique view onto the dome surface (Fig. 3.1). The Doppler radar operated from Jan. 9, 17:30 UTC to Jan. 13, 17:30 UTC and recorded 157 events. In 2007 Santiaguito erupted 1.5 times per hour which guaranties several eruptions during a short deployment (here 4 days of overlapping datasets). At a line-of-sight distance of 2700 m, the approximate field of view of the radar beam is about 70 m and hence much smaller than the dome (diameter of 200 m). More details on the general aspects of the experiment can be found in *Johnson et al.* (2008) and a detailed analysis of the Doppler radar data is given in *Scharff et al.* (2012). In this paper we use the terms event and explosion as synonyms to describe the Vulcanian activity, at which explosive degassing events produce white or gray plumes about every 40 minutes.

3.3 Data Processing and Results

3.3.1 2D Cross-correlation of Doppler Radar Data

The Doppler radar records the velocity of ash particles and echo power, which is a measure for the amount of material moving inside the radar beam with the respective velocity. Note that the velocity as measured by the radar is only the radial component of the particles true velocity. Hence the measured velocities depend highly on the sounding geometry. Particle velocities are sampled at a rate of about 10 Hz. More details on the measurement technique and the sounding geometry of this experiment can be found in *Scharff et al.* (2012).

70% out of 157 events measured at Santiaguito volcano, Guatemala, show a repetitive, streak-like pattern with more than two pulses (see velocigram in 3.2). A diagonal streak can be interpreted as ballisticly transported material (*Scharff et al.*, 2012). Particles start at a high velocity and decelerate until the velocity is zero. Passing their highest point, the particles accelerate again until they eventually reach the ground (for details on this see *Scharff et al.*, 2012). Without friction, a single particle moving through the radar beam therefore appears as a diagonal line in the velocigram, the slope of which is being controlled by the gravitational acceleration.

Scharff et al. (2012) argue that a sudden increase in maximum velocity and echo power at the beginning of a streak during an eruption can best be explained by particles that are accelerated below the dome's surface in fractures or channels (i.e. outside of the field of view). This means that each streak represents a pulsed release of gas and particles.

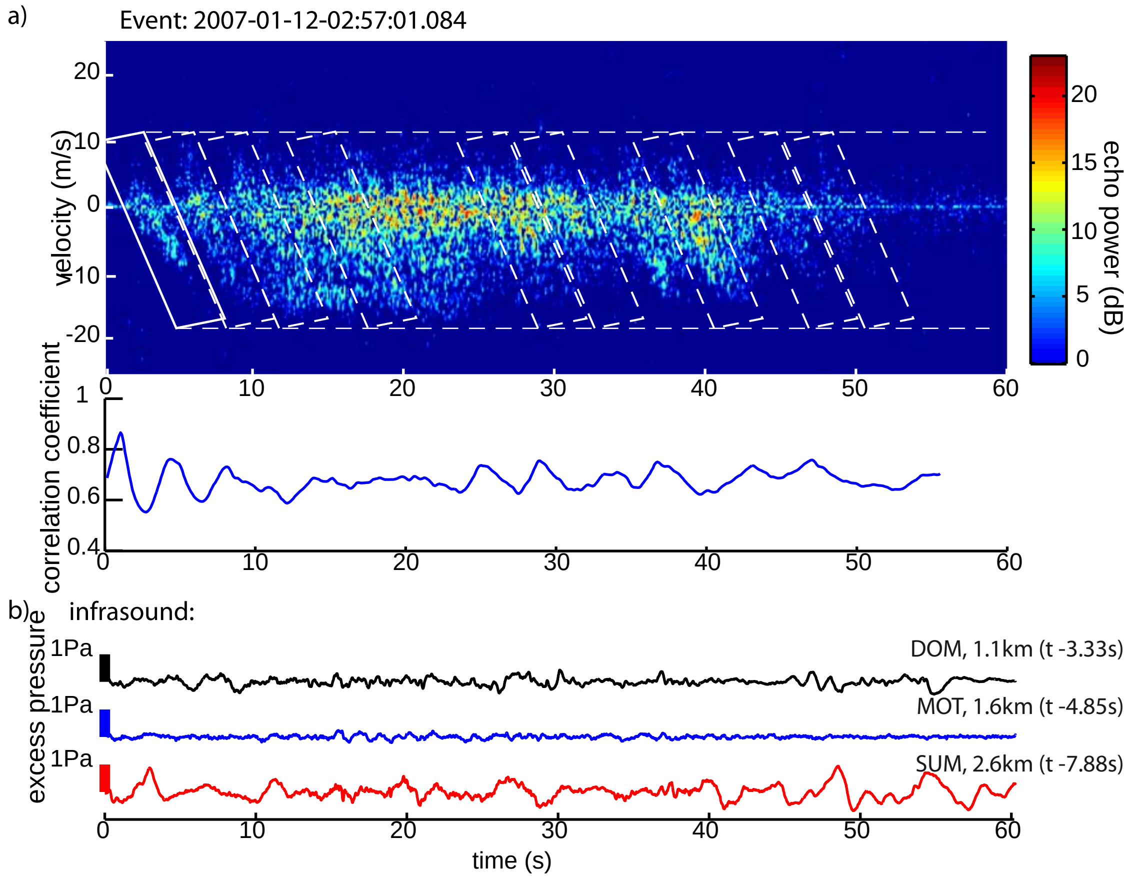

Figure 3.2: a) Velocigram of an eruption on Jan 12, 2007, 2:57:01 UTC. Echo-power (color-coded) is plotted as a function of time (x-axis) and velocity (y-axis). This means that each point in a velocigram holds the information of how much material (color) moves inside the radar beam at a certain radial velocity (y-value) at a particular time (x-value). Note that the colors resemble the ratio of echo power and background noise in dB, meaning values <1 (blue) are background noise. The solid white box highlights the pulse used for the 2D cross-correlation (the pulse is moved over the velocigram along the white dashed lines). The result of the 2D cross-correlation is plotted below the velocigram. Secondary pulses revealed by elevated correlation coefficients are highlighted with dashed white boxes in the velocigram. Note that the auto-correlation of the first pulse results in a value less than one because I smoothed the sample data to reduce the effect of noise. b) Excess pressure recorded at stations DOM (black), MOT (blue) and SUM (red). Traces are filtered between 1–15 Hz and shifted in time according to the hypothetical signal travel time (speed of sound 330 m/s). The signal amplitude has not been corrected for propagation effects. Note that there is neither a correlation between stations nor with the correlation coefficient time line.

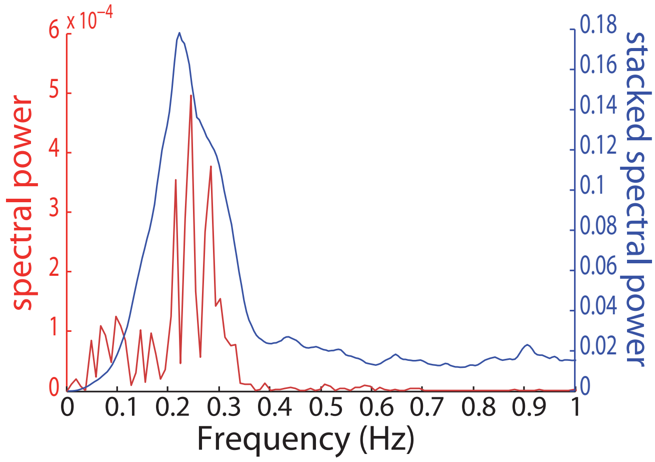

Figure 3.3: Fourier transform of correlation coefficients given in Fig. 3.2 (red). The main energy lies between 0.2 and 0.3 Hz. The blue line represents the sum of all 157 spectra of the respective correlation coefficients. Due to artifacts introduced by the limited signal length (shortest signal <7 s), values below 0.15 Hz are suppressed (high pass filter). Again a clear peak between 0.2–0.3 Hz and a plateau at 0.3 Hz are apparent.

Fig. 3.2 shows an event where one can clearly distinguish many pulses. These pulses occur at an almost constant frequency throughout the event. We applied a 2D cross-correlation of the first streak (see box with solid white line in Fig. 3.2) to the subsequent velocigram to determine the onset times of secondary pulses (dashed white boxes in Fig. 3.2). The result of the 2D cross-correlation is shown below the velocigram and the local maxima clearly correspond to the onset of secondary pulses. A frequency analysis of this cross-correlation reveals a frequency between 0.2 and 0.3 Hz (see Fig. 3.3, red line).

Using a smoothed version of the first pulse of Fig. 3.2a as a master event, we identified pulses in all 157 recorded eruptions. Length and number of pulses throughout one event vary significantly. Stacking the frequency analysis of all events most of the energy is found above 0.2 Hz with a little plateau at 0.3 Hz. This supports our previous observation derived from one event that pulses at Santiaguito occur periodically every 3–5 s.

3.3.2 Dissecting the Signals of Single Eruptions

Is the pulsed nature of events also visible in other datasets of the experiment? In Fig. 3.2b the infrasonic amplitude is too small to permit an interpretation in terms of sub-events. For this event the velocities as well as echo power are small too, suggesting a rather low mass flux that results in the observed weak atmospheric disturbance. In Fig. 3.4 we show two examples of events where sub-events are clearly visible in the Doppler radar and infrasound data.

Both velocigrams in Fig. 3.4 show a peak in echo power at the lowest resolvable velocity of +0.39 m/s (first vertical line, A), which can be associated with dome uplift prior to explosive degassing pulses (subsequent lines, B–D, see *Scharff et al.* (2012) for more details). The infrasonic signal is also coincident with dome uplift (*Johnson and Lees*, 2010). The initial infrasonic amplitude (between lines A and B) of event #1 is larger than that of event #2. Interestingly, this corresponds to a higher echo power in the velocigram of event #1 compared to event #2 and a longer duration of the signal (between A and B). It can be shown[2] that

[2]Consider a particle that is moving at a velocity $v_p = v_i + \alpha dv$, between two velocity samples (v_i and $v_i + dv$). The echo power of that particle will be distributed to those velocity samples with respect to α. The

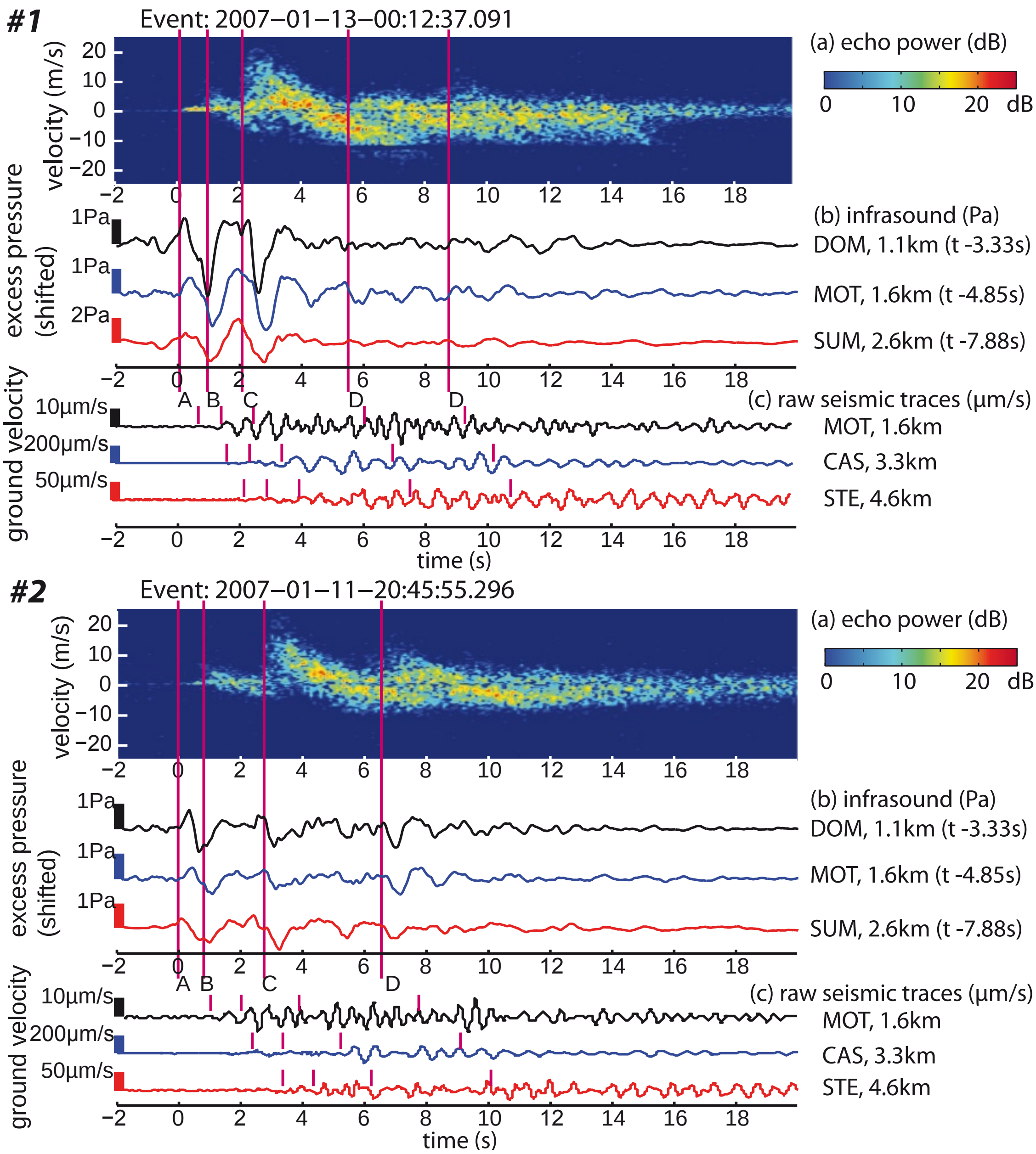

Figure 3.4: Doppler radar, infrasonic, and seismic data of two example eruptions. In the velocigram (a) the amount of particles inside the radar beam (color coded) is plotted as a function of particle velocity and time. (b) Infrasonic signal at the three nearest stations (DOM, MOT and SUM). The signal is filtered between 1–15 Hz and shifted in time according to the hypothetical signal travel time (speed of sound 330 m/s). The signal amplitude has not been corrected for propagation effects. (c) Raw vertical seismic traces of three nearest stations (MOT, CAS and STE). The instrument response is not removed, traces are not filtered and not shifted. Vertical pink lines show from left to right: the onset of dome deformation (A), explosive degassing in the center (B), explosive degassing at the circumference (C), and subsequent pulses (D). Pink lines in panels c are shifted in time according to a hypothetical signal travel time (v_S =1500 m/s)

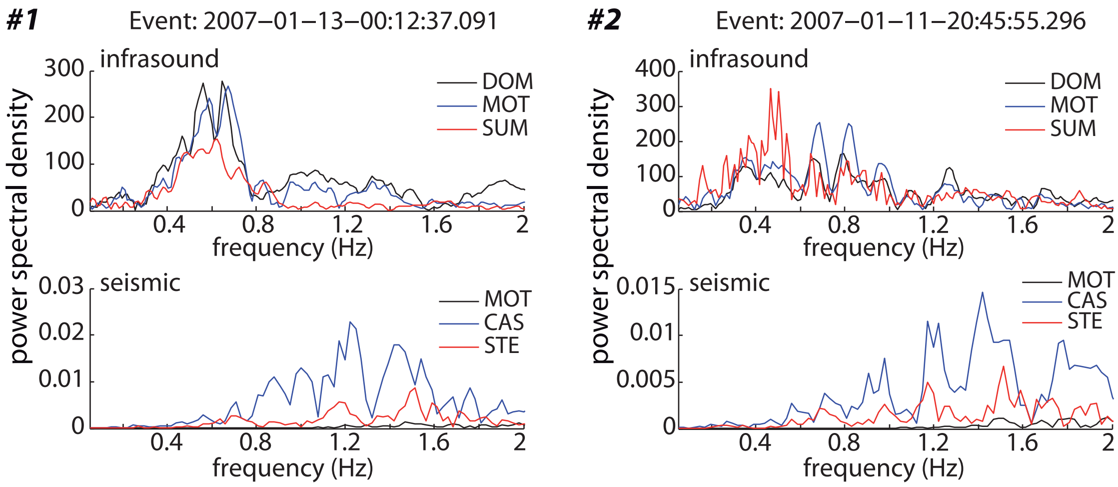

Figure 3.5: Power spectral density of infrasonic and seismic signals shown in Fig. 3.4. Infrasound is filtered between 1–15 Hz. The seismic signal is unfiltered and the instrument response is not removed. Line colors are the same in Fig. 3.4.

this higher echo power means that the velocity of the object moving inside the radar beam is closer to 0.39 m/s for #1 than for #2.

The first degassing pulse in both examples (second vertical line, B) occurs 1.5 s after the uplift begins. This timing varies only a little between eruptions (spanning 1–2 s). In the infrasound, we cannot identify a clear explosion pulse. However, the N-shaped waveform produced by complete dome uplift changes and it appears that it is superposed by a second N-shaped pulse with an amplitude that is of a smaller magnitude than that of the uplift-related amplitude.

The faster dome uplift in event #1 compared to event #2 might be related to the shorter period between first and second pulse. Because the second pulse occurs later in event #2, it also leaves a detectable signal in the infrasound. Subsequent pulses occur with decreasing strength and leave almost no infrasonic signal (*Meier et al.*, 2012). In the seismic data pulses and event onset are hardly identifiable (pink lines in Fig. 3.4 mark hypothetical signal changes inferred from the Doppler radar timing and theoretical travel time). It is not clear if weak degassing events leave a signal in the seismic data. However, *Johnson et al.* (2008) used their PIV-inferred dome uplift history for the initial uplift (between lines A,B in Fig. 3.4) to calculate synthetic seismograms. They were able to reproduce timing and frequency content of the onset of seismicity. Hence we propose that the seismic signal is produced by dome uplift and processes in the conduit rather than by surface degassing.

In Fig. 3.5 the low frequency content of the infrasonic and seismic signals of events #1

echo power of the slow moving dome surface will hence be distributed between 0 m/s and the smallest velocity sample located at dv =0.39 m/s. However, for data processing reasons the echo power around 0 m/s is being filtered out by a comb notch filter and can not be used to deduce the particle's true velocity. Now if we assume that in both events #1 and #2 the object moving inside the beam is the same (the entire FOV is filled by the dome surface) a higher echo power at 0.39 m/s in case of #1 means that here the velocity is is closer to 0.39 m/s than in #2, i.e. the dome surface uplift is faster in event #1, which is also supported by the higher infrasound amplitude.

and #2 is shown. The seismic energy is associated to frequencies above 0.7 Hz, whereas significant infrasonic energy lies below 0.8 Hz, although low frequencies where attenuated by a second order Butterworth bandpass-filter[3] (1–15 Hz). For the more impulsive event #1, all three infrasonic signals peak around 0.6 Hz, with almost no energy at higher frequencies. The less intense event #2 shows a broader frequency spectrum, but with comparable amplitudes and harmonics (peaks at 0.33, 0.65 and 1.3 Hz, in DOM and MOT).

3.3.3 Summary of Observations

Our multi-parameter study revealed several features, that are typical for eruptions at Santiaguito volcano:

1. Eruptions start with a significant dome surface uplift (up to 0.5 m vertical) starting in the center, propagating outwards (videos, seismic data, *Johnson et al.* (2008));
2. first explosive degassing starts in the center ∼1.5 s after uplift begins (Doppler radar data, videos);
3. when the surface deformation front reaches the outer circumference of the dome, explosions occur favorably at vents at that outer ring (Doppler radar data, videos);
4. periodically repeating pulses during the eruption (Doppler radar data), and
5. almost linear surface subsidence between eruptions (Deformation measurement using the Doppler radar, *Scharff et al.* (2007); *Hort et al.* (2010)).

Apparently, Santiaguito volcano shows periodicity on three (or even more) time scales. The average extrusion rate varies on a decadal timescale (*Harris et al.*, 2003) between 0.2 and 1 m^3/s. Explosive events occur 1–2 times per hour on a very regular basis and the Doppler radar measurement revealed the pulsed behavior of events, with a pulse period of 3–5 s. The variation in extrusion rate (*Harris et al.*, 2003) and the cause of regularly occurring events have been studied before (e.g. *Barmin et al.*, 2002). In the following we therefore focus on the mechanism that produces the observed pulsed events.

3.4 A Mechanical Model for Pulsed Events

We explain the pulsed nature of events with a harmonic oscillator, where compressible magma acts as spring. Magma compressibility depends on its bubble and crystal content, hence is a function of depth. Crystals lower the compressibility, bubbles increase it. Because bubbles are filled with gas and the compressibility of gas is inversely proportional to pressure, the

[3]Note that the corner frequencies of a filter define the corners of the flat pass-band of frequencies rather than cut-off values. Hence frequencies above and below the corner frequencies are attenuated by a factor that increases with distance to the corner frequencies. The filter was needed to suppress an intense signal at and below 0.1 Hz most probably related to ocean-induced noise.

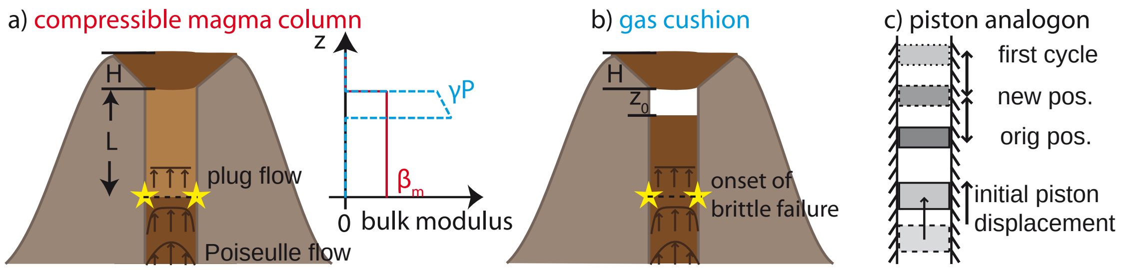

Figure 3.6: Two end-member cases for a compressible magma column. The carapace (height H) is incompressible due to the lack of gas bubbles and its high crystallinity. a) In the compressible magma column model (red, end member 1) the whole magma column (length L) above the onset of brittle failure has a constant compressibility. b) The zero order approximation for a foam beneath the carapace is a gas pocket (dashed blue, end member 2) of height z_0. The bulk modulus of gas depends on the pressure, thus increases with depth. In this case, the magma column below the gas cushion is incompressible. c) Analogon to the gas cushion model in b) using pistons in a pipe. The lower piston is moved to a new position, thereby compressing the air between both pistons. The induced overpressure in the gas accelerates the upper piston, which overshoots its new equilibrium position by twice the initial displacement of the lower piston. The gas decompresses and eventually forces the upper piston back down (in addition to gravity). As in model b) the gas acts as a spring.

bubble's influence on bulk compressibility is highest at shallow levels, where pressure is low. However, at the shallowest levels (uppermost tenths of meters) cooling of the magma leads to stiffening and a plug or carapace forms (most probably conically shaped, *Tuffen et al.*, 2008). The fact that *Holland et al.* (2011) report repose degassing of the dome suggests that the solid carapace is permeable to gas flow even between eruptions. Nevertheless, the permeability decreases with depth caused by the increasing lithostatic pressure. Exsolution of especially CO_2, and SO_2 happens deeper in the conduit due to the solubility (see e.g. *Dixon and Stolper*, 1995) of these gases. Hence the exsolved volatiles rise in the magma (although very slow due to the high viscosity of dacitic magma). At a certain depth, the pressure dependent permeability of the magma column is very low and that is where a part of the rising volatiles becomes trapped, reproducing a magma of high bubble number density, a foam-like structure. The upper part of the column, the carapace, is very gas poor, hence extremely viscous.

Upward stick-slip motion of the lower part of the magma column (as a consequence of localized shear-fragmentation at the conduit walls, *Gonnermann and Manga*, 2003; *Holland et al.*, 2011) compresses the bubbly upper part below the carapace. The bubbly magma foam acts as a spring and an oscillation is initiated in case the overpressure overcomes the friction and the carapace is lifted. In this scenario we find two end-member cases (see Fig. 3.6): a magma column with constant compressibility or bubble/crystal content (a, red profile) and a gas pocket beneath the carapace (as zero order approximation to the foam layer, b, blue profile). The oscillation frequency is independent of the initial displacement of the magma column below the foam. However, the peak-to-peak amplitude of the first oscillation cycle, which is — neglecting friction — twice the initial displacement (see Fig. 3.6c), equals the uplift of the dome surface. In both end-member-case models, the amount of compression depends on the slip-length d of the magma column at the beginning of an event, which can be estimated using the extrusion rate q, the conduit radius r and the average number of events per hour τ_E:

$$d(r) = \frac{q}{\pi r^2 \tau_\mathrm{E}} \quad . \tag{3.1}$$

The averaged syn-eruptive displacement $d(r)$ strongly depends on the conduit radius, which has been estimated to lie between 18 m (*Holland et al.*, 2011) and 35 m (*Bluth and Rose*, 2004). For 2007, we estimate the extrusion rate to be $q = 0.4\,\mathrm{m}^3/\mathrm{s}$ (*Harris et al.*, 2003) and τ_E to be $1.5\,\mathrm{h}^{-1}$. This leads to averaged syn-event displacements between $d(r = 18\,\mathrm{m}) = 0.94\,\mathrm{m}$ and $d(r = 35\,\mathrm{m}) = 0.25\,\mathrm{m}$. Since *Johnson et al.* (2008) observed uplift in the order of 0.5 m, we further use a conduit radius of 35 m. In the following we present both end-member-case models and discuss their implications.

3.4.1 A Compressible Magma Column

At a certain depth (marked by stars in Fig. 3.6a) local fragmentation at the conduit walls decouples the magma column from the wall rock over a certain distance. This leads to plug flow and exerts a sudden acceleration on the overlying magma column and a pressure wave travels through the compressible magma. Because the wavelength of the pressure wave is long compared to the column height L, the whole column undergoes a compression-dilatation cycle at once. The compressible magma reacts with longitudinal oscillations with a frequency f of (see Appendix B.1 for a derivation of equations):

$$f = \frac{1}{2\pi}\sqrt{\frac{3K_m(1-2\nu)}{\rho_m L^2 + 1/3\rho_c H L\left(\frac{R^2}{r^2} + \frac{R}{r} + 1\right)}}, \tag{3.2}$$

where K_m is the bulk modulus, ν is Poisson's ratio, r and R are the radius of the conduit and the overlying conically shaped carapace (lower and upper radius), ρ_m and ρ_c the density of the magma column and the carapace, and H is the height of the carapace.

Length of the Magma Column

In the model presented above (equation (3.2)) the frequency depends on several parameters of which bulk modulus, carapace height and length of the magma column are the most important. Densities of magma and carapace as well as Poisson's ratio ($\nu = 0.3$, typical value for e.g. seismic wave velocity calculations) can be fixed to commonly used values (see Table 3.1). The dome radius $R = 100\,\mathrm{m}$ is known from observations and we previously estimated the conduit radius r to be 35 m.

In Fig. 3.7 the dependency of frequency on the three free parameters (H, K_m, L) is shown. The main factor that controls the frequency is the bulk modulus of the magma column. The

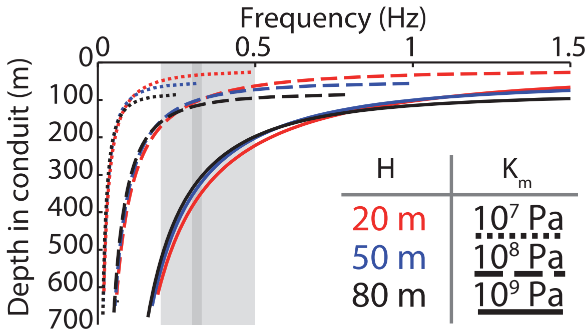

Figure 3.7: Results of Model A: The frequency of compression-dilatation cycles depends on the depth of fragmentation in the conduit ($L + H$). Line styles refer to different bulk moduli of the magma column (length L), line colors depict different carapace thicknesses (H). The shaded area marks the frequency range that has been observed with Doppler radar, dark gray marks the most important frequency. For the calculations we used a conduit radius of 35 m, ν=0.3, ρ_m=2000 kg/m^3, and a carapace density of ρ_c=2500 kg/m^3.

depth of fragmentation, i.e. the onset of brittle failure, defines the length of the oscillating magma column. The shorter the column, i.e. brittle failure at shallower depths, the higher is the frequency.

Huppert and Woods (2002) calculated the effective compressibility (C=10^{-8}–10^{-10} Pa^{-1}), which is the inverse of the bulk modulus, of crystal and bubble bearing magmas deep in the conduit (>2 km). Their graphs suggest that the compressibility at shallow depths (<2 km) increases to values of 10^{-7} Pa^{-1} due to gas exsolution (dotted lines in Fig. 3.7). At low bulk moduli, i.e. high compressibility, the oscillation frequency is much smaller than the observed frequency (0.33 Hz, shaded dark gray), when brittle failure occurs below 100 m in the conduit. This finding disagrees with the estimates of *Sahetapy-Engel et al.* (2008), *Sanderson et al.* (2010), and *Holland et al.* (2011) who found the onset of brittle failure between 140 and 600 m depth. However, the frequency highly depends on the bulk modulus and hence on bubble and crystal content of the magma. To produce an oscillation of 0.33 Hz, an increase in bulk modulus (e.g. from 10^8 to 10^9 Pa) caused by higher crystal or lower bubble content needs to be compensated immediately by a deeper onset of fragmentation and vice versa. The weight of the carapace (here parameterized by its height H, colors in Fig. 3.7) plays only a minor role. However, whether a physical relationship between the depth of fragmentation and the magma's bulk modulus exists has not yet been investigated.

3.4.2 The Gas Cushion Model

In the second end-member case of a compressible magma column, we restrict compressibility to a layer of gas directly below the carapace. This gas cushion is a zero order approximation to a magma foam, whose compressibility mostly depends on the gas compressibility. The magma column as well as the carapace are assumed to be incompressible. Sudden upward displacement of the underlying magma compresses the gas cushion. This sudden overpressure exerts a pressure force on the carapace and, assuming that the forces acting on the system exceed the yield strength of the carapace, the whole carapace is accelerated upwards. The gas pocket expands and pressure inside the pocket is reduced. During uplift the carapace is decelerated by gravity, but because of its high momentum overshoots its new equilibrium position, where gas pressure equals gravitational forces. Hence, once at its maximum height, the gas pressure in the pocket is too low to withstand the carapace's mass and it sinks back down, thereby compressing the gas pocket. The pressure inside the gas pocket rises and the carapace is again decelerated. An oscillation with the eigenfrequency

$$f = \frac{1}{2\pi}\sqrt{\frac{\gamma P_{\mathrm{eq}}}{\rho_c H z_{\mathrm{eq}}}\frac{3}{\left(\left(\frac{R}{r}\right)^2 + \frac{R}{r} + 1\right)}} \tag{3.3}$$

occurs. For a derivation of all equations see Appendix B.2. Here γ is the adiabatic exponent and z_{eq} and P_{eq} are equilibrium position and the respective pressure. All other symbols are given in Tab. 3.1. Due to the compression of the gas cushion (initially at equilibrium pressure) the compressed gas cushion height $z_0 = z_{\mathrm{eq}} - d(r)$ is directly related to the initial overpressure in the system:

$$\Delta P_0 = P_{\mathrm{eq}}\left(\left(1 + \frac{d(r)}{z_0}\right)^{\gamma} - 1\right) \quad . \tag{3.4}$$

The peak-to-peak amplitude X of the damped oscillation is

$$X = d(r)\left(1 + \mathrm{e}^{-\frac{1}{2\tau f}}\right) \quad , \tag{3.5}$$

where $\tau = 2\mu_f/m$ is the characteristic time of amplitude decay (see Eq. (B.5)) and depends on the friction coefficient μ_f and the carapace mass $m = 1/3\rho_c \pi H\left(R^2 + r^2 + rR\right)$.

At the carapace margins, where the highest strain rates occur, cracks and fractures open up, thereby enabling gas escape from the gas cushion during an eruption. Degassing pathways close, when the carapace settles back down. Using Darcy's law for flow through porous media (e.g. *Turcotte and Schubert*, 2002)

$$Q = -K_f \frac{A_d}{\mu_g}\frac{d}{dz}P, \tag{3.6}$$

and a parameterization of the friction force acting during carapace movement ($F_r = -\mu_f \dot{z}$), we find the equation of motion: (see Appendix B.2)

$$-\frac{\frac{d}{dt}(Q)}{A_c} - \frac{\tau Q}{2A_c} = \frac{d^2}{dt^2}(\Delta z) + \omega^2(Q)\Delta z + \frac{\tau}{2}\frac{d}{dt}(\Delta z) \tag{3.7}$$

where Q is volumetric gas flux out of the volcano (Eq. (3.6)), A_c conduit cross sectional area, and Δz the deviation from equilibrium height.

Because the gas volume beneath the plug decreases due to gas outflow (Eq. (3.6)), the

Table 3.1: Governing parameters of both models and their range of values (if any).

ρ_c	density of the carapace	$2500\,\mathrm{kg/m^3}$
H	height of the carapace	20–80 m (*Johnson et al.*, 2008)
R	upper radius of the carapace	100 m
r	radius of the conduit	18–35 m, see above
u	extrusion rate	$0.4\,\mathrm{m^3/s}$ (*Harris et al.*, 2003)
special to model A		
K_m	bulk modulus of bubbly magma	10^8–10^9 Pa (*Huppert and Woods*, 2002)
ν	Poisson's ratio	0.3
ρ_m	density of magma	$2000\,\mathrm{kg/m^3}$
L	length of the magma column	to be determined
special to model B		
γ	adiabatic index for polyatomic gases at high temperatures	1.1 (see *Lighthill*, 1978, p. 7f)
μ_f	friction coefficient	to be determined
z_0	initial height of the gas cushion	to be determined
K_f	permeability of gouge zone and carapace	to be determined

equilibrium position of the carapace z_{eq} decreases (Eq. (B.3) in Appendix 3) and hence the frequency increases slightly during the oscillation (see Eq. (3.3)). Given that degassing during uplift phases is limited, a damped oscillation develops, periodically releasing gas during dome surface uplift.

Friction Coefficient

From the mathematical model (Eq. (3.3)) we see that the oscillation frequency depends on a small set of parameters (see Tab. 3.1). The standard values for adiabatic index and density of dome material are held constant during our model runs. The carapace height H is well constrained by the seismic study of *Johnson et al.* (2008), who found $H = 20$–80 m.

The friction term μ_f controls whether and for how long oscillations occur (see Fig. 3.8). At Santiaguito volcano explosive events last 10–120 s. Note that this is the time span ash is detected inside the radar beam. After the ash settled down, no oscillation, but steady subsidence has been observed (*Scharff et al.*, 2007). Therefore the oscillation duration must be less than 10–120 s. From event duration and Fig. 3.8 we estimate μ_f to be in the range of 10^8–10^9 kg/s. These values also satisfy the criterion for under-critical damping ($D<1$) i.e. oscillations are possible. Because damping has only a minor effect on the frequency (see Appendix B.2), we choose μ_f to be 5×10^8 kg/s for all following model calculations. The friction coefficient of the gouge material may change with time due to repeated fracturing and healing, ash loss, etc. Varying μ_f one order of magnitude changes the event duration by also one order of magnitude. When the carapace sinks to its initial position, we assume in our model that all fractures are temporarily closed and the friction coefficient suddenly increases to 10^{11} kg/s. This avoids that the carapace sinks below its initial position, which is impossible due to its assumed conical shape.

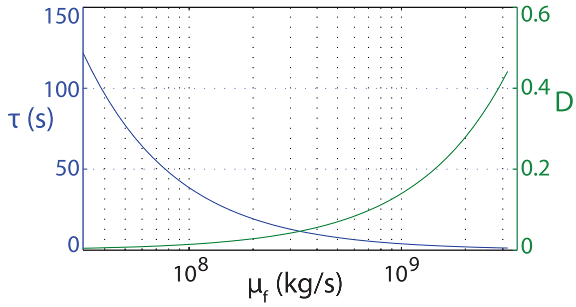

Figure 3.8: Oscillation duration τ and oscillation criterion D (see Eq. (B.5)) as a function of the friction coefficient μ_f. The viscosity of the highly fractured gouge material is the main parameter controlling friction. A damped harmonic oscillation occurs when the criterion for under-critical damping $D<1$ is satisfied.

Gas Volume and Carapace Height

The initial overpressure is the driving force of the oscillation. Equation (3.4) shows that it depends on the carapace mass (parameterized by its height), the extrusion rate and the initial gas mass (parameterized by the compressed gas cushion height z_0). Figure 3.9 shows the frequency dependence on those three free parameters (upper diagrams) and the peak-to-peak amplitude of the oscillation (lower diagrams). From Fig. 3.9 we see that besides the conduit radius the main parameter controlling the initial uplift is the extrusion rate (displayed by line style, almost vertical lines in lower diagrams). The measured uplift of 0.2–0.5 m constrains the conduit radius to 35 m (Fig. 3.9a,c). In addition the extrusion rate translates almost one by one to uplift and hence is limited to 0.2–0.4 m^3/s.

In our spring-mass model, the spring constant is given by the mean compressibility of the gas ($\gamma \times P_{eq}$) divided by its equilibrium volume. An increase in initial gas pocket height (z_0) or extrusion rate (increased q) lead to a decrease in frequency. For a carapace height >50 m (blue and black lines overlay in Fig. 3.9a,b) the frequency exclusively depends on the gas pocket height, i.e. initial gas volume. To the other end ($H < 50$ m, red line) the carapace thickness also influences the frequency.

Johnson et al. (2008) constrain plug height to $H = 20$–80 m using seismic measurements. From a photogrammetric study they determine the initial uplift to 0.2–0.5 m. These values, together with the pulse frequency of 0.3–0.33 Hz observed by the radar, can be reproduced by assuming an extrusion rate of 0.4 m^3/s with a fixed conduit radius of 35 m and finally a gas cushion height of 0.5 m. Given that the oscillation frequency is nearly stable from one event to the next, our model constrains the initial gas volume. The rather variable uplift, however, can be explained by variations in q.

Permeability of the Dome

The above parameter estimations are all based on a damped free oscillation. In Eq. (3.7) however, we introduce an external constraint to the oscillation, i.e. gas out flux. The frequency depends on an existing gas volume below the carapace, hence a requirement for oscillations is to limit permeability during the pulses. We solved the coupled equations (3.7) and (3.6) using two combined forth-order Runge-Kutta schemes for the timely evolution of the absolute

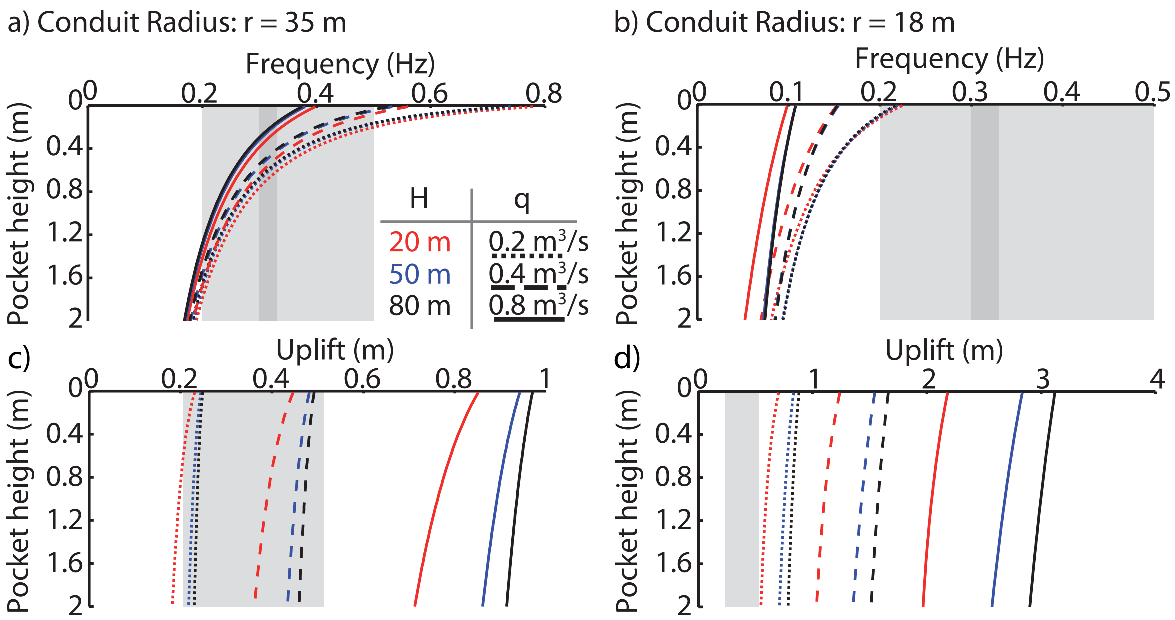

Figure 3.9: Results of model B: Frequency (a+b) and maximum initial uplift (c+d) as a function of magma extrusion rate (line style), carapace thickness (line color) and initial gas pocket height for two conduit radii. Light gray area marks the range of observed oscillation frequencies and the observed initial uplift (peak-to-peak amplitude) of 0.2–0.5 m, respectively. The mean frequency of 0.33 Hz is marked in dark grey. a+b) Conduit radius $r = 35$ m. b+d) The same plot as in a+b), but with a smaller conduit radius $r = 18$ m. It appears that none of the parameter combinations shown here can reproduce the observed frequency and uplift using the small conduit diameter.

pressure P inside the gas cushion and the position of the carapace z (above the bottom of the gas cushion).

The overall dome surface subsidence (red dashed line in Fig. 3.10) is controlled by the rate of gas out-flux Q. Here we assume degassing to stop completely when the carapace is at its initial height ($z = z_0$). However, when the carapace sinks back (negative velocity) pathways slowly close. Therefore, repeated degassing pulses occur only when the carapace is lifted and fractures open.

Figure 3.10 shows the results of two model runs where only the permeability of the gouge material has been varied. Dome height was chosen to be $H = 80$ m, which results in reasonable oscillation frequencies (see Fig. 3.9) and realistic gas velocities (see below). Following our results shown in Fig. 3.9 we use an extrusion rate of 0.4 m^3/s. The value for initial gas pocket height was adjusted to result in an oscillation with 0.33 Hz and initial peak-to-peak amplitude of 0.5 m (see Fig. 3.9). All other parameters are held constant (for values see Fig. 3.10). The amplitude decay is mainly controlled by friction (note the different time scales).

Assuming the gas mainly consists of water vapor at a temperature of 950°C (*Sahetapy-Engel et al.*, 2004), the gas viscosity can be estimated to be $\mu_g = 4.5 \times 10^{-5}$ Pas (*Sengers and Watson*, 1986). More important is the permeability K_f. Following *Bear* (1972) the permeability of highly fractured rocks can reach up to 10^{-8} m^2. *Gonnermann and Manga*

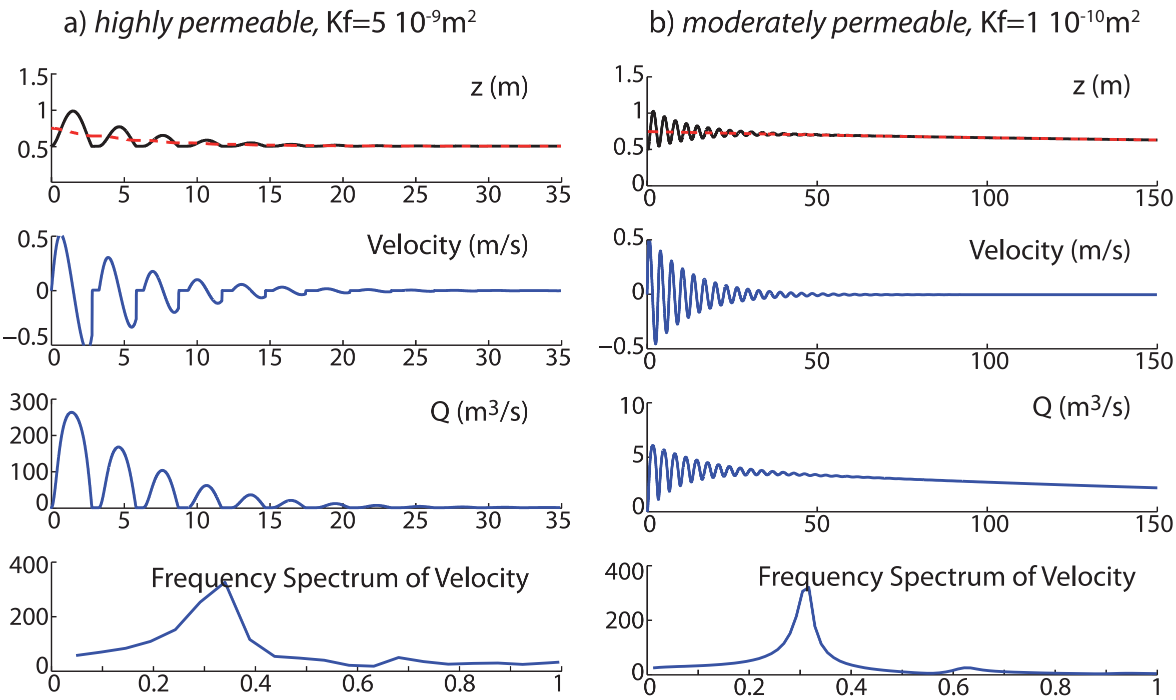

Figure 3.10: Results of two model runs with varied permeability. Displayed are as a function of time (diagrams from top to bottom): absolute height of gas cushion z (black line) and equilibrium position z_{eq} (red dashed line); plug velocity $\frac{d}{dt}(\Delta z)$; volumetric gas flux Q. The bottom diagram shows the frequency spectrum of the plug velocity. Note the different time scales in both models. a) Permeability of the highly fractured annulus around the plug equals that of gravel $K_f = 5 \times 10^{-9}\,\mathrm{m}^2$ (Turcotte and Schubert, 2002). b) Low permeability $K_f = 10^{-10}\,\mathrm{m}^2$ (sand, see Turcotte and Schubert (2002)) leads to a longer series of pulses and very slow, almost linear subsidence. However, oscillation frequency is not affected. Repose degassing (during plug subsidence) commences for 1500 s. Following values are the same in both model runs: $H = 80\,\mathrm{m}$, $q = 0.4\,\mathrm{m}^3/\mathrm{s}$, $z_0 = 0.5\,\mathrm{m}$, $r = 35\,\mathrm{m}$, $R = 100\,\mathrm{m}$, $\mu_f = 5 \times 10^8\,\mathrm{kg/s}$, $T = 950°\mathrm{C}$, $\mu_g = 4.5 \times 10^{-5}\,\mathrm{Pas}$. For a detailed analysis see text.

(2003) speculate that 'shear-induced fragmentation may create, at least temporarily and locally, a magma consisting of individual fragments bound by an interconnected fracture network of high permeability.' In our model, permeabilities $\geq 10^{-8}\,\mathrm{m}^2$ enable fast degassing where the complete overpressure is released during the first pulse and the plug instantly sinks back to its initial height and seals all degassing pathways. Assuming a high permeability, equal to that of gravel ($K_f = 5{\times}10^{-9}\,\mathrm{m}^2$, see e.g. Turcotte and Schubert, 2002), the oscillation results in a series of 6 pulses in $\sim$17 s (see Fig. 3.10a), which broadly corresponds to the Doppler radar observations. After eight pulses the carapace comes to rest closing all pathways. No repose degassing occurs. A total gas volume of $2.177\,10^5\,\mathrm{m}^3$ has been released.

Klug and Cashman (1996) determined values for K_f to be less than $10^{-11}\,\mathrm{m}^2$ for vesicular magma. Here we show the results for a permeability of $K_f = 10^{-10}\,\mathrm{m}^2$ (sand, in Turcotte and Schubert, 2002). However, with such a low permeability, the cap's subsidence is very slow due to weak degassing. After the oscillation stopped (due to friction) the carapace is still above its initial height, floating on the gas pocket (see Fig. 3.10b). Up to this time (t =∼50 s) a total gas volume of $0.365\,10^5\,\mathrm{m}^3$ has been released. Repose degassing through the minor permeable carapace stops after 1500 s, when it finally reaches its initial position (not shown in Fig. 3.10b). Until then it released a total gas volume of $1.925\,10^5\,\mathrm{m}^3$. Such subsidence of the dome surface has been quantified to be 6 cm in the first four minutes after the end of the pulsed event (*Scharff et al.*, 2009) and is presumably continuing.

3.5 Discussion and Outlook

Based on our multi-disciplinary dataset and previous studies we developed a simple mechanical model of the shallow conduit dynamics at Santiaguito volcano that describe both the uplift of the dome surface and the periodic explosive degassing quite well.

In the following we will address several aspects of our observations as well as modeling effort to substantiate the robustness of our findings. First we turn to the limitations of our mechanical models. Afterwards we compare our findings to the observations of our multidisciplinary dataset. Finally we discuss a wider range of alternative models for periodic behavior at volcanoes.

3.5.1 Mechanical Models

We introduced two mechanical models to explain the pulsed nature of events. Both models represent end member cases of the same process: a magma column consisting of compressible bubble-bearing magma with vertically varying gas content is compressed by magma rise. This promotes uplift of an overlying carapace and fractures open through which gas can escape. The mass of the carapace and the compressibility of the magma column represent a spring-mass-oscillator. In one model, the magma column has a constant compressibility, in the other, the magma column is incompressible and physically separated from the carapace by a layer of gas. Most likely, the truth will be somewhere in between. The bulk modulus (i.e. the inverse of compressibility) decreases towards shallow levels due to increasing bubble content of degassing magma. The bulk compressibility of bubble-bearing magmas not only depends on the gas compressibility, which is proportional to gas pressure, but also on bubble content and shape, and magma properties like compressibility and viscosity, because magma has to deform when the bubbles become compressed. Hence the relationship between the applied pressure and the magma foam compressibility is rather complex and beyond the scope of this paper.

The magma column of constant compressibility (Eq. 3.2) undergoes longitudinal oscillations, whose frequency depends on the length of the column, bulk modulus of the magma, and the overlying weight (i.e. the carapace's thickness, which can be assumed constant). The depth of brittle failure at conduit walls is assumed to vary significantly (100–600 m, *Sahetapy-Engel et al.*, 2008). To result in the same oscillation frequency, the bulk modulus of the magma has to vary one order of magnitude to compensate the variable column length. The process of degassing is not included in this model. It is simply assumed that the available gas flows through a network of fractures and escapes from the system, when the carapace is uplifted.

With our gas cushion model (Eq. 3.7) and a reasonable choice of parameters (see Tab. 3.1) we can reproduce pulse frequency, initial uplift, and duration of the observed events. For simplicity we included a rigid (although permeable) carapace in our calculations. We do not model the deformation of carapace and gouge zone during initial uplift as schematically drawn in Fig. 3.12. In the shear-fragmentation model (e.g. *Holland et al.*, 2011), the magma column degases and gas flows through an interconnected network of fractures at the conduit walls. This network develops, when the brittle failure criterion is reached at depth and the magma column rises. Fractures stay open until the gas supply from depth ends (*Caricchi et al.*, 2011). The depressurization of the magma column during dome surface uplift might lead to enhanced degassing, in turn stabilizing or even enforcing the oscillation. In our 1D-models we neglect any gas influx into the gas pocket from below during an event. Hence we do not account for a possible difference in gas volume between the first (in the dome center) and secondary pulses (at the outer ring vents). The incorporation of more sophisticated processes like spontaneous degassing, foam generation, and the passing of a rarefaction wave is again beyond the scope of this paper and subject to further research.

Our findings support the 'floating carapace' model of *Johnson et al.* (2008), however, in our model gas accumulation beneath the carapace is not by diffusion, disequilibrium degassing and heterogeneous flow. In this regard we agree with *Holland et al.* (2011, and references therein) that the process of shear-induced fragmentation and the preferred occurrence of pathways at conduit walls triggers degassing and gas rise. This might even be the most important process of gas release in the conduit. The processes at the surface, however, are dominated by uplift and explosive degassing at distinct vents. Doppler radar data reveals that most of the events start with a small degassing event at the dome's center before the main explosion at the outer-ring vents produces ash-loaded plumes, eventually rising buoyantly (*Scharff et al.*, 2012). Due to the 1D-nature of our model, the outward propagation of explosions as seen by *Johnson et al.* (2008) and in our Doppler radar data is not part of our simple mechanical model.

Our gas cushion model depends on several input parameters which are hard to constrain. Parameters used to calculate Q (as we see in our Eq. B.6, μ_g and K_f) are adjusted to result in a finite series of pulses, which we observed in our radar data. A change in permeability or gas viscosity significantly changes volumetric flux (see Fig. 3.10). Pulsed gas flux either ends, when the dome no longer oscillates (due to damping or geometrical constrictions), or when the pressure gradient becomes insignificant (not shown here). A high permeability leads to complete drainage of the gas cushion at first uplift. As our choice of parameters for μ_g and K_f are not unreasonable we take this as an indication that our model works reasonably well. The same holds for the parameterization of friction: With too high a friction coefficient, there is no oscillation and constant degassing occurs.

Another critical parameter one can verify is the overpressure in the gas cushion. From scaled shock-tube experiments *Chojnicki et al.* (2006) conclude that initial total conduit pressures are about 4–7.5 MPa. When correcting for lithostatic pressure, the result is still one order of magnitude larger than the estimates of *Johnson et al.* (2008) who approximate values for the initial overpressure inside the chamber to 0.003–0.1 MPa. In our model the initial overpressure is mostly affected by the initial uplift of the magma column and our model gives 1.05 MPa initial overpressure (4.12 MPa for $r = 18\,\mathrm{m}$) which lies in-between the estimates of *Johnson et al.* (2008) and *Chojnicki et al.* (2006).

In our calculations, we assume that the average extrusion rate can be translated directly into a syn-event uplift. This means that the magma flux in the upper part of the conduit (above the brittle failure constraint) occurs stepwise (stick-slip behavior) and that there is no movement between eruptions. Also the stepwise displacement is assumed to be regular in time and magnitude. This assumption is valid only for homogeneous magma with a constant supply from deeper in the conduit. The brittle failure criterion depends on the local properties of the magma (viscosity, temperature, strain rate, etc.) and hence, local inhomogeneities may greatly influence the actual extrusion rate and hence syn-event uplift. However, the concurrent change in pulse frequency is minor.

3.5.2 Bringing Together Models and Observations

We can also give a rough estimate for the carapace thickness from the Doppler radar. Assuming that the fastest particles measured by the radar travel at gas speed, we find that the gas is initially released at 30–60 m/s (vertical). The time difference between initial uplift and the first degassing pulse is 1.5 s. Assuming the gas originates from the hypothetical foam layer beneath the plug and travels at a constant speed vertically through a system of interconnected fractures, we may approximate the carapace thickness H (i.e. the travel distance) to 45–90 m.

Johnson and Lees (2010) have shown that the dome surface uplift produces a clear infrasonic signal. We argue that pulsed gas release is coupled to repeated dome surface uplift due to the spring-mass oscillation of the top of the magma column. The infrasonic signal is thus a superposition of two source processes: surface uplift and explosive degassing. Hence the localization of pulses is always biased and tends towards the center of uplift. Additionally, both source processes alternate. Given that initial surface uplift is 1.5 s earlier than the first pulse, and pulses occur every 3 s, the N-shaped infrasonic signals are produced every 1.5 s, resulting in double the frequency (see Fig. 3.5).

The force initiating uplift also acts on the ground and produces seismic waveforms, which can be calculated. *Johnson et al.* (2008)'s comparison of synthetic and measured waveforms reveals that LP-events at Santiaguito can be related to surface near dynamics. However, they do not explain the length of their signal as one forced pulse produces only a very short waveform. Dome vibration will, however, produce a repetitive force and may account for the duration of the LP-events. In the seismic spectra shown in Fig. 3.5 there is no energy in the frequency range that corresponds to the pulses. This absence might be explained by attenuation of seismic waves in gas-charged magma (*Collier et al.*, 2006), where seismic waves are absorbed by magmatic foam. The seismic waveforms that occur concurrently to an event at the surface stem from the sudden displacement of the magma column due to brittle failure and the occasional fracturing of the conduit wall rock. The induced dome surface uplift and following oscillation and explosive degassing can not be seen in the seismic data.

As already mentioned in the introduction, *Sanderson et al.* (2010) used pseudo-tilt measurements to constrain the average volume loss during one eruption to 10^2–10^3 m^3 at 250 m depth below the summit vents. In our model degassing stops when the gas cushion comes to rest at its initial position, i.e. when the overpressure (initially imposed by the stick-slip motion of the underlying magma column) decreases to zero. We can calculate the average gas volume that is released during a model eruption to $d\pi r^2 \approx 960\,\mathrm{m}^3$ (with $r = 35\,\mathrm{m}$ and at 80 m depth), which lies in the same order of magnitude, but at a different depth. However, *Sanderson et al.* (2010) use a volumetric Mogi source, which might oversimplify the complex source of gas. In our model, the released gas volume is only temporarily stored at 80 m depth and might originate from deeper in the conduit.

3.5.3 Review of Models for Oscillatory Activity

In addition to the previously discussed models there exist several ideas of mechanisms that try to explain pulsed behavior at volcanoes. In the following, we will give a short overview of those models and discuss their applicability for Santiaguito.

Lees and Bolton (1998) proposed, in analogy to a pressure cooker used in the kitchen, that pulsed gas release at Karymsky volcano, Kamchatka, might be explained by the opening and closing of a pressure limiting valve. Depending on the heat influx, the pressure cooker reaches a state of unstable equilibrium between the constraining weight and the internal pressure. With their model, *Lees and Bolton* (1998) are able to explain pulse frequencies of > 1 Hz. Interestingly, when considering the carapace as the weight that closes the valve, then we would observe uplift shortly before gas release. However, to reproduce the recurrence period of 3 s and maximum uplift of $\sim$0.5 m, the carapace's diameter would be limited to 3 m, which is two orders of magnitude smaller than the observed diameter of $\sim$200 m.

Pulsed gas release is most likely coupled to pulsed gas flow through the conduit. *Julian* (1994) showed that unsteady flow through a dike can lead to seismic tremor with frequencies in the order of 1–10 Hz. In his model, a fluid flows through an irregular shaped channel. Velocity disturbances lead to pressure perturbations. When accounting for elastic conduit walls, these may respond to pressure disturbances by widening or closing the conduit, in turn leading to new velocity disturbances in the fluid. Non-linear and chaotic behavior is the consequence. Adjusting the model parameters (fluid viscosity $<10^4$ Pa s, conduit length

>200 m) one can reproduce the 3 s pulsing period found at Santiaguito. However, the tremor model of *Julian* (1994) does not explain pre-eruptive uplift. Additionally, a steady background flux of volatile-rich magma is needed, where the flux rate oscillates. A periodically opening and closing of pathways for explosive degassing cannot be explained.

More recently a model to explain seismic tremor and/or harmonic behavior of volcanoes has been published by *Jellinek and Bercovici* (2011). They envision the plug as a column of highly viscous magma surrounded by a magma foam, sitting inside the conduit. Some excitation might bend the plug to one side, thereby compressing the magma foam on one side. Like in our model, the foam acts as a gas spring and eventually the whole column wags. Using their equation (1) and arbitrary but reasonable parameters we may obtain an oscillation frequency of 0.3 Hz. Assuming that surface degassing is only associated with a dilatation or compression of the magma foam (and not shearing), we would get two pulses per oscillation and hence the observed pulse frequency is twice the oscillation frequency. The observed period of surface activity is 3 s. To reproduce observed values and using a viscosity of 4×10^9 Pa s (*Harris et al.*, 2001) the wagging magma column would have a minimum length of 1370 m (Eq. (2) in *Jellinek and Bercovici*, 2011). However, gas release might also occur due to shearing of the foam at the sides of the column (perpendicular to the oscillation), in which case gas release would be more continuous rather than pulsed.

3.6 A Mechanism to Explain the Apparent Widening of the Upper Conduit

Barmin et al. (2002) and *Gonnermann and Manga* (2003) proposed a stick-slip mechanism where brittle failure or shear-induced fragmentation change the migration pattern of magma in the conduit above a certain depth from steady Poisseuille flow to plug flow (see Fig. 3.11a). A constant magma supply from depth generates shear stress at the conduit walls. Simple-shear experiments (*Caricchi et al.*, 2011) revealed that bubbles deform under shear and further localize shear stress to the conduit walls. At a certain depth the brittle failure criterion is reached at the conduit walls and magma locally fragments displacing the plug, i.e. the whole magma column above the onset of brittle failure (see Fig. 3.11). A connected network of deformed gas bubbles develops. Viscous retardation of bubble growth due to the high viscosity of dacitic magma (>10^9 Pas), results in an elevated gas pressure inside the gas network that might exceed the confining pressure at some depth. The pore pressure in the wall rock would increase, eventually triggering localized extensional fracturing of the conduit walls (*Caricchi et al.*, 2011). This conduit wall fracturing happens every event, hence every event repeatedly increases the conduit radius at shallow depth. *Lavallée et al.* (2012) recently showed that conduit wall fracturing in turn can induce local fragmentation of the near-wall magma, which in our model would widen the network of degassing pathways into the magma and provide a source for juvenile ash.

Bluth and Rose (2004) describe the activity in January 2002 as confined mainly to a

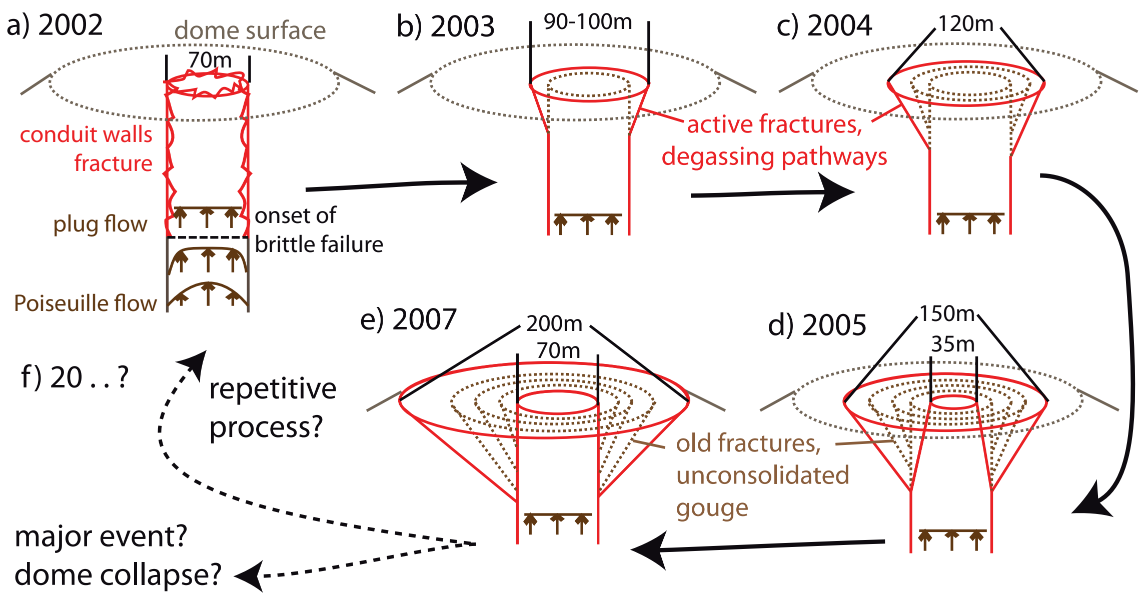

Figure 3.11: Hypothetical conduit processes at the Santiaguito dome. a) Shear fracturing leads to plug flow of the uppermost part of the magma column. Gas pore pressure fractures the conduit walls. b–c) Repeated fracturing steadily widens the upper part of the conduit (radius increases 12.5 m per year on average). Due to low temperature and pressure near the surface, fractures can not heal and a conical zone of unconsolidated gouge material develops. Degassing is confined to the conduit walls. The vent diameters of a)–c) are taken from *Bluth and Rose* (2004). d) At a certain inclination of the arcuate fractures (i.e. at a certain diameter of the outer ring) the local stress field can not further widen the conduit and the magma column in the center breaks the overlying cold carapace. The activity splits into inner and outer ring features. e) Depending on the local stress field, the fracturing process continues at inner and outer ring and widens both. f) The whole process is either repetitive (i.e. the outer rings become inactive and the process repeats) or leads to a highly unstable system.

ring of vents with a diameter of 70 m. Occasionally for the larger events, explosions migrate outwards and occur all over the dome. They also note that the diameter of the ring of vents became larger over the years (90–100 m in 2003 and 120 m in 2004). A further increase in diameter to 150 m is observed by *Sahetapy-Engel and Harris* (2009a). This steady increase in diameter of roughly 25 m per year suggests that the conduit's diameter at shallow levels increases from one event to the next and has a conical shape. In fact, in January 2007, the outer-ring had a diameter of approximately 200 m.

Using an overlay of thermal and visual photographs taken in January 2005 *Sahetapy-Engel and Harris* (2009a) are the first who also show that a second hot surface region (diameter of 36 m) exists within the outer ring of vents. In 2007 this regions diameter also increased to 70 m. Assuming that gas pressure fractures the conduit walls at every event (*Caricchi et al.*, 2011) the shallow conduit steadily widens (Fig. 3.11a–c) and the conduit walls become more and more inclined. After some time the local stress field exerted by the extruding plug might favor the build of a new fracture system directly above the lower unaffected conduit (see Fig. 3.11d). Explosions occur at both active fracture systems as they also serve as degassing pathways. The inner ring undergoes the same repeated fracturing process and steadily widens (Fig. 3.11e). Whether the outer ring vents seal and become inactive in the future (repetitive process begins again with Fig. 3.11a) or stay active and result in a dome collapse or similar is an open question.

3.7 Conclusion

In his paper we presented a mechanical model that explains repeated release of gas during explosive events and the associated pre-event uplift. In Fig. 3.12 we sketch our idea of the processes that go on during a typical event. Between events, the magma column degasses, but due to the high viscosity of the dacitic magma gas bubbles rise very slowly. The upper part of the conduit is filled by degassed, highly viscous magma (here named carapace). This carapace is surrounded by a conically shaped zone of highly fractured unconsolidated gouge material (gouge zone) that occasionally grows with an event (see Fig. 3.11b,c,d,e). *Holland et al.* (2011) show using viscosity modeling that at temperatures below 700°C, which is the approximate temperature of the conduit walls, fracture healing (by sintering) can only occur at depths below 35–50 m. At higher temperatures (∼800°C, carapace center), fractures heal during the repose time (*Tuffen et al.*, 2003; *Holland et al.*, 2011). Gouge zone and (to a lesser degree) carapace are permeable, thus enabling repose degassing.

Magma column displacement, initiated by strain-induced fragmentation, compresses the foam layer located below the carapace, which in turn exerts a pressure force onto the carapace. The carapace is laterally constrained thus it deforms and uplift starts in the center. Deformation creates or reactivates fractures in the carapace and opens pathways for the foam to degas. At the same time local fragmentation along the conduit margins below the foam builds a network of interconnected fractures that enable gas rise (see Fig. 3.12c). This gas stems from spontaneous degassing of the fragmented area and rises until it reaches the compressed foam layer. The foam is not permeable enough to promote gas flux from the plug margins to the carapace center pathways, thus gas preferentially accumulates below the carapace circumference. The fresh gas drives the detachment and breakup of the gouge zone and parts of the wall rock. When those fractures reach the surface, explosive degassing occurs at the outer annulus, i.e. the circumference of the gouge zone. Here the gouge zone may act as a source of cold ash that is entrained and 'accidentally' erupted. Repeated material failure at the face between gouge zone and conduit walls causes a constant widening of the gouge zone and hence a widening of the outer annulus, where the more emergent and hotter degassing pulses have been observed (see Fig. 3.11).

At some point during the carapace uplift the foam has decompressed. Due to inertia, the carapace overshoots this new equilibrium position, is decelerated and eventually sinks back down. On its way down the carapace deformation is reversed and center pathways close, thus stopping further degassing of the foam (see Fig. 3.12d). The same holds for the gouge material. Due to its weight, it falls back down and closes fractures. Carapace and

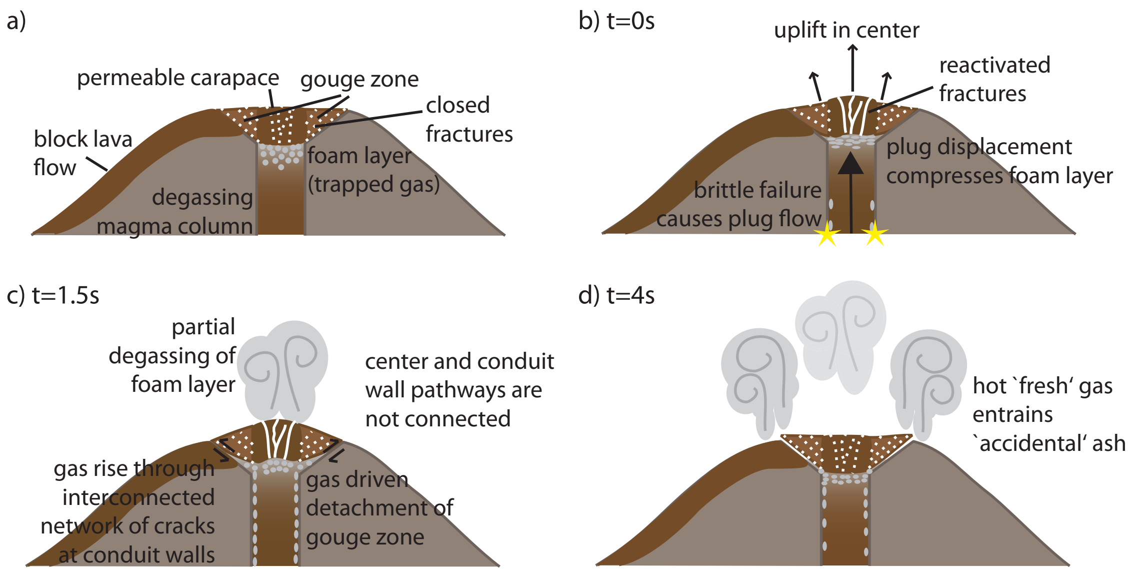

Figure 3.12: Hypothetical scheme of dome processes at Santiaguito volcano. a) Repose degassing trough the permeable carapace (degassed, highly viscous magma), which is sitting on a foam layer. Depending on pressure and temperature conditions, fractures in carapace and gouge zone heal by sintering, thereby maintaining a certain permeability, to enable repose degassing. Due to the limitedness of the permeability, gas gets trapped and the foam layer grows. b) Shear-induced fragmentation causes a sudden upward displacement of the magma column (plug), compressing the foam layer. This pressure build-up in turn causes deformation and uplift of the laterally constrained carapace. The deformation reactivates and/or creates fractures that enable increased gas release. c) 1.5 s after the deformation starts, gas is released (explosively) at the surface. At the same time, fresh hot gas rises from depth through the fragmented annulus at the conduit walls. The foam layer is not permeable enough to enable gas flow from the conduit walls to the center pathways. Continued uplift exerts a drag force on the gouge zone and creates concentric shear-fractures in the conduit walls which immediately fill with the fresh gas, which further drives the detachment of the gouge zone. d) Due to its weight, the carapace sinks back and compresses the foam. At the same time center pathways close. As soon as the fractures in the gouge zone reach the surface, fresh hot gas is released explosively, thereby entraining ash. Later pathways at the outer annulus close, degassing stops. Depending on the remaining gas volume in the foam and the overpressure exerted by the inertia of carapace and gouge material, secondary uplift/explosive degassing circles might occur.

gouge material compress the remaining foam and gas — provided not all gas escaped during the uplift. This compression in turn exerts an upward pressure force that initiates the next uplift/explosion cycle, without another fragmentation event and subsequent magma column displacement.

Acknowledgments

Success of the field portion of this experiment was made possible with support from many people but a special thanks goes to Alexander Gerst who installed and maintained the Doppler radar during the experiment. We further acknowledge the support and hard work of Raul Salguero, Rudiger Wolf (of Michigan Tech), Oto Matias and Eddy Sanchez (of INSIVUMEH, Guatemala), Bill Elderbaum (of USAID, Guatemala), Bill Rose (of Michigan Tech), Richard Sanderson and Omar Marcillo (from University of New Hampshire), the tourist police from Panajachel, the staff at the Santiaguito Observatory, IRIS PASSCAL (Program for Array Studies of the Continental Lithosphere, New Mexico Tech, providing expertise and the seismic and infrasound loggers), and Nick Varley (University of Colima). Furthermore, we thank Anna Zoporowski for the inspiration to the mechanical model. Funding for the field work of this project was provided in part by NSF EAR Grant #0440225 and DFG grant Ho1411 16-3. LS was supported through a stipend by the University of Hamburg and through DFG Grant Ho1411 20-1.

Chapter 4

Weak Volcanic Clouds at Colima Volcano

To study the dynamics of developing volcanic clouds in their first 100–300 m of rise, I installed a Doppler radar system at Colima volcano, Mexico (see Fig. 4.1a)) in 2009. A preliminary experiment was setup on the way back from the Santiaguito experiment (see chapters 2 and 3) in Guatemala in 2007. The Doppler radar was installed on the south flank near the Barranca de Montegrande at ∼2500 m asl and 3000 m slant distance from the crater rim (see Fig. 4.1c)). Contrary to the setup at Santiaguito, the Doppler radar was aiming atop the crater rim and looking from below into the sky (see Fig. 4.1c).

4.1 Recent Activity of Colima Volcano

Volcán de Colima is located in the western part of the trans-Mexican volcanic belt (TMVB, Fig. 4.1a) and is one of the most active volcanoes of Mexico. Its magma is of calc-alkalic composition (producing andesitic domes), which is typical for the subduction zone setting. After the last Plinian eruption in 1913, Volcán de Colima was relatively quiet until the recent phase of unrest began in November 1998 with an effusive eruption and a fast dome growth (*Zobin et al.*, 2002). Since then dome growth periods of varying duration (2 days – 5 years) alternate with large — partially dome destroying — Vulcanian events (*Varley et al.*, 2010). The last vigorous phase of fast dome growth and Vulcanian eruptions of larger magnitude occurred from September 2004 to September 2005. Since February 2007 a very slow effusive episode (average extrusion rate of 0.02 m^3/s, *Sulpizio et al.*, 2010; *González-Mellado et al.*, 2011) is growing a dome that until now (April 2012) partially fills the crater. Due to the eccentric vent the dome edge has reached the western crater rim and produces rockfalls and small block-and-ash flows that slide down the western flank (see Fig. 4.2).

This recent effusive period is accompanied by daily explosions with highly varying ash content ranging from white steam explosions to grayish plumes. Those weak volcanic plumes rise up to 1–3 km above the vent. Their source forcing is short-lived (tens of seconds to

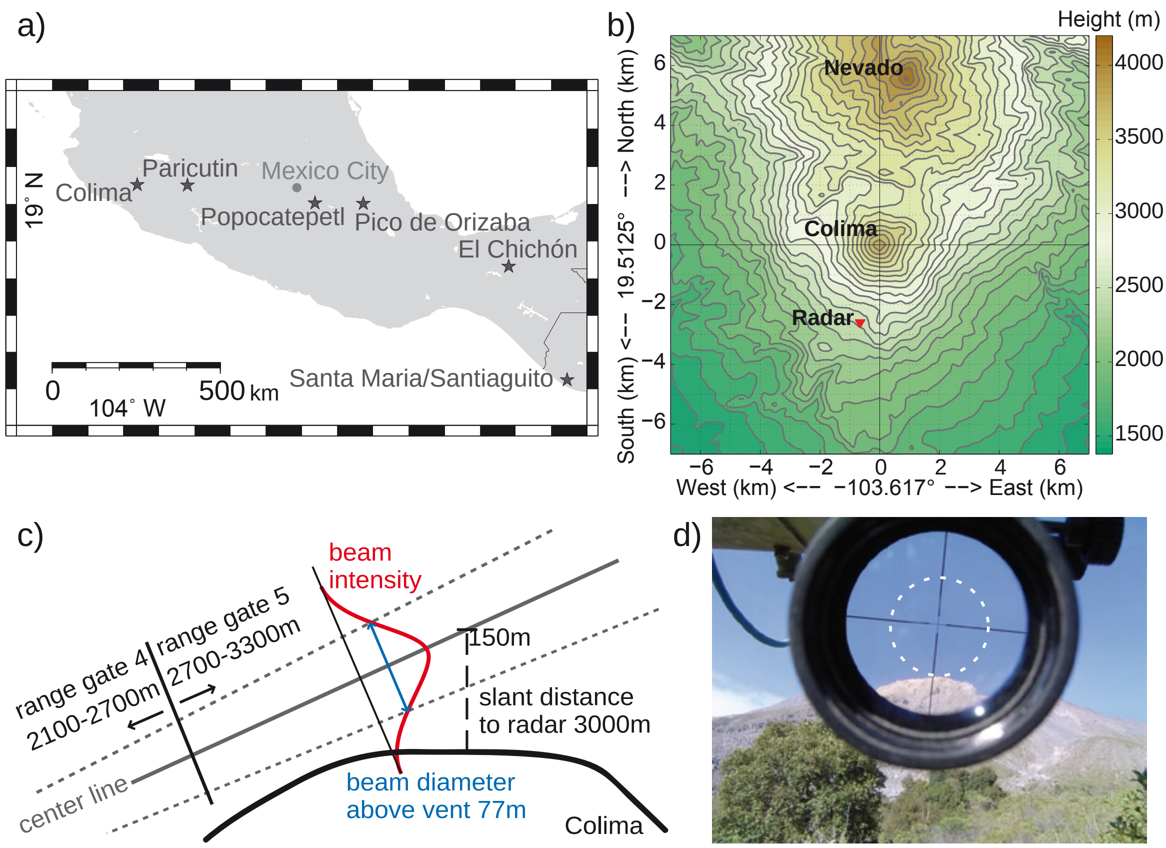

Figure 4.1: a) Colima volcano belongs to the trans-Mexican volcanic belt (TMVB) volcanoes and is the most active volcano of Mexico. The map was produced using the Generic Mapping Tools (GMT) package (`http://gmt.soest.hawaii.edu/`). b) Topographic map of Colima volcano (centered on the crater) and the ancient parent volcano Nevado de Colima, including the location of the Doppler radar (DEM data from *USGS*, 2004a; *Farr et al.*, 2007). c) Schematic drawing of the measurement setup at Colima volcano. The radar is installed at the South flank of the volcano and points above the crater rim (inclination is 31°upwards). d) View through the telescopic sight, which is aligned to the radar beam and used to aim the beam to a defined location. Note that the true field of view (FOV) of the radar beam is approximately the inner half of the telescope's FOV.

few minutes) and they are often bent by the background wind field because of their limited inertial momentum and buoyancy.

History and the ongoing effusive eruption suggest that a new vigorous explosive phase of dome collapse and large scale Vulcanian events is to occur within the near future.

4.2 The Doppler Radar Monitoring Station

4.2.1 Preliminary Installation in Spring/Summer 2007

During the first installation in February and March 2007, the system consisted of one Doppler radar (MVR4) and a data logger for on site data storage. Both devices were also used in

(a) view from NNW, above crater rim

(b) view from E, at crater rim

(c) view from SW, at height of crater rim

Figure 4.2: (a) The dome at Volcán de Colima viewed from a fly-by in February 2010 (view towards ESE). The depression in the crater rim on the upper right side is the Montegrande ravine (width of approximately 80 m) that is clearly visible from the Doppler radar. On the lower right (towards east) the dome grows beyond the crater rim and gradually breaks off. On the left side (towards north) the dome reaches the crater rim. For a size estimation, (b) shows Jörg Hasenclever (blue jacket and helmet) during sampling on the north edge of the dome. Note that the view of (b) is towards W. (c) shows a small break-off event that happened during the fly-by in February 2010. The view is towards NE. All three photos are courtesy of Jörg Hasenclever.

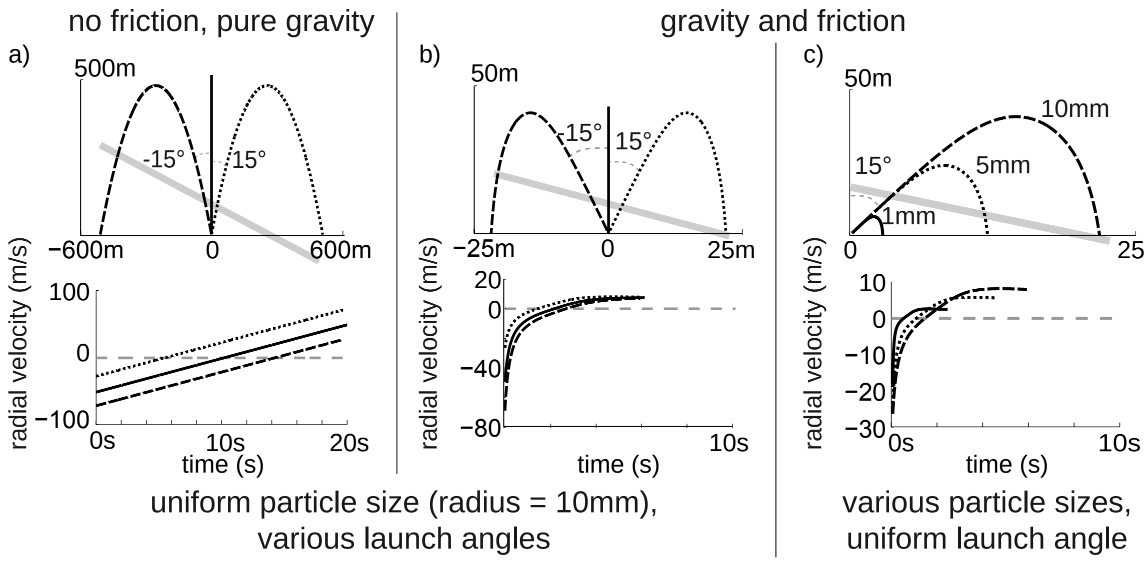

Figure 4.3: Simple examples of ballistic particle transport in non-moving air and their time lines of radial velocity (pseudo velocigram) as it would be measured with the Doppler radar at Colima volcano (compare Fig. 2.2 for the Santiaguito setup). The top diagrams show the particle trajectories. In these examples particle transport is confined to the image plane. All particles are initialized with an absolute velocity of 100 m/s. The gray bar represents the radar beam direction. The lower diagrams show the pseudo velocigram, i.e. the particles radial velocity as a function of time. Note that in a pseudo velocigram the echo power of all particles is assumed constant and equal to unity. The horizontal gray dotted line marks the zero velocity. A particle's trajectory and the corresponding pseudo velocigram are represented by the same line style. Examples (a), (b) and (c) are the same as in Fig. 2.2, only the measurement setup, i.e. the observation angle is different. Contrary to the Santiaguito setup (Fig. 2.1) the Doppler radar at Colima (Fig. 4.1c)) looks into the erupting cloud from below, hence the radial velocities switch their signs.

the Santiaguito experiment in January 2007. The data logger was designed and built by Alexander Gerst during his PhD project (*Gerst*, 2010). The long distance between Doppler radar and crater required a large antenna with a diameter of 1.2 m (compared to 90 cm at Santiaguito or 60 cm at Erebus (*Gerst*, 2010) and Stromboli (*Hort et al.*, 2003)). As a consequence the amplitudes of echo power of the Santiaguito and Colima experiments are only comparable when corrected for the antenna gain (see Eq. 1.2 on page 7), which is unknown. In addition, the assignment of rising and settling particles is the opposite of the Santiaguito setup (see Fig. 2.1), caused by the different sounding geometry. In the Colima data rising particles, which mainly depart from the radar, are recorded with negative radial velocities, whereas settling particles approach the radar and have a positive radial velocity (compare Fig. 2.2, p. 12, and Fig. 4.3).

The entire system was powered by an array of 5 solar panels (85 W each) and 4 truck batteries (∼30 Ah each). Maintenance of the station was carried out about once a month and comprised a complete data recovery and an inspection of the power distribution and batteries. To limit the amount of data a software trigger has been implemented that switches between maximum sampling rate (~10 Hz, in case of an event) and 1 Hz sampling rate (between events, averaging) in real-time. While the Doppler radar is continuously recording at maximum sampling frequency and sending data to the logger to analyze each spectrum, the switch is used to reduce the amount of data actually stored on hard drive. A pre-event buffer ensures that high resolution data is available for 2 s before the triggered event. The trigger was set up as a simple threshold search of the summed echo power of a defined range of velocities at a certain distance (range gate above the crater rim). Technical problems made it necessary to change the trigger configuration several times to avoid false triggers. 99% of the trigger-events were false and hence the protocols cannot be used to identify events. On the other hand the trigger worked well in that 89% of all recorded events were detected, and the remaining 11% were very short (2–5 s) and weak events (in terms of echo power and velocity). In addition, some event codas have not been detected and are only available at the coarse time resolution of 1 Hz. However, those small-amplitude events and codas are not critical for the analysis presented and conclusions drawn in this study. The procedure used for manual event picking is described in appendix C.2.

4.2.2 Extension in December 2008 until Present

In December 2008 we[1] re-installed the Doppler radar (MVR4, connected via Ethernet) and equipped the system with an additional video camera, a newly designed data logger and a wireless local area network (WLAN). In February 2009 we[2] installed a second Doppler radar (MVR3) at the same location to simultaneously record the dynamics at two heights of a developing plume. The second Doppler radar is slightly different as it is connected via the serial port and has a maximum sampling rate of 1 Hz. I have modified the data recording software (originally developed by Malte Vöge during his Ph.D. project, *Vöge*, 2007) such that it is now possible to simultaneously control two Doppler radars and the video camera with a single data logger.

The logging unit is a fully functional PC104+ based computer running Windows XP (designed following the example of Alexander Gerst, and adjusted to the Colima monitoring purpose). Local data transmission is based on an Ethernet network. GPS-based timing is provided by a NTP-server and an intelligent rebooting device (iBoot, `www.dataprobe.com`) can force a reboot of the whole system in case the data logging computer stalls. The software trigger has been modified to control whether the camera takes pictures at a defined interval or records a movie (during triggered events). In addition, the data logger toggles a relay that switches off the camera during night time.

The whole system consumes a power of approximately 70 W. An array of 10 solar panels is able to provide a peak-power of 725 W during cloud-free daytime and charges an array of batteries to power levels sufficient to supply the system for two cloudy days and nights. The

[1] My colleague Arturo Montalvo Garcia and myself.
[2] My advisor Matthias Hort and myself.

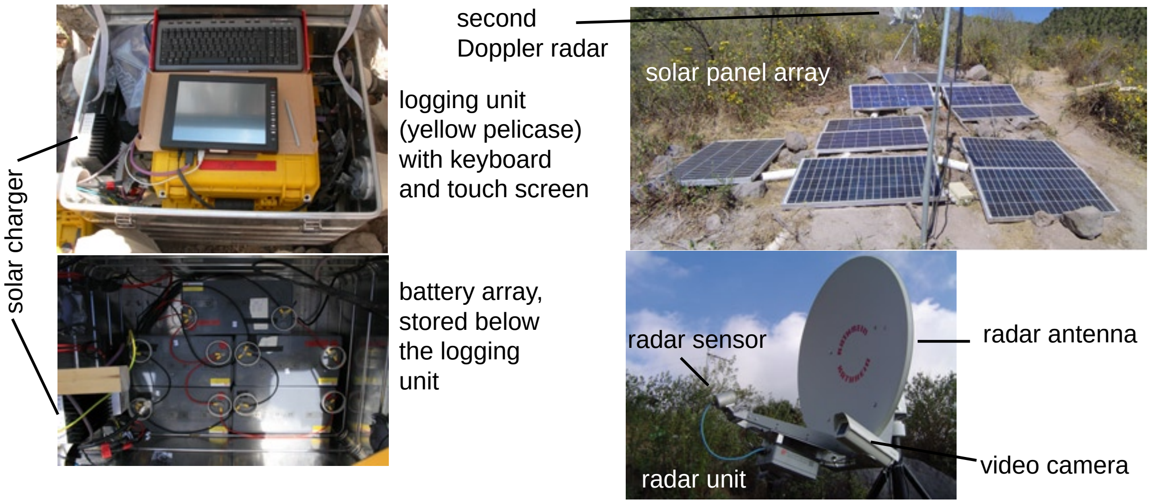

Figure 4.4: Pictures of the current Doppler radar monitoring system. Batteries, solar charger, power distribution box (not shown) and data logger are stored in an aluminum box, which sits in a small bunker. This “bunker” is a hole in the ground, paved with concrete and built such that water flows around and not into it. An aluminum roof protects the box from direct sunlight and rain. The sloped ground allows to place the solar panels directly on the ground with an angle of approx. 10° to the horizontal and directed south. The two Doppler radars are set up about 30 m apart (above and below the solar panel array). The lower Doppler radar is equipped with the video camera (lower right picture).

battery charging status is monitored continuously via the solar chargers serial port, connected to the logging unit.

Data transmission from the volcano to the university (28.5 km direct line) is realized by a wireless local area network. The use of the WLAN technique is especially important to maintain remote access to the station in times of a volcanic crisis. The network consists of two simple radios (designed by Arturo Montalvo Garcia) operating at 2.4 GHz and radiating 100 mW. The radios are mounted at the mast next to the antennas, so that the the power loss by long antenna cables for analog data transfer between radio and antenna is minimized. The radios are powered via their Ethernet cable (power over Ethernet, PoE).

At the base station at the University office in Colima, the radio (a network bridge) is directly connected to a computer, on which the data is stored and available for immediate checking and processing. The automatic data download has been realized by using a commercial software for folder-synchronization and several self-written batch-scripts that ensure correct data storage and import into a database. A complete description of the data download process is given in appendix C.3. Two way data transmission enables us to login to the logging unit at the radar station from the office to check the status of the Doppler radars, the video camera, and the charging status of the batteries. The WLAN connection also provides full control over reconfiguration, and even allows rebooting of the whole system or single devices for remote troubleshooting.

Technical problems and a concurrent decrease in volcanic activity, however, have so far impeded simultaneous data recording of both Doppler radars and camera during an eruption. In the following, I will therefore use the 2007 dataset for a classification of dynamic regimes and a comparison of at-vent- (Santiaguito experiment) and starting-plume-dynamics (150 m above the vent, Colima 2007 experiment).

4.3 The Dataset of 2007 and Preliminary Results

The Doppler radar was almost continuously measuring from March 2nd to July 18th, 2007 (see Fig. 4.5). The long downtime in March was caused by an overfull hard drive, which kept the data logger down. Note that the trigger was not running until that time because configuring of the threshold-based event detection requires temporarily unstacked data. Afterwards the trigger was set up, but the same issue occurred again in May because of a too sensitive trigger configuration (too many false alarms). The outages in June and July resulted from the cloud coverage during the rainy season. A total of 91 events have been detected (see Fig. 4.5). The detection of less events during the rainy season (mid June to mid October) is caused by the fact that no events can be detected during rain fall (see chapter C.2 and *Vöge*, 2007).

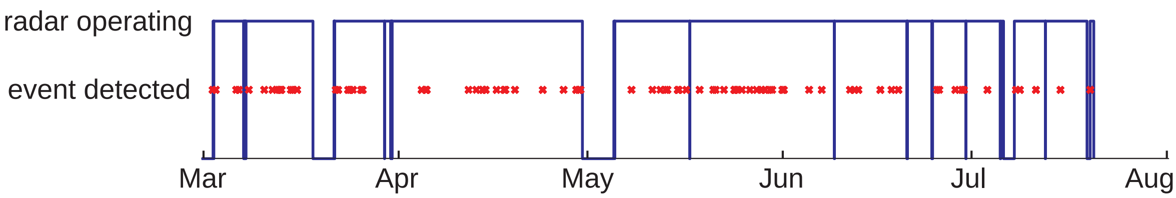

Figure 4.5: Operation times of the radar (blue line) and manually picked events that were detected with the Doppler radar (red crosses).

During the 2007 installation no camera was observing the events, hence a visual classification of the events is not possible. Fortunately one set of pictures associated to a rather big event on March 2nd was photographed by Florian Ziemen and John Stevenson on their way to service the instrument (see Fig. 4.6a). The same eruption was recorded by the Doppler radar. The data are shown in the velocigram[3] representation in Fig. 4.6a) below the pictures. Unfortunately the time stamp of the pictures is neither synchronized to UTC nor to local time, which it precedes by approximately one minute. Given that it needs some seconds to spot the eruption, stop the car, get out and have the camera ready, I assume that this set of pictures corresponds to the second period of activity (from 70 s onward). However, it is clearly visible that the fluctuations in velocity and echo power measured by the radar (see velocigram in the lower panel of Fig. 4.6a) can not be identified in the pictures.

The example shown in Fig. 4.6a) is representative of 14% of the 91 eruptions, which are characterized by a long duration and many consecutive streak-like pulses. The echo power of those eruptions is highly variable, as are the recorded velocities. Fig. 4.6b shows a typical example of pure ballistic motion in the atmosphere (compare to the parametric study in

[3]The velocigram shows the echo power (color coded) as a function of radial velocity and time.

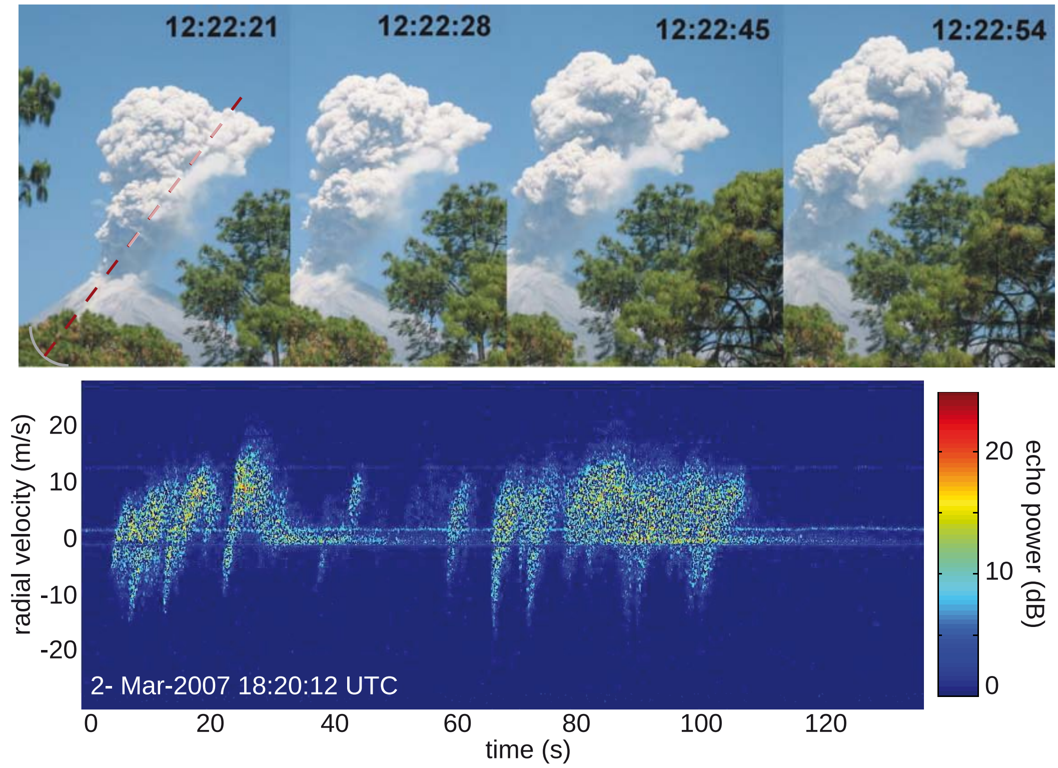

(a) Photographs and velocigram for a long-lasting ballistic event on March 2, 18:20:12 UTC.

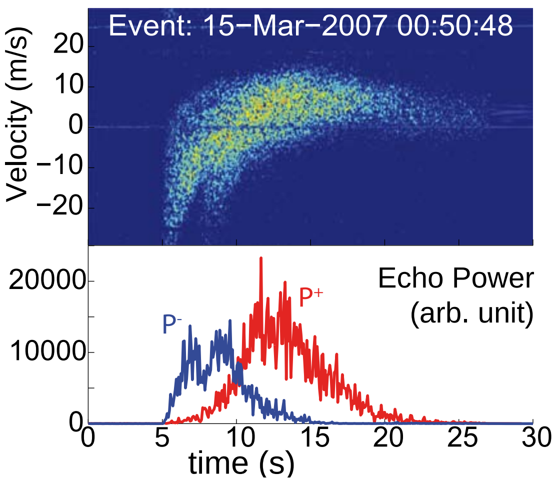

(b) Example of a ballistic event on March 15, 00:50:48 UTC.

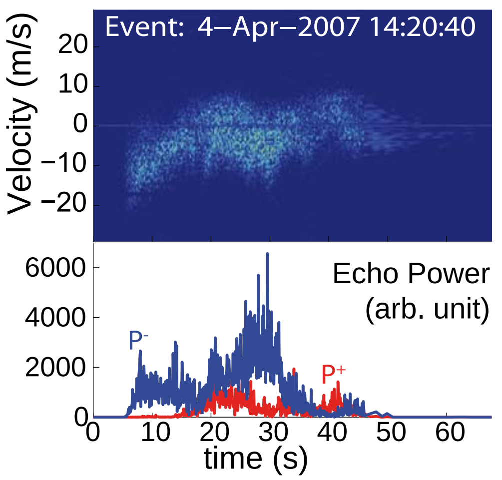

(c) Example of a non-ballistic event on April 4, 14:20:40 UTC.

Figure 4.6: Three typical and representative example eruptions. a) The time stamp in the pictures is set by the camera and precedes local time by ~60 s. The dashed red line in the first picture indicates the direction of the radar beam. The photographs most probably correspond to the second phase of pulses (from 70 s onward) in the corresponding velocigram, shown below the pictures. The color bar (representing echo power) is the same for all velocigrams. Photographs were taken by Florian Ziemen. b) Typical example of a ballistic event, which comprises two pulses 2.5 s apart. The curves of echo power given below the velocigram are calculated using Eq. (2.1) (p. 14). c) Example of a non-ballistic event. Note that the trigger failed to detect the end of the eruption and therefore the time resolution changes after ~46 s.

chapter 2). Those events are characterized by a short duration (20–40 s), a sudden increase in negative velocities (up to 55 m/s radial), a steep increase in P^- and a gradual increase in P^+ somewhat later[4]. In the following I term those events 'ballistic events'. Note that this example has two pulses ~2.5 s apart. These pulses can be identified in P^- with equal echo power. During the second pulse some ash of the first pulse still moves inside the field of view (FOV), and hence an equal echo power of both pulses indicates that the second pulse ejects smaller particles or less ash.

Interestingly, the individual pulses in Fig. 4.6a are similar to either of the streaks in Fig. 4.6b when the velocigram of Fig. 4.6a is stretched such that the scaling of the time axes are equal. Hence those long lasting events are also dominated by ballistic motion, but they comprise more pulses. Using this discrimination about 40% of the recorded events are ballistic events.

All 91 events are recorded at a height of 150 m above the vent (center of FOV). The radar beam has a diameter of 77 m, hence a particle must reach a minimum height of 110 m to be recorded. In the case of no wind only larger particles might reach the FOV because of their higher momentum that dominates air drag. Those particles certainly move on ballistic trajectories and hence appear as streaks in the velocigram. A certain initial kinetic energy is required to transport larger particles to and into the FOV on ballistic trajectories so that ballistic events can be associated with highly energetic explosions. Remember that the particles receive their kinetic energy from the expanding gas phase.

The example showing multiple pulses (Fig. 4.6a) seems to be caused by several pulses releasing ballistic particles, i.e. individual consecutive impulsive explosions that nonetheless form a single volcanic cloud — a process that is difficult to be visually resolved. Hence the mass flux that builds these eruption clouds is not steady and even 20 s long periods of quiescence (see Fig. 4.6a) are hidden within the cloud.

An example of a non-ballistic event is given in Fig. 4.6c. This event also shows a sudden increase in velocity, but the velocity decay is much slower and appears to be linear. In addition, 'secondary pulses' are introduced by a gradual velocity increase rather than a sudden step. Note that the echo power is orders of magnitude less than in the previous examples. This is indicative for fewer and/or smaller particles in the field of view (FOV). Non-ballistic events have a maximum along-beam rising velocity of <30 m/s. In the example in Fig. 4.6c the echo power that can be attributed to rising particles (P^-) is much larger than P^+, which corresponds to falling particles. In other non-ballistic events, only falling particles are detected. All non-ballistic events (60%) can neither be explained by ballistic motion, nor be reproduced by the synthetic Doppler radar model Qradar[5], which means that the majority of particles in the FOV does not move on ballistic trajectories. The fact that those

[4] P^- and P^+ are the echo power attributed to rising and settling particles, resp., and given by Eq. (2.1) in chapter 2.

[5] See chapter 2 and appendix A.1 for a detailed description. Qradar calculates particle trajectories through a parameterized atmosphere and outputs the corresponding velocigrams as would be measured by a Doppler radar.

presumably smaller particles reach a height of 110 m and above requires the atmosphere to transport them and hence an updraft must exist (i.e. the air drag force dominates the momentum). I attribute this upward gas movement to (a) near-vent gas jetting and (b) buoyant updraft caused by convective entrainment and heating of ambient air. The buoyancy effect is only crudely parameterized in Qradar (see appendicees A.1 and A.2) and, therefore non-ballistic particle movement cannot be reproduced with these approximations. Instead more sophisticated models are needed, which account for turbulence and entrainment as well as a proper parameterization of the interaction between gas and particles. In the next chapter I will introduce two eruption cloud models — ATHAM and PDAC — and couple them with that part of Qradar that calculates the echo power of particles moving through the radar beam. The particle trajectories are taken from the output files of ATHAM and PDAC. The resulting synthetic velocigrams will be used to test the hypothesis that non-ballistic events are buoyancy dominated eruptions.

Chapter 5

Numerical Modeling of Eruption Clouds

In the last chapter I showed that the dynamics within developing clouds are more complex than purely ballistic transport of ash particles through a parameterized atmosphere. Large pressure gradients accelerate the gas phase in the conduit and in the jet region immediately above the vent, and high concentrations of ash of various grain sizes interact with the gas. Here the feedback between particle and gas motion is strongest and should be accounted for in numerical models. During the adiabatic gas expansion several processes occur simultaneously that mainly control the behavior of the developing cloud:

- The juvenile (i.e. erupted) gas cools adiabatically,
- particles are accelerated by air drag forces and decelerate the gas,
- ambient air is entrained into the ash-rich region by turbulence,
- the hot particles exchange heat with the entrained air, which decreases the bulk density, and
- latent heat resulting from phase changes of water inside the plume may provide or consume energy (freezing and sublimation, respectively) and thus affect the plume height.

In case the bulk density falls below the local atmospheric density the cloud rises buoyantly. The cloud collapses if the decrease in bulk density has not been sufficient. The potential energy of the rising cloud has to come from the initial kinetic energy (mainly stored in the pressurized magma) and the thermal energy. A more detailed introduction into the development of volcanic clouds is given in the introduction (chapter 1.2 and references therein).

The numerical simulation of all these processes is a challenging task. It requires the accurate description of multi-phase fluid dynamics, where the equations of motion, energy, and continuity are coupled between the gaseous and solid phases. A good review of the advances in numerical eruption cloud modeling until 2005 is given by *Textor et al.* (2005). Models for all scales (2 km to global) are presented including a conduit model, which can be used as lower boundary condition for eruption cloud models. Both models presented and applied here (PDAC and ATHAM) are newer versions of the mesoscale-gamma (2–20 km, some tens of minutes of cloud evolution) and mesoscale-beta (20–200 km, some hundreds of minutes) cloud models resp., described in that review. The new versions are able to solve three dimensional problems in parallel and include a more accurate description of the real topography in 3D or a topographic profile in 2D.

Until now, sustained (i.e. constant for the duration of cloud formation) vent conditions have been applied as source feeding for 1D (*Sparks et al.*, 1997), 2D (see *Textor et al.*, 2005, and references therein) and 3D (e.g. *Neri et al.*, 2007; *Esposti Ongaro et al.*, 2007, 2008; *Herzog and Graf*, 2010) models of Plinian eruptions for which this assumption may be reasonable. The Doppler radar datasets of Santiaguito volcano (see chapters 2 and 3) and Colima volcano (see chapter 4), however, clearly demonstrate that Vulcanian events are comprised of several short-lived pulses rather than a steady mass flux at the vent. The Colima data even shows that visually larger plumes, which seem to result from steady mass flux, are also formed by a series of discrete explosions up to 20 s apart.

The main questions arising from the Santiaguito and Colima datasets are:

- Up to which cloud height can those pulses be detected by Doppler radar?
- Can stable (non-collapsing) clouds be produced by pulsed feeding?
- What are the source dynamics of the (non-)ballistic eruptions observed at Colima volcano?

In this chapter I use two sophisticated models for particle transport rather than a simple parameterized atmosphere (which is part of Qradar) to produce the synthetic Doppler radar data. In the following two sections I introduce the two numerical models ATHAM and PDAC, which are used in this study. This is followed by the description of the coupling of the numerical eruption cloud models to the synthetic Doppler radar calculations (Qradar). Afterwards the two numerical eruption cloud models are compared and their different methodical approaches are discussed. Finally, a set of numerical experiments is used to explore the importance of initial velocity, duration and non-steady source feeding on the dynamics of the developing cloud.

5.1 ATHAM — Active Tracer High-resolution Atmospheric Model

The eruption cloud model ATHAM has been introduced by *Oberhuber et al.* (1998) and *Herzog et al.* (1998). It is designed to simulate the dispersal of pyroclastic material under realistic atmospheric background conditions in two and three dimensions and is conceptually an atmospheric circulation model for cloud-resolving scales extended by the scheme of dynamically active tracers. The equations of motion are solved for the gas-particle mixture. The exchange of momentum and heat between the solid, liquid and gaseous components as well as their concentrations are computed diagnostically, i.e. they are obtained at every time step from the current bulk pressure, temperature and velocity. Note that the bulk properties (or 'volume mean' properties) are derived by averaging over the components properties with respect to their volumetric concentration. Turbulence is accounted for by diffusion of turbulent energy. All equations and model assumptions are described in full detail in *Oberhuber et al.* (1998) and *Herzog et al.* (1998), therefore only the most important features are mentioned here.

The model is capable of transporting tracers within the flow field. For example, a tracer may be an ash particle or rain drop that is transported and its trajectory can be used to map streamlines. Usually those tracers are passive, which means that they do not affect the flow. In ATHAM, tracers may be active, which means that depending on their concentration they affect the volume mean properties and thereby change the flow pattern. In this study all solid, liquid and gaseous components are active tracers and no passive tracers are used. The main power of ATHAM is the incorporation of cloud microphysics, which account for the phase changes of water in the atmosphere (e.g. vapor, cloud water, precipitable water, ice crystals, and snow/hail). Compared to global or regional atmospheric models, ATHAM has a high resolution, which was the reason for its name: *Active Tracer High-resolution Atmospheric Model*.

As mentioned above the equation of motion and the continuity equation are solved for the volume mean properties of the mixture rather than for each single phase (see multiphase numerical models in section 5.2). This simplification is based on the assumption that the particles are in dynamic and thermodynamic equilibrium with the surrounding gas. In brief, dynamic equilibrium means that the particles' inertia can be neglected and that the liquid and solid components always move with their terminal fall velocity relative to the gas (hence only their vertical velocity component deviates from the bulk velocity). It also means that the pressure force on each component equals the bulk pressure force. Thermodynamic equilibrium means that the in-situ temperature of the components is identical to the in-situ bulk temperature. Therefore the heat conduction inside the non-gaseous tracers is assumed to be efficient enough to establish a thermal equilibrium between particles and the surrounding gas at all times. Due to these assumptions only small particles ($r < 0.5\,\text{mm}$) can be treated accurately.

The solid, liquid and gaseous tracers (active and passive) can be arbitrarily configured. There is no restriction considering the number of solid tracers like for example ash of different sizes. Liquid and gaseous tracers, however, are used in the microphysics module and care has to be taken that all water phases (vapor, cloud water, cloud ice, precipitable water and snow/hail) are defined. Due to the calculation of volume mean flow, additional tracers (active or passive) do not significantly increase computing time, which mainly depends on the number of grid points.

The above assumptions are valid for the simulation of large scale volcanic clouds (meso-scale-beta, 20–200 km, hundreds of minutes, *Textor et al.*, 2005), where the particles that are dragged upward in the buoyant cloud are small. In those volcanic clouds vapor condensation, entrainment of ambient humid air, and eventually precipitation are important and significantly affect the rise height and lateral spreading of the volcanic plume. Those simulations require grids that span tens of kilometers in horizontal and vertical direction to avoid boundary effects. Due to computational limitations they have a minimum grid resolution of a few 100 m.

ATHAM has been used primarily for parametric case studies on the influence of ambient atmospheric conditions (*Graf et al.*, 1999), phase changes of water (*Herzog et al.*, 1998), particle aggregation and gas scavenging (*Textor et al.*, 2006a,b) on the development of the eruption cloud, as well as the injection of volcanic gases into great heights and the gases influence on regional weather (*Textor et al.*, 2003). Several extensional modules exist to simulate e.g. particle aggregation, radiation, gas phase chemistry, and gas scavenging by hydrometeors (*Herzog and Graf*, 2010, and references therein). In the simulations presented here, however, all those modules (besides the microphysics module) are switched off, because they do not significantly impact the plume development on the examined time and height scales.

The application of ATHAM to weak volcanic clouds has never been done before. *Oberhuber et al.* (1998) state in their conclusions that "on the small-scale end of the spectrum of possible applications [...] depressurization in the neighborhood of a crater, for instance, yields accelerations and thus a pronounced disequilibrium in all spatial directions". Note that in ATHAM the gas-particle mixture enters the computational domain at atmospheric pressure. After introducing the second numerical eruption cloud model PDAC and describing how the eruption cloud models are coupled to Qradar, I will discuss the main difficulties when using ATHAM for small scale eruptions and compare both models.

5.2 PDAC — Pyroclastic Dispersial Analysis Code

The second numerical model I used in my work is the *Pyroclastic Dispersial Analysis Code* introduced by *Neri et al.* (2003, 2D) and *Esposti Ongaro et al.* (2007, 3D). Again, all equations and assumptions are given in those two publications in full detail. Here I focus on the most important features that are needed to understand how the model works.

In PDAC, solid and gaseous components are treated as inter-penetrating continua with individual constitutive equations. The equations of mass conservation, momentum balance and energy balance (in terms of enthalpy) are solved for each component (also termed phase). Phase changes or chemical reactions are not included — the model calculation is stopped for instance if water vapor begins to condensate. The momentum balance equation includes gas-solid as well as solid-solid interactions (air drag and collisions, respectively). The energy balance equation accounts for heat transfer between gas and solid components.

For the gas-particle interaction, a stress tensor is introduced whose components describe the force vectors that result from the relative velocity of gas and particles. Those forces also depend on the local volumetric fraction of solids and the local particle Reynolds number[1]. The particle-particle interaction is introduced by an additional drag force, which describes the probability of particle collisions and their effects on the bulk motion. This drag force has been empirically defined by laboratory experiments and is accurate for particle diameters up to a few millimeters (*Neri et al.*, 2003).

Gaseous and solid phases (i.e. chemical components and ash size classes, respectively) have to be configured in advance: the number of chemical components of the gas and their respective mass fractions (weight percent of total gas mass) can be different for the background atmosphere and the vent inlet. Up to seven gas species can be used, namely: O_2, N_2, CO_2, H_2, H_2O, Air, and SO_2. Atmospheric air is considered as a single component with averaged properties. The solid phases are defined by their diameter, density and volume fraction. There is no limit on the number of solid phases. However, due to the multiphase approach, every component increases the number of coupled equations to be solved and hence increases the computation time.

PDAC has been used primarily for the simulation of pyroclastic fountains, flows and collapsing columns. Only one study has focused so far on the transition between collapsing and partly stable regimes (*Di Muro et al.*, 2004). Parametric studies on the influence of particle sizes (*Neri and Macedonio*, 1996; *Neri et al.*, 2003) and magma composition (*Neri et al.*, 1998) on the run-out distance of pyroclastic flows have been conducted as well as on the mass partition between buoyant cloud and pyroclastic flow (*Neri et al.*, 2002). Case studies for volcanic hazard and risk estimation have been conducted for Vesuvius (Italy, e.g. *Esposti Ongaro et al.*, 2007; *Neri et al.*, 2007), Campi Flegrei (Italy *Todesco et al.*, 2006), and Soufrière Hills volcano (Montserrat, West Indies, *Esposti Ongaro et al.*, 2008). For a realistic estimation of the path of a pyroclastic flow, the actual topography can be used as lower boundary condition.

5.3 Coupling ATHAM and PDAC to Qradar

The synthetic Doppler radar model (Qradar) has already been introduced in chapter 2.5.1. It consists of two main parts: (1) the ballistic transport of arbitrary particles in arbitrarily parameterized atmospheres and (2) the concurrent calculation of synthetic Doppler radar

[1]The Reynolds number is the ratio of inertial to viscous forces (*Turcotte and Schubert*, 2002). Considering a sphere moving in a fluid, the Reynolds number is given by $Re = \rho(v - v_s)2r/\mu$, where ρ and μ are the fluids density and viscosity, r is the sphere radius and v and v_s are the fluid's and sphere's velocity. A small Reynolds number indicates laminar flow, a Reynolds number larger than a critical value (> 2200 for a sphere in an unlimited fluid) indicates turbulent flow. Depending on the flow regime, the dependency of the drag (or friction) force on the relative velocity changes significantly.

spectra. Because of its modular structure, the two parts of Qradar can be used independently, which is especially useful when the calculation of particle motion is done externally by ATHAM or PDAC. The coupling of the models is simple, but not trivial. ATHAM and PDAC are written in parallel Fortran90, are highly optimized for calculation speed, and can be executed on multiple CPUs. Qradar is written in vectorized MATLAB (its first version was written in C++). Hence, a simultaneous calculation of synthetic spectra and particle motion (using ATHAM or PDAC) would only be possible by reimplementing the synthetic Doppler radar model in Fortran. The easier and faster way is to use the output files (written at discrete time intervals) as external source for the momentary particle properties and to calculate synthetic Doppler radar velocity spectra based on this information.

To calculate a Doppler spectrum, particle properties such as radius, position and velocity vector at a certain time are needed. Qradar is a Lagrangian model, which calculates for each particle (representing an entity of tracers with equal radius and density) the temporal evolution of its position and velocity. Those properties are given in the output files of ATHAM and PDAC, however in different formats. Both cloud models are Eulerian models, which calculate those particle properties in terms of concentrations (volume or mass-concentration for each predefined particle class) on a grid. Hence a conversion of grid-based concentrations to particles with spatial position and velocity is needed. Reasonably, only grid points above the topography are used. The number of particles of one size class at each grid point is used as a 'Lagrangian entity' of particles with the same properties. This means that the backscatter cross-section, which only depends on the particle size, is calculated for one particle of each class and scaled by the number of identical particles afterwards. When using a relatively coarse grid resolution of 10x10 m (compared to the radar beam cross-section of about 80 m above the vent) only a few grid points contribute to the Doppler spectra. Those few points may also show very different dynamics due to the small scale behavior of the developing plume. This leads to relatively sparse synthetic velocigrams in which contributions of individual grid points are clearly distinguishable. To overcome this issue, I implemented an optional resampling of the grid and linear spatial interpolation of all values onto the new positions in the finer grid. In the following I describe the conversion of the output values of ATHAM and PDAC separately.

ATHAM: As mentioned above, ATHAM solves the equations of motion and mass conservation for the bulk properties of the gas-particle-mixture. Liquid and solid tracers (active and passive) have to be defined beforehand, meaning their properties like radius and density are constant and known. For every predefined tracer i, the output files contain information on the respective mass-concentration q_i and vertical velocity anomaly w_i relative to the bulk velocity $\vec{v} = (u, v, w)$, which is also provided together with the bulk density ρ and temperature T. Note that the bulk temperature is equal to the gas and particle temperature at all times, because thermal equilibrium is always assumed. In addition, ATHAM provides the pressure anomaly relative to the layered atmospheric pressure. All these values are given for each grid point at distinct time intervals. Because ATHAM has a dynamic time stepping scheme[2] the output files may not be equidistant in time. Output files are generated, when the current time at the end of a time step is larger than $n \times dt_{plot}$, where n is the consecutive number of the output-file and dt_{plot} is a predefined time interval for data output.

For every grid point above the topography, a number of particles N_i of the respective class i is obtained by dividing the total mass of the respective particle class (Mq_i) by the mass of one particle m_i

$$N_i = \frac{V_{\text{cell}}\,\rho\,q_i}{m_i}$$

where V_{cell} is the cell volume associated with the respective grid point and M and ρ are the total mass and bulk density at that same point. The velocity vector $\vec{v_i}$ of the N_i particles at this position is simply given by:

$$\vec{v_i} = (u, v, w - w_i)$$

The specialty of ATHAM is the microphysics module, where the phase changes of water (vapor, ice, snow and hail) are calculated. Those water phases are active tracers and their concentration and velocity anomaly are given as well. Note that water phases have highly varying reflection characteristics that also significantly differ from ash reflection parameters. Therefore we can use or neglect those wet tracers in the calculation of spectra to get an idea of the importance of rain droplet and ice dynamics in the Doppler radar data of the eruption cloud. The complex refractive index of water is 22.5+32.13i (*Meissner and Wentz*, 2004), of ice 3.155+0.002i (*Koh*, 1992), and that of ash 2.458+0.02197i (*Adams et al.*, 1996). The sizes of water droplets and snow/hail are predefined to be equal to the size of fine ash (15 μm).

PDAC: In PDAC, volume concentrations of the predefined particle classes are given for every grid point. Because solids and gases are separately treated in the multiphase flow algorithm, particle temperatures and three-component velocity vectors exist for each solid phase. The conversion of volume concentrations ϵ_i to number of particles is done using the particle's volume $V(r_i) = 4/3\pi r_i^3$:

$$N_i = \frac{\epsilon_i V_{\text{cell}}}{V(r_i)}.$$

5.3.1 The Modeled Gas Flow Field as Background Atmosphere

ATHAM and PDAC only account for very small particle radii up to 0.5 and 2.5 mm, respectively. However, night-time videos of incandescent material and long-time exposures show that weak vulcanian plumes also incorporate larger, ballistically moving particles, so incorporating large particles would be desirable. The early version of Qradar calculated the

[2] ATHAM adjusts the time step length dt for the next time step based on the current maximum ratio of grid resolution and velocity (Courant-Friedrichs-Lewy condition, CFL condition, *Courant et al.*, 1928).

trajectories of arbitrary sized particles in a parameterized atmosphere. This atmosphere can easily be replaced by the gas flow field calculated by ATHAM or PDAC, which are more realistic approximations of gas jet velocity and buoyant updraft and even account for turbulence. However, using the gas flow fields of ATHAM or PDAC as background atmosphere is still an approximation to reality as it is based on the assumption that the larger particles do not affect the gas flow, which is probably only a good zeroth order approximation.

The atmospheric properties, required for additional particle transport are: gas velocity field $\vec{v_g}$, gas viscosity η, and gas density ρ_g. Neither ATHAM nor PDAC provide gas viscosity or density, but both values can be obtained from other values. The viscosity mostly depends on the gas temperature T_g (*Meschede*, 2002), which is provided in both models.

$$\eta = \eta_0 \sqrt{\frac{T_g}{T_0}} \qquad \text{with} \qquad \eta_0 = 1.74 \times 10^{-5}\,\mathrm{Pa\,s} \qquad \text{at} \qquad T_0 = 273.15\,\mathrm{K}$$

The gas density can be calculated (in ATHAM) from the bulk density ρ and the mass fractions q_i and densities ρ_i of the solids:

$$\frac{1}{\rho_g} = \frac{1}{\rho} - \sum_i^{n_{solid}} \frac{q_i}{\rho_i}$$

or the ideal gas law weighted with the gas mass fractions y_i and the gas molecular weights m_{gmw}:

$$\rho_g = \frac{P_g}{RT_g} \sum_i^{n_{gas}} y_i m_{gmw}$$

Note that the gas mass fractions in PDAC are relative to the total gas mass, i.e. they sum up to one, whereas in ATHAM the mass fractions for gaseous tracers are normalized to the total mass of solids, liquids and gas.

5.3.2 Spatial Resolution: The Missing Dimension

Both cloud models exist in a 2D and 3D version. Here I use the 2D cylinder-coordinate version of both models to keep them comparable and simple, and to reduce the time needed to compute results. As mentioned above, ATHAM calculates a 2D slice, in which the vent is positioned in the center so that no nearby boundary conditions can influence the vent near dynamics. PDAC makes use of the problem's symmetry and positions the vent at the left boundary, which is defined as a symmetry boundary with free slip in the vertical direction and no horizontal flux allowed.

The Doppler radar measurement is a 3D measurement, because the along-beam component of the three-dimensional velocity vector of each particle inside the beam volume contributes to the signal. Essentially, the velocity spectrum is a weighted histogram of the measured velocities, in which the weight is the back-scatter cross-section of each particle.

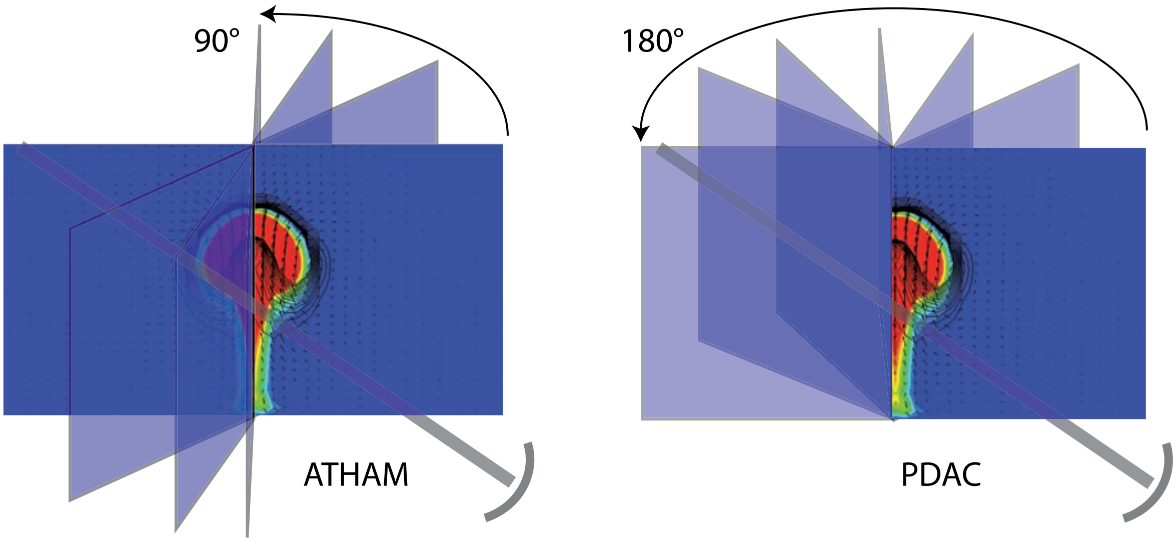

Figure 5.1: Schematic drawing of how a cylinder-coordinate 2D model domain is converted into a three dimensional volume before being used with Qradar. In ATHAM, the relative angle between radar beam and 2D slice has to be varied between 0 and 90°, and all slices between those end-members contribute twice. In PDAC, the angle has to be varied between 0 and 180°, because the 2D slice only covers half of the ATHAM-slice.

Producing a velocity spectrum with the Doppler radar being aligned with the slice gives a significantly different spectrum than if the radar beam is perpendicular to the slice. Nevertheless, both spectra can be calculated and summed up. Because the slice is a profile through a radial-symmetrical 3D-velocity field in which the symmetry axis is one boundary (PDAC) or the middle axis (ATHAM), all relative angles between the synthetic radar beam and the 2D slice have to be accounted for in order to calculate a spectrum for the associated 3D volume. Since only the angle between slice and beam is important for this calculation, and arbitrary radar locations are already considered in Qradar, I account for this issue by rotating the radar location around the volcano rather than rotating the slice.

Fig. 5.1 illustrates the range of relative angles, for which synthetic spectra need to be calculated. Because the Doppler radar does not measure horizontal velocity components that are perpendicular to the radar, it does not discriminate whether a particle moves right or left of the vent. Hence all spectra can be used twice, with the exceptions being, when beam and slice are aligned (PDAC and ATHAM) or perpendicular to each other (ATHAM). A sensitivity test showed that a 10° increment between radar positions is sufficient to avoid artifacts caused by the relative rotation of radar position and slice. This results in a 9-step rotation in case of a slice produced by ATHAM and 18 steps for PDAC runs, respectively.

5.3.3 Time Resolution: Discrete Output Files

The Doppler radar measurement is an integrating measurement, not a snapshot of the dynamics. Using the output files, which essentially are shapshots, poses the question whether the measured and the synthetic data will be comparable. A simple solution is to use linear

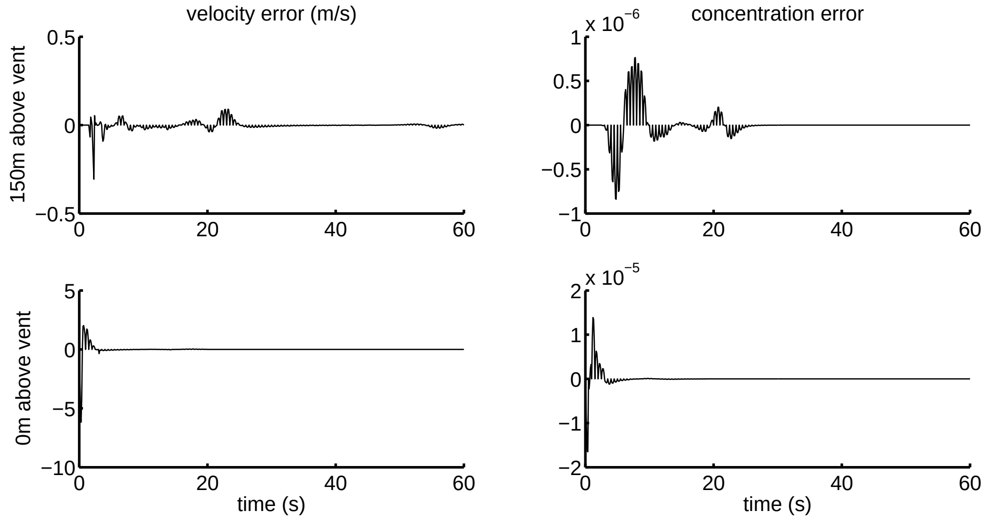

(a) possible error in particle velocity (left) and volume concentration (right) at different heights above the vent

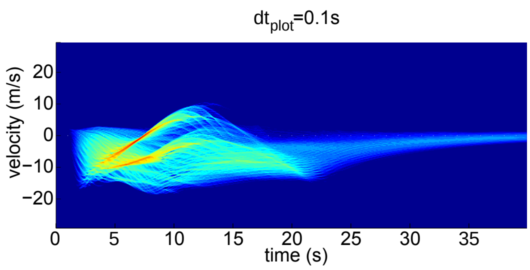

(b) velocigram of high temporal resolution

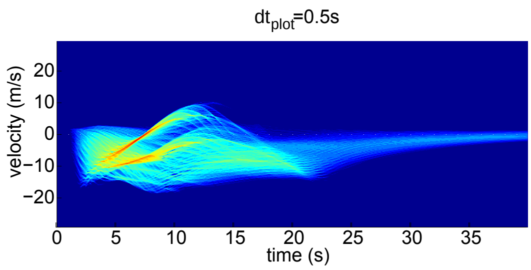

(c) velocigram of low temporal resolution

Figure 5.2: (a) Differences in velocity (left) and concentration of fine ash (right) at two different heights above the vent are calculated by (1) a linear interpolation of the low temporal resolution output files ($dt_{plot} = 0.5\,\mathrm{s}$) to a five times higher time resolution and (2) subtracting these values from the high temporal resolution output files ($dt_{plot} = 0.1\,\mathrm{s}$). (b) and (c) show the velocigrams using the high temporal resolution output files (b) and the low temporal resolution output files (c). The color scale for echo power is the same as in Fig. 4.6 (p. 72).

interpolation again, now in time rather than space, to fill the gap between consecutive output files. Qradar then calculates spectra for a much higher sample rate than that predetermined by the number of output files.

In Fig. 5.2 two identical PDAC runs are compared that only differ in the output time interval. Note that this is different from simply applying a skip value at plotting due to the non-uniform time stepping and the non-equidistant output files. From the profiles it is obvious that the use of linear interpolation is valid in the later stages of the simulation, when the changes in velocity are small. At the beginning of the eruption, a linear interpolation between output files might not capture the highly emergent velocity changes. However, the respective velocigrams look similar. Using an even coarser output interval results in visible differences (not shown). Hence the output interval of all runs is set to $dt_{plot} = 0.5\,\mathrm{s}$.

5.4 Discussion — ATHAM versus PDAC

A comparison of two numerical models, which are based on the same physical process (multiphase flow) but have very different numerical approximation strategies is a first step towards cross-validation. A first comparison has been done by *Neri et al.* (2003) (although they did not explicitly name any other numerical model). They tested whether the assumption of thermal and dynamic equilibrium in the cloud are valid and found that in regions of significant entrainment of air a thermal non-equilibrium between gaseous and solid phases develops with temperature differences of up to 80°C (*Neri et al.*, 2003). In addition, the slip velocities (velocity difference between gas and particle) are significantly smaller than the terminal fall velocities due to the additional consideration of particle-particle drag and the viscous and pressure terms in the momentum equations (*Neri et al.*, 2003). In regions of high density the particle-particle drag dominates the gas-particle drag and hence the assumption of dynamic equilibrium may not be appropriate for the beginning of an eruption. From this study it is questionable if weak volcanic clouds can be simulated accurately in ATHAM.

Neither of the models includes fragmentation and development of ash aggregates — which have been found to occur during ash transport (*Wohletz et al.*, 1989) and fall-out (see *Bonadonna and Phillips*, 2003, and references therein) — because only a limited number of prescribed particle sizes can be used in the simulation. Nevertheless, the effects on the initial cloud dynamics investigated here should be small. Phase changes (e.g. water vapor condensation) are calculated in ATHAM but not in PDAC. Hence the release or consumption of latent heat, which may influence cloud height is only captured in ATHAM model runs. In addition, a particle deposition scheme only exists in ATHAM. In PDAC all particles remain 'fluidized' (in solution) at all times (as a consequence of mass conservation), which may significantly affect the run-out distances of pyroclastic currents. Nonetheless, particle deposition is of minor importance in the development and rise of eruption clouds.

5.4.1 Using Identical Boundary Conditions

A qualitative (and quantitative) comparison of two numerical models requires the use of identical boundary conditions. In this study I use the same mesh and topography profile for both models to ensure that differences caused by interpolation are minimized (see Fig. 5.3). The topography profile is extracted from the DEM of the area around Colima volcano (*USGS*, 2004a; *Farr et al.*, 2007) and extends from the volcano top to the South towards the Doppler radar (see Fig. 4.1b). The vent radius is set to $r_v = 30\,\mathrm{m}$. On photographs of eruptions (not shown here) it can be clearly seen that for the smaller eruptions the crater with a diameter of 300 m is significantly wider than the jet region feeding the plume. The inlet profile (i.e. the horizontal profile across the vent) is fixed for ATHAM, where the bulk velocity decreases quadratically towards the vent edges:

$$w(dx) = w_0 \left(1 - \left(\frac{dx}{r_v}\right)^2\right)$$

with dx being the radial distance between grid point and vent center, w_0 is the predefined centerline velocity (see Tab. 5.1) and $w(dx)$ the bulk velocity at the respective grid point. In PDAC, the profile is defined by

$$w_i(dx) = w_{i0} \times r_w \left(1 - \left(\frac{dx}{r_v}\right)^{\frac{1}{r_w - 1}}\right),$$

where $w_i(dx)$ are the gas or solid velocity at the respective grid point, which depend on the use of the predefined gas or solid velocity w_{i0} (see Tab. 5.1). r_w is the ratio between the maximum (centerline) and the average vertical velocity w_{i0} over the vent. Using $r_w = 1.5$ results in identical velocity profiles given w_{i0} is adjusted appropriately (see Tab. 5.1). Given that particles in ATHAM are in dynamic equilibrium with the surrounding gas, they leave the vent with their terminal settling velocity with respect to the gas velocity. This velocity deviation is accounted for in the definition of the solid phases velocities in PDAC to achieve identical at vent particle velocities in both models.

As both numerical models are capable of calculating several gaseous as well as solid phases, the same particles and volatiles have to be configured. Because of the more stringent limitation of particle size in ATHAM than in PDAC, a maximum particle size of 0.5 mm radius is assumed. Those particles are herein further referred to as lapilli. Two additional particle sizes of 0.015 mm (fine ash) and 0.1 mm (coarse ash) are used and the gaseous components are H_2O, SO_2 and Air. Note that solid phases in PDAC are defined by their diameter rather than their radius (ATHAM).

Another complication results from ATHAM using mass fractions for all tracers (gaseous and active incompressible tracers) and PDAC using volumetric fractions for solid phases and an average mass fraction for gas components (mass fractions of gaseous phases must sum up to one). The conversion of mass concentrations q_i to volume concentrations ϵ_i can be done using the individual density of the phases ρ_i and the bulk density ρ

$$\epsilon_i = \frac{q_i}{\rho_i}\rho$$

The bulk density is given by

$$\frac{1}{\rho} = \sum_{i=solid} \frac{q_i}{\rho_i} + \frac{\sum q_g}{\rho_g}$$

Here q_g are the volume concentrations of the gaseous tracers and ρ_g the gas bulk density at the vent. The used concentrations and velocities are listed in Table 5.1.

As this study focuses on transient weak plumes the boundary conditions at the inlet (also

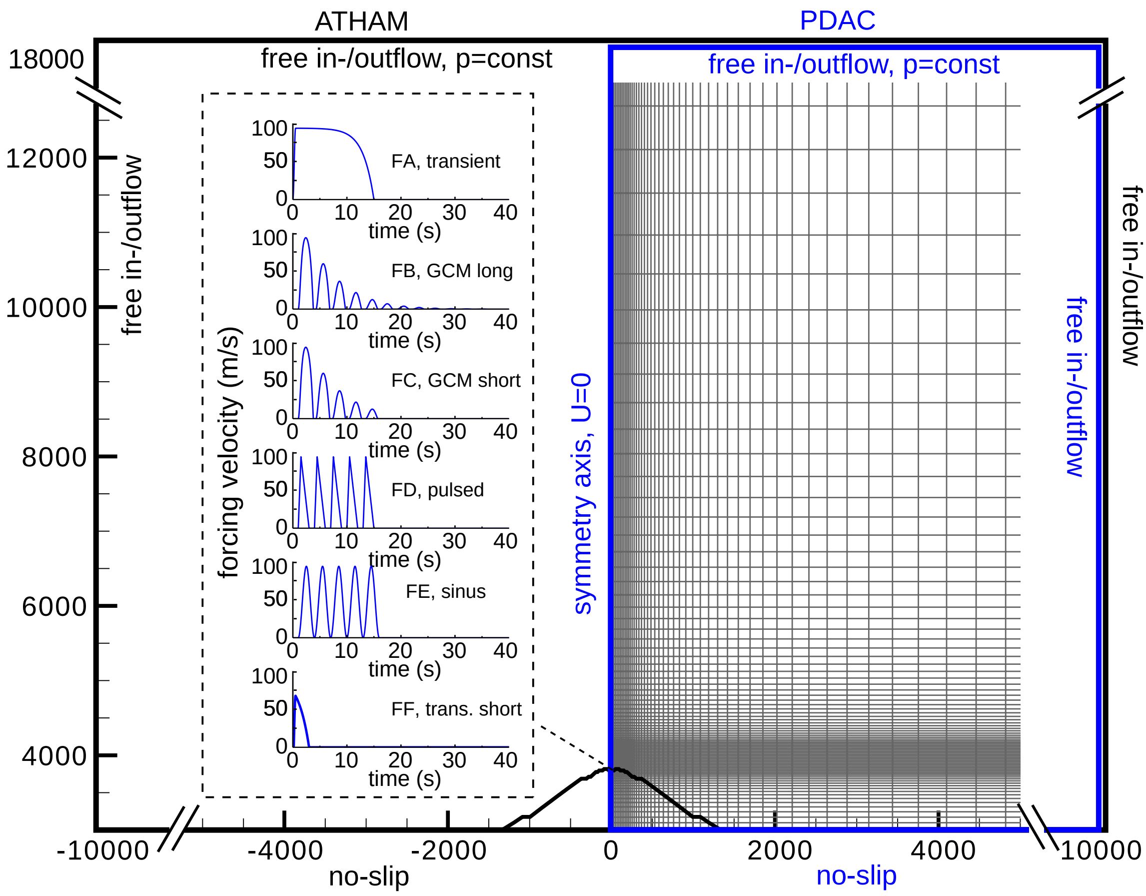

Figure 5.3: Boundary conditions for all numerical experiments with ATHAM (black box) and PDAC (blue box). The mesh is shown for the non-uniform part and it is identical in both numerical models. The extension in horizontal and vertical direction is done by adding cells of the maximum cell size. ATHAM calculates both sides of the 2D axis-symmetric problem to avoid the implementation of a symmetry boundary condition above the vent. Note that the grid is only shown for the right side and is identical for the left side. The boundary conditions for both models are fixed at the grid boundaries (black = ATHAM, blue = PDAC). The inset (dashed box) shows the six different volcanic inlet conditions applied in this study. A change in inlet mass flux is realized in both numerical models by changing the bulk velocity.

referred to as forcing) are time-dependent. I have implemented several forcing functions as lookup tables into both models (see Fig. 5.3 and Tab. 5.1). The forcing is achieved by modulating the centerline velocity as a function of time, because the mass flux $\dot{m}$ directly depends on the velocity v:

$$\dot{m} = A\rho v. \tag{5.1}$$

Note that currently neither ATHAM nor PDAC provide the possibility to change the vent area A (caused by crater erosion) or the bulk density ρ (as a consequence of a possible change in gas-mass fraction) during a simulation.

Table 5.1: Parameters defining the forcing for the model runs used in this study. Combinations of parameters are referred to in the text as e.g. PB-VC-FE, which for this combination means: Only small particles were used with slow initial velocities (50 m/s) and a sinusoidal forcing that modulates the initial velocity between zero and maximum for a duration of 15 s.

		ATHAM	PDAC
Particle Size Distributions		`voltrac(1:3)`[a]	`ep_solid(1:3)`[b]
PA	intermediate	0.16, 0.61, 0.16	0.155e-3, 0.592e-3, 0.155e-3
PB	only fine ash	0.93, 0, 0	not used
PC	more mass	not used	0.0023, 0.0086, 0.0023
Initial Velocity		`volvel`[c]	`w_gas; w_solid(1:3)`[d]
VA	100 m/s	100	67.0; 66.4, 65.5, 63.7
VB	150 m/s	150	100.0; 99.4, 98.5, 96.7
VC	50 m/s	50	33.0; 32.4, 31.5, 29.7
Forcing,see Fig. 5.3		duration	(same for both)
FA	transient	15 s	
FB	gas cushion model (long)	35 s	
FC	gas cushion model (short)	15 s	
FD	pulsed	15 s	
FE	sinus	15 s	
FF	transient short	3 s	

[a] Mass concentrations q_i for r=0.015, 0.1, 0.5 mm; Gas components are H_2O=0.05, SO_2=0.01, and Air=0.01. `voltrac` is the key word for q_i in the configuration file.
[b] Volume concentrations ϵ_i for d=0.03, 0.2, 1.0 mm; Gas components are H_2O=0.7, SO_2=0.15, and Air=0.15. Note that PDAC requires mass fractions for gaseous phases and the closure relation requires that they sum up to 1. `ep_solid` is the key word for ϵ_i in the configuration file.
[c] ATHAM uses the bulk velocity for forcing (assuming dynamic equilibrium, Key word `volvel`)
[d] Note that PDAC uses the average velocity over the input profile, whereas ATHAM uses the maximum (centerline) velocity as input. The given values result in comparable input velocity profiles over the vent (Key words `w_gas` and `w_solid` for gas and solid's velocity).

For conducting a numerical study, one has to compromise between accuracy (in terms of resolution in time and space) and computing time. The latter can nowadays be decreased easily by the use of very fast CPU's and parallel computing (e.g. MPI). Unfortunately, neither ATHAM nor PDAC have a parallel version for 2D axis-symmetric simulations as their parallel versions are restricted to fully three-dimensional problem types. Accuracy can be increased by smaller time steps (increasing computing time due to more iterations) and/or finer grids (increasing computing time due to more degrees of freedom).

The Courant-Friedrichs-Lewy criterion (CFL-criterion, *Courant et al.*, 1928) defines a relationship between grid resolution and time step length and is a criterion for numerical stability. It states that the time step must be smaller than the ratio of minimum grid resolution and maximum speed. Therefore a finer grid also requires more time steps and both together significantly increase computing time. Numerical diffusion on a too coarse grid can transport physical properties at an artificially high rate, which can lead to non-physical thermal, velocity, and concentration fields. The minimum grid resolution and time step can hence be found by testing whether the results of model runs with decreasing grid resolution converge to the same solution. These tests and the corresponding results are given in the next two sections for ATHAM and PDAC separately.

5.4.2 ATHAM — Minimum Grid Resolution and Maximum Particle Size

Weak volcanic clouds are transient small-scale phenomena, which require a high resolution in time and space. Unfortunately, in ATHAM the assumptions of dynamic and thermodynamic equilibrium counteract the numerical stability criterion in the definition of minimum grid resolution and maximum particle size. The numerical stability criterion (CFL condition, see above) defines the maximum possible time step as the time that a particle needs to cross its grid cell. A grid resolution of 20 m at the vent and the initially high exit velocity of the mixture, e.g. 100 m/s, result in a maximum time step of 0.2 s. The thermodynamic equilibrium assumption, however, defines a maximum particle size for which heat can be transported from the particle's center to its surroundings (characteristic diffusion length scale $l = \sqrt{\kappa t}$, *Turcotte and Schubert*, 2002) during the time step. A typical value for the thermal diffusivity κ of rocks is $10^{-6}\,\mathrm{m}^2/\mathrm{s}$. Therefore the maximum particle radius that can be treated accurately (by means of thermal equilibrium) is about 0.45 mm. In ATHAM larger particles would be assumed to cool too rapidly so that too much of their internally stored thermal energy adds to the thermal energy of the wet ash-gas-mixture leading to enhanced buoyancy.

The dynamic equilibrium requires that the acceleration phase of a particle in response to gravity or a change in gas velocity is small compared to the time step size. In ATHAM, particles are assumed to always travel with their terminal fall velocity. Hence, if particles are large and their acceleration takes long, they are transported along the grid with a wrong velocity. In Fig. 5.4 the acceleration phase of differently sized particles is plotted. It is assumed that the gas velocity increases instantaneously at the beginning of the time step from 1 m/s to 2 m/s in (a) and (b) and from 1 m/s to 10 m/s in (c) and (d). In the left diagrams a purely vertical motion is assumed and gravitational acceleration is considered. Hence the particles get accelerated towards their terminal fall velocity relative to the gas. In the right diagrams, gravity is set to zero and hence those calculations are valid for the horizontal velocity component, where the particles are assumed to move with the gas. It is obvious, that very small particles ($r < 0.05$ mm) reach their prescribed velocity (terminal fall velocity for vertical and gas velocity for horizontal motion) within a fraction of a second and hence within the hypothetical time step of about 0.2 s. For the velocity of larger particles ($r > 0.5$ mm), however, significant deviations from their velocity assuming dynamic equilibrium

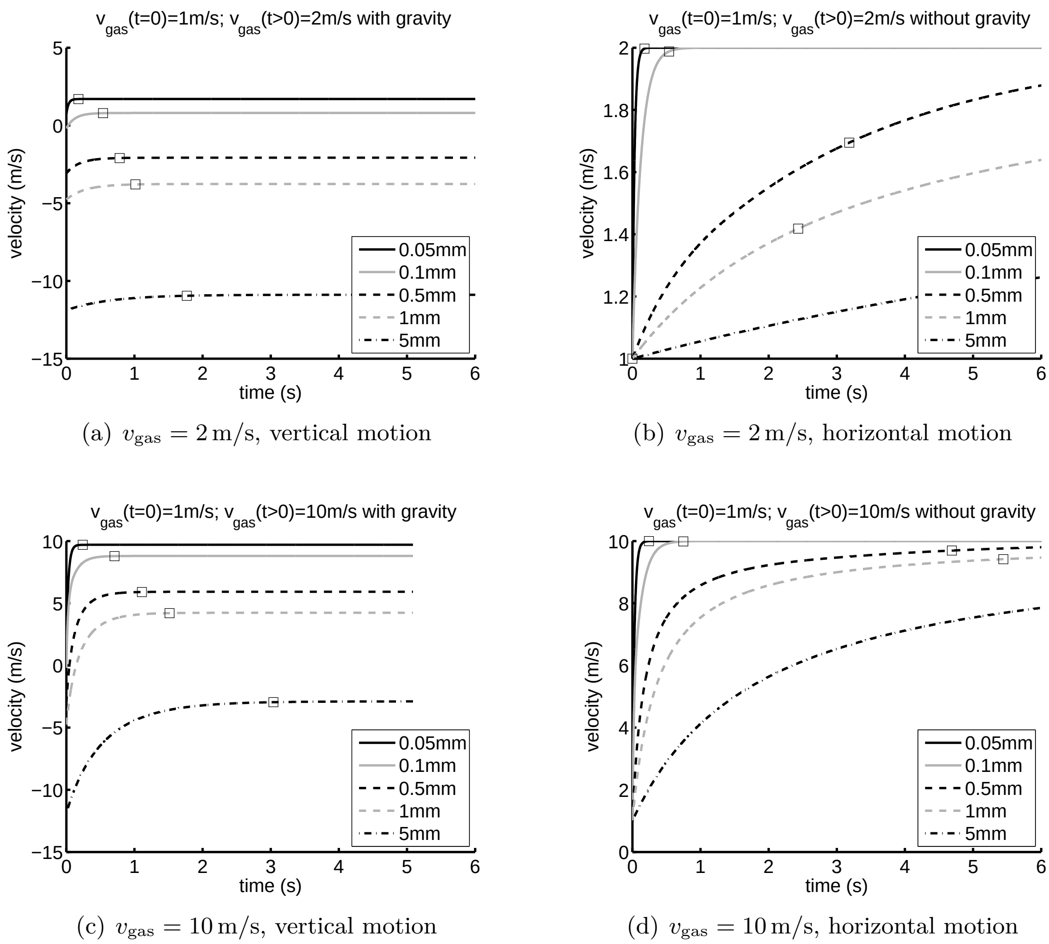

(a) $v_{\text{gas}} = 2\,\text{m/s}$, vertical motion

(b) $v_{\text{gas}} = 2\,\text{m/s}$, horizontal motion

(c) $v_{\text{gas}} = 10\,\text{m/s}$, vertical motion

(d) $v_{\text{gas}} = 10\,\text{m/s}$, horizontal motion

Figure 5.4: Velocity evolution of particles moving in a steady gas flow. All particle sizes are particle radii. The particles are initially moving with their terminal fall velocity (for vertical motion, a and c) relative to the gas or with the initial gas velocity (horizontal motion, b and d) of 1 m/s. The gas speed instantly increases to 2 m/s (a and b) or 10 m/s (c and d) and the particles get accelerated by the gas-particle drag force. The time, when the acceleration of a particle decreased to values $<0.1\,\text{m/s}^2$ is marked by a square on each line.

occur. The particle's response to a suddenly increased gas velocity is quite intuitive: The larger the difference between particle and gas velocity, the longer takes the acceleration phase. Interestingly, there is a large difference between horizontal and vertical acceleration of particles. In the vertical case, the acceleration of particles is the sum of gas-particle interaction and gravity, and hence is higher than in the horizontal case, which is why particles reach their final velocity earlier when moving only in vertical direction (compare Figures 5.4(a) and (b)). From Fig. 5.4 it is obvious that larger particles (>0.1 mm) should not be used in combination with small time steps (<1 s), thus small grid spacing. The above estimate for a maximum time step based on the chosen minimum grid resolution of 20 m directly at the vent leads to the maximum accurately treated particle size of $r < 0.1\,\text{mm}$, which is very fine ash. From these estimates I conclude that a calculation of weak volcanic clouds using ATHAM has to be done with care.

I conducted a resolution test (Fig. 5.5) in which three different grid sizes are compared. The coarsest grid (left column) has a resolution of 20x20 m near the vent and finer grids were obtained by splitting every coarse cell into four cells (i.e. 10 m resolution, middle column) and 16 cells (i.e. 5 m resolution, right column). In the coarse grid the highest resolution near the vent is constant for 200 m horizontal and 400 m vertical distance. Beyond, the grid cells grow by a factor less than 1.1 until the maximum grid resolution of $dx = 360$ m and $dz = 580$ m is reached at $x = \pm 5$ km and $z = 10$ km. Note that the same grid has been also used for the PDAC resolution tests (see next chapter and Fig. 5.7). Only fine ash (0.015mm) was used to ensure dynamic equilibrium for all grid sizes. The fine ash has a mass concentration of 0.93 at the vent and the remaining void fraction is filled by H_2O (0.05), SO_2 (0.01) and Air (0.01). All boundary conditions are given in Fig. 5.3 and Tab. 5.1.

Figure 5.5 shows snapshots at characteristic stages of the cloud evolution and the time since the onset of the eruption is given in each figure. Stage 1 (top row) shows the detachment of the upper half of the vortex structure (two separate dark red regions, hard to see). In stage 2, the plume detaches from the ground (two separate regions of fine ash content) and in stage 3 (third row) the centerline temperature decreased below 400 K.

Despite many similarities between the three calculations there exist some major differences in the temporal evolution of the clouds and the cloud structure. The coarsest grid (20x20 m at the vent, left column) produces a very diffuse plume that cools quickly (due to numerically enhanced thermal diffusion). The structures and timing significantly differ from the results of the finer grid runs (middle and left column). The finer the grid, the more constrained is the plume and the earlier the mushroom-shaped plume structure develops because stronger velocity gradients can be resolved. The buoyant updraft, which solely depends on the bulk density of the plume, is stronger in the coarse model and the first particles reach heights of 4800 m about 10 s earlier than in the fine grid run. An interesting feature of the fine grid run is that the particle concentration is not homogeneous in the plume tail. Instead small convection cells develop.

The differences in cloud evolution are also visible in the synthetic velocigrams (bottom row in Fig. 5.5), which have been calculated for each model for the entire duration of the simulation (arrows atop the velocigram mark the times at which the 3 stages take place). The three velocigrams show similarities and differences: The eruptions all start with a large range of velocities, however, the maximum negative velocities differ. In addition the maximum negative velocity increases (meaning the absolute value increases[3]) for 10 s in the coarse grid run (between 5 and 15 s), whereas it decreases in the same time period in the fine grid run. The overall velocity decrease afterwards, between 15 and 20 s, is less pronounced for the coarse grid run.

[3]Note that I use the terms increasing and decreasing to describe the evolution of the absolute value of the along-beam velocity. In this sense, an increase in negative velocity hence means that the absolute value, rather than the value itself increases. I use the terms of acceleration and deceleration in a slightly different way: acceleration and deceleration are defined for the increase and decrease of the true velocity of a particle. This means that in the case of acceleration the along-beam velocity (for the Colima setup) decreases (for positive velocities, i.e. falling particles) and increases (for negative velocities, i.e. rising particles).

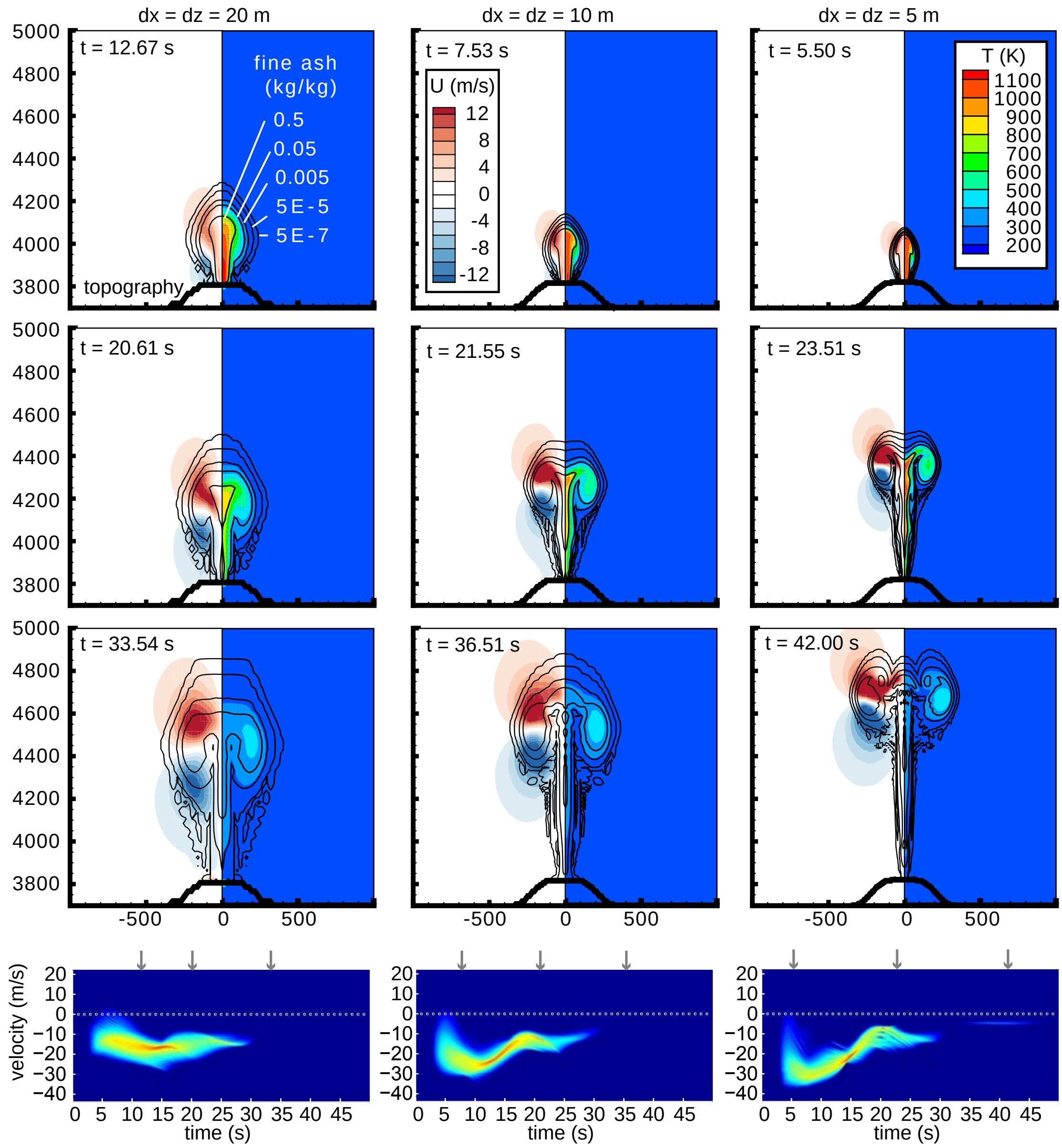

Figure 5.5: Snapshots and synthetic velocigrams of three ATHAM runs with varying grid resolution (all PB-VA-FA, see Tab. 5.1). The grid extends 10 km radially and 15 km vertically in all cases. The mesh resolution is described in the text. The snapshots show the horizontal bulk velocity on the respective left (red corresponds to outward, blue to inward velocities), and the gas temperature (colors) on the respective right side of each diagram. The light contours show the concentration of fine ash ($r = 0.015$ mm). The color bars in the upper row diagrams are the same for all plots. The thick black line depicts the topography. For each run, three snapshots are shown each representing a characteristic feature of the dynamics. Note that those features do not occur at the same times. In the upper row, the outward motion at the plume head is separated from the at vent outward motion for the first time (dark red contours separated). The second row shows the detachment of the fine ash rising in the plume from the ground. In the third row, the plume temperature has decreased significantly caused by vigorous convective entrainment. The bottom row shows the corresponding synthetic velocigrams. The measurement geometry is the same as in the Colima experiment (see Fig. 4.1). The FOV extends roughly between 3900 and 4000 m with the Doppler radar aiming into the cloud from below at an angle of 31° to the horizontal. The gray arrows mark the times of the corresponding snapshots. The color scale for echo power is the same as in Fig. 4.6.

The observed large range of velocities at the beginning of the event (left of the first arrow, Fig. 5.5) can be explained by the plume head crossing the FOV, where horizontal velocity components are large (see Fig. 2.8 and Fig. A.4). Behind the plume head (right of the first arrow) the particle motion is constrained to a more vertical direction and the velocity band becomes narrower (for the intermediate and fine grid). At the first arrow (time of the first snapshot), no positive velocities (towards the radar) are measured, i.e. the upward directed jet dominates the motion and the plume head has left the FOV to the top.

The difference between the initial maximum negative velocity and the subsequent increase or decrease is caused by the strong velocity gradient between jet and atmosphere, which is only crudely resolved by the coarse grid. Above the vent the strong velocity gradient between the centerline and the surroundings of the jet (at ± 2 grid points) cannot be resolved and hence the jet becomes too slow. A fine grid better resolves the flow in the jet region (± 4 grid points wide) and the centerline velocity is faster. In addition, entrainment in the plume center is reduced so that buoyant updraft is delayed (second arrow). The acceleration of particles and especially the absence of a deceleration phase in the coarse model supports the finding that entrainment and hence buoyancy development is enhanced by the coarse grid. At the third arrow, only the highest resolution model has retained enough fine ash in the FOV to produce a measurable echo power. Interestingly, no falling particles (positive along-beam velocities) can be observed in these model calculations.

From timing, plume structure and velocigrams it appears that the difference between the intermediate and coarse grid runs is significantly larger than between the fine and intermediate grid runs. The important dynamical features (strong deceleration and secondary acceleration phase, between 15–25 s) are captured by the 10 m and 5 m grid runs. Hence a 5 m-grid should be used for the calculation of plumes, but it may also be sufficient to use a 10 m-grid to save computing time.

Resolution is not the only important grid-defining variable that needs to be tested. Total box height and width are also very important as the interaction of the multi-phase flow and domain boundaries may produce artifacts, which should be avoided, or at least known and discussed. In Fig. 5.6 the pressure differences in three model runs with varying box width are shown. The grids with a larger radial or vertical extend were built by extending the coarse grid discussed above by adding coarse cells until the respective distance was achieved. In the left diagram, the difference of a 10 km wide to a 5 km wide box is shown for pressure at different heights as a function of time. The right diagram shows the differences between a 20 km wide and a 10 km wide box. The most prominent deviation, a negative pressure pulse at 30 s (left) and 63 s (right) occurs at all heights of the small box almost at the same time. The timing indicates that the initial pressure wave (exerted by the sudden injection of particles) is reflected at the lateral boundary of the smaller domain. The initial pressure disturbance travels through the atmosphere as a (infra-)sound wave at the speed of sound ($\sim 330\,\mathrm{m/s}$) and an amplitude decay of $1/r$. Thus, the larger the extend of the box (vertically and horizontally), the longer the travel time and the lower the amplitude of the

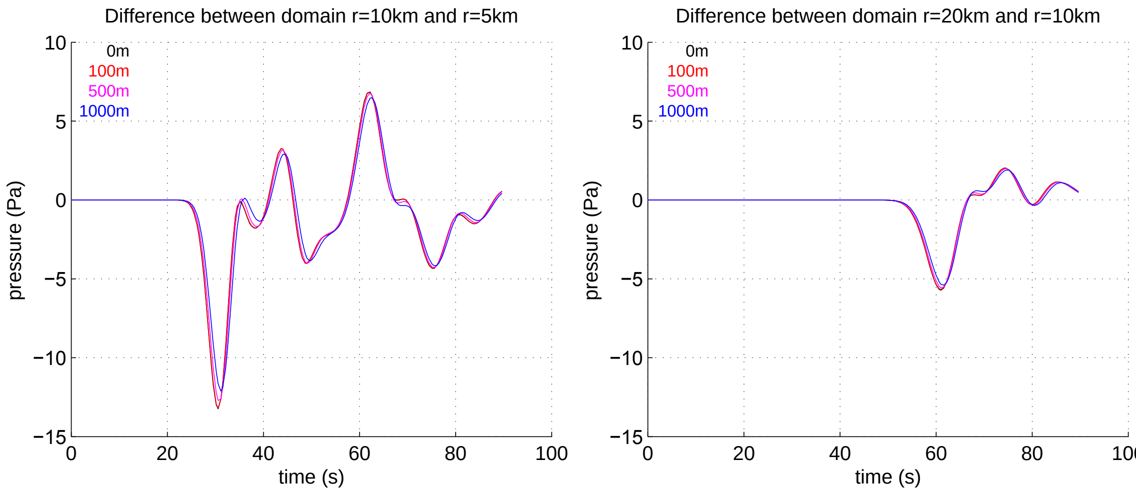

Figure 5.6: Pressure residuals as a function of time at different heights (color coded). The residual is defined as the difference between two pressure values (same time and height) of different model runs with varying horizontal grid extend (or box width). Three model runs (5 km, 10 km, and 20 km) are compared. a) Pressure residual between a box width of 5 km and 10 km. b) Pressure residual between a box width of 10 km and 20 km.

reflected pressure wave, which is an artifact that might disturb the flow — especially for the small-scale eruptions studied here. The secondary pulse at 63 s in the left diagram (positive amplitude) corresponds to the reflected pressure wave traveling in the 10 km-wide box. Note that timing and amplitude, although with the opposing sign, are the same for the secondary pulse in the left and the first pulse in the right plot.

The same findings are true for the vertical extend of the box. Artifacts caused by pressure wave reflection occur later and their amplitude is reduced for larger boxes. From this test I conclude that a box of 10 km horizontal and 20 km vertical extent is large enough to compromise between potential artifacts caused by a reflected pressure wave and computing time, which depends on the number of grid points. After 60 s cloud formation of small eruptions has taken place and the amplitude of the reflected pressure wave is small compared to the pressure gradients in the cloud.

5.4.3 PDAC — Minimum Grid Resolution

In PDAC, the grid resolution is only constrained by the CFL-criterion (*Courant et al.*, 1928) for numerical stability, which means that the travel distance of the fastest particle in one time step must be smaller than the corresponding grid cell. Because the highest resolution is fixed typically near-vent to resolve the highly energetic flow, and the highest velocities occur most probably also directly at the vent, a grid resolution of 5 m and an initial velocity of 100 m/s requires a time step of $dt < 0.05$ s, which is still larger than the manually set time step of 0.01 s. Nevertheless, using such a high resolution requires a large number of grid points, because the domain needs to be large in horizontal and vertical direction to avoid boundary artifacts caused by pressure wave reflection (see above). A comparison of three runs where only the horizontal extend of the grid was varied (5 km, 10 km and 20 km), showed the same reflected pressure wave as in ATHAM. In the larger boxes the pressure amplitude decays to 0.05% and can hence be neglected. Therefore a grid of 10 km radial extend and 20 km vertical is large enough and further used in this study.

In Fig. 5.7 the difference between calculations of 20 m, 10 m, and 5 m at-vent-resolution are shown. The grid is the same as used in Fig. 5.5 (10 km horizontal, 3–18 km vertical coverage) but the injected particle sizes differ. Here three particle sizes are used ($r = 0.5, 0.1, 0.015$ mm, PB in Tab. 5.1), because no dynamical equilibrium is assumed in PDAC. The snapshots in Fig. 5.7 correspond to the detachment of the upper vortex structure (separated red regions in the upper row), the detachment of the ash loaded plume (second row) and the appearance of several small vortex structures in the plume tail (third row), which are reminiscent of a Kármán vortex street.

It can be seen in the synthetic velocigrams (lowest row) that the main features identified above (wide range of initial velocities, deceleration after the end of forcing and secondary acceleration caused by buoyancy) are reproduced by the PDAC runs. The most prominent difference between the ATHAM and PDAC model runs are the overall higher maximum velocities and much higher echo power, which result from the usage of larger particles in the PDAC runs (PB in ATHAM versus PA in PDAC, see Tab. 5.1). A difference between the PDAC runs is the lack of a secondary acceleration phase in the coarse grid run compared to the finer grids (acceleration between second and third arrow). This can be explained again by the number of grid points that represent the vent and attain an influx boundary condition and the fact that PDAC imposes a rim around the vent to simulate a crater. In the 20 m grid, only one additional grid point (in every direction from the vent center) belongs to the vent and the 'crater rim' is 20 m high (constrained by the grid resolution). This crater rim promotes the upward motion and hence the shape of the developing plume significantly differs from the the higher resolution models, in which walls are only 10 m and 5 m high. As a consequence of this enhanced upward flow, buoyancy develops above the FOV in the coarse grid model (no secondary acceleration phase). The second prominent and very important difference to the ATHAM runs in Fig. 5.5 are the slow but constant positive velocities that indicate that in the PDAC runs some particles settle down during the eruption. This effect may again be attributed to the additional usage of larger particles in the PDAC runs (see Tab. 5.1). While the coarse grid run significantly deviates from the finer grid runs, convergence between intermediate and fine grid runs becomes apparent. Hence an at-vent grid resolution of 10 m can be used to capture the overall dynamics.

5.5 Discussion — Real versus Synthetic Doppler Radar Data

After introducing and testing both numerical models, I will use PDAC for the small scale near-vent dynamics and both models to study the large scale dynamics (i.e. cloud height). The most prominent difference between the synthetic velocigrams of the high resolution runs

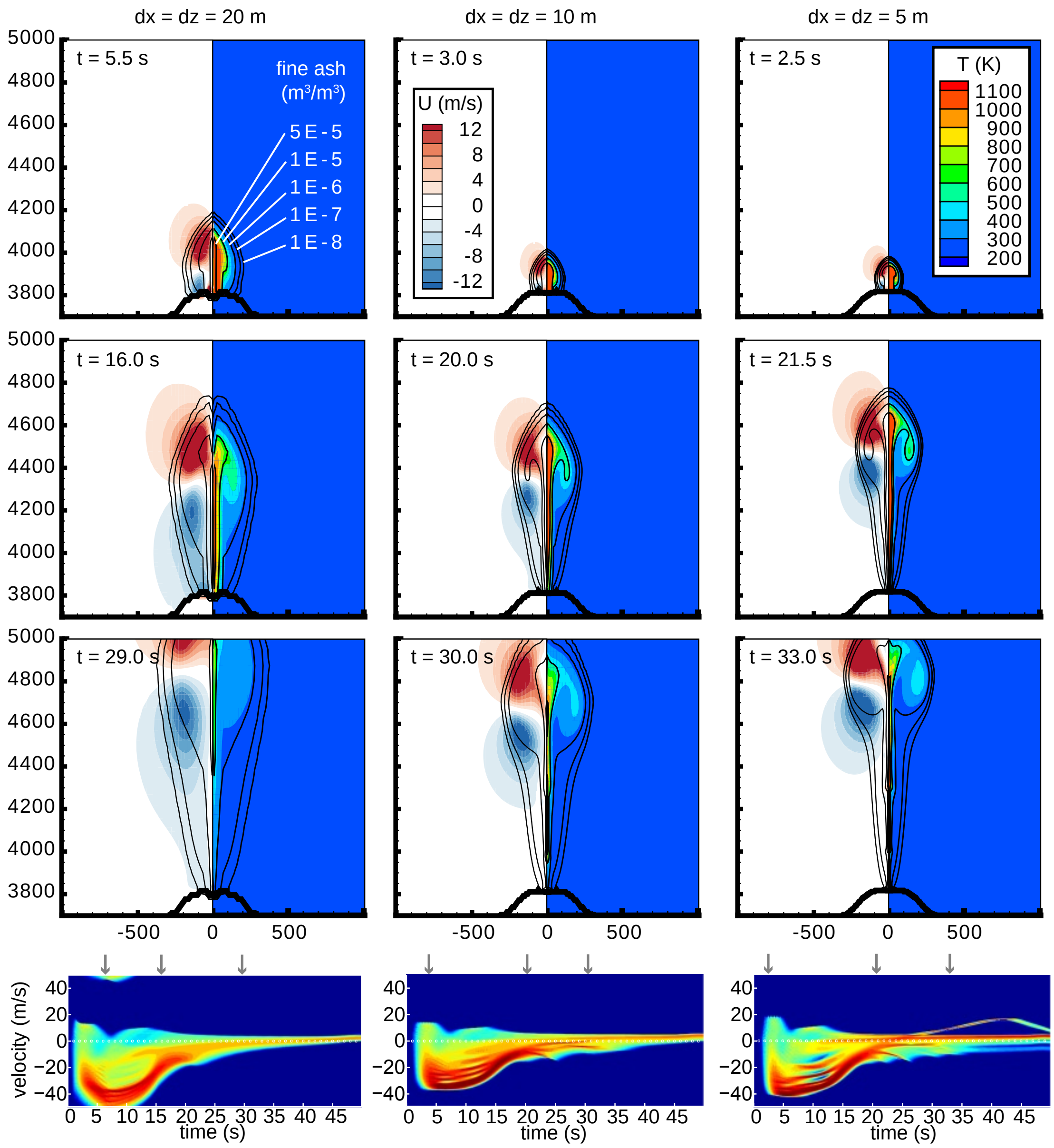

Figure 5.7: Snapshots and synthetic velocigrams of three PDAC runs with varying grid resolution (all PA-VA-FA, see Tab. 5.1). The grid extends 10 km radially and 15 km vertically in all cases. For the mesh see Fig. 5.3. The snapshots show the horizontal bulk velocity on the left (red corresponds to outward, blue to inward velocities), and the gas temperature (colors) on the right side of every diagram. The light contours show the concentration of fine ash ($r = 0.015$ mm). The legends in the upper row diagrams are the same for all plots. The thick black line depicts the topography. For all runs, three snapshots are shown that each represent a characteristic feature of the dynamics. Note that those features do not necessarily occur at the same times. In the upper row, the outward motion at the plume head is separated from the at vent outward motion for the first time (red contours separated). The second row shows the detachment of the fine ash rising in the plume from the ground. In the third row, several trailing vortex structures have developed and the lower ones begin to settle down. The bottom row shows the corresponding synthetic velocigrams (assuming the setup geometry of the Colima experiment). The gray arrows mark the times of the corresponding snapshots. The color scale of the echo power is the same as in Fig. 4.6.

(Fig. 5.5 and Fig. 5.7, right columns) and the three exemplary velocigrams given in chapter 4, Fig. 4.6, is the time evolution of the maximum negative and positive velocities. Both ballistic events in Fig. 4.6a,b) show short-lived peaks in negative (upward) velocity followed by a streak-like pattern, with every streak ending with high positive (downward) velocities. The duration of each single streak is about 15 s. The velocigrams given in Fig. 5.7 (right column), for example, show an almost constant or slowly decreasing maximum negative velocity for 15 s, which is the duration of the forcing function (FA). Only after the end of the jetting phase, when the inlet velocity is 0 m/s, the maximum negative velocity decreases significantly. In the real data, such a constant maximum negative velocity does not exist, which means that the forcing function FA does not represent the timely evolution of mass flux at the vent. In addition, in all simulations the particles are faster (40 m/s) than in the real data (10–30 m/s in the non-ballistic events), which means that the inlet velocity of 100 m/s is too high.

Fig. 5.8 shows a more explosive type of forcing function (FF, 3 s duration). In all nine velocigrams, the short duration of the signal is visible, despite the long coda of very small negative velocities, which are indicative for settling particles that move with their terminal fall velocity. Interestingly, the secondary acceleration phase (marked by ② in Fig. 5.8), which is caused by buoyant updraft, becomes dominant at lower heights (left column), and slower inlet velocities (bottom row), because the jet ① ceases at a lower height and the momentum of particles is consumed at shallower levels. However, because the particles used in the simulations are small and the bulk density of the ejected mixture is only slightly higher than the atmospheric density, even the slow jet (bottom row) is able to entrain enough ambient air to become buoyant.

It seems that the transition between gas thrust and buoyant region of the plume is exactly captured in the middle velocigram of Fig. 5.8. The jet is characterized by a peak-like maximum in negative velocity ① that is accompanied by a wide range of radial velocities. As explained above, this range of velocities is caused by the passing of the plume head through the FOV. When a buoyantly rising plume enters the FOV ③ the maximum negative velocity as well as the measured range of velocities increases, because the plume head moves upwards with the average speed of the convecting cloud. The wide velocity band that follows represents the convective part of the plume.

None of the velocigrams in Fig. 5.8 shows all characteristics of a ballistic event. The velocigrams measured at the vent (left column) show a streak like pattern but the high positive velocities, attributed to fast falling particles, are missing. However, this is not surprising because only very small particles have been used in this calculation, which mainly follow the gas motion. In contrast, Fig. 5.9 shows the characteristics of ballistic events (short-lived, streak pattern and fast settling velocities). In those simulations, the same particle sizes as in the other PDAC runs are used, but with a 7.5 times higher volumetric fraction (PC). The three runs shown here have different inlet velocities and are measured with the same sounding geometry (Colima, 150 m above the vent). They correspond to the middle row in Fig. 5.8. In all three simulations, the plume collapsed due to the high mass loading. In

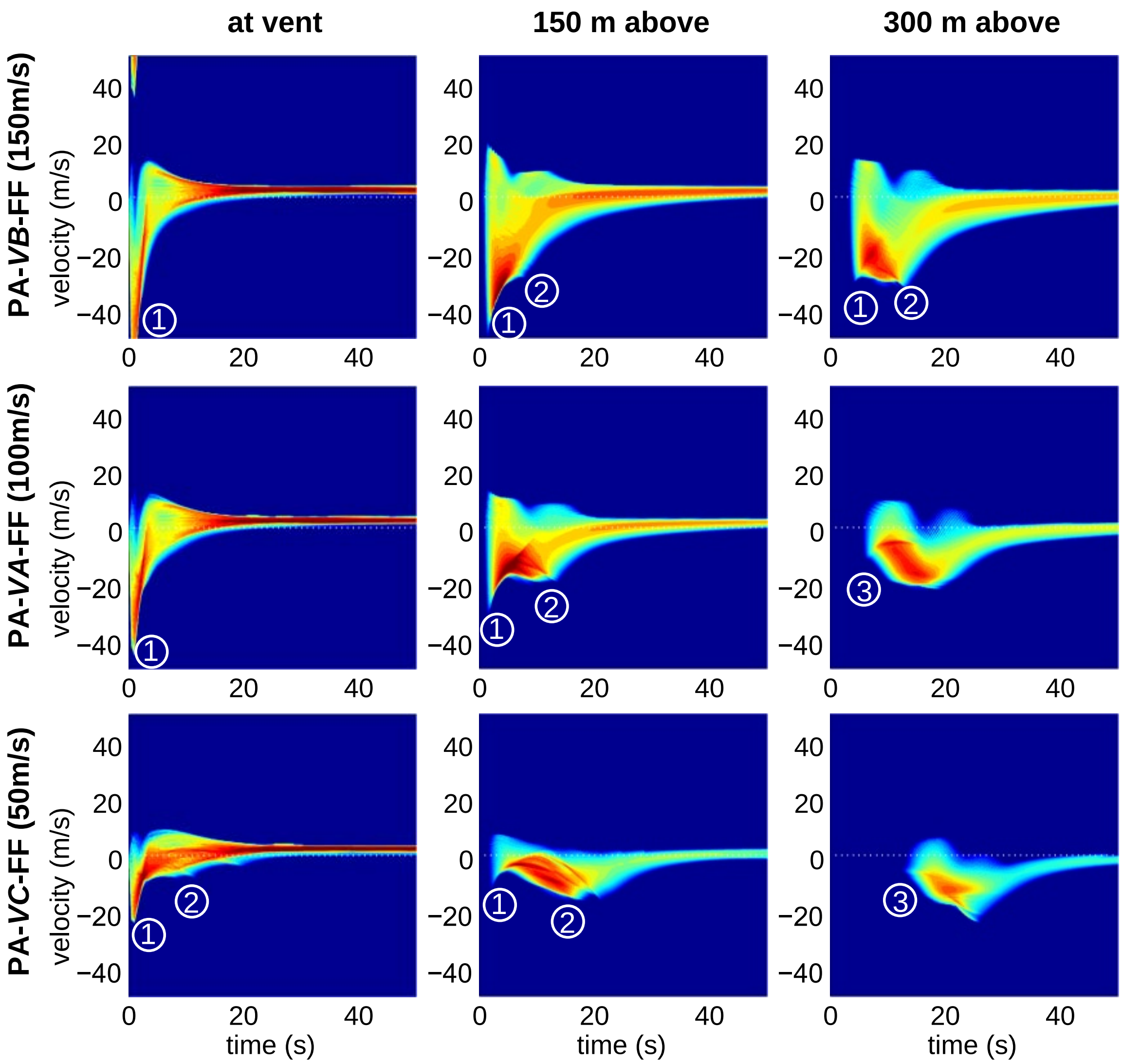

Figure 5.8: Velocigrams of three model runs (rows) with differing inlet velocity measured at three different heights at and above the vent (columns). All runs used mainly coarse ash (0.1 mm radius, PA) and the shortest forcing FF (3 s duration). The maximum inlet velocity decreases from top to bottom: 150 m/s (VB), 100 m/s (VA), and 50 m/s (VC). The velocigrams all are calculated using the Colima sounding geometry (see Fig. 4.1c), looking from below. However, in the left columns, the Doppler radar aims directly at the vent, which is impossible in reality. Note that left velocigrams can be compared to the Santiaguito datasets by reversing the velocity axis. In the right column, the Doppler radar aims at 300 m above the vent, which corresponds to the target location of the second Doppler radar installed in 2009. The encircled numbers are referenced in the text.

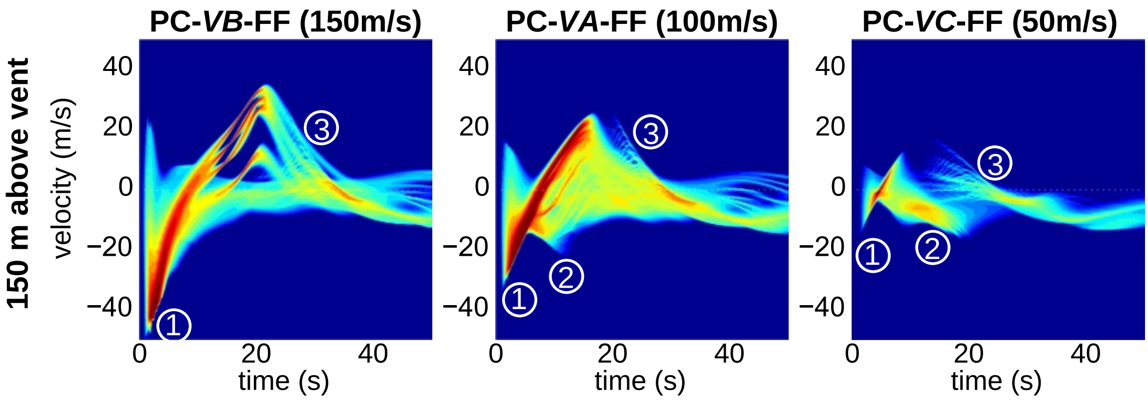

Figure 5.9: Velocigrams of three model runs with differing inlet velocity measured at 150 m above the vent. All runs used mainly coarse ash (0.1 mm radius, PC) and the shortest forcing FF (3 s duration). The maximum inlet velocity decreases from left to right: 150 m/s (VB), 100 m/s (VA), and 50 m/s (VC). The velocigrams were calculated using the Colima sounding geometry (see Fig. 4.1c), looking from below. The encircled numbers are referenced in the text.

addition, the maximum negative velocities are higher and the jet region ① reaches to a greater height, due to the higher momentum of the gas-particle mixture. Interestingly, the collapse pattern appears as ballistic motion in a velocigram and it seems that the bulk motion follows a ballistic trajectory. However, in contrast to the ballistic events the coda (particles falling with their terminal fall velocity) is missing. Instead a fraction of particles is re-entrained in the already rising buoyant plume ②, which develops directly above the collapsing column. This can be seen in the velocigrams as a third acceleration phase (③, from 20 s on in the middle and right velocigram). In this secondary buoyant plume ③ only a small amount of the initial material is incorporated, which can be seen in the relative values of echo power. The processes of re-entrainment and buoyant rise above a collapsing plume have already been described by *Neri et al.* (2002).

To summarize, non-ballistic events can be attributed to buoyantly rising clouds passing the FOV. They show a large variation of dynamic patterns (i.e. patterns in a velocigram), which mainly depend on the relative height of the jet-to-buoyant-rise-transition and the FOV. The main characteristic that distinguishes them from ballistic events is the lack of an initial peak in maximum negative velocity, which can be associated with the gas jet. Typical patterns of ballistic events are either caused by large particles moving on ballistic trajectories decoupled from the gas motion or a large mass fraction that causes plume collapse. In any case, the initial velocity of the particles has to be high enough that the jet reaches the FOV.

Of the 91 events measured at Colima volcano, 14% show pulsed behaviour. Interestingly those events are all of the ballistic type and hence the question arises up to which height pulses may be observed. Fig. 5.10 shows velocigrams of two model runs with different forcing functions (FB, top row, and FD, bottom row), again measured at different heights at and above the vent. From these velocigrams it can be clearly seen that individual pulses can be distinguished at the vent and in the jet region. However, in the latter, they may only be

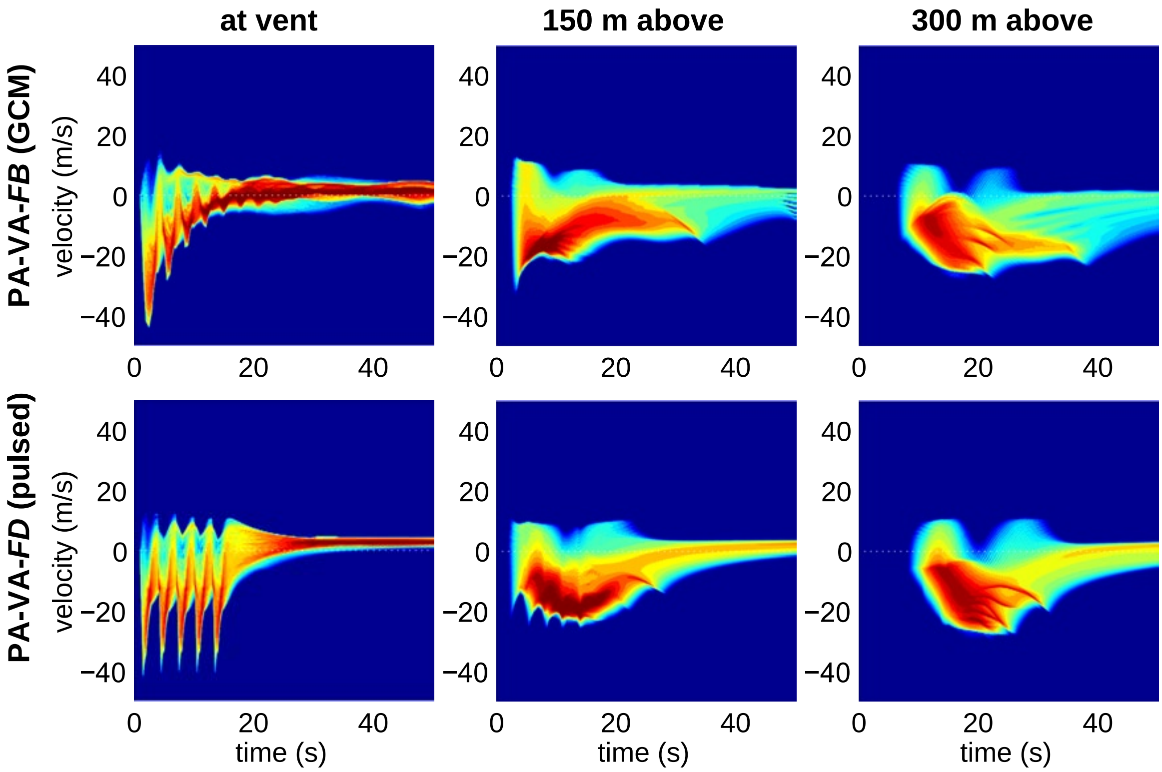

Figure 5.10: Velocigrams of two model runs (rows) with differing forcing function measured at three different heights at and above the vent (columns). All runs used mainly coarse ash (0.1 mm radius, PA) and a maximum inlet velocity of 100 m. In the upper row the FB-forcing function is used, which represents the timing and gas release of the modeling results of chapter 3, Fig. 3.10a. The lower row uses a pulsed forcing function (FD). The velocigrams are calculated using the Colima sounding geometry (see Fig. 4.1c), looking from below. However, in the left column, the Doppler radar aims directly at the vent, which is impossible in reality. Note that left velocigrams can be compared to the Santiaguito datasets by reversing the velocity axis. In the right column, the Doppler radar aims at 300 m above the vent, which corresponds to the target location of the second Doppler radar installed in 2009.

resolved when the relative strength of secondary pulses exceeds or equals that of earlier ones (compare the velocigrams in the middle column of Fig. 5.10). In the pure buoyant region (right column in Fig. 5.10) closely timed pulses cannot be resolved. This explains why pulses in Vulcanian eruptions have not been detected earlier by weather Doppler radars, which observe the clouds at higher altitudes where they rise buoyantly.

An ongoing debate exists whether a Doppler radar is capable to resolve plume center dynamics, i.e. how deep the radar beam penetrates into the dense part of the eruption cloud. In the present work I assumed that the clouds are transparent to the Doppler radar. Effects like multiple scattering and beam attenuation by particles are neglected in the calculation of synthetic spectra, however, they do exist and are important. A simple geometric estimation can be used to asses the effect of attenuation. In Fig. 5.11 the distribution of fine ash, the true velocity vectors and the theoretical along-beam velocity (colors) for a radar beam of 31° inclination into an ATHAM-simulation is shown. The convection in the plume head produces

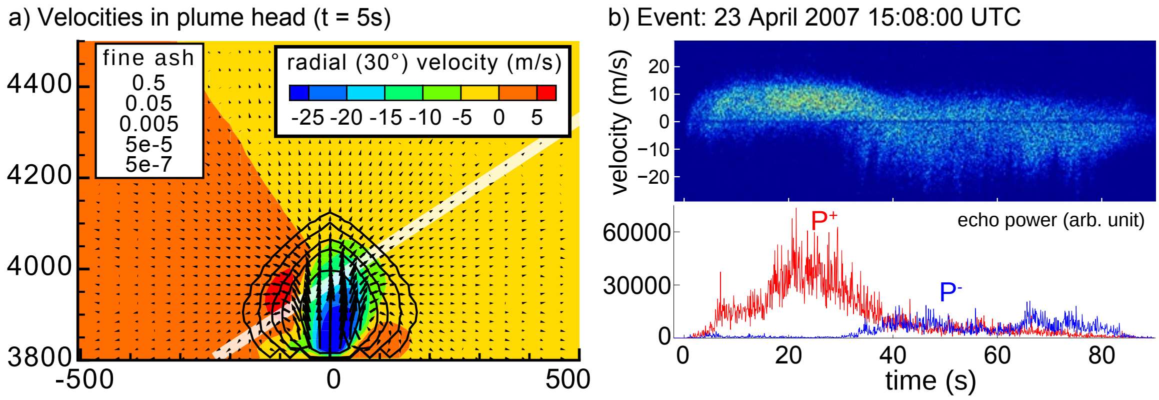

Figure 5.11: a) Distribution of along-beam velocities and fine ash in a starting plume (snapshot at 5 s of ATHAM-PA-VA-FA, 20 m resolution). The arrows are velocity vectors of the true flow field (the length corresponds to the absolute speed). The white line shows the direction of the radar beam (looking from below into the cloud, angle 31°). The colors correspond to the along-beam (radial) velocity that is measured by the radar. The contours show the mass concentration of fine ash ($r = 0.015$ mm). b) Event of 23.4.2007 15:08:00 UTC at Colima volcano. The color bar is the same as for Fig. 4.6. For more explanation see text.

a significant positive velocity. The highest negative along-beam velocities are measured at the back-side of the plume (dark blue). If the plume carries a large amount of ash, the back side may not be visible and only the positive along-beam velocities of the plume head convection may be visible in the velocigram. This effect can possibly be seen in an example of Colima volcano (Fig. 5.11b). The eruption begins with a very high echo power and high positive velocities (without any negative velocities) and the later part (starting at about 40 s into the eruption) is characterized by high negative velocities. This means that the first 35 s of the eruption are dominated by particles that approach the radar, which means they fall down or have a significant horizontal velocity component towards the radar. One explanation for this could be wind, blowing all particles towards the radar. However, the later part of the eruption is dominated by rising particles, so either the wind must have suddenly stopped or must have changed its direction within seconds, which could be the case at the beginning of the eruption but probably not ∼35 s later. A somehow more intuitive explanation is attenuation. The first part of the eruption has a significantly higher echo power, which suggests that a high amount of particles is within the FOV. Keeping in mind that every particle absorbs incoming electromagnetic energy and also produces a ‘shadow’, the beam intensity decreases as it penetrates into the cloud. Hence only those particles at the frontal part of the cloud are recorded, which mainly have negative radial velocities (see Fig. 5.11). Later in the eruption the plume head has left the FOV to the top and the plume tail appears, which is then dominated by upward motion (i.e. negative velocities). To summarize, attenuation is likely to have an effect on the measurement and should not be neglected. However, its signature (an intense eruption that appears to begin with falling particles) clearly identifies the affected datasets, whose interpretation should then be treated with care.

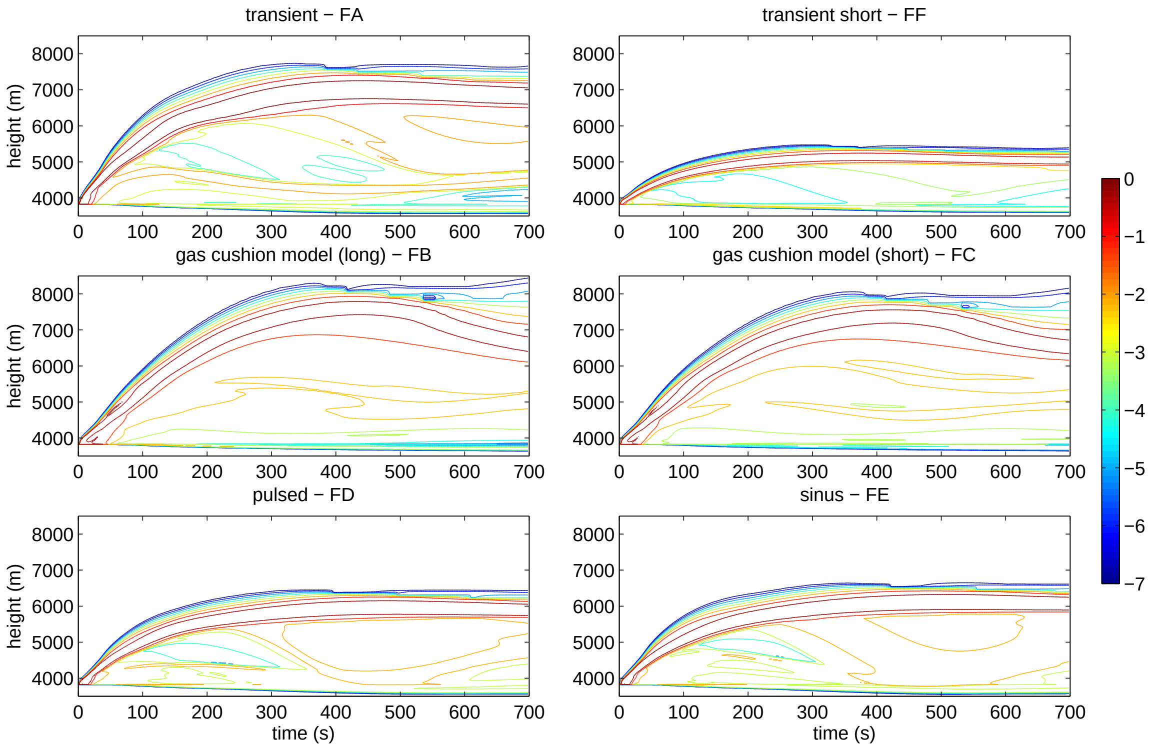

Figure 5.12: Profiles of ash volume concentration per unit height as a function of time for six simulations of ATHAM with different forcing functions (FA to FF, see Tab. 5.1 and Fig. 5.3). In all simulations only fine ash was used and the initial velocity was set to 100 m/s (PB-VA-F*). The colored lines are contour levels and correspond to values of 10^{-7}, 10^{-6}, 10^{-5}, 10^{-4}, 10^{-3}, 10^{-2}, 10^{-1}, and $1\,\mathrm{m^3/m}$ (from blue to red). In each diagram, time is plotted on the horizontal and height on the vertical axis.

5.6 Pulsed Eruptions, Steady Clouds?

An important quantity concerning eruption clouds is the injection height of fine ash into the atmosphere. It is commonly assumed that most fine ash is released from the cloud in the umbrella region, where the gas-ash-mixture reached the height of neutral buoyancy and spreads laterally. However, most weak volcanic clouds do not produce umbrella clouds and dissolve (visibly spoken) during their ascent. Compared to a Plinian eruption cloud the actual ash mass in a weak volcanic cloud is very small. But the frequency at which those weak plumes are generated is much higher and hence the cumulative ejected mass per year (or any longer time period between two Plinian eruptions) is comparable to the mass ejected by one large Plinian eruption. It is therefore interesting to know to which height the ash is transported, as this can be seen as a steady contribution of aerosol-like input into the atmosphere.

In Fig. 5.12 the vertical ash concentration profiles of six ATHAM simulations are shown, in which only the forcing function is varied (PB-VA-F*[4]). A vertical profile is calculated at each time step by horizontal integration over tracer concentrations, which results in a cumulative particle loading per unit height and time. Fig. 5.12 shows the large scale plume rise over time when different at-vent velocities are assumed. Remember that the forcing is realized by a variation of the inlet velocity with time (Eq. (5.1) and Fig. 5.3). Interestingly all simulations result in plume heights between 1.5 and 4 km above the vent, which corresponds to the typical rise heights of weak volcanic plumes. Note that the profiles in Fig. 5.12 do not show ash dispersion and dilution of the cloud at height because ash content is integrated at every height. Hence the local volume concentration decreases with an increasing cloud radius and eventually falls below the visibility threshold of $10^{-7}\,\mathrm{m}^3/\mathrm{m}^3$ (*Neri et al.*, 2003).

Fig. 5.12 shows that the plume rise significantly depends on the at vent conditions. The difference between the high-rising cloud in FA compared to FF is the duration of the eruption (15 s compared to 3 s of constant mass flux, see Fig. 5.3). The total mass injected into the FA-simulation is larger than the one of FF, which results in a larger thermal energy that potentially can be converted into buoyancy. Curiously, other forcing functions show a completely different cloud behavior. The highest clouds are produced by two simulations that inject a series of regularly pulsed jets with decreasing strength (FB and FC, see Fig. 5.3). These two forcing functions correspond in timing and gas release to the modeling results of chapter 3, Fig. 3.10a. The difference between FB and FC is the duration of forcing. The first 15 s of both functions are identical, but FB continues for another 20 s with pulsed feeding, however, the pulse amplitude (inlet velocity) becomes very small. FC produces a slightly higher cloud than FA although they have the same duration, and although mass flux and total ejected mass of FC are significantly smaller. However, in simulations FB and FC the maximum concentration level reaches a maximum height and decreases afterwards indicating an overshooting of the plume. None of the other simulations shows this pattern. Interestingly, the main cloud height controlling process appears to be the decreasing strength (inlet velocity) of consecutive pulses. Two control simulations that use a repeated sawtooth-like modulation (FD) and sinusoidal modulation (FE) of the inlet velocity produce clouds that only rise to 2 km above the vent. This could be caused by repeated destruction of the developing entrainment vortex by secondary pulses (FD and FE) in contrast to mildly pulsed feeding of an established entrainment vortex, which then acts like a pump (FB and FC).

In all simulations shown in Fig. 5.12 a significant amount of fine ash reaches great heights (highest concentrations and heights for simulations FB and FC). Note that this is also the case for simulations done with PDAC. Table 5.2 lists the cloud heights for all simulations that were carried out during this study. The maximum cloud height (MCH) is defined as highest level where the specific volumetric concentration of fine ash exceeds a local volume concentration of $10^{-7}\,\mathrm{m}^3/\mathrm{m}^3$, which approximately corresponds to the visible boundary of the eruption cloud (*Neri et al.*, 2003). The neutral buoyancy height (NBH) is defined as the height, at which the plume bulk density equals the ambient air density. At the NBH the

[4]The '*'-symbol is used here as a wild-card for the characters A, B, C, D, E, and F, i.e. FA, FB, FC, ...

Table 5.2: Erupted mass, simulated maximum cloud height (MCH) and neutral buoyancy height (NBH), and time needed to reach MCH. Values in parenthesis could not be determined accurately, because the concentration profiles show multiple peaks.

	ATHAM (PB-VA-F*)				PDAC (PA-VA-F*)				PDAC (PC-VA-F*)			
	mass	time	MCH	NBH	mass	time	MCH	NBH	mass	time	MCH	NBH
	10^6 kg	s	m	m	10^6 kg	s	m	m	10^6 kg	s	m	m
FA	3.287	380	7500	6700	4.829	256	10400	9500	31.686	250	13000	(6000)
FB	1.051	386	8000	6500	1.564	266	9400	8200	10.262	276	10400	5500
FC	0.997	406	7800	6500	1.485	266	9000	7800	9.746	270	10300	5500
FD	1.312	396	6400	6000	1.894	250	7200	6400	12.425	250	15700	(10000)
FE	1.968	420	6500	6100	2.840	250	7700	6900	18.637	256	14200	(10000)
FF	0.286	300	5400	5200	0.462	266	6800	6300	6.012	260	8500	(6000)

eruption cloud stops rising and spreads out laterally. In the vertical profiles (Fig. 5.12) the NBH is given by the height at which the maximum concentration of fine ash is reached. Note that like in the simulations FA, FD, FE, and FF the NBH in simulations FB and FC is finally also reached after 700 s.

Early 1D models predicted a relationship between the mass flux at the vent and the final height of the eruption column (see *Sparks et al.*, 1997, and references therein). In those 1D models a constant buoyancy flux (constant particle temperature, velocity, bulk density and vent radius) is assumed at the vent and a corresponding steady state plume is obtained. Note that the term ‘eruption column’ in this case is a synonym for ‘eruption cloud’, because the 1D model describes a steady state cloud. As mentioned above, the assumption of constant vent conditions may be reasonable for Plinian eruptions. Empirical studies found that the theoretical relationship is indeed valid for Plinian and sub-Plinian eruption columns (*Sparks et al.*, 1997; *Mastin et al.*, 2009). They derived two empirical formulas from a regression through historical records of large eruptions (mostly of Plinian style). In addition *Mastin et al.* (2009) derived a relationship between total erupted volume and column height.

In Fig. 5.13 I plot the empirically derived curves together with the cloud heights obtained in this study (see Tab. 5.2). The empirical formulas are given for plume height above the vent, but the term ‘plume height’ lacks a clear definition. The end-members to plume height are certainly maximum cloud height and neutral buoyancy height and hence open (NBH) and filled (MCH) symbols (of equal style and color) may be used as error margins for the respective simulation. As suggested by theory, the same forcing function (symbols of constant color in Fig. 5.13a)) produce higher MCHs and NBHs with increasing mass eruption rate (PDAC runs use more mass than ATHAM runs, see Tab. 5.2). Collapsing columns[5] show no concentration maximum and hence no clear NBH (open diamonds in Fig. 5.13a should be treated with care). The simulated plume heights significantly scatter around the empirical curves but roughly follow the trend. However, when only simulations of the same particle size distribution (equal symbols) are compared the trend of the curves differs from the trend of the model runs. For example the runs with the smallest eruption rates, FB and FC, produce

[5]Note that due to the high mass loading all PDAC runs with the PC particle size distribution, which corresponds to 7.5 times PA, collapsed. In those simulations higher clouds were obtained, but only a fraction of the initial mass was incorporated into the rising cloud.

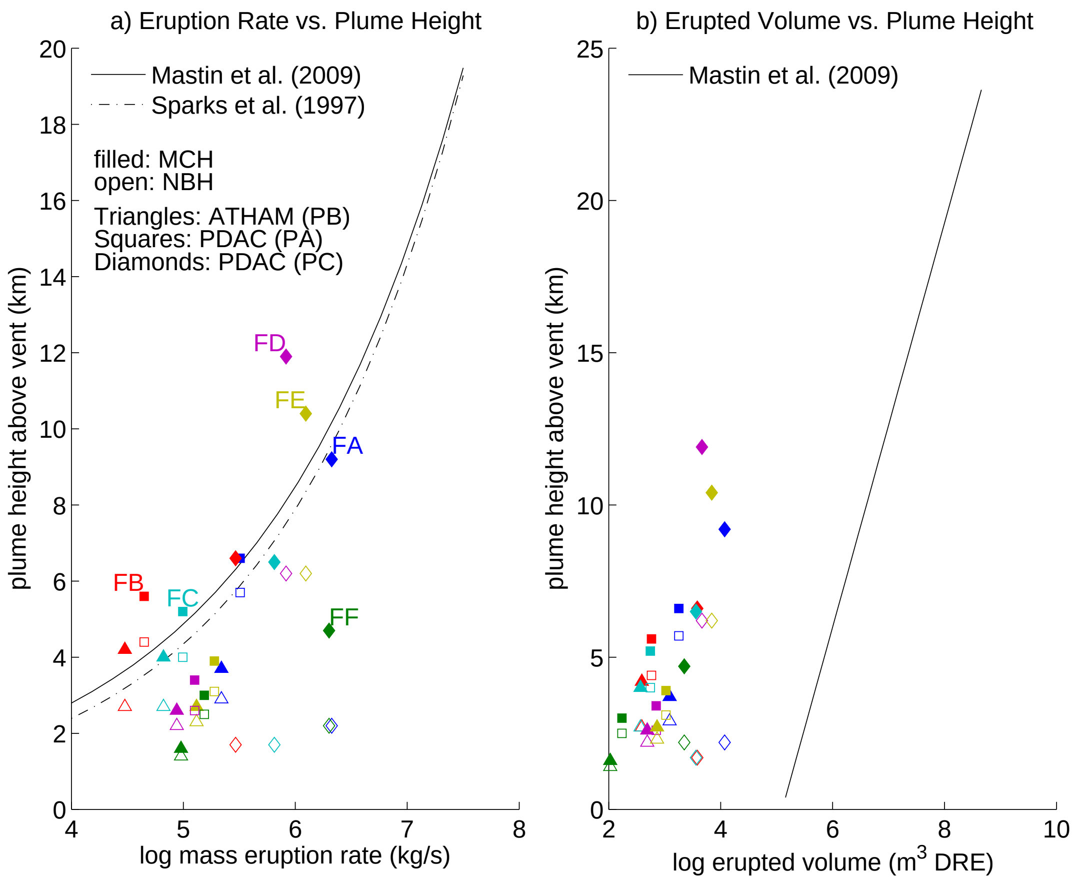

Figure 5.13: Maximum cloud height (MCH, filled symbols) and neutral buoyancy height (NBH, open symbols) as a function of eruption rate (a) and total erupted volume (b). The triangles in both plots refer to the cloud heights above the vent shown in Fig. 5.12 of example calculations with ATHAM (PB-VA-F*). Note that MCH and NBH plotted here are reduced by the vent height (3800 m) compared to the absolute values given in Fig. 5.12 and Tab. 5.2. The color of a symbol refers to the forcing function used in the respective simulation and the codes are given in Tab. 5.1 and Fig. 5.3. In addition the same simulations have been carried out twice with PDAC using (1) larger particles (squares, PA-VA-F*) and (2) more mass (diamonds, PC-VA-F*). Note that the simulations corresponding to the diamonds (i.e. PDAC runs with 7.5 times more mass) all result in collapsing fountains, in which only a small fraction of the total mass stays in the rising buoyant plume. a) The eruption rate was calculated by dividing the total erupted mass by the duration of the forcing and hence represents an average mass flux. The two lines show the empirically derived formulas of *Sparks et al.* (1997) and *Mastin et al.* (2009). b) The erupted volume (in m^3 DRE, dens-rock-equivalent) was obtained by dividing the erupted ash mass by a density of 2500 kg/m^3. The black line shows the empirical relationship by *Mastin et al.* (2009). Note that only erupted volumes above 10^5 m^3 were used in their correlation.

higher clouds than FD (pulsed), FE (sinus), and FA (for ATHAM, where only fine ash was used). In the PDAC calculations (squares) FB is the second highest cloud, although it has the smallest mass eruption rate.

The empirical relationship between cloud height and total erupted volume (solid line in Fig. 5.13b) was found for erupted volumes between 10^{-4}–$3\,\mathrm{km}^3$ DRE[6], which is orders of magnitude larger than the range of erupted volumes used in this study (symbols in Fig. 5.13b). The duration of the eruptions used here would have to be extended to 10 h to result in erupted volumes that are covered by the empirical formula. The erupted ash volumes used in this study result in negative plume heights. However, the simulations excluded all particles with a radius larger than 0.5 mm. In the last section I showed that in the ballistic events a large amount of larger particles is ejected. Those would contribute to the total ejected volume but might not significantly influence plume height, because they fall out early during the plume rise and take out a significant amount of heat. Hence the erupted volumes in Fig. 5.13b might be orders of magnitude larger.

Both empirically derived formulas are used by the VAACs (Volcanic Ash Advisory Centers) to estimate the eruption rate, total erupted volume and ash injection height from the observed cloud height (*Mastin et al.*, 2009). These "eruption source parameters" are needed for the VAAC's ash dispersion models. Cloud height is usually measured by observation, ground based weather radars or at remote volcanoes by satellite. The present study shows that pulsed forcing alters the dynamics at the vent significantly and that even small Vulcanian clouds with a low eruption rate may reach great heights and carry fine grained ash to 8–10 km during a period of minor activity. Therefore the use of the empirical formulas may significantly overestimate the true eruption rate and ash content of the smaller clouds.

The model runs presented here only cover mass eruption rates $\dot{m}$ at the lower end of the validity range of the formulas and also incorporate even significantly smaller total erupted volumes. The total mass involved in an eruption is determined by:

$$M_{total} = \int_{t_{start}}^{t_{end}} \dot{m}\,\mathrm{dt} = \int_{t_{start}}^{t_{end}} A_{vent}(t)\rho_{bulk}(t)v(t)\,\mathrm{dt},$$

where A_{vent} is the vent area, ρ_{bulk} is bulk density, and v bulk velocity at the vent. The eruption occurs between t_{start} and t_{end}. All these variables (duration, vent area, bulk density and velocity) may be changed in order to increase the total mass. In addition, vent area, bulk density and bulk velocity may change during an eruption. In the present study only the velocity was allowed to change during an eruption, which already had a significant effect on the dynamics. However, the vent area is likely to change during larger eruptions because of crater erosion, and the bulk density represents the mass fraction, grain size distribution and magma composition (i.e. water content) in one single parameter. An increase in mass fraction potentially leads to column collapse and a change in grain size distribution may change the overall dynamics, because larger particles decouple from the gas flow field. Hence, a more

[6]Dense rock equivalent is commonly used to describe the volume of volcanic deposits instead of their true volume because of their highly varying density (compare e.g. bubbly pumice and volcanic glass.

detailed parameter study has to be done for cross-validation of the numerical models and the empirical formulas.

In the presented study, the plume was forced to be axis-symmetric. This may significantly influence the dynamics of pulses. In three dimensions a secondary pulse may deviate from the vertical axis above the vent center to the side instead of interacting with or destroying the convection of previous pulses. So the questions arise whether a fully three-dimensional numerical model of multi-phase flow reproduces the empirical relationship between cloud height and mass eruption rate, and whether a pulsed mass eruption rate has the same significant effect on the cloud height.

In ATHAM (in general) as well as in PDAC (in this study) the jets are assumed to be fully expanded, which means that they enter the atmosphere at ambient pressure. In the literature (*Sparks*, 1997; *Clarke et al.*, 2002; *Ogden et al.*, 2008b,a; *Orescanin et al.*, 2010; *Ogden*, 2011; *Carcano et al.*, 2012) it is commonly assumed that Vulcanian jets are under-expanded, resulting from overpressure within the conduit, and that they leave the vent as a super-sonic flow of ash and gas. As a consequence, a Mach disk develops, where the jet velocity suddenly changes from super-sonic to sub-sonic. The dynamics of under-expanded jets differ tremendously from the jets simulated here. However, since the Doppler radar measures the velocity of particles in the jet and the maximum measured velocities are significantly smaller than the speed of sound ($<55\,\mathrm{m/s}$ along-beam at Colima and $<30\,\mathrm{m/s}$ at Santiaguito) I conclude that the jets at Santiaguito and Colima indeed leave their vents at atmospheric pressure and the expansion occurs below the surface.

Chapter 6

Conclusion and Outlook

In this work, a combined analysis of measured Doppler radar data and numerical modeling was used to shed new light on the dynamics of Vulcanian explosions and the development of the associated weak eruption clouds. Two measurement campaigns were carried out, one at Santiaguito volcano (Guatemala) and the other one at Volcán de Colima (Mexico). These two volcanoes have been chosen because their topological setting provides the possibility to observe eruption processes directly at the vent from above (at Santiaguito volcano) and the early stages of the developing eruption cloud from below (Colima volcano). For the interpretation of the complex Doppler radar data, a simple ballistic model and two sophisticated multi-phase fluid dynamics models, ATHAM and PDAC, designed to study volcanic clouds, were used. The ballistic trajectories and flow fields of ATHAM and PDAC were then converted into synthetic Doppler radar data using the software Qradar.

By a comparison of real and synthetic Doppler radar data I found that the Vulcanian eruptions that produce weak volcanic clouds were fed by series of subsequent explosions rather than a steady mass flux through the vent. At Santiaguito those sub-event pulses occur all over the dome surface at a nearly regular frequency. Using the simple ballistic model, I was able to show that the grain size distribution at Santiaguito comprises a high amount of millimeter- to centimeter-sized particles which move decoupled from the gas phase on ballistic trajectories.

To explain the above mentioned regularity of the pulsed events at Santiaguito volcano, I developed a simple mechanical model with a compressible magma column beneath a highly viscous carapace. In this model, two end-member scenarios have been investigated: (1) a magma column of constant compressibility and (2) a gas cushion (as approximation to a foam layer) beneath the carapace. The stick-slip (step-wise) rise of the deeper part of the magma column, caused by shear induced fragmentation at the conduit walls, compresses the upper bubbly part of the magma column. The compressible magma column or the gas cushion then act like a spring and trigger the oscillation of the overlying carapace.

The Doppler radar dataset of Colima volcano, which shows the dynamics of the developing eruption cloud 150 m above the vent, can be separated into two event classes: ballistic and non-ballistic events. The ballistic events show a similar dynamic pattern when compared to the events observed at Santiaguito volcano and also show pulses. It appears that the ballistic events at Colima also comprise a large fraction of mm- to cm-sized tephra, moving on ballistic trajectories. The rise height of those large particles is limited by their initial kinetic energy; highest rise velocities of up to 55 m/s along the radar beam are measured for ballistic events.

I compared the two sophisticated multi-phase fluid dynamic models ATHAM and PDAC and used them to investigate the physical processes during the so called non-ballistic events. Because of the assumption of dynamic equilibrium in ATHAM, its use for small scale eruption clouds is limited. Using PDAC I was able to show that the dynamics of the gas thrust (jet) and buoyant region can clearly be distinguished in the Doppler radar data, and that the dynamics of non-ballistic events are dominated by buoyant rise inside the cloud.

Both, Doppler radar data and numerical modeling show that pulsed forcing significantly affects the dynamics of the developing cloud at the vent, which leads to a considerably increased cloud height when compared to the empirical prediction at equal — but constant — eruption rate. The relative strength of consecutive pulses controls whether a secondary pulse disturbs the developing buoyant rise of the previous pulse or supports it, i.e. either acting as as a pump or a restrictor. Even weak volcanic clouds rise to heights of 8–10 km, which means that dome growing volcanoes with Vulcanian activity may carry high amounts of fine grained ash to flight levels during periods of minor activity. The "eruption source parameters" used by the VAACs for the modeling of ash transport and dispersion in the atmosphere may therefore be significantly wrong, in that they underestimate the impact of weak volcanic clouds. The short-lived fluctuations in mass flux at the vent are local phenomena and can only be observed in the jet region of the eruption cloud in the first few hundred meters of rise. As a consequence weather Doppler radars are not well suited for the observation of such pulses.

This study is the first to quantify the effect of a fluctuating mass flux at the vent on cloud rise. Based on my first rough exploration of the parameter space controlling explosive eruptions a more detailed parameter study is needed to understand the interplay of mass eruption rate, event duration, forcing function, particle velocity and mass loading of pulses and their influence on plume height and especially the injection height of particles into the atmosphere, which is strongly required for all ash dispersion models.

More work has to be done in quantifying the radar beam attenuation in the eruption cloud. I showed that it is possible to identify those events in the Doppler radar data that are possibly affected by attenuation. However, in those events the knowledge on the relationship between the bulk density of the cloud and attenuation could be used for a minimum estimate of the total mass inside the probed volume of the radar beam.

For monitoring purposes a reliable automatic event detection and classification algorithm is needed. The discrimination of the Colima data set into ballistic and non-ballistic events was done visually from the 'shape' of the eruption in a velocigram. This could be replaced in the future by the application of the 2D-cross-correlation used for pulse detection in the

Santiaguito study in real time. An even more sophisticated idea is the use of a 2D wavelet transformation that would, in addition to the detection of an event, give information on the duration and maximum velocities in the event or even in each pulse. Those informations could be put into 2D eruption cloud models so that a theoretical ash injection height could be retrieved for each eruption in near-real-time.

Appendix A

Appendix to Chapter 2

A.1 Doppler Radar Forward Model[1]

The Doppler radar forward model comprises two main parts: a) the description of the movement of particles, and b) the determination of the reflected energy from the particles moving through a hypothetical radar beam. For the dynamic part we use a Lagrangian formulation of ballistic particle transport. For every time step, every particle updates its position and velocity. A fourth order Runge-Kutta algorithm is used to calculate the new velocity from the sum of forces (accelerations) acting on the particle, namely gravity and atmospheric friction. Here we assume that all particles are spheres. Following *Herzog et al.* (1998) atmospheric friction is calculated for both Newtonian and Stokian friction for each particle and the higher of both values is applied to the particle. Acceleration due to Newtonian friction depends on the drag coefficient c_w, the ratio of densities ρ_g and ρ_s (gas and solid respectively), the particle radius r, and the squared relative velocity $\vec{v} = \vec{v}_s - \vec{v}_g$:

$$\vec{a}_N = -c_w \frac{3\rho_g v^2}{8\rho_s r} \frac{\vec{v}}{|v|} \quad . \tag{A.1}$$

Newtonian friction typically applies to faster particles. For slower particles the acceleration due to Stokes friction is dominant because it only depends on the single relative velocity, the gas viscosity μ and the squared radius

$$\vec{a}_S = -\frac{9\mu}{2\rho_s r^2}\vec{v} \quad . \tag{A.2}$$

[1]The original model has been written by Florian Ziemen, who is a co-Author of the published paper. He implemented the synthetic Doppler radar part of the model and the Runge-Kutta algorithm for particle transport. The original model is written in `C++`, uses a different initialization of initial velocities and lacks the parameterization of the gas jet. During my work with his model, I rewrote the code using MATLAB® (`www.mathworks.com`) to implement the gas jets and to ease the use of the model for other applications (the combination with ATHAM or PDAC, see chapter 5). I describe the model here, although it is not entirely my own work, because its description is also included in the original publication. Florian Ziemen wrote his Diploma thesis in German, which makes a reference to his work in an international publication difficult.

We calculate an isothermal atmosphere at $T = 300\,\mathrm{K}$ with a density of $\rho_0 = 0.897\,\mathrm{kg/m^3}$ at vent elevation z_v and a constant viscosity of $\mu = 1.82 \times 10^{-5}\,\mathrm{Ns/m^2}$. Density decreases with height z

$$\rho_g = \rho_0 e^{-g\frac{z-z_v}{R_{air}T}} \quad , \tag{A.3}$$

where $R_{air} = 287\,\mathrm{J/kg/K}$ is the specific gas constant of air. Here we neglect density and viscosity variations with changing gas temperature, as we do not calculate the expansion and cooling of the ejected volatiles. The drag coefficient is a function of the Reynolds number, i.e. the ratio of inertial to viscous forces (see *Pfeiffer et al.*, 2005, for a review of models to calculate terminal fall velocity). Due to our parameterization of the friction forces, we only need the drag coefficient at high Reynolds numbers (high velocities), where we follow *Pfeiffer et al.* (2005) and use $c_W = 1$ as an approximation for irregularly shaped volcanic particles.

To calculate the friction terms the relative velocity between particle and gas is needed. The gas velocity is calculated at every particle position $\vec{X}_p = [x_p, y_p, z_p]$ as the superposition of background wind (constant in time and space), gas jet (see below, Eq. (A.4)) and a parameterization for buoyant updraft (see below, Eq. (A.5)). Note that only the background wind provides horizontal gas velocity components to the model. The gas jet is parameterized following *Dubosclard et al.* (2004) as a column of vertical wind centered at the vent with the gas speed decreasing exponentially with height (*Blackburn et al.*, 1976). In addition the gas speed decreases radially from the maximum speed at the vent center (inspired by *Carey and Sparks*, 1986). The initial gas velocity $w_{g0}(t)$ (as a function of time), vent position $\vec{X}_v = [x_v, y_v, z_v]$ and radius r_v (center and half width at half maximum of the Gaussian distribution), as well as a reference height z_{ref} are prescribed. At the reference height the gas speed has decreased to 1%.

$$w_{\mathrm{jet}}(t) = w_{g0}(t)\,\underbrace{e^{-4.6\frac{(z_p-z_v)}{z_{\mathrm{ref}}}}}_{\text{vertical}}\,\underbrace{e^{-\frac{(x_p-x_v)^2+(y_p-y_v)^2}{r_v^2}}}_{\text{horizontal}} \quad . \tag{A.4}$$

The thermal or buoyant updraft due to entrainment of ambient air is parameterized by an additional cylindrical column of vertical wind $w_{\mathrm{plume}}(t)$, which is here assumed to be constant with height (*Sahetapy-Engel and Harris*, 2009b). Horizontally the updraft velocity $w_{\mathrm{buoy}}(t)$ follows a Gaussian distribution and is a function of time (buoyancy develops due to entrainment and is not part of the initial inertia budget of the eruption).

$$w_{\mathrm{plume}}(t) = w_{\mathrm{buoy}}(t) e^{-\frac{(x_p-x_b)^2-(y_p-y_b)^2}{r_b^2}} \tag{A.5}$$

Position $\vec{X}_b = [x_b, y_b, z_b]$, radius r_b (center and half width at half maximum of the Gaussian distribution) and the timing of the updraft velocity are prescribed parameters. This implementation of the atmosphere distinguishes our model from the one developed by *Dubosclard et al.* (2004) and *Gouhier and Donnadieu* (2008).

In our model an eruption is described as a superposition of single pulses. A pulse has the following properties: gas jet velocity evolution (maximum velocity, decay, duration), vent position, vent radius, particle size distribution (PSD, mean size, shape parameter and total volume), and opening angle, which is the maximum deviation of initial particle trajectories from the vertical. Pulses are allowed to overlap in time and/or space. Therefore we can describe scenarios of a steady one-vent eruption that endures several minutes as well as a series of short duration pulses that emanate synchronously from different vents distributed arbitrarily.

After the particles new position and velocity is calculated, new particles are created at the vent and particles whose new position is below the topography are destroyed. A prescribed number of particles is created in every time step. The particles radius is selected randomly within a specified range, such that the underlying Weibull distribution is satisfied. It has been shown in previous studies that the PSD is well described by a Weibull distribution (*Weibull*, 1951; *Marzano et al.*, 2006, see also Fig. 2.9), which is in turn defined by three parameters: total volume, mean particle size, and a shape parameter. Following *Chouet et al.* (1974) we assume the particle launch velocity $|v_{p0}|$ to depend on the particle radius r

$$|v_{p0}(r,t)| = w_{g0}(t) - \sqrt{\frac{8g\rho_s}{3c_w\rho_g}r} \quad . \tag{A.6}$$

$w_{g0}(t)$ is equal to the gas jet velocity and varies with time according to a prescribed function (constant, linearly increasing or decreasing). The launch angle is chosen randomly within the opening angle. All particles with a negative velocity (i.e. a diameter larger than $(w_{g0}(t)/k)^2$) are removed from the calculation because they would not exit the vent.

Once particle size, location, and velocity of the particles are determined from the ballistic part of the model described above, we calculate a velocity spectrum. The total back-scattered energy for each velocity sample in a range gate P_i is the sum of the back-scattered energy σ_j of each of the N_i scattering particles moving in the respective distance interval at that velocity.

$$P_i = \sum_{j=1}^{N_i} \sigma_j \frac{f(\phi_j)}{R_j^4} \tag{A.7}$$

R_j is the along beam distance of the particle and $f(\phi_j)$ is the beam intensity at angular distance ϕ_j from the beam axis. The intensity inside the synthetic radar beam follows a Gaussian distribution, which means that the intensity decreased to 50% at the half opening angle $\phi = 0.75°$. We include geometric spreading but neglect absorption, multiple scattering, and interference.

Scattering of electromagnetic waves at ash particles is calculated using Mie theory (*Mie*, 1908). In brief, Mie describes the interplay of internal and external electro-magnetic fields. In the Mie region, the external field wavelength and the particle size are of the same order of magnitude. Here a so-called creeping wave (*Currie*, 1989) travels around the particle interfering constructively or destructively, hence the amount of back-scattered energy strongly depends on the ratio of particle size and wavelength. In the end member case, when the wavelength of the external field is small compared to the particle size, the internal field will almost match the external field and the particle's back-scattering cross section is almost equal to its geometric cross section. In the Rayleigh region, when the particle is very small compared to the wavelength, the energy is scattered almost isotropically in all directions, hence only a very small fraction is back scattered towards the radar. Because we assume that size and dielectric properties do not change significantly over time, the back-scatter cross sections σ_j need to be calculated only once for each particle size. This is done by an external program in advance. The complete description of theory and algorithm is given in *Dave* (1969) and *Toon and Ackerman* (1981).

For a realistic synthetic spectrum we also account for the signal processing procedure inside the Doppler radar. Because our radar is a FMCW Doppler radar, several processing steps including two FFTs (Fast Fourier transform) are applied to the raw data to retrieve the velocity spectra (*Barrick*, 1973).

A.2 The Influence of Eruption Geometry, Vent Conditions, Buoyant Updraft and Wind on the Doppler Radar Measurement

This section has the purpose of giving a deeper insight into the interpretation of Doppler radar data. Using the ballistic model described above, we are able to produce velocigrams for a wide range of vent conditions and particle size distributions.

In the left column of Fig. A.1, all particles are ejected vertically (α=0°). In the middle and right column, the particle ejection directions follow a normal distribution with a maximum angle of $\alpha = \pm 25°$ to the vertical. As described above, the particle's initial velocity depends on its radius and a reference velocity at the vent exit (Eq. (2.3)). In Fig. A.1, this reference velocity is held constant at 50 m/s for 1.5 s (left and middle column) or decreases linearly from 50–10 m/s over 1.5 s. After this period, no new particles are added into the model. Particle size distribution (see Fig. 2.9) and observation geometry (see Fig. 2.4b) are the same in all 15 calculations shown in Fig. A.1.

Each row in Fig. A.1 shows a set of velocigrams produced with identical environmental conditions in the ballistic model.

1. frictionless: The simplest case is a particle transport without particle-air interaction (frictionless, upper row). It is clearly visible that the acceleration acting on the particles is constant and negative (simply gravity). The two maxima in echo power in the upper left velocigram (and to a smaller degree in the upper middle) show, that the initially fastest particles leave the FOV on their way up and eventually, when falling back, they

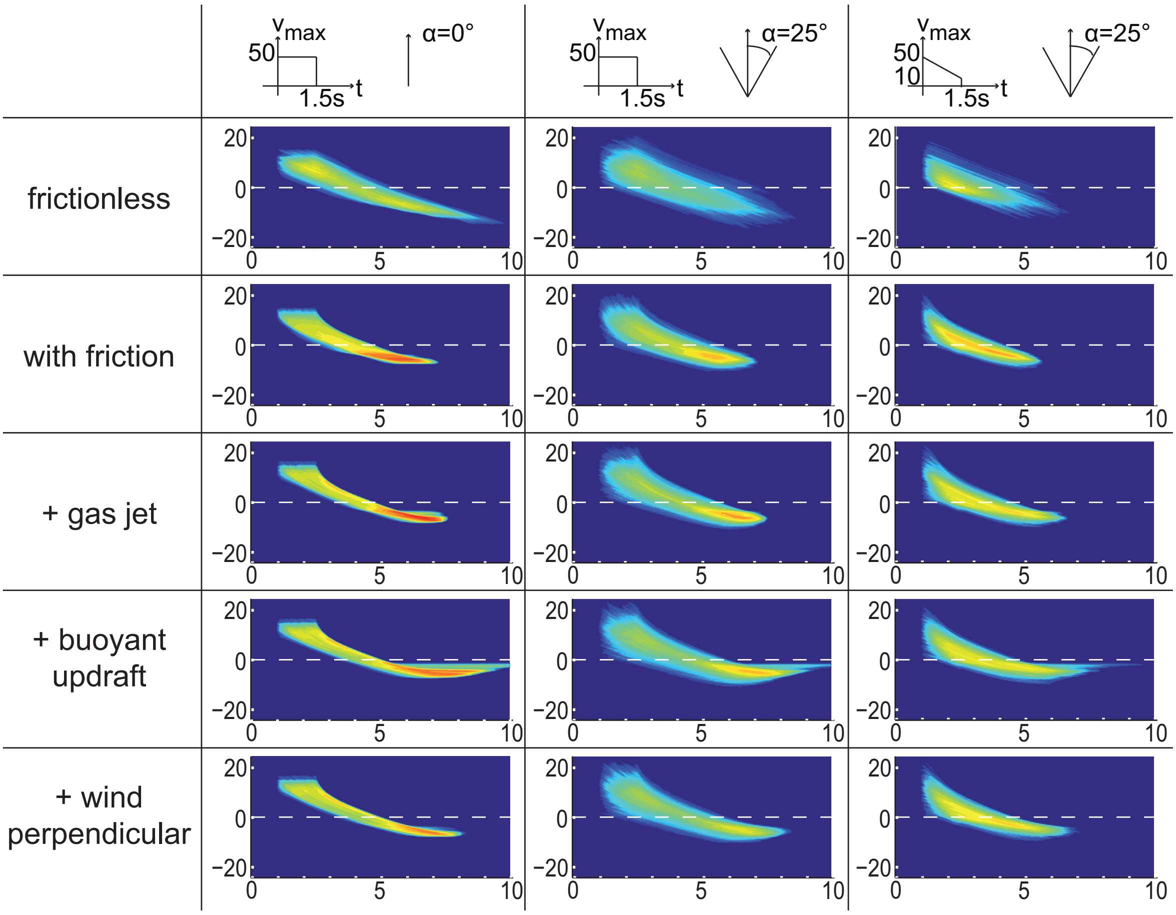

Figure A.1: Synthetic velocigrams of 15 different parameter combinations. Varied are: opening angle and time evolution of maximum velocity (constant over columns). In each row the particle transport in the ballistic model gets more complex. The first row shows pure ballistic transport without any friction. From the second row down, friction with air is included. The third row introduces the gas jet that comes out of the vent, buoyant updraft is included in the fourth row and finally a side wind (perpendicular to radar beam) is superposed in the bottom row. The sounding geometry and PSD (see Fig. 2.9, black line) are held constant during all calculations. Every velocigram shows the echo power (color coded) as a function of time (x-axis in seconds) and velocity (y-axis in m/s). The color bar is the same as in Fig. 2.11. More explanation in the text.

enter the FOV again. However, when particles are ejected with a decreasing gas velocity (upper right), we see that most particles do not leave the FOV. This can be concluded from the maximum in echo power around zero velocity, because particles are removed from the model as they hit the ground. Thus slow or non moving particles that leave a clear signal in the velocigram are at their highest-/turning point. However, during processing of the data in the radar the zero-velocity echo power is suppressed. Ejecting particles on inclined trajectories (middle and right velocigram) leads to a wider range of measured velocities, because the radar only measures one component of the three dimensional velocity vector (see Fig. 2.2).

2. with friction: In the second row, the particles are affected by air drag in non-moving air (i.e. no wind). Acceleration is no longer constant so that the diagonal streak gets bended towards the particles terminal settling velocity (i.e. the velocity where size dependent air drag and gravity acceleration cancel out). However, particles hit the ground and are hence removed from the model before they reach their terminal settling velocity. In the left velocigram where all particles are ejected vertically (and hence settle vertically) the high echo power around zero velocity suggests that all particles stay within the FOV. Since air drag also acts on horizontal velocity components, we can expect that no particles leave the FOV to either side even when an opening angle of 25° is considered.

3. with gas jet: The next level of complexity is the gas jet that erupts in mixture with the particles (third row in Fig. A.1). Upon exiting the vent the gas behaves like a jet in the upward direction. This jet is simulated here by prescribing a vertical wind. The jet velocity equals $v_{\max}$ directly at the vent, and decreases exponentially with height and lateral distance from the vent. Due to the velocity initialization all particles move with their terminal fall velocity relative to the surrounding gas. That means, inside the jet, all particles are dragged upwards with a velocity that depends on the local gas velocity and the particle radius. The smaller a particle, the faster is its absolute velocity inside the jet. Particles are dragged upwards with the jet and produce a very long coda in the velocigram when they finally fall through the FOV after the jet fades either at some pre-defined elevation (here: 50 m) or time (here: after 1.5 s). In comparison to the above 'still air'-case, some particles reach their terminal settling velocity before hitting the ground as they have been dragged to greater heights during their flight.

4. with buoyant updraft: Another key feature of ash-laden eruptions is the buoyant updraft caused by a thermal instability resulting from entrainment and heating of ambient air (herein also termed plume). Again, this updraft is implemented as a vertical wind component with a velocity of 5 m/s (constant with time and height) but laterally decaying according to a Gaussian distribution (see Appendix A.1). The most prominent effect in the velocigrams in row four is the long coda that consists of a broadened band of high echo power at negative velocities. Compared to the third row (no thermal plume) the maximum echo power is shifted towards positive velocities. In the left velocigram of the first four rows, all particles move vertically, i.e. they stay inside the plume. Because the particles terminal settling velocity is relative to the surrounding wind, their absolute velocity is shifted by the updraft velocity. The maximum negative velocity however equals the maximum negative velocity without plume or jet. This means again that the biggest particles (which have the largest terminal settling velocity) are not affected by air drag at all.

5. with background wind: The atmosphere is rarely at rest at a volcano. Side wind can significantly affect the velocigrams. Here (bottom row) we introduce a wind blowing at 10 m/s from right to left (perpendicular to radar beam) and explore the effects on the radar data. One can clearly see that plume effects on the coda are strongly reduced.

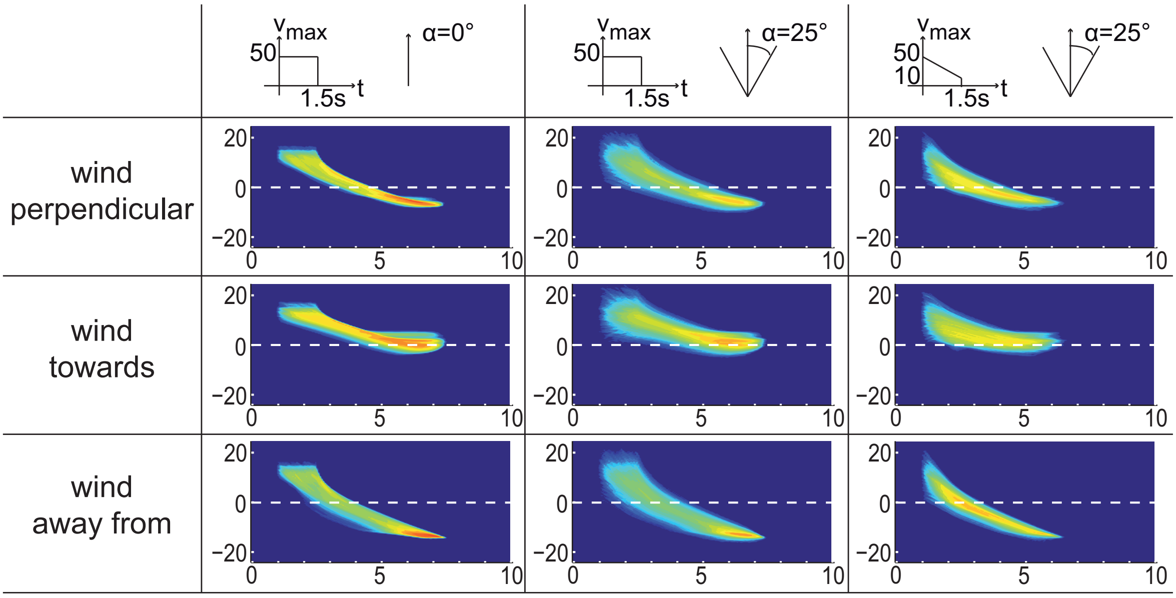

Figure A.2: Synthetic velocigrams of 9 different parameter combinations that show the effects of wind (10 m/s). The geometry, PSD and vent conditions are the same as in Fig. A.1 (third row), i.e. friction with air and the gas jet are included. We neglect buoyant updraft here because the radar is pointing directly at the vent exit. We vary only the direction of the background wind (perpendicular and along the radar beam). The 'along beam'-direction is modeled separately for wind towards and away from the radar. The color bar is the same as in Fig. 2.11. More explanation in the text.

> Particles that would rise in the plume are simply blown away and fall down as they exit the region of buoyant updraft. In the middle and right velocigram, particles that would exit the plume to the right due to their inclined ejection velocity get blown into the plume again. The main difference to the jet-simulations (third row) is that particles are carried upwards by jet and plume and sidewards by the wind so that they eventually leave the upwind region and fall down with their terminal settling velocity.

One key feature of all 15 calculations is that maximum velocities are recorded only at the beginning of the events, where particles are ejected out of the vent with their highest velocity. However, ejecting particles on inclined trajectories widens the range of recorded velocities, because the radar only measures the radial velocity component. Hence the geometrical feature of non-vertically ejected particles can lead to an overestimation of the gas velocity, when inferred by vertical correction of the maximum radial velocity recorded by the radar.

In Fig. A.2 we further explore the effects of background wind blowing from different directions (cross-beam, along-beam) at 10 m/s. Again the velocigrams are calculated for different vent conditions (see also Fig. A.1). In contrast to the lower row in Fig. A.1, we do not include buoyant updraft in these calculations. Only friction and the gas jet are used. In the upper row, wind is blowing perpendicular to the beam. The most important difference to the model without wind (Fig. A.1, third row, gas jet) is the lower echo power at negative velocities, some particles are simply blown out of the FOV. The middle and lower row show models with along-beam wind. Depending on the wind direction (towards or away from the radar), the later part of the velocigram (after the gas jet faded, after second 2.5 in Fig. A.2) is shifted to positive or negative velocities, respectively.

A.3 Auxiliary Material to Chapter 2

Figures A.3 and A.4 are taken from the auxiliary material of the publication, given in chapter 2. In addition to the two figures, the auxiliary material comprises three animations that show particle motions and particle properties, calculated by Qradar. The animations can be found in the online version of the published paper.

In Fig. A.3 the effects of the particle size distribution on the dynamics of the eruption and the measurement are shown for all four beam target locations. The first pulse is most obvious in C and IR, whereas the echo power of outer ring pulses is higher in OR and B. Using a smaller mean grain size results in a too high echo power for the first pulse compared to the later pulses, when targeting C. A bigger mean grain size gives better fitting trends in P^+ and P^-, when targeting C, IR or OR, but the first pulse almost vanishes.

Fig. A.4 shows the theoretical velocigrams of particles that move (a) on a circular path and (b) on a vortex ring. In the circular case, there are always particles that move perpendicular to the beam and even more particles that move almost along the beam. The maximum radial velocity is the same for positive and negative and coincides with the maximum in echo power. The maximum velocity is also the true velocity of the particles. In the case of a vortex ring, most particles move perpendicular to the beam. Only few particles move in the direction of the radar beam. Hence the maximum positive and negative velocities do not coincide with the maximum echo power. But the maximum velocities still represent the true particle velocity. In both cases, the velocities are mirrored with respect to the zero velocity axis, when the overall position of the circle and vortex ring is constant. When the ring moves, the mirror axis is shifted by the radial component of the ring motion.

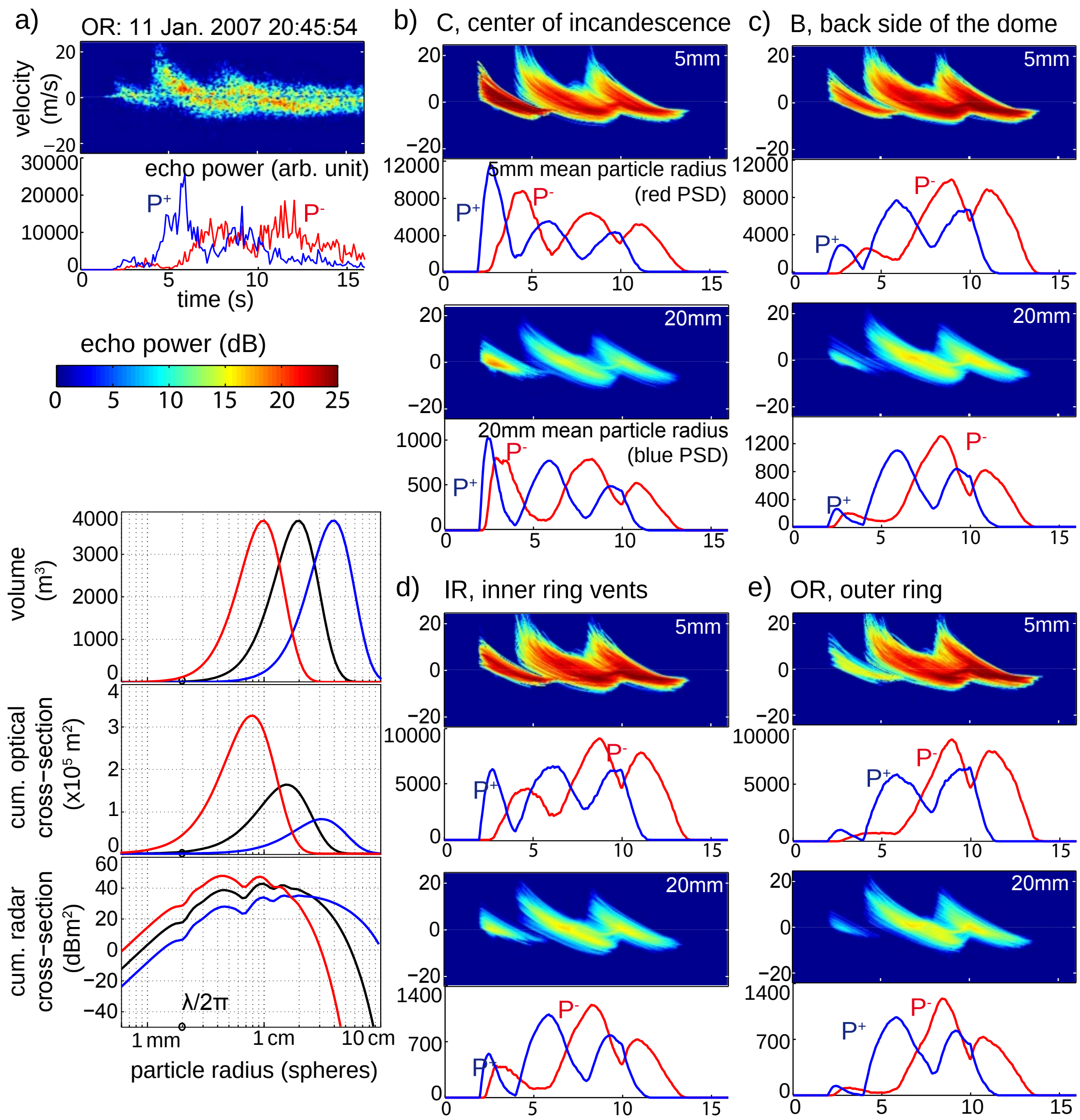

Figure A.3: a) Real data and b)-e) synthetic datasets of one eruptive event, observed for different beam target locations. We show the velocigram (upper panel) and the total reflected energy for positive and negative radial velocities (lower panel). A velocigram shows the echo power (color coded) as a function of velocity (y-axis) and time (x-axis). Note that the colors represent the ratio of echo power and background noise in dB for the real data (a) and the ratio of transmitted to received power for the synthetic data (b-e). The amount of reflected energy as a function of time is calculated from Eq. (2.1). The blue line refers to the total energy reflected by particles having a positive radial velocity, the red one to negative radial velocities, respectively. On the lower left is the particle size distribution, that were used to calculate the synthetic data. It is the same figure as Fig. 2.9. The range of particles and the total volume is constant, but the mean particle radius is varied from 5 mm (top, red PSD) to 20 mm (lower, blue PSD). The model parameters (vent conditions and eruption geometry) are given in Figure 2.10 and the same as in Figures 2.11 and 2.12. e) is the same as Fig. 2.12, b)-d) show the synthetic data sets for a smaller (upper) and a bigger (lower) mean particle size as in Figure 2.11.

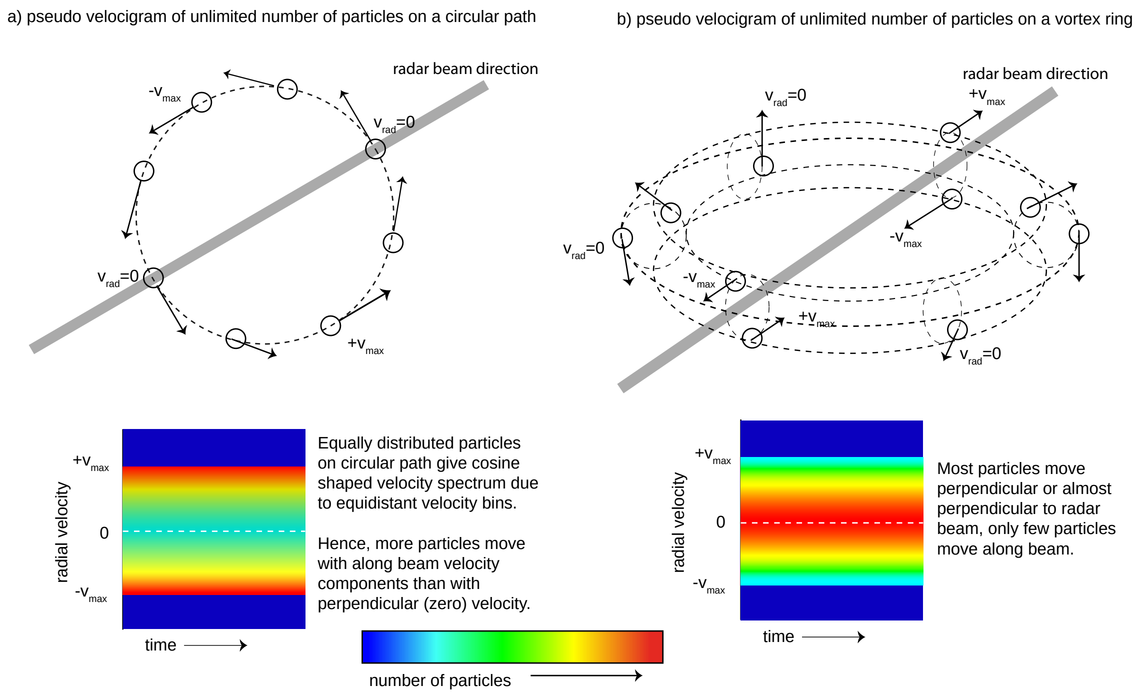

Figure A.4: Trajectories and pseudo velocigram of several particles that move with a uniform velocity on a circular path (a) on a vortex ring (b). Here every particle reflects the same amount of energy, hence the color in the pseudo velocigram represents the true number of particles.

Appendix B

Appendix to Chapter 3

B.1 The Squeezed Plug Model

We can rewrite Hooke's law:

$$\sigma_z = E\epsilon_z \quad \Leftrightarrow \quad \frac{F_z}{A} = E\frac{\Delta l}{L},$$

where σ_z is stress exerted on a plane normal to z, ϵ_z is strain in z-direction, E is Young's modulus, Δl is the length change of an object of length L in z-direction, and A is the area of the cross section of the object, to

$$F_z = \frac{EA}{L}\Delta l = Mg.$$

Now we have the equation of a spring-mass-oscillator with the eigenfrequency of

$$\omega^2 = \frac{EA}{LM},$$

with mass $M = \rho * A * L + m$ (m is the mass of the carapace). Knowing the bulk modulus K and Poisson's ratio ν, instead of E, we can rewrite the eigenfrequency to

$$\omega^2 = \frac{3K(1-2\nu)A}{L(\rho * A * L + m)}.$$

B.2 The Gas Cushion Model

Assume a cylindrical pipe with radius r and a closed bottom that resembles the conduit. At the top the pipe is widening conically to radius R. In the conical part of the pipe rests a carapace on a gas cushion (Fig. B.1a). When the carapace is at rest, the pressure inside the gas cushion balances its mass (gravity) and the upload of the overlying atmosphere. This position is termed equilibrium height z_{eq}.

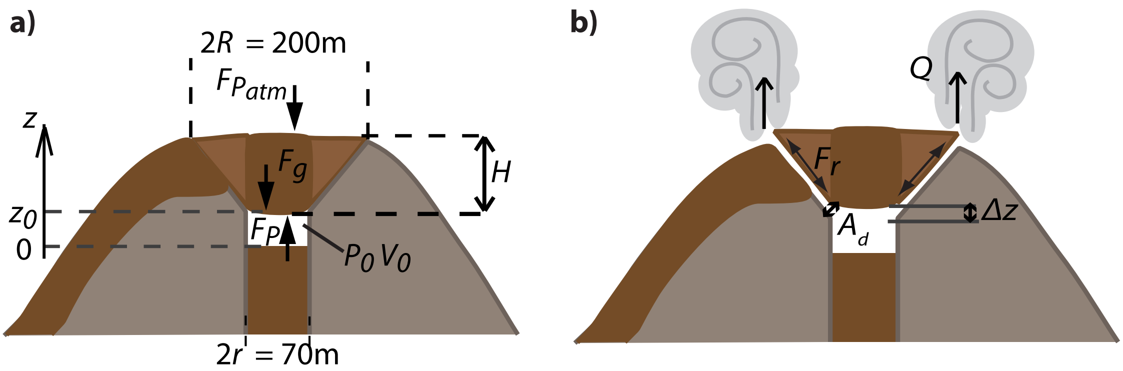

Figure B.1: The gas cushion model. a) An impermeable carapace of thickness H is sitting on a pressurized gas cushion with height z_0. The atmospheric pressure force $F_{P_{atm}}$ and gravity F_g counteract the pressure force F_P. Whether the bottom of the gas cushion ($z = 0$) is a geometrical boundary or just the surface of incompressible magma in the conduit or both is not part of this model study. b) During uplift of the plug viscous friction counteracts inertia. Because of shear-fracturing pathways for degassing develop preferentially at the conduit walls (white lines) and gas can escape.

The force balance of the system is:

$$F = -F_g - F_{P_{atm}} + F_r + F_P, \tag{B.1}$$

F_g gravity force, $F_{P_{atm}}$ atmospheric pressure force, and F_r friction. The pressure force F_P is exerted by the absolute pressure P inside the gas cushion beneath the carapace, resulting in an acceleration in case an overpressure is introduced and the friction along the margins is overcome. We assume that the friction mainly depends on the velocity (Stokes friction) and use a general friction coefficient μ_f to parameterize the highly complex processes of inter-particle friction inside the gouge zone:

$$F_r = -\mu_f \dot{z}$$

When the carapace is uplifted it exerts a drag force onto the surrounding gouge material. This is comparable to elastic shear deformation of a solid body or viscous flow of a fluid. On the other hand, when the carapace sinks to its initial position, the friction with conduit walls must increase by several orders of magnitude to hinder it from sinking below. Introducing an expression for the overpressure inside the gas pocket

$$\Delta P = P - P_{eq}$$

with equilibrium pressure $P_{eq} = \rho g H - P_{atm}$, H being the plug height and ρ its density, Eq. (B.1) reduces to

$$m\ddot{z} = A\Delta P + F_r, \tag{B.2}$$

with A being the cross section area of the conduit and $m = 1/3\rho\pi H\left(R^2 + r^2 + Rr\right)$ the mass of the carapace.

Assuming that the forces acting on the system exceed the yield strength, the whole plug is accelerated upwards. This will reduce the overpressure inside the gas pocket. The change in ΔP is calculated using the adiabatic equation of state (PV^{γ} =const), thus

$$\frac{dP}{dV} = -\frac{\gamma P}{V}.$$

Approximating dV by $A\Delta z$ it follows:

$$\Delta P = -\frac{\gamma P}{V} A\Delta z\,.$$

Here $\Delta z = z - z_{eq}$ is the displacement from equilibrium height z_{eq}, which is given by initial position z_0 and initial overpressure $\Delta P_0 = P_0 - P_{eq}$ using the adiabatic equation of state:

$$z_{eq} = z_0 \left(1 + \frac{\Delta P_0}{P_{eq}}\right)^{1/\gamma} \tag{B.3}$$

Assuming dP and Δz are small and because z_{eq} is constant, we can rewrite Eq. (B.2) to

$$0 = \frac{d^2}{dt^2}(\Delta z) - \frac{\tau}{2}\frac{d}{dt}(\Delta z) + \omega_0^2 \Delta z. \tag{B.4}$$

Eq. (B.4) is the equation of a damped harmonic oscillation around equilibrium height z_{eq} with eigenfrequency

$$\omega_0^2 = \frac{\gamma P A^2}{Vm} \qquad \Longrightarrow \qquad f = \frac{1}{2\pi}\sqrt{\frac{\gamma P_{eq}}{\rho H z_{eq}} \frac{3}{\left(\left(\frac{R}{r}\right)^2 + \frac{R}{r} + 1\right)}}$$

and damping

$$\tau = \frac{2m}{\mu_f}. \tag{B.5}$$

During uplift the carapace is decelerated by gravity, but because of its high momentum it overshoots its new equilibrium position, where gas pressure compensates gravitational forces. Hence, once the carapace reaches its maximum height, the gas pressure in the pocket is too low to withstand the carapace's mass and it sinks back down, thereby repressurizing the gas pocket. The resulting oscillation only occurs when damping is under-critical:

$$D = \frac{1}{\tau\omega_0} < 1$$

with τ being the characteristic time in which the amplitude decays to 1/e. The damped oscillation has the modified frequency

$$\omega_1 = \omega_0\sqrt{1-D^2}.$$

At the conduit walls, where the highest strain rates occur, cracks and fractures open up, thereby enabling gas escape from the cushion during an eruption. Degassing pathways close, when the carapace settles down. The volumetric flux Q through the gouge zone is approximated using Darcy's law for flow through porous media (*Turcotte and Schubert*, 2002):

$$Q(P,z) = -\frac{K_f A_d}{\mu_g}\frac{\Delta P + \rho g H}{H - z + z_0}\Theta(z - z_0) \tag{B.6}$$

Θ is the Heaviside step function and enables flow if the carapace is above its initial height. K_f is the gouge zone permeability and μ_g the gas viscosity. A_d is the cross section area of the flow, i.e. the cross section of the gouge material displacement, which depends on the position. A_d can be found by a simple geometrical relationship:

$$A_d = \pi(z - z_0)\sqrt{1 + \frac{R-r}{H}}(2r + (z - z_0)\frac{R-r}{H}).$$

Using initial conditions and the ideal gas law

$$PV = N(t)k_B T \tag{B.7}$$

we can calculate the initial number of gas molecules inside the gas pocket N_0:

$$N_0 = \frac{P_0 V_0}{k_B T_0},$$

where k_B is the Boltzmann-constant. During an eruption gas molecules escape the pocket due to the volumetric flux Q. Hence N changes with time, described by

$$N(t) = N_0 - \int_0^t \frac{PQ(P,z)}{k_B T}\,dt. \tag{B.8}$$

Depressurization due to gas out-flux is slow, compared to the oscillation pressurization, and can hence be approximated by an isothermal process: T =const. Neglecting the change in pressure due to oscillations the time derivative of Eq. (B.7) is:

$$P\frac{d}{dt}(V) = \frac{d}{dt}(N)k_B T$$

In combination with Eq. B.8 it follows

$$\frac{d}{dt}(V_{eq}) = Q(P_{eq}, z) \quad \Leftrightarrow \quad \frac{d}{dt}(z_{eq}) = \frac{Q(P_{eq}, z)}{A}$$

During the oscillation gas outflux is enhanced, but follows the same equations. Because Δz is the displacement from equilibrium height z_{eq}, which is no longer constant during the oscillation incorporating gas escape, the assumption for Eq. (B.4) is no longer valid and $\frac{d}{dt}(\Delta z) = \frac{d}{dt}(z) - \frac{d}{dt}(z_{eq})$ and $\frac{d^2}{dt^2}(\Delta z) = \frac{d^2}{dt^2}(z) - \frac{d^2}{dt^2}(z_{eq})$ introduce external forcing. Eq. (B.4) becomes

$$\frac{\frac{d}{dt}(Q)}{A} + \frac{\tau Q}{2A} = -\frac{d^2}{dt^2}(\Delta z) - \omega^2(Q)\Delta z - \frac{\tau}{2}\frac{d}{dt}(\Delta z).$$

The gas volume V inside the cushion depends on Q and therefore the oscillation frequency changes during an eruptive event. Given that degassing during uplift phases is limited, a damped oscillation develops, periodically releasing gas during dome uplift. Between eruptions, when the carapace is at z_{eq}, all values inside Eq. (B.6) are constant, thus a constant gas outflux through the slightly permeable carapace leads to a constant dome surface deflation.

Appendix C

Details of the Colima Monitoring Station

The following three sections are excerpts from three manuals I wrote during my work with the Doppler radar, especially for the purpose of technical support for the Colima monitoring station. Those manuals describe (1) the software to control and run the Doppler radars (*HowTo...* `Radar`*Server*, 47 pages), (2) the software to easily visualize Doppler radar data (*HowTo...* `Radar`DB *View*, 43 pages), and (3) the details of the monitoring station at Colima (*HowTo...* Colima System, 35 pages), including a chapter that summarizes known bugs and issues and their respective solutions. The radar software was originally written by Malte Vöge, and I did only minor changes and adjustments. Therefore I do not include the complete manuals (1 and 2) here. The manual of the Colima monitoring station contains many informations that are only interesting for the responsible person on site. Therefore it is also not part of this work. If one is interested in reading one of those manuals, they can be provided upon request.

C.1 Calibration of the Doppler Radars

Because the radar beam is invisible and the geometry of transmitter and antenna hinders a good estimation of the beam target location, we install a telescopic sight at the radar box. This telescopic sight needs to be calibrated to be aligned in parallel to the radar beam. This calibration needs to be done every time the so-called 'calibration-wing' (see Fig. C.1) has been unmounted (or even if somebody accidentally turned one of the screws).

To find the beam target location, we setup a synthetic signal, i.e. a constantly moving reflector. This is realized by four corner reflectors attached to an electric motor, further named propeller (see Fig. C.2). The propeller is fixed to a mast and set up at ∼100–300 m distance from the radar. The best position has a direct line of sight with no vegetation in between. Every moving item near the radar beam disturbs the signal of the propeller and may even completely cover it.

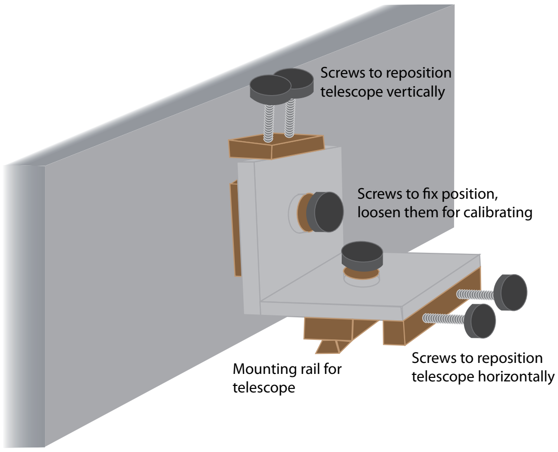

Figure C.1: Instrument to adjust the telescope horizontally and vertically to the beam target location.

For the calibration a minimum of two people is needed, one handles the antenna (aiming at different locations), while the other one observes the real-time signal and reports whether the signal increases or decreases.

The calibration procedure is to scan in the vertical and horizontal direction for the best signal (highest echo power). When the absolute maximum is found, which means that the radar beam aims at the approaching corner reflector, the telescope has to be aligned to the radar beam such that it also points to the propeller. The offset of telescopic sight and the center of the radar beam has to be accounted for during the alignment (see Fig. C.2).

If the aiming of the telescopic sight is slightly wrong, telescope and radar beam are not parallel. With a calibration at short distances the angle between them might be rather big and the mis-aiming of the radar increases with greater distance. To avoid this error, an aiming triangle should be used (see Fig. C.2). Another option is to redo the calibration with the propeller installed at increasing distances.

C.2 Event Picking and Overview Plots

One way to get a compact and first overview of the recorded data is to plot the whole data as black and white velocigram (or “Flo-Plot”, named after the inventor Florian Ziemen).

The software `mvr_overview` produces a velocigram rotated by 90°. Time is from bottom to top with major tick marks every hour and minor tick marks every 15 min. The x-axis is composed of all recorded range gates. One horizontal line equals one complete spectrum, where the reflected energy is color coded. A vertical line resembles the time evolution of the amount of particles that move at the corresponding velocity. In Fig. C.3 6 hours of data from Colima volcano (June 24, 2007, 12:00–18:00 UTC) are plotted. Here spectra consist of 5 range gates. The first vertical line on the left is the line of zero velocity of the second range gate. Because all range gates have the same number of velocity lines, the other lines

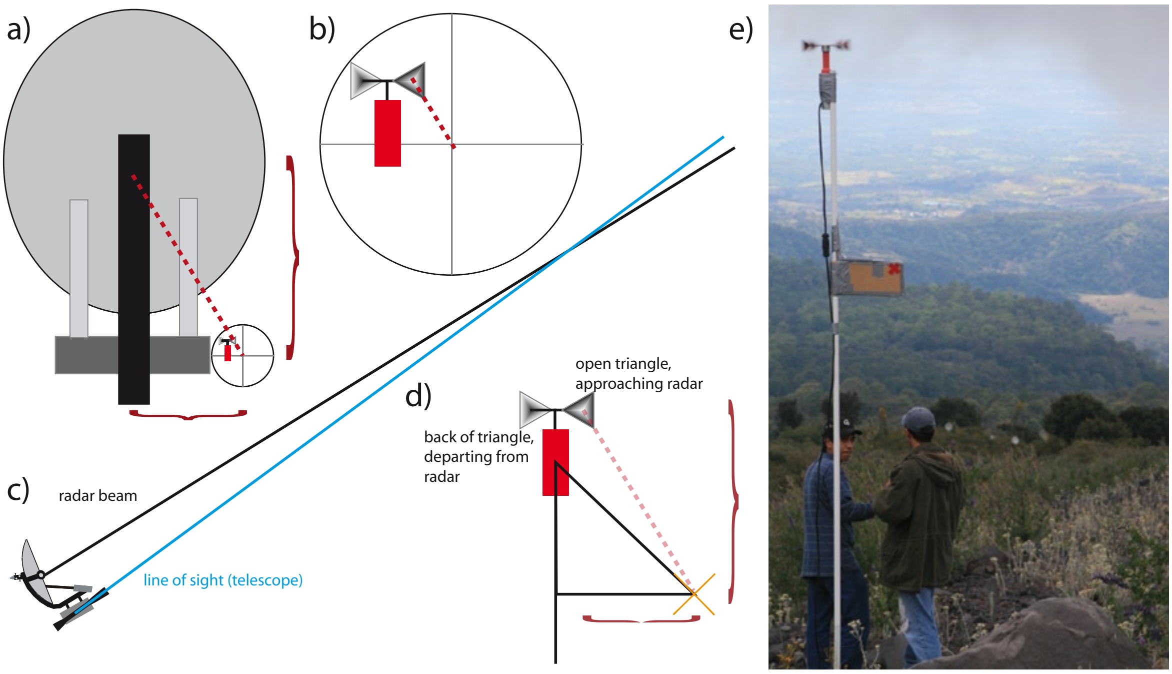

Figure C.2: a) Offset of potential radar beam center and telescopic sight (attached to the radar box). b) Schematic view through the telescopic sight. The radar beam focuses on the approaching corner reflector, the telescopic sight must not focus there. c) Possible parallax due to false aiming of the telescopic sight. In 3000 m distance (above the crater) the radar beams actual target might lie several tens of meters below the telescopes field of view. d) Schematic drawing of an aiming triangle. The telescope should be aimed to the yellow cross (lower right) to avoid false calibration. e) Propeller and aiming 'triangle' in Colima (re-calibration in Feb. 2010). The two white dots right of the heads of the two Mexican students are the two Doppler radar antennas (photographed by Jörg Hasenclever). Note that the schematic drawings (a–d) are valid for the lower radar, which has the telescopic sight attached to the right. The picture in (e), however, shows the calibration setup of the upper radar, at which the telescope is attached to the left.

of zero velocity (equally spaced vertical lines) can easily be found. The residual vertical lines (slightly changing horizontal position with time) are disturbances and should be ignored. Constant horizontal lines are so called 'panic spectra'. Both types of lines are artifacts from the radars internal processing and will hopefully be suppressed in the future.

In Fig. C.3 one eruption at 13:46 UTC can be identified. The main energy is concentrated in range gates 2 and 3. The increased echo power at 16:30 and from 17:00 UTC to the end is a clear signature of rain. Because rain drops are mainly falling, the echo power is confined to the positive velocities, i.e. right of the zero velocity lines. A second indicator for rain is the duration and persistence of the signal and the fact that is is visible in all range gates. Using these overview plots (6h-long) the interesting time frames for a second round of event search can be picked. All identified time frames are loaded into the software `RadarDB` *View* where the exact beginning and end of the eruptions (i.e. the time stamps of the first and last relevant spectrum) are picked manually.

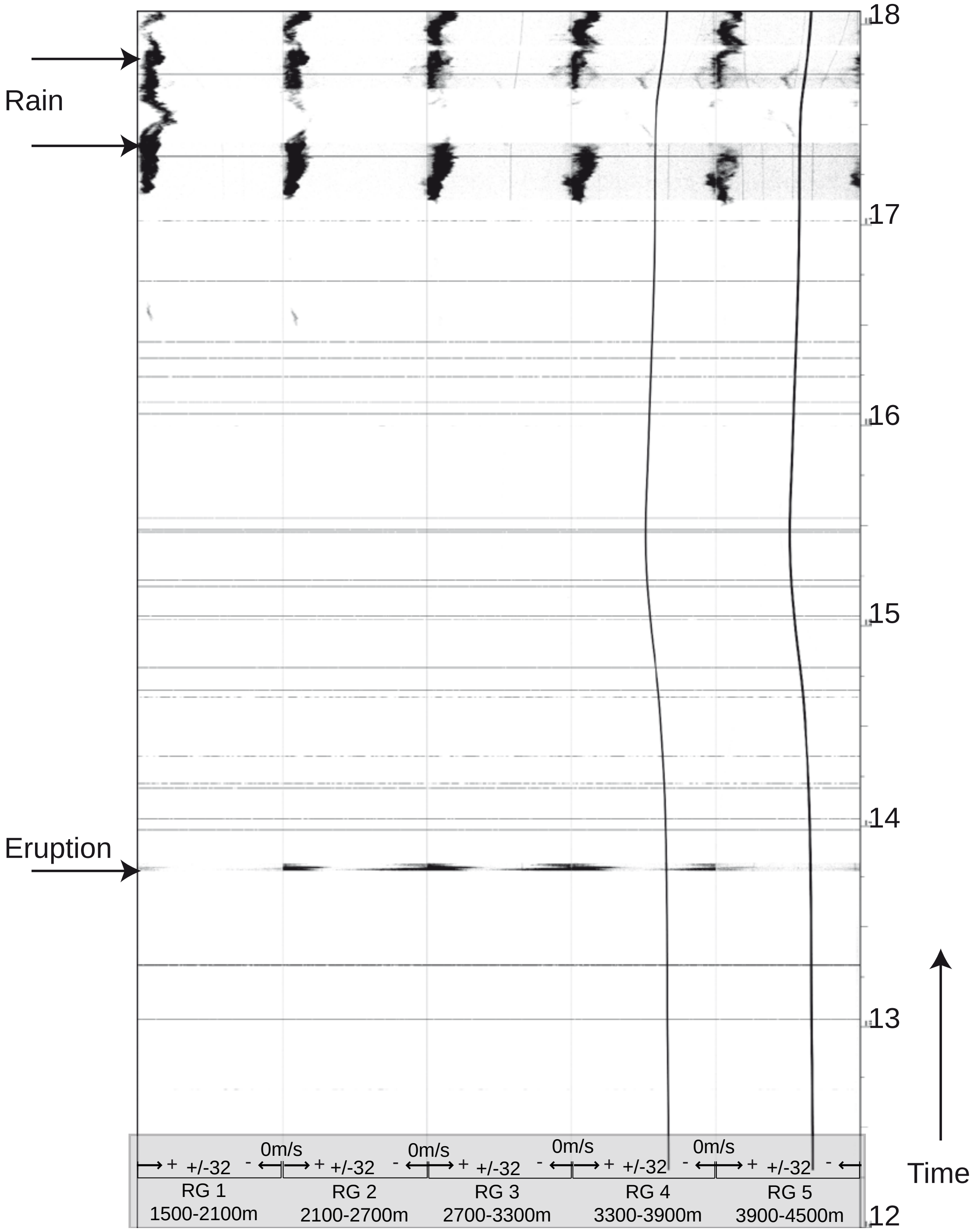

Figure C.3: Example overview plot of Colima volcano, June 24, 2007, 12:00–18:00 UTC. Time is from bottom to top, labeled each hour, major tick marks every 30 minutes and minor ticks every 15 minutes. At this time 5 range gates (distance intervals) were recorded. They are plotted on the x-axis next to each other with the distance increasing from left to right. The left half of a range gate shows the positive velocities, associated to falling particles, the right half negative velocities, which can be attributed to rising particles. Therefore rain (top hour) can be easily distinguished from events (at 13:46 UTC) due to their velocities (mainly falling particles versus fast rising particles, respectively).

C.3 Data Download

As described before, data of both Doppler radars, the camera, and the solar charger, as well as some logging information is handled and stored by the data logger. The following table displays the relevant folders, their paths and contents.

D:\RadarDataMVR4\'yyyymm'	.log, .raw, .bz2-files
\RadarDataMVR3\'yyyymm'	.log, .raw, .bz2-files
\ColimaCam\Pictures	.jpg-files
\TriStar\'yyyymm'	text files
\Videos	.avi-files
C:\	*.cfg-files
\logs	some log files (`Radar`*Server*, WatchDogs)
\Windows\system32	domtime*.log

Because a simple batch-file download would rely on Windows build-in copy routines, which might not account for file updates (log-files) or network outages, we use a software called AllwaySync (`www.allwaysync.com`).

The software AllwaySync is commonly used to synchronize several computer's home directories to guarantee similar complete up-to-date directory trees on every computer, the user logs on. Here these abilities are used to grant integrity of the downloaded data. AllwaySync uses several intelligent algorithms to identify the most recent version of files, hereby comparing modification date, size, and other crucial parameters.

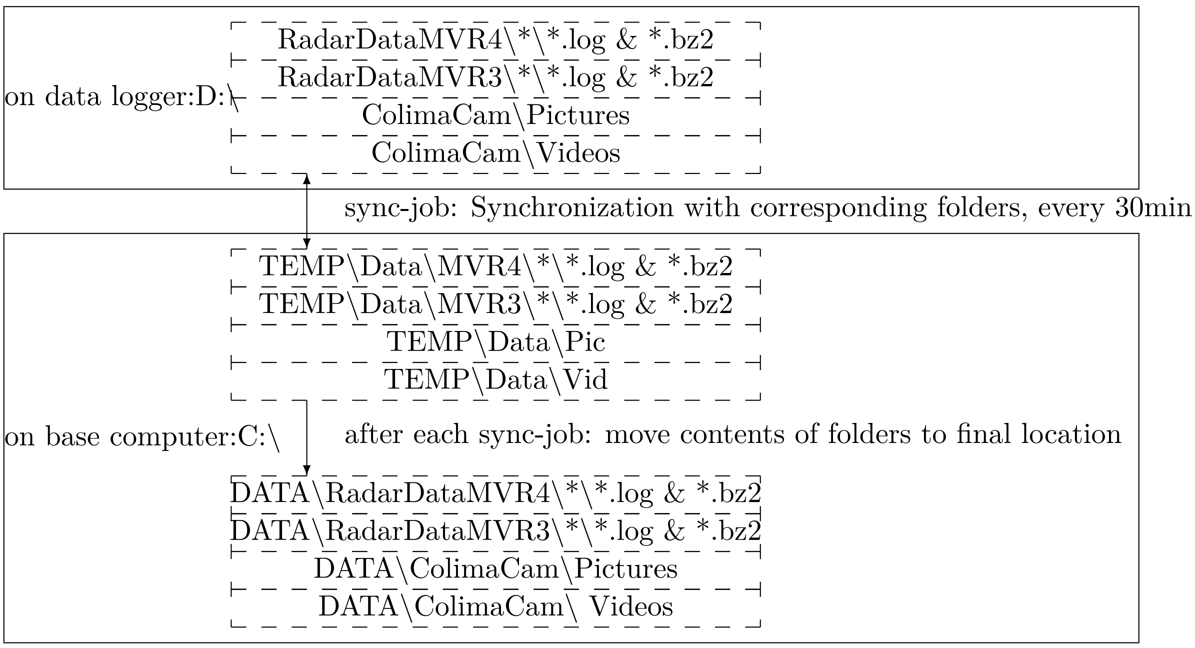

Figure C.4: Scheme of data download.

AllwaySync starts `mv_after_sync.bat` when a sync-job has finished, i.e. when all new data has been copied to the TEMP-directory on the base computer. This batch-file first passes all names of the downloaded files to a log-file (in DATA-directory). Then all files are unzipped (keeping the zipped files) and imported into the MySQL-database. This is done by a standalone batch-script called `import_all.bat`. After successful import, the unzipped files are deleted and the zipped files are moved to their final destination in DATA-directory.

Because of the last performed action 'delete' (second part of the 'move' command) in the 'TEMP'-folder, the previously copied files will be deleted on the data logger upon the next sync-job, unless they have been changed on logger side. This usually concerns only the *.log-files, as only zipped data files are synced and zipping is done after completion of a data file.

Every first of a month, all *.raw files that have not been zipped by `Radar`*Server*(e.g. manual program stop, reboot of the system) and that hence have not been transfered by AllwaySync, are zipped by a batch-file (prepare-monthly-files.bat). At the next sync-job, they are treated like every other file and hence they will be downloaded. This batch file runs as a scheduled task on the data logger, every first of month at noon (UTC).

Two days later (third of month at 6:00 AM UTC) a job `send_monthly_files.bat` is executed. It packs last months data into tar-balls and sends them to `ftp.zmaw.de` (Hamburg University's ftp-server), where a scheduled task-batch script downloads the data to my computer (at fifth of month at noon UTC).

Bibliography

Ackerman, T. P. and Toon, O. B., 1981. Absorption of visible radiation in atmosphere containing mixtures of absorbing and nonabsorbing particles. *Applied Optics*, 20(20):3661 – 3667. doi: 10.1364/AO.20.003661.

Adams, R. J., Perger, W. F., Rose, W. I. and Kostinski, A., 1996. Measurements of the complex dielectric constant of volcanic ash from 4 to 19 GHz. *J Geophys Res*, 101(B4): 8175–8185. doi: 10.1029/96JB00193.

Barmin, A., Melnik, O. and Sparks, R. J. S., 2002. Periodic behavior in lava dome eruptions. *Earth Planet Sci Lett*, 199:173–184. doi: 10.1016/S0012-821X(02)00557-5.

Barrick, D. E. FM/CW radar signals and digital processing. Technical Report ERL 283-WPL 26, NOAA, Environmental Research Laboratories, Boulder, Co., July 1973.

Barsotti, S. and Neri, A., 2008. The VOL-CALPUFF model for atmospheric ash dispersal: 2. application to the weak Mount Etna plume of july 2001. *J Geophys Res*, 113:B03209. doi: 10.1029/2006JB004624.

Bear, J. *Dynamics of fluids in porous media*. American Elsevier Publishing Company, Inc., New York, ausgabe 1 edition, 1972.

Blackburn, E. A., Wilson, L. and Sparks, R. S. J., 1976. Mechanisms and dynamics of strombolian activity. *J Geol Soc*, 132:429–440.

Bluth, J. S. and Rose, W. I., 2004. Observations of eruptive activity at Santiaguito volcano, Guatemala. *J Volcanol Geotherm Res*, 136:297–302. doi: 10.1016/j.jvolgeores.2004.06.001.

Bonadonna, C. and Phillips, J. C., 2003. Sedimentation from strong volcanic plumes. *J Geophys Res*, 108(B7):2340. doi: 10.1029/2002JB002034.

Carcano, S., Bonaventura, L., Esposti Ongaro, T. and Neri, A. Non-equilibrium and transient processes in under-expanded volcanic jets. In *European Geosciences Union General Assembly*, number EGU2012-5568, 2012.

Carey, S. and Sparks, R. S. J., June 1986. Quantitative models of the fallout and dispersal of tephra from volcanic eruption columns. *Bull Volcanol*, 48(2-3):109 – 125. doi: 10.1007/BF01046546.

Caricchi, L., Pommier, A., Pistone, M., Castro, J., Burgisser, A. and Perugini, D., 2011. Strain-induced magma degassing: insights from simple-shear experiments on bubble bearing melts. *Bull Volcanol*, 73(9):1245–1257. doi: 10.1007/s00445-011-0471-2.

Chojnicki, K., Clarke, A. B. and Phillips, J. C., 2006. A shock-tube investigation of the dynamics of gas-particle mixtures: implications for explosive volcanic eruptions. *Geophys Res Lett*, 33:L15309. doi: 10.1029/2006GL026414.

Chouet, B., Hamisevicz, N. and McGetchin, T. R., 1974. Photoballistics of volcanic jet activity at Stromboli, Italy. *J Geophys Res*, 79:4961–4976. doi: 10.1029/JB079i032p04961.

Clarke, A. B., Voight, B., Neri, A. and Machedonio, G., February 2002. Transient dynamics of vulcanian explosions and column collapse. *Nature*, 415:897–901. doi: 10.1038/415897a.

Collier, L., Neuberg, J., Lensky, N., Lyakhovsky, V. and Navon, O., 2006. Attenuation in gas-charged magma. *J Volcanol Geotherm Res*, 153(1-2):21–36. ISSN 0377-0273. doi: doi:10.1016/j.jvolgeores.2005.08.009.

Courant, R., Friedrichs, K. and Lewy, H., 1928. Über die partiellen Differenzengleichungen der mathematischen Physik. *Mathematische Annalen*, 100(1):32–74. doi: 10.1007/BF01448839.

Currie, N., editor. *Radar reflectivity measurement: techniques and applications.* Artech House, Norwood, MA, 1989.

Dave, J. V., 1969. Scattering of electromagnetic radiation by a large, absorbing sphere. *IBM J Res Dev*, 13(3):302.

de Michieli Vitturi, M., Clarke, A. B., Neri, A. and Voight, B., 2008. Effects of conduit geometry on magma ascent dynamics in dome-forming eruptions. *Earth Planet Sci Lett*, 272:567 – 578. doi: 10.1016/j.epsl.2008.05.025.

Di Muro, A., Neri, A. and Rosi, M., 2004. Contemporaneous convective and collapsing eruptive dynamics: The transitional regime of explosive eruptions. *Geophys Res Lett*, 31: L10607. doi: 10.1029/2004GL019709.

Dixon, J. and Stolper, E., 1995. An experimental study of water and carbon dioxide solubilities in mid-ocean ridge basaltic liquids. part II: Applications to degassing. *Journal of Petrology*, 36(6):1633. ISSN 0022-3530.

Donnadieu, F., Gouhier, M., Fournet-Fayard, J. and Hervier, C. Applications of pulsed ground-based Doppler radar to the study and monitoring of volcanoes. In *Ground-based radars for volcanoes workshop*. Environmental Systems Science Centre, Univ. Reading (UK), 2008.

Donnadieu, F., Valade, S. and Moune, S., 2011. Three dimensional transport speed of wind-drifted ash plumes using ground-based radar. *Geophys Res Lett*, 38:L18310. doi: 10.1029/2011GL049001.

Dubosclard, G., Cordesses, R., Allard, P., Hervier, C., Coltelli, M. and Kornprobst, J., 1999. First testing of a volcano Doppler radar (VOLDORAD) at Mount Etna, Italy. *Geophys Res Lett*, 26(22):3389–3392. doi: 10.1029/1999GL008371.

Dubosclard, G., Donnadieu, F., Allard, P., Cordesses, R., Hervier, C., Coltelli, M., Privitera, E. and Kornprobst, J., 2004. Doppler radar sounding of volcanic eruption dynamics at Mount Etna. *Bull Volcanol*, 66:443–456. doi: 10.1007/s00445-003-0324-8.

Edmonds, M. and Herd, R. A., 2007. A volcanic degassing event at the explosive-effusive transition. *Geophys Res Lett*, 34. doi: 10.1029/2007GL031379.

Esposti Ongaro, T., Cavazzoni, C., Erbacci, G., Neri, A. and Salvetti, M. V., 2007. A parallel multiphase flow code for the 3D simulation of explosive volcanic eruptions. *Parallel Computing*, 33:541–560. doi: 10.1016/j.parco.2007.04.003.

Esposti Ongaro, T., Clarke, A. B., Neri, A., Voight, B. and Widiwijayanti, C., 2008. Fluid dynamics of the 1997 Boxing Day volcanic blast on Montserrat, West Indies. *J Geophys Res*, 113:B03211. doi: 10.1029/2006JB004898.

Ewert, J. W. and Miller, C. D. The USGS/OFDA volcano disaster assistance program. U.S.Geological Survey Open-File Report 95-553, 1995. URL: http://vulcan.wr.usgs.gov/Vdap/Publications/OFR95-553/OFR95-553.html.

Farr, T. G., Rosen, P. A., Caro, E., Crippen, R., Duren, R., Hensley, S., Kobrick, M., Paller, M., Rodriguez, E., Roth, L., Seal, D., Shaffer, S., Shimada, J., Umland, J., Werner, M., Oskin, M., Burbank, D. and Alsdorf, D., 2007. The Shuttle radar topography mission. *Rev Geophys*, 45:RG2004. doi: 10.1029/2005RG000183.

Gerst, A. *The first second of a strombolian volcanic eruption.* PhD thesis, Department of Geosciences, University of Hamburg, 2010. URL: http://www.sub.uni-hamburg.de/opus/volltexte/2010/4251/. urn: urn:nbn:de:gbv:18-42516.

Gerst, A., Hort, M., Kyle, P. R. and Vöge, M., 2008. 4D velocity of strombolian eruptions and man-made explosions derived from multiple Doppler radar instruments. *J Volcanol Geotherm Res*, 177(3):648–660. doi: 10.1016/j.jvolgeores.2008.05.022.

Gerst, A., Hort, M., Aster, R. C., Johnson, J. B. and Kyle, P. R., 2012. The first second of a Strombolian volcanic eruption — energies, pressures, mechanisms. *submitted to J Geophys Res*.

Gonnermann, H. M. and Manga, M., 2003. Explosive volcanism may not be an inevitable consequence of magma fragmentation. *Nature*, 426:432–435. doi: 10.1038/nature02138.

González-Mellado, A. O., De la Cruz-Reyna, S. and Navarro-Ochoa, C., 2011. Applications of a simplified equation of state for the density of silicate hydrous magmas: The Volcán de Colima (Mexico) buoyancy-driven dome growth process similarities and differences with the popocatépetl volcano domes. *J Volcanol Geotherm Res*, 205:17–29. doi: 10.1016/j.jvolgeores.2011.03.009.

Gouhier, M. and Donnadieu, F., 2008. Mass estimations of ejecta from Strombolian explosions by inversion of Doppler radar measurements. *J Geophys Res*, 113(B10202):1–17. doi: 10.1029/2007JB005383.

Gouhier, M. and Donnadieu, F., 2011. Systematic retrieval of ejecta velocities and gas fluxes at Etna volcano using L-Band Doppler radar. *Bull Volcanol*, 73(9):1139–1145. doi: 10.1007/s00445-011-0500-1.

Graf, H.-F., Herzog, M., Oberhuber, J. M. and Textor, C., 1999. Effect of environmental conditions on volcanic plume rise. *J Geophys Res*, 104(D20):24309–24320. doi: 10.1029/1999JD900498.

Hale, A. J. and Wadge, G., 2003. Numerical modelling of the growth dynamics of a simple silicic lava dome. *Geophys Res Lett*, 30(19). doi: 10.1029/2003GL018182.

Harris, A., Flynn, L., Matías, O. and Rose, W., 2001. The thermal stealth flows of Santiaguito dome, Guatemala: Implications for the cooling and emplacement of dacitic block-lava flows. *Geol Soc Am Bull*, 114:533–546.

Harris, A. J. L. and Ripepe, M., 2007. Synergy of multiple geophysical approaches to unravel explosive eruption conduit and source dynamics — A case study from Stromboli. *Chemie Erde-Geochemistry*, 67:1–35. doi: 10.1016/j.chemer.2007.01.003.

Harris, A. J. L., Rose, W. I. and Flynn, L. P., 2003. Temporal trends in lava dome extrusion at Santiaguito 1922–2000. *Bull Volcanol*, 65:77–89. doi: 10.1007/s00445-002-0243-0.

Heliker, C. and Mattox, T. N. *The First Two Decades of the Pu'u 'Ō'ō-Kūpaianaha Eruption: Chronology and Selected Bibliography*, volume 1676 of *Professional Paper*, chapter 1, pages 1–28. U.S. Geological Survey, 2003. URL: http://pubs.usgs.gov/pp/pp1676/pp1676_01.pdf.

Herzog, M. and Graf, H.-F., 2010. Applying the three-dimensional model ATHAM to volcanic plumes: Dynamic of large co-ignimbrite eruptions and associated injection heights for volcanic gases. *Geophys Res Lett*, 37:L19807. doi: 10.1029/2010GL044986.

Herzog, M., Graf, H.-F., Textor, C. and Oberhuber, J. M., 1998. The effect of phase changes of water on the development of volcanic plumes. *J Volcanol Geotherm Res*, 87:55 – 74.

Holland, A. S. P., Watson, I. M., Phillips, J. C., Caricchi, L. and Dalton, M. P., 2011. Degassing processes during lava dome growth: Insights from Santiaguito lava dome, Guatemala. *J Volcanol Geotherm Res*, 202:153–166. doi: 10.1016/j.jvolgeores.2011.02.004.

Hort, M. and Seyfried, R., 1998. Volcanic eruption velocities measured with a micro radar. *Geophys Res Lett*, 25(1):113–116. doi: 10.1029/97GL03482.

Hort, M., Seyfried, R. and Vöge, M., 2003. Radar Doppler velocimetry of volcanic eruptions: theoretical considerations and quantitative documentation of changes in eruptive behaviour at Stromboli Volcano, Italy. *Geophys J Int*, 154:515–532. doi: 10.1046/j.1365-246X.2003.01982.x.

Hort, M., Vöge, M., Seyfried, R. and Ratdomopurbo, A., 2006. In situ observation of dome instabillities at Merapi Volcano, Indonesia: A new tool for hazard mitigation. *J Volcanol Geotherm Res*, 153:301–312. doi: 10.1016/j.jvolgeores.2005.12.007.

Hort, M., Scharff, L., Gerst, A., Meier, K., Ripepe, M. and Johnson, J. B. How do volcanoes deform immediately prior to an eruption: Observations of deformation inside a vent and on an active dome. In *Eos Trans. AGU Fall Meet. Suppl.*, 2010.

Huppert, H. E. and Woods, A. W., 2002. The role of volatiles in magma chamber dynamics. *Nature*, 420:493–495. doi: 10.1038/nature01211.

Jellinek, A. M. and Bercovici, D., 2011. Seismic tremors and magma wagging during explosive volcanism. *Nature*, 470:522–526. doi: 10.1038/nature09828.

Johnson, J. B. and Lees, J. M., 2000. Plugs and chugs—seismic and acoustic observations of degassing explosions at Karymsky, Russia and Sangay, Ecuador. *Journal of Volcanology and Geothermal Research*, 101(1-2):67 – 82. ISSN 0377-0273. doi: 10.1016/S0377-0273(00)00164-5.

Johnson, J. B. and Lees, J. M., 2010. Sound produced by the rapidly inflating Santiaguito lava dome, Guatemala. *Geophys Res Lett*, 37(L22305). doi: 10.1029/2010GL045217.

Johnson, J. B., Harris, A. J., Sahetapy-Engel, S. T., Wolf, R. and Rose, W. I., 2004. Explosion dynamics of pyroclastic eruptions at Santiaguito Volcano. *Geophys Res Lett*, 31:L06610. doi: 10.1029/2003GL019079.

Johnson, J. B., Lees, J. M., Gerst, A., Sahagian, D. and Varley, N., November 2008. Long-period earthquakes and co-eruptive dome inflation seen with particle image velocimetry. *Nature*, 456:377–381. doi: 10.1038/nature07429.

Johnson, J. B., Lees, J. M. and Varley, N. R., 2011. Characterizing complex eruptive activity at Santiaguito, Guatemala using infrasound semblance in networked arrays. *J Volcanol Geotherm Res*, 199:1–14. doi: 10.1016/j.jvolgeores.2010.08.005.

Jones, K. R. and Johnson, J. B., 2011. Mapping complex vent eruptive activity at Santiaguito, Guatemala using network infrasound semblance. *J Volcanol Geotherm Res*, 199:15–24. doi: 10.1016/j.jvolgeores.2010.08.006.

Julian, B. R., 1994. Volcanic tremor: Nonlinear excitation by fluid flow. *J Geophys Res*, 99 (B6):11859–11877. doi: 10.1029/93JB03129.

Kienle, J. and Shaw, G. E., 1979. Plume dynamics, thermal energy and long-distance transport of vulcanian eruption clouds from Augustine Volcano, Alaska. *J Volcanol Geotherm Res*, 6:139–164. doi: 10.1016/0377-0273(79)90051-9.

Klug, C. and Cashman, K. V., 1996. Permeability development in vesiculating magmas: implications for fragmentation. *Bull Volcanol*, 58:87–100.

Koh, G., 1992. Dielectric constant of ice at 26.5–40 GHz. *J Appl Phys*, 71(10):5119–5122.

Lavallée, Y., Benson, P. M., Heap, M. J., Flaws, A., Hess, K.-U. and Dingwell, D. B., 2012. Volcanic conduit failure as a trigger to magma fragmentation. *Bull Volcanol*, 74:11–13. doi: 10.1007/s00445-011-0544-2.

Lees, J. M. and Bolton, E. W. Pressure cookers as volcano analogues. In *EOS Trans. AGU, Fall Meet. Suppl.*, number S22C-10, 1998.

Lesage, P., Mora, M. M., Alvarado, G. E., Pacheco, J. and Métaxian, J.-P., 2006. Complex behaviour and source model of the tremor at Arenal volcano, Costa Rica. *J Volcanol Geotherm Res*, 157:49–59. doi: 10.1016/j.jvolgeores.2006.03.047.

Lighthill, J. *Waves in Fluids*. Cambridge University Press, New York, 1978.

Löffler-Mang, M., Kunz, M. and Schmid, W., 1999. On the performance of a low-cost K-band Doppler radar for quantitative rain measurements. *J Atmos Oceanic Technol*, 16:379–387. doi: 10.1175/1520-0426(1999)016<0379:OTPOAL>2.0.CO;2.

Marchetti, E., Ripepe, M., Harris, A. J. L. and Donne, D. D., 2009. Tracing differences between vulcanian and strombolian explosions using infrasonic and thermal radiation energy. *Earth Planet Sci Lett*, 279:273–281. doi: 10.1016/j.epsl.2009.01.004.

Marzano, F. S., Barbieri, S., Vulpiani, G. and Rose, W. I., November 2006. Volcanic ash cloud retrieval by ground-based microwave weather radar. *IEEE Trans Geosci Remote Sens*, 44(11):3235 – 3246. doi: 10.1109/TGRS.2006.879116.

Massol, H. and Jaupart, C., 2009. Dynamics of magma flow near the vent: Implications for dome eruptions. *Earth Planet Sci Lett*, 279:185–196. doi: 10.1016/j.epsl.2008.12.041.

Mastin, L. G., Guffanti, M., Servanckx, R., Webley, P., Barsotti, S., Dean, K., Durant, A., Evert, J. W., Neri, A., Rose, W. I., Schneider, D., Siebert, L., Stunder, B., Swanson, G., Tupper, A., Volentik, A. and Waythomas, C. F., 2009. A multidisziplinary effort to assign realistic source parameters to models of volcanoc ash-cloud transport and dispersion during eruptions. *J Volcanol Geotherm Res*, 186:10–21. doi: 10.1016/j.jvolgeores.2009.01.008.

Meier, K., Hort, M., Tessmer, E. and Wassermann, J., 2012. Infrasound wave propagation in the presence of small volcanic clouds. *J Geophys Res*, submitted.

Meissner, T. and Wentz, F. J., 2004. The complex dielectric constant of pure and sea water from microwave satellite observations. *IEEE Trans Geosci Remote Sens*, 42(9):1836–1849. doi: 10.1109/TGRS.2004.831888.

Melnik, O. and Sparks, R. S. J., 2005. Controls on conduit magma flow dynamics during lava dome building eruptions. *J Geophys Res*, 110:B02209. doi: 10.1029/2004JB003183.

Meschede, D., editor. *Gerthsen Physik*. Springer, 2002.

Mie, G., 1908. Beiträge zur Optik trüber Medien, speziell kolloidaler Metallösungen. *Annalen der Physik*, 330(3):377–445. doi: 10.1002/andp.19083300302.

Miller, T. P. and Casadevall, T. J. *Encyclopedia of Volcanoes*, chapter Volcanic Ash Hazards to Aviation, pages 915–930. Academic Press, San Diego, 2000.

Neri, A. and Macedonio, G., 1996. Numerical simulation of collapsing volcanic columns with particles fo two sizes. *J Geophys Res*, 101(B4):8153–8174. doi: 10.1029/95JB03451.

Neri, A., Papale, P. and Macedonio, G., 1998. The role of magma composition and water content in explosive eruptions: 2. pyroclastic dispersion dynamics. *J Volcanol Geotherm Res*, 87:95–115. doi: 10.1016/S0377-0273(98)00102-4.

Neri, A., Di Muro, A. and Rosi, M., 2002. Mass partition during collapsing and transitional columns by using numerical suimulations. *J Volcanol Geotherm Res*, 115:1–18. doi: 10.1016/S0377-0273(01)00304-3.

Neri, A., Esposti Ongaro, T., Macedonio, G. and Gidaspow, D., 2003. Multiparticle simulation of collapsing volcanic columns and pyroclastic flow. *J Geophys Res*, 108. doi: 10.1029/2001JB000508.

Neri, A., Esposti Ongaro, T., Menconi, G., De'Michieli Vitturi, M., Cavazzoni, C., Erbacci, G. and Baxter, P. J., 2007. 4d simulation of explosive eruption dynamics at Vesuvius. *Geophys Res Lett*, 34:L04309. doi: 10.1029/2006GL028597.

Oberhuber, J. M., Herzog, M., Graf, H.-F. and Schwanke, K., 1998. Volcanic plume simulation on large scales. *J Volcanol Geotherm Res*, 87(1-4):29–53. ISSN 0377-0273. doi: 10.1016/S0377-0273(98)00099-7.

Ogden, D., 2011. Fluid dynamics in explosive volcanic vents and craters. *Earth Planet Sci Lett*, 312:401–410. doi: 10.1016/j.epsl.2011.10.032.

Ogden, D. E., Glatzmaier, G. A. and Wohletz, K. H., 2008a. Effects of vent overpressure on buoyant eruption columns: Implications for plume stability. *Earth Planet Sci Lett*, 268: 283–292. doi: 10.1016/j.epsl.2008.01.014.

Ogden, D. E., Wohletz, K. H., Glatzmaier, G. A. and Brodsky, E. E., 2008b. Numerical simulations of volcanic jets: Importance of vent overpressure. *J Geophys Res*, 113:B02204. doi: 10.1029/2007JB005133.

Orescanin, M. M., Austin, J. M. and Kieffer, S. W., 2010. Unsteady high-pressure flow experiments with applications to explosive volcanic eruptions. *J Geophys Res*, 115:B06206. doi: 10.1029/2009JB006985.

Parfitt, E. A. and Wilson, L. *Fundamentals of Physical Volcanology*. Blackwell Publishing, 2008.

Patrick, M., Varley, N., Ramos, E., Blankenbicker, A. and Johnson, J. Ash plume dynamics at Santiaguito volcano, Guatemala from thermal and high resolution video. In *EOS Trans. AGU, Fall Meet. Suppl.*, volume 88, 2007. Abstract V31E-0707.

Patrick, M. R., 2007a. Dynamics of strombolian ash plumes from thermal video: motion, morphology, and air entrainment. *J Geophys Res*, 112:B06202. doi: 10.1029/2006JB004387.

Patrick, M. R., 2007b. The gas content and buoyancy of strombolian ash plumes. *J Volcanol Geotherm Res*, 166:1–6. doi: 10.1016/j.jvolgeores.2007.06.001.

Pfeiffer, T., Costa, A. and Macedonio, G., 2005. A model for the numerical simulation of tephra fall deposits. *J Volcanol Geotherm Res*, 140:273–294. doi: 10.1016/j.jvolgeores.2004.09.001.

Ripepe, M., Rossi, M. and Saccorotti, G., 1993. Image processing of explosive activity at Stromboli. *J Volcanol Geotherm Res*, 54:335–351. doi: 10.1016/0377-0273(93)90071-X.

Sahetapy-Engel, S. T. and Harris, A. J. L., 2009a. Thermal structure and heat loss at the summit crater of an active lava dome. *Bull Volcanol*, 71(1):15–28. doi: 10.1007/s00445-008-0204-3.

Sahetapy-Engel, S. T. and Harris, A. J. L., 2009b. Thermal-image-derived dynamics of vertical ash plumes at Santiaguito volcano, Guatemala. *Bull Volcanol*, 71(7):827–830. doi: 10.1007/s00445-009-0284-8.

Sahetapy-Engel, S. T., Harris, A. J. L. and Marchetti, E., 2008. Thermal, seismic and infrasound observations of persistent explosive activity and conduit dynamics at Santiaguito lava dome, Guatemala. *J Volcanol Geotherm Res*, 173:1–14. doi: 10.1016/j.jvolgeores.2007.11.026.

Sahetapy-Engel, S. T. M., Flynn, L. P., Harris, A. J. L., Bluth, G. J., Rose, W. I. and Matias, O., 2004. Surface temperature and spectral measurements at Santiaguito lava dome, Guatemala. *Geophys Res Lett*, 31:L19610. doi: 10.1029/2004GL020683.

Sanchez Bennett, E. H., Rose, W. I. and Conway, F. M., 1992. Santa María, Guatemala: A decade volcano. *EOS Trans Am Geophys Union*, 73(48):521–522.

Sanderson, R. W., Johnson, J. B. and Lees, J. M., 2010. Ultra-long period seismic signals and cyclic deflation coincident with eruptions at Santiaguito volcano, Guatemala. *J Volcanol Geotherm Res*, 198:35–44. doi: 10.1016/j.jvolgeores.2010.08.007.

Scharff, L. Die Eruptionsdynamik des Stromboli: Eine kombinierte Auswertung von Doppler Radar und Infrasound Daten. Master's thesis, Universität Hamburg, 2006.

Scharff, L., Gerst, A., Hort, M. and Johnson, J. B. The dynamics of explosions at Santiaguito volcano, Guatemala. In *Eos Trans. AGU Fall Meet. Suppl.*, volume 88(52), pages Abstract V31E–0718. Eos Trans. AGU, 2007.

Scharff, L., Hort, M., Harris, A. J., Ripepe, M., Lees, J. and Seyfried, R., 2008. Eruption dynamics of the SW crater of Stromboli volcano, Italy. *J Volcanol Geotherm Res*, 176:565 – 570. doi: 10.1016/j.jvolgeores.2008.05.008.

Scharff, L., Hasenclever, J. and Hort, M. Oscillating dome at Santiaguito? A simple model to explain inter-eruptive pulses. In *Eos Trans. AGU Fall Meet. Suppl.*, volume 90(52), pages Abstract V23D–2146. Eos Trans. AGU, 2009.

Scharff, L., Ziemen, F., Hort, M., Gerst, A. and Johnson, J. B., 2012. A detailed view into the eruption clouds of Santiaguito volcano, Guatemala, using Doppler radar. *J Geophys Res*, 117. doi: 10.1029/2011JB008542.

Sengers, J. V. and Watson, J. T. R., 1986. Improved international formulations for the viscosity and thermal conductivity of water substance. *J Phys Chem Ref Data*, 15(4): 1291–1314.

Sparks, R. S. J., 1997. Causes and consequences of pressurisation in lava dome eruptions. *Earth Planet Sci Lett*, 150:177–189. doi: 10.1016/S0012-821X(97)00109-X.

Sparks, R. S. J., Bursik, M. I., Carey, S. N., Gilbert, J. S., Glaze, L. S., Siggurdsson, H. and Woods, A. W. *Volcanic plumes*. John Whiley, New York, 1997.

Steinberg, G. S. and Babenko, J. I., 1978. Experimental velocity and density determination of volcanic gases during eruption. *J Volcanol Geotherm Res*, 9(3):89–98.

Sulpizio, R., Capra, L., Sarocchi, D., Saucedo, R., Gavilanes-Ruiz, J. C. and Varley, N. R., 2010. Predicting the block-and-ash flow inundation areas at Volcán de Colima (Colima, Mexico) based on the present day (February 2010) status. *J Volcanol Geotherm Res*, 193: 49–66. doi: 10.1016/j.jvolgeores.2010.03.007.

Suzuki, Y. J., Koyaguchi, T., Ogawa, M. and Hachisu, I., 2005. A numerical study of turbulent mixing in eruption clouds using a three-dimensional fluid dynamics model. *J Geophys Res*, 110:B08201. doi: 10.1029/2004JB003460.

Taisne, B. and Jaupart, C., 2008. Magma degassing and intermittent lava dome growth. *Geophys Res Lett*, 35:L20310. doi: 10.1029/2008GL035432.

Textor, C., Graf, H.-F., Herzog, M. and Oberhuber, J. M., 2003. Injection of gases into the stratosphere by explosive volcanic eruptions. *J Geophys Res*, 108(D19):4606. doi: 10.1029/2002JD002987.

Textor, C., Graf, H.-F., Longo, A., Neri, A., Esposti Ongaro, T., Papale, P., Timmreck, C. and Ernst, G. G., 2005. Numerical simulation of explosive volcanic eruptions from the conduit flow to global atmospheric scales. *Annals of Geophysics*, 48:817–842. doi: 10.4401/ag-3237.

Textor, C., Graf, H.-F., Herzog, M., m> Oberhuber, J., Rose, W. I. and Ernst, G. G., 2006a. Volcanic particle aggregation in explosive eruption columns. part I: Parameterization of the microphysics of hydrometeors and ash. *J Volcanol Geotherm Res*, 150:359–377. doi: 10.1016/j.jvolgeores.2005.09.007.

Textor, C., Graf, H.-F., Herzog, M., m> Oberhuber, J., Rose, W. I. and Ernst, G. G., 2006b. Volcanic particle aggregation in explosive eruption columns. part II: Numerical experiments. *J Volcanol Geotherm Res*, 150. doi: 10.1016/j.jvolgeores.2005.09.008.

Todesco, M., Neri, A., Esposti Ongaro, T., Papale, P. and Rosi, M., 2006. Pyroclastic flow dynamics and hazard in a caldera setting: Application to Phlegrean Fields (Italy). *Geochem Geophys Geosyst*, 7(11). doi: 10.1029/2006GC001314.

Toon, O. B. and Ackerman, T. P., 1981. Algorithms for the calculation of scattering by stratified spheres. *Appl Opt*, 20(20):3657 – 3660. doi: 10.1364/AO.20.003657.

Tuffen, H., Dingwell, D. B. and Pinkerton, H., 2003. Repeated fracture and healing of silicic magma generate flow banding and earthquakes. *Geology*, 31(12):1089–1092.

Tuffen, H., Smith, R. and Sammonds, P. R., 2008. Evidence for seismogenic fracture of silicic magma. *Nature*, 453:511–514. doi: 10.1038/nature06989.

Turcotte, D. L. and Schubert, G. *Geodynamics*. Cambridge University Press, 2nd edition, 2002.

USGS. Shuttle radar topography mission, 3 arc second scene SRTM_n19w104, unfilled unfinished 2.0. Global Land Cover Facility, University of Maryland, College Park, Maryland, 2004a. URL: http://dds.cr.usgs.gov/srtm/version2_1/SRTM3/North_America/.

USGS. Shuttle radar topography mission, 3 arc second scene SRTM_n14w092, unfilled unfinished 2.0. Global Land Cover Facility, University of Maryland, College Park, Maryland, 2004b. URL: http://dds.cr.usgs.gov/srtm/version2_1/SRTM3/South_America/.

Valade, S. and Donnadieu, F., 2011. Ballistics and ash plumes discriminated by Doppler radar. *Geophys Res Lett*, 38(L22301). doi: 10.1029/2011GL049415.

Valade, S., Donnadieu, F., Lesage, P., Mora, M. M., Harris, A. J. and Alvarado, G. E., 2012. Explosion mechanisms at Arenal volcano, Costa Rica: An interpretation from integration of seismic and Doppler radar data. *J Geophys Res*, 117:B01309. doi: 10.1029/2011JB008623.

Varley, N. R., Arámbula-Mendoza, R., Reyes-Dávila, G., Stevenson, J. A. and Harwood, R., 2010. Long-period seismicity during magma movement at Volcán de Colima. *Bull Volcanol*, 2(9):1093–1107. doi: 10.1007/s00445-010-0390-7.

Vöge, M. *Doppler Radar Monitoring of Lava Dome processes at Merapi volcano, Indonesia*. PhD thesis, Institute of Geophysics, University of Hamburg, Hamburg, Germany, 2007.

Vöge, M. and Hort, M., 2008a. Automatic classification of dome instabilities based on Doppler radar measurements at Merapi volcano, Indonesia: Part I. *Geophys J Int*, 172:1188–1206. doi: 10.1111/j.1365-246X.2007.03605.x.

Vöge, M. and Hort, M., 2008b. Automatic classification of dome instabilities based on Doppler radar measurements at Merapi volcano, Indonesia: Part II. *Geophys J Int*, 172:1207–1218. doi: 10.1111/j.1365-246X.2007.03665.x.

Vöge, M. and Hort, M., 2009. Installation of a Doppler Radar monitoring system at Merapi Volcano, Indonesia. *Geoscience and Remote Sensing, IEEE Transactions on*, 47(1):251–271. doi: 10.1109/TGRS.2008.2002693.

Vöge, M., Hort, M. and Seyfried, R., 2005. Monitoring volcano eruptions and lava domes with Doppler radar. *EOS Trans Am Geophys Union*, 86(51):537, 541.

Voight, B. and Elsworth, D., 2000. Instability and collapse of hazardous gas-pressurized lava domes. *Geophys Res Lett*, 27(1):1–4. doi: 10.1029/1999GL008389.

Weibull, W., 1951. A statistical distribution function of wide applicability. *Journal of Applied Mechanics*, pages 293 – 297.

Wilson, L., Sparks, R. S. J., Huang, T. C. and Watkins, N. D., 1978. The control of volcanic column heights by eruption energetics and dynamics. *J Geophys Res*, 83(B4):1829 – 1836. doi: 10.1029/JB083iB04p01829.

Wohletz, K. H., Sheridan, M. F. and Brown, W. K., 1989. Particle size distributions and the sequential fragmentation/transport theory applied to volcanic ash. *J Geophys Res*, 94 (B11):15703–15721. doi: 10.1029/JB094iB11p15703.

Yamamoto, H., Watson, I. M., Phillips, J. C. and Bluth, G. J., 2008. Rise dynamics and relative ash distribution in vulcanian eruption plumes at Santiaguito Volcano, Guatemala, revealed using an ultraviolet imaging camera. *Geophys Res Lett*, 35:L08314. doi: 10.1029/2007GL032008.

Ziemen, F. Theoretische Betrachtungen zu Dopplerradarmessungen an Vulkanen. Master's thesis, Institut für Geophysik, Universität Hamburg, 2008. URL: http://www.mpimet.mpg.de/fileadmin/staff/ziemenflorian/diplomarbeit.pdf.

Zobin, V. M., Luhr, J. F., Taran, Y. A., Bretón, M., Cortés, A., Cruz-Reyna, S. D. L., Domínguez, T., Galindo, I., Gavilanes, J. C., Muñíz, J. J., Navarro, C., Ramírez, J. J., Reyes, G. A., Ursúa, M., Velasco, J., Alatorre, E. and Santiago, H., 2002. Overview of the 1997-2000 activity of Volcán de Colima, México. *J Volcanol Geotherm Res*, 117(1-2):1–19. ISSN 0377-0273. doi: 10.1016/S0377-0273(02)00232-9.

List of Figures

List of Tables

Acknowledgments — Danksagung

Ein großer Dank gebührt meinem Betreuer Prof. Dr. Matthias Hort, der, ohne es zu beabsichtigen, mit seiner Entscheidung nach Hamburg zu kommen, meinen Lebensweg geprägt hat. Ebenfalls danke ich Armin Freundt, dass er sich als Zweitgutachter zur Verfügung gestellt hat.

Danke an meine Vorgänger, Mitstreiter und Nachfolger in Sachen Dopplerradar, insbesondere (in the order of appearance):

Kristina Meier	mit der zusammen ich das Löten gelernt und so manche Nacht mit Versuchsprotokollen zugebracht habe,
Malte Voege	der mir unter anderem das Programmieren erst richtig beigebracht hat,
Alexander Gerst	der mir gezeigt hat, dass man nie genug Ersatzteile dabei haben kann,
Florian Ziemen	der mir so ganz nebenbei den effektiven Umgang mit Computern vermittelt hat und
Jörg Hasenclever	der mit Feuer und Köpfchen jede noch so fest sitzende Schraube wieder fit bekommen und damit mein Experiment gerettet hat.

Im Anschluss ein Dankeschön an die gesammte Arbeitsgruppe und an alle Mitarbeiter des Institut für Geophysik dafür, dass ihr mich all die Jahre unterstützt habt.

Der Firma Metek, und insbesondere Berndt Fischer und Gerhard Peters danke ich für die sehr gute Zusammenarbeit und die Unterstützung während des gesamten Projekts.

A special thanks goes to Nick Varley, for his effort and on-site support for many years. Furthermore I would like to thank John Stevenson and Florian Ziemen for maintaining the radar during the preliminary installation. All the students at CIIV that helped during the years are gratefully acknowledged: Hester, Erin, Andrew, Gemma, Adi, Laura, Martin, Sarah, Genevieve, Rose, Martin, Philip and Johannes. Special thanks go to Proteción Civil de Colima for providing a car and driver (thank you Edgar) during the final installation in February 2009. All cars, drivers and students made a tremendous contribution to the success of the installation.

Muchas gracias a Arturo Montalvo García por toda su ayuda durante la instalación del segundo radar. Estos WiFis si simples y geniales y las cajitas electronicas mágicas me han sirvado un montón.

Michael Herzog, Hans Graf, Christiane Textor und allen weiteren Entwicklern und Programmierern von ATHAM sei gedankt. Es war mir ein großes Vergnügen über Jahre hinweg Support und Unterstützung zu genießen und dafür nach Cambridge zu fahren :)

Un sentito ringraziamento a Augusto Neri e Tomaso Esposti Ongaro per avermi permesso di usare PDAC e per il supporto (a Pisa e online).

Diese Arbeit wurde zum Teil durch ein Stipendium der Universität Hamburg und die Deutsche Forschungsgemeinschaft DFG im Projekt Ho1411 20-1 finanziert.

Einen herzlichen Dank möchte ich Jörg Hasenclever aussprechen: Danke für alles!! Diese Arbeit wäre ohne deinen unermüdlichen Einsatz komplett unverständliches Kauderwelsch.

Meiner Mama und meiner Familie möchte ich für die Unterstützung und die positive Lebenseinstellung danken. Ohne euch hätte ich das nicht nur nicht geschafft, sondern wahrscheinlich nie versucht...

Zu allerletzt noch einen Dank an die Swingtonics, die mir jeden Montag abend einen Grund geliefert haben, zu einer „normalen“ Zeit aus dem Büro zu verschwinden.

Schließen möchte ich mit einem Zitat einer Email aus Freiberg, der ich mich in vollem Umfang anschließe:

> danke, danke, danke
>
> @–)—–